DEVELOPMENT OF AN ADDITIVE MANUFACTURING PROCESSING ROUTE FOR HIGH ENTROPY ALLOYS USING POWDER BED FUSION

By

PENG CHEN

A thesis submitted to the
University of Birmingham
For the degree of
DOCTOR OF PHILOSOPHY

School of Metallurgy and Materials
College of Engineering and Physical Sciences
University of Birmingham
November 2021

Abstract

Laser powder bed fusion (LPBF) is an additive manufacturing (AM) technique that can produce components from digital models in a layer-by-layer fashion using metallic powders. The customisation of pre-alloyed powders used by LPBF is expensive and time-consuming, making LPBF not ideal for alloy development. In-situ alloying approaches using blended powders as raw materials are therefore carried out to shorten the alloy development process. Recently, high entropy alloys (HEAs) have drawn growing scientific attention. The HEA concept is of great compositional flexibility, allowing vast composition spaces and advanced properties to be explored. The CoCrFeMnNi HEA has been widely studied as a representative face-centred-cubic (FCC) HEA. The feasibility of the LPBF in-situ fabrication of the CoCrFeMnNi HEA and its body-centred-cubic (BCC) variation, AlCoCrFeNi, is the subject of this study.

This study aims to develop an AM processing route for HEAs through LPBF in-situ alloying. Elemental Mn and Al powders were blended with pre-alloyed CoCrFeNi powder for quasi-equiatomic composition, respectively. The in-situ alloying printability was evaluated via the parametric study based on densification and defect assessments. The chemical homogenisation and phase formation in the as-built samples was examined and correlated to the laser heat input. The results showed that Mn could be in-situ alloyed into the FCC CoCrFeNi matrix with homogeneity, indicating good printability of the CoCrFeMnNi HEA. However, the attempt to in-situ fabricate the AlCoCrFeNi HEA failed to produce samples free of cracking/porosity, despite the investigation of a wide range of parameters. The resultant defects and Al segregations suggested that the BCC HEA cannot be realised using this approach.

The tensile and compression properties of the in-situ alloyed CoCrFeMnNi HEA were compared with the LPBFed CoCrFeMnNi HEA fabricated using pre-alloyed powder. The tensile strength was reinforced by the oxide-dispersion-strengthened (ODS) effect, because Mn oxides were introduced during the process. Submicron voids were observed around the oxides in the deformed samples, which were responsible for the early failure during the tensile deformation. The Mn oxides were identified as MnO and Mn_2O_3 and their forming mechanisms were analysed.

To understand the underlying mechanisms of the LPBF in-situ alloying processes, elemental homogenisation and grain development were further investigated through single-track, single-layer and three-layer experiments. The experimental meltpool dimensions were compared with the predicted ones, showing that the processing window for in-situ alloying was operated in the keyhole mode. Remelting was found to be the main mechanism of elemental homogenisation. Crystalline characteristics were found to be inherited during the accumulation of tracks, reflecting parameter-structure correlations.

In conclusion, the results of this study have shown that LPBF in-situ alloying had the potential for HEA development, and raised topics for further research. A comprehensive understanding of the process will help to shorten the period from alloy design to microstructural tailoring.

Acknowledgements

First of all, as a student of the Joint PhD Training Program offered by the University of Birmingham (UoB) and Southern University of Science and Technology (SUSTech), I would like to thank the UoB and SUSTech for their support for my studies in both universities. The experience in different universities and countries will be a precious memory in my life.

I would like to express gratitude to my supervisor at the UoB, *Prof. Moataz Attallah*. You are always inspiring and cheerful. Your knowledge and guidance have helped me to get over many difficulties and extended my scientific scope. Your encouragement and support can always recharge me to move on. Working with you has become a pleasant experience in this academic journey. I am also deeply grateful to *Dr. Ming Yan*, my supervisor at the SUSTech. You offered me the great opportunity to become a researcher. Over the past five years, you have always been available to help me. Your hardworking and enthusiasm will be an example to motivate me in the future.

Great thanks to my colleagues from the UoB and SUSTech: *Dr. Yinghao Zhou* for his selfless help and expertise, especially in microstructural characterisation; *Dr. Sheng Li* for the training and knowledge of additive manufacturing, as well as the Chinese New Year's dinner; *Mr. Ranxi Duan* for introducing the lab and campus, and more importantly helping me to get used to the study life at the UoB; *Dr. Shulong Ye* for his patient guide to chemical analysis and heat treatments. I would also like to express my appreciation to *Dr. Sam Cruchley, Dr. Luke Carter, Dr. Amanda Field, Dr. Rachel Jennings, Dr. Nicholas Adkins, Mr. Xiyu Yao, Mr. Dawei Wang,* and *Mr. Yangping Dong* for their expertise and kindly assistance. Special thanks to *Ms. Feng Huang* and *Ms. Kathleen Waldron* for their timely support. It has been a pleasure to work in the groups at the UoB and SUSTech.

I am also grateful to *Dr. Edwin Mayes* at the RMIT University for his efforts and expertise in TEM analysis; *Dr. Chaolin Tan* at the South China University of Technology for sharing his experience in research; *Mr. Junquan Chen* and *Mr. Ke Ma* at the Shenzhen University for the assistance in nano-indentation.

I would also like to thank my friends. It has been a long journey, but with my friends, it has never been lonely.

Finally, I would like to express my heartful thanks to my family. They have always respected and supported my choices. They are the reason that I can move forward without worries.

Table of Contents

List of Abbreviations

Term	Description
AM	Additive Manufacturing
BCC	Body-Centred-Cubic
BD	Building Direction
BF	Bright-Field
BSE	Back-Scattered Electron
CAD	Computer-Aided Design
CALPHAD	Calculation Of Phase Diagrams
CCT	Continuous Cooling Transformation
CS	Cross-Section
DED	Directed Energy Deposition
DED-L	Laser-Based Directed Energy Deposition
DF	Dark-Field
DLD	Directed Laser Deposition
DSC	Differential Scanning Calorimetry
Dv	Volume Distribution
EBSD	Electron Back-Scattered Diffraction
ECCI	Electron Channelling Contrast Imaging
EDM	Electrical Discharge Machining
EDS	Energy Dispersive Spectrometer/Spectroscopy
EPMA	Electron Probe Micro Analyser
FCC	Face-Centred-Cubic
FIB	Focused Ion Beam
FWHM	Full-Width at Half-Maximum
HCP	Hexagonal-Close-Packed
HEA	High Entropy Alloy
HIP	Hot Isostatic Pressing
ICP-OES	Inductively Coupled Plasma-Optical Emission Spectrometry
IPF	Inverse Pole Figure
KAM	Kernel Average Misorientation

LED	Linear Energy Density
LPBF	Laser Powder Bed Fusion
MEA	Medium Entropy Alloy
MPEA	Multi-Principal Element Alloy
ODS	Oxide-Dispersion-Strengthened
OM	Optical Microscope
PBF	Powder Bed Fusion
PF	Pole Figure
RT	Room Temperature
SAED	Selected Area Electron Diffraction
SD	Scanning Direction
SE	Secondary Electron
SEBM	Selective Electron Beam Melting
SEM	Scanning Electron Microscopy/Microscope
SFE	Stacking Fault Energy
SLM	Selective Laser Melting
STEM	Scanning Transmission Electron Microscopy
TD	Transverse Direction
TEM	Transmission Electron Microscopy/Microscope
TTT	Temperature-Time-Transformation
TWIP	Twinning-Induced Plasticity
VED	Volumetric Energy Density
XPS	X-Ray Photoelectron Spectroscopy
XRD	X-Ray Diffraction
XRF	X-Ray Fluorescence

Chapter 1: Introduction

This chapter provides a brief background of laser powder bed fusion (LPBF) and high entropy alloys (HEAs), as well as the significance of LPBF in-situ alloying for the HEA development. The aim and objectives of this study are then raised. The thesis is presented in an alternative format, and the main chapters are published papers associated with specific objectives.

1.1 Laser Powder Bed Fusion as an Additive Manufacturing Technique

Additive manufacturing (AM) is the process that fabricates components from 3D models by joining raw materials in the forms of powder, filament, sheet, or liquid, which is opposite to conventional subtractive manufacturing [1]. To produce components with complex geometries by conventional routes, some geometrically functional structures must compromise with the capability of manufacturing techniques. But the production can still be time-cost and expensive, especially at the developing and validating stage of new designs. The net-shape capability and freedom of design make AM techniques ideal for rapid prototyping. Furthermore, by topological optimisation of structures, AM products can realise competitive performance with fewer components, which could lower the cost of massive production.

Laser powder bed fusion (LPBF), also known as selective laser melting (SLM), is a mainstream AM technique to produce metallic components with high forming accuracy. Before the LPBF process, a 3D model is firstly sliced into layers of 2D patterns by slicing software, and the sliced patterns consist of 1D routes. At the beginning of the process, a powder layer is spread on a substrate and scanned by laser beams to form a 2D pattern. Then the following layer is recoated on the previous layer to produce the next 2D pattern. This process repeats until the entire 3D geometry is built. Finally, the as-built component needs to be removed from the substrate for post-treatments. Meanwhile, the unmelted powder can be collected for recycling. To ensure the good printability of the process, the raw powders used by LPBF are mostly pre-alloyed powders with spherical shapes. Since the customisation of pre-alloyed powders demands time and cost, LPBF is not considered as an ideal alloy development technique in the first place.

1.2 High Entropy Alloys

High entropy alloys (HEAs) have drawn growing attention in the field of metallic materials over the past decade. On the contrary to conventional alloy systems with a single principal element, the HEA concept allows multiple principal elements to co-exist in one HEA system, each concentration between 5 and 35 at. %, and form a single or dual-phased solid solution. Thus, HEAs are also referred to as multi-principal element alloys (MPEAs) [2]. The discovery of HEAs reveals the unexplored central areas in phase diagrams and brings new potential for alloy development. With different compositions, the properties of HEAs can cover or even extend the knowing property maps of metallic materials.

As a blooming field of alloy development, the research of HEAs requires compositional modification frequently. Conventionally, HEAs are mostly in the forms of ingot or film produced via arc melting or deposition methods to ensure the chemistry homogeneity. However, the geometric flexibility of such methods is limited and often requires considerable post-machining for further applications. To efficiently produce HEAs with compositional and geometric flexibility is a fundamental demand regarding the development of HEAs.

1.3 Significance and Challenges of In-Situ Alloying

By introducing additional elements using elemental powders, in-situ alloying has the potential for combining the compositional flexibility of HEAs and the geometric flexibility of LPBF.

The compositions of blended powders are more flexible than pre-alloyed powders. Therefore, the efficiency of alloy development can be improved by using blended powders. Moreover, the cost of powders can be saved as well. The high cooling rate (up to 10^6 K/s) during the LPBF process can restrain the chemical segregation during the solidification of HEAs [1]. Regarding the prototyping of HEA parts, it will enjoy the advanced net-shape capability of LPBF.

The use of blended powder for LPBF in-situ alloying is still at an initial stage for academia [3]. Two significant challenges have been raised:

- The printability of blended powders is often limited compared with pre-alloyed powders.
- Phase formation and chemical homogeneity are compromised.

Unlike single-principal element alloys with minor contents of additional elements, the compositions of HEAs are mostly quasi-equiatomic, which means a considerable ratio of alloying elements needs to be introduced by in-situ alloying, hence making the elemental homogenisation even challenging.

1.4 Aim and Objectives

To realise the LPBF in-situ alloying of HEAs, the overall aim of this thesis is presented as follows:

To develop an additive manufacturing route to produce HEAs with microstructural homogenisation and outstanding mechanical properties via LPBF.

As a vast number of alloys exist in the HEA family, this research starts with the notable FCC CoCrFeMnNi HEA and its BCC variation, AlCoCrFeNi HEA. The FCC CoCrFeNi HEA is selected as the base alloy, while Mn and Al are the alloying elements. To evaluate the feasibility of LPBF in-situ alloying, the aim is separated into concise objectives:

Objective 1: Optimise LPBF parameters to fabricate bulk HEAs from blended powders.

Objective 2: Characterise the phase formation and elemental homogenisation of the in-situ alloyed HEAs.

Objective 3: Test the mechanical properties of the in-situ alloyed HEAs and investigate structure-property correlations.

Objective 4: Reveal the underlying mechanisms during the LPBF in-situ alloying processes.

1.5 Thesis Structure

The thesis is presented in an alternative format, including published papers that correlate to the specific objectives. The thesis structure is detailed as follows:

Chapter 1: General introduction of the thesis

Chapter 2: Literature review, including the backgrounds of HEAs, AM, and in-situ alloying

Chapter 3: Experiments, to describe the details of the materials and methods used in this study

Chapter 4: Fabricating CoCrFeMnNi high entropy alloy via selective laser melting in-situ alloying (Paper A, *Objectives 1 & 2*)

Chapter 5: In-situ alloying of AlCoCrFeNi high entropy alloy via laser powder bed fusion with pre-heating (Paper B, *Objectives 1 & 2*)

Chapter 6: In-situ alloyed, oxide-dispersion-strengthened CoCrFeMnNi high entropy alloy fabricated via laser powder bed fusion (Paper C, *Objective 3*)

Chapter 7: In-situ alloyed CoCrFeMnNi high entropy alloy: microstructural development in laser powder bed fusion (Paper D, *Objective 4*)

Chapter 8: Conclusions, general discussion and future work, to summarise the important conclusions, and raise further possible topics

The processing development and sample preparation of papers A, B and C were carried out at the UoB, while microstructural characterisation and mechanical testing were carried out at the UoB and SUSTech. All the experiments in Paper D were conducted at the SUSTech.

1.6 List of Publications and Relevant Contributions

Paper A: Fabricating CoCrFeMnNi high entropy alloy via selective laser melting in-situ alloying

Peng Chen, Sheng Li, Yinghao Zhou, Ming Yan, Moataz M. Attallah

Journal of Materials Science & Technology, 43 (2020) 40-43.

Peng Chen was the lead investigator, designed and performed the majority of experiments, analyses, drafted the original article. Co-authors contributed to LPBF preparation, mechanical testing, conceptualisation, supervision, reviewing and editing the manuscript.

Paper B: In-situ alloying of AlCoCrFeNi high entropy alloy via laser powder bed fusion with pre-heating

Peng Chen, Sheng Li, Ming Yan, Moataz M. Attallah

Additive Manufacturing Letters, under review

Peng Chen was the lead investigator, designed and performed the majority of experiments, analyses, drafted the original article. Co-authors contributed to LPBF preparation, mechanical testing, conceptualisation, supervision, reviewing and editing the manuscript.

Paper C: In-situ alloyed, oxide-dispersion-strengthened CoCrFeMnNi high entropy alloy fabricated via laser powder bed fusion

Peng Chen, Chao Yang, Sheng Li, Moataz M. Attallah, Ming Yan

Materials and Design, 194 (2020) 108966.

Peng Chen was the lead investigator, designed and performed the majority of experiments, analyses, drafted the original article. Co-authors contributed to LPBF preparation, mechanical testing, TEM characterisation, conceptualisation, supervision, reviewing and editing the manuscript.

Paper D: In-situ alloyed CoCrFeMnNi high entropy alloy: microstructural development in laser powder bed fusion

Peng Chen, Xiyu Yao, Moataz M. Attallah, Ming Yan

Journal of Materials Science & Technology, in press.

Peng Chen was the lead investigator, designed and performed all the experiments, analyses, drafted the original article. Co-authors contributed to SEM characterisation, conceptualisation, supervision, reviewing and editing the manuscript.

1.7 References

[1] T. DebRoy, H.L. Wei, J.S. Zuback, T. Mukherjee, J.W. Elmer, J.O. Milewski, A.M. Beese, A. Wilson-Heid, A. De, W. Zhang, Additive manufacturing of metallic components – Process, structure and properties, Progress in Materials Science 92 (2018) 112-224. http://doi.org/10.1016/j.pmatsci.2017.10.001.

[2] D.B. Miracle, O.N. Senkov, A critical review of high entropy alloys and related concepts, Acta Materialia 122 (2017) 448-511. http://doi.org/10.1016/j.actamat.2016.08.081.

[3] S.L. Sing, S. Huang, G.D. Goh, G.L. Goh, C.F. Tey, J.H.K. Tan, W.Y. Yeong, Emerging metallic systems for additive manufacturing: In-situ alloying and multi-metal processing in laser powder bed fusion, Progress in Materials Science 119 (2021) 100795. http://doi.org/10.1016/j.pmatsci.2021.100795.

Chapter 2: Literature Review

This chapter reviews the literature on the fundamental metallurgy of HEAs, specifically the CoCrFeMnNi and AlCoCrFeNi HEAs; metal AM techniques, specifically the features of LPBF; the AM approaches to HEAs, specifically LPBF of CoCrFeNi based-HEAs; LPBF in-situ alloying of HEAs; the ODS alloys produced via LPBF. Gaps in the literature are summarised at the end of this chapter.

2.1 High Entropy Alloys

High entropy alloys (HEAs), as a new class of alloys, were firstly reported independently by Yeh et al. [1] and Cantor et al. [2] in 2004. HEAs are also introduced as multi-principal element alloys (MPEAs), multi-component alloys, or complex concentrated alloys [3]. One early compositional definition of HEAs is "the alloys composed of five or more principal elements with equiatomic compositions". Moreover, single-phase solid solutions, like face-centred-cubic (FCC), body-centred-cubic (BCC) or hexagonal-close-packed (HCP), can form with such combinations instead of complex intermetallics, e.g., FCC CoCrFeMnNi HEA and BCC VNbMoTaW HEA [4-6]. Figure 2.1 presents the representative crystalline structures of HEAs, where the atoms of principal elements are randomly distributed. In the following studies of HEAs, the compositional definition has been expanded to "the concentrations of principal elements between 5 and 35 at. %", and the expanded definition has been widely adopted in the literature [6-11].

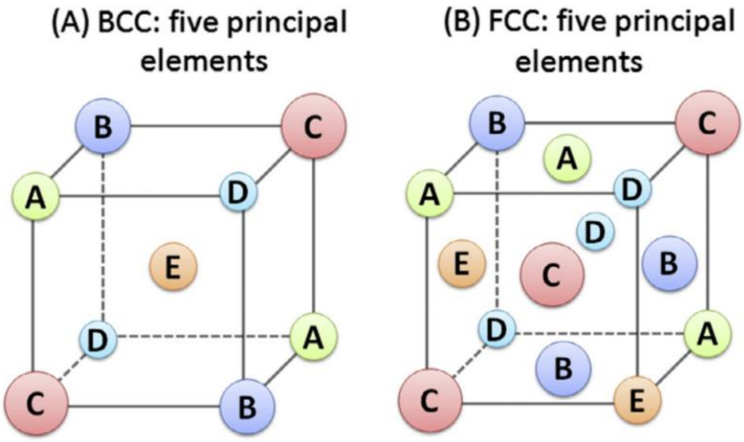

Figure 2.1 Schematics of (a) BCC and (b) FCC crystalline solid solutions composed of multi-principal elements [4].

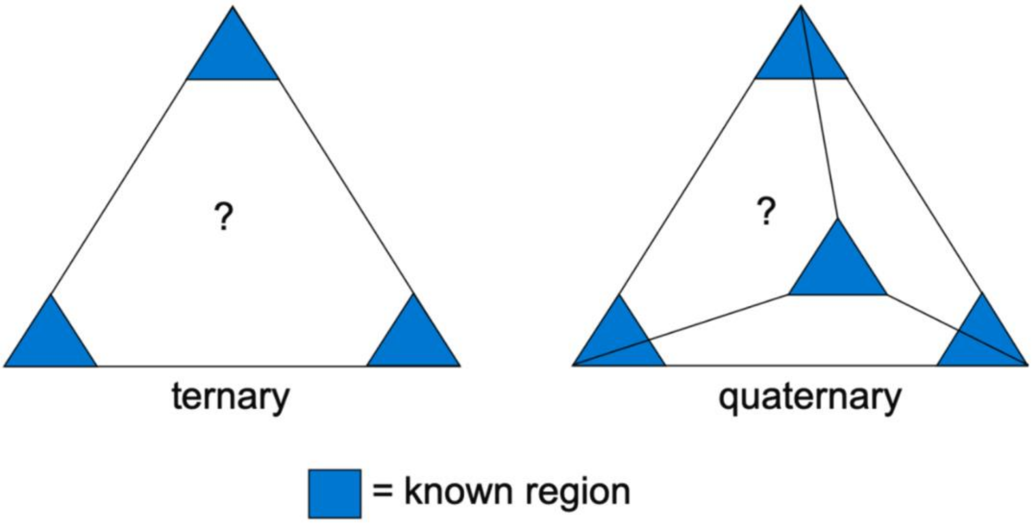

Figure 2.2 Schematics of ternary and quaternary phase diagrams showing the known and unexplored regions [12].

Unlike most conventional alloy systems with single-principal elements, i.e., steels, Ti alloys, and Ni alloys, which cluster at the corners of phase diagrams, the HEA concept allows researchers to explore the vast compositions near the centres of phase diagrams, especially in quaternary and higher-order systems, as shown in Figure 2.2. Moreover, the phase formation is no longer restricted to single-phase solid solutions. HEAs with dual-phase solid solutions, intermetallics, carbides/oxides, short-range ordering, etc., have been reported [13-20]. The compositional flexibility of HEAs has raised novel possibilities of alloy development. By 2017, a statistic has shown 408 HEAs been reported, and the number has been growing over the recent years [5]. The frequency of elements in the reported HEAs is summarised in Figure 2.3.

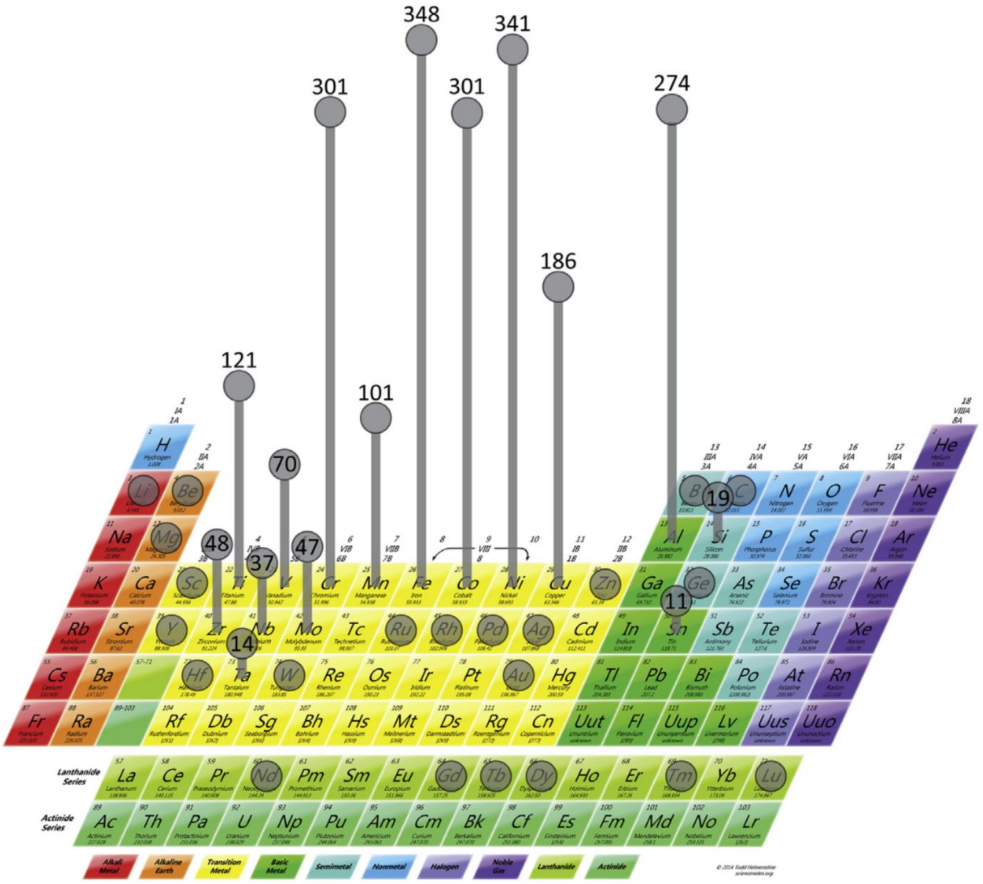

Figure 2.3 The frequency of elements in HEAs (by 2017) [5].

2.1.1 Terminology

The formation of single-phase solid solutions with quasi-equiatomic compositions is a novel feature of HEAs. Yeh et al. [1] attributed it to the high configurational entropy of mixing (ΔS_{mix})

of high-order systems. The ideal ΔS_{mix} of an equiatomic alloy composed of x elements is given by:

$$\Delta S_{mix} = R\ln x \tag{2.1}$$

where R is the Boltzmann's constant, then the relative Gibbs free energy (ΔG_{mix}) of forming an ideal solid solution is:

$$\Delta G_{mix} = \Delta H_{mix} - T\Delta S_{mix} = \Delta H_{mix} - TR\ln x \tag{2.2}$$

where ΔH_{mix} is the enthalpy of mixing, and T is the temperature. For quaternary and quinary systems, the ΔS_{mix} are $1.39R$ and $1.61R$, respectively. As the number of principal elements increases, the entropic contribution ($-T\Delta S_{mix}$) to the free energy also increases. Consequently, the formation of other intermetallics is suppressed at elevated temperatures, see Figure 2.4. Therefore, the alloys with five or more principal elements were defined as high entropy alloys at the beginning stage [1, 6, 21]. More recent studies have found that the solid solution phases of many equiatomic HEAs were metastable at room temperature, e.g., some HEAs are initially single-phase, but intermetallics can participate from the matrix after annealing [22-25]. Some ternary and quaternary systems without equiatomic compositions can also form single-phase solid solutions, which are not well explained by the high-entropy hypothesis [26-28]. The efforts to understand and predict the phase formation of HEAs are still being carried out. Nevertheless, the term “high entropy alloy” is catchy and has been widely accepted by researchers.

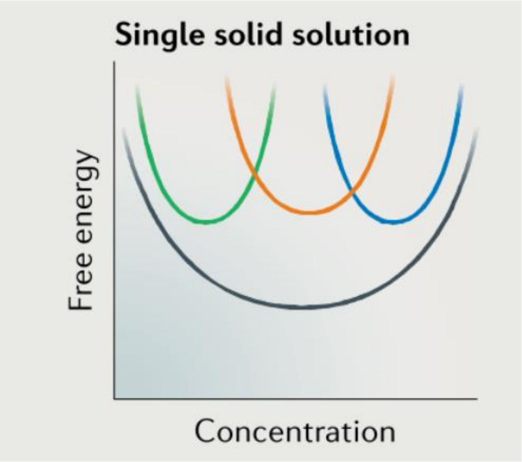

Figure 2.4 Schematic of an ideal single-phase solution of a ternary system, where the free energy of forming a single solid solution (black) suppresses other intermetallics (green, red and blue) [6].

2.1.2 CoCrFeMnNi HEA

Among the vast number of HEAs, the CoCrFeMnNi HEA, also known as the Cantor alloy, is one of the most extensively studied HEAs by far. It is a notable HEA with a quinary equiatomic composition that forms an FCC single-phase solid solution, whose lattice parameter is ~0.359 nm, see Figure 2.5. This alloy was initially discovered as an FCC single-phase precipitation in a twenty-component alloy studied by Cantor et al. [3]. By far, a vast number of alloys have been developed from the original Cantor alloy.

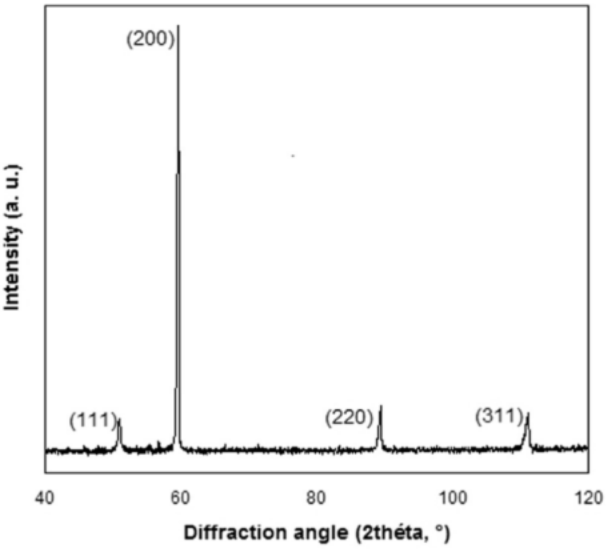

Figure 2.5 A representative X-ray diffraction (XRD) spectrum of equiatomic CoCrFeMnNi HEA [29].

2.1.2.1 FCC stability of CoCrFeMnNi variations

Though the initial composition of Cantor alloy was equiatomic, Brocq et al. [29-31] further investigated the compositional tolerance of the CoCrFeMnNi system by modifying the content of individual elements. The results showed that the modified alloys could maintain an FCC single phase in wide compositional ranges (at.), i.e.,10–50% of Co, 0–25% of Cr, 0–50% of Fe, 0–50% of Mn and 10–100% of Ni. Quaternary alloys including CoFeMnNi, CoCrFeNi and CoCrMnNi, ternary alloys including CoCrNi and FeNiCo; and pure Ni are contained in the FCC single-phase space of the CoCrFeMnNi system.

Furthermore, the FCC single-phase space has been further expanded via adding equiatomic elements, e.g., Cu, Nb; replacing elements, e.g., replacing Mn with Cu; adding non-equiatomic elements, e.g., 2 at. % of Ti; replacing with non-equiatomic elements, e.g., replacing Mn with 11 at. % of Al [12].

2.1.2.2 Microstructures of CoCrFeMnNi HEA

The CoCrFeMnNi HEA produced by casting possesses a dendritic structure as solidified, with a typical <001> texture [2, 12]. Figure 2.6 presents a typical microstructure of the as-cast CoCrFeMnNi HEA. Elemental segregations with minor compositional variations can be observed in the dendrite spines and interdendritic areas due to the different melting points of the composing elements. The dendrites are enriched in the elements with high melting points, i.e., Co, Cr and Fe, while the interdendritic areas are enriched in the rest elements with low melting points [29]. To achieve an atomic-level random solution, such segregations can be fully homogenised after annealing at 1100 °C for 6 h and followed by rapid cooling. Brocq et al. [29] measured the solidus and liquidus temperatures of the CoCrFeMnNi HEA by differential scanning calorimetry (DSC), indicating a solidification range ΔT = 50 °C between its liquidus temperature T_l = 1340 °C and solidus temperature T_s = 1290 °C, see Figure 2.7(a).

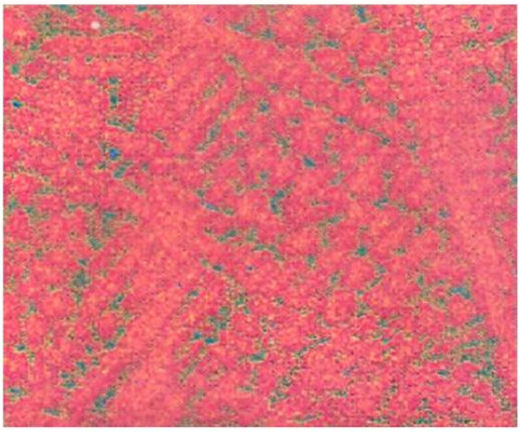

Figure 2.6 SEM image with corresponding energy dispersive spectrometer (EDS) mapping showing the dendritic Fe segregation (red) in casted CoCrFeMnNi HEA [12].

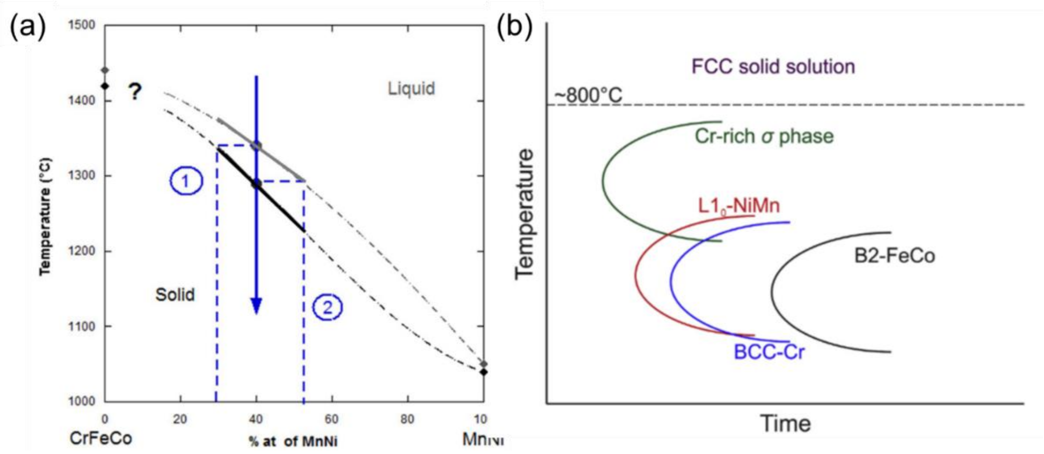

Figure 2.7 (a) Schematic phase diagram at the solidification temperature [29] and (b) hypothesised temperature-time-transformation (TTT) curves of CoCrFeMnNi HEA [32].

By the calculation of phase diagrams (CALPHAD), the CoCrFeMnNi HEA is suggested to be FCC-stable at temperatures above 1100 ℃. Meanwhile, the alloy is also predicted to be multi-phase at room temperature instead of the FCC single phase [30]. Cr-rich precipitates including $M_{23}C_6$ carbide and topologically close-packed σ phase have been observed at the grain boundaries of casted CoCrFeMnNi HEA aged at 700 ℃ for 500 h [22]. Otto et al. [32] carried out 500-day annealing at temperatures of 500, 700 and 900 ℃ and plotted the temperature-time-transformation (TTT) curves based on their results, see Figure 2.7(b). Besides the σ phase, Cr-rich BCC, MnNi-rich $L1_0$ and FeCo-rich B2 phases were observed in the sample annealed at 500 ℃. Although such secondary precipitates cannot form in as-cast CoCrFeMnNi HEAs, decomposition could be promoted in the CoCrFeMnNi HEAs with nanocrystalline structures [23]. Taken together, the CoCrFeMnNi HEA is thermal-dynamically stable at high temperatures (> 800 ℃), and the FCC single phase can be retained as a metastable state at room temperature with regular cooling rates (e.g., arc melting, casting) [5, 6, 30].

2.1.2.3 Mechanical properties of CoCrFeMnNi HEA

Otto et al. [33] investigated the tensile properties of the CoCrFeMnNi HEA with grain sizes of 4.4, 50 and 155 μm at different temperatures. The samples with 50 and 155-μm grain sizes performed similarly in the tests. Thus the representative tensile curves of the samples with 4.4 and 155-μm grain sizes are provided in Figures 2.8(a) and (b), respectively. The yield strength and ultimate tensile strength increased as the temperature (T) decreased from 800 to –196 °C (1073 to 77 K). One exception was that the alloy with 4.4-μm grain size showed no work hardening at 800 °C [33]. It was noted that both the tensile strength and tensile elongation improved dramatically with prolonged work hardening at the cryogenic temperature, reaching ~1 GPa and ~100%, respectively. The strength of the CoCrFeMnNi HEA with 4.4-μm grain size was overall improved compared with 155-μm grain size, following the Hall-Petch relationship, as shown below:

$$\sigma_{HP}=\sigma_0+kd^{-1/2} \tag{2.3}$$

σ_{HP} is the Hall-Petch contribution to the yield strength, σ_0 stands for the friction stress, k stands for the Hall-Petch coefficient, and d denotes the grain size. The k and σ_0 summarised by Otto et al. are listed in

Table 2.1 [33]. A recent study also suggested a similar value of the Hall-Petch coefficient (490 MPa/$\mu m^{1/2}$) at room temperature, but a slightly higher value of friction stress (194 MPa) [34].

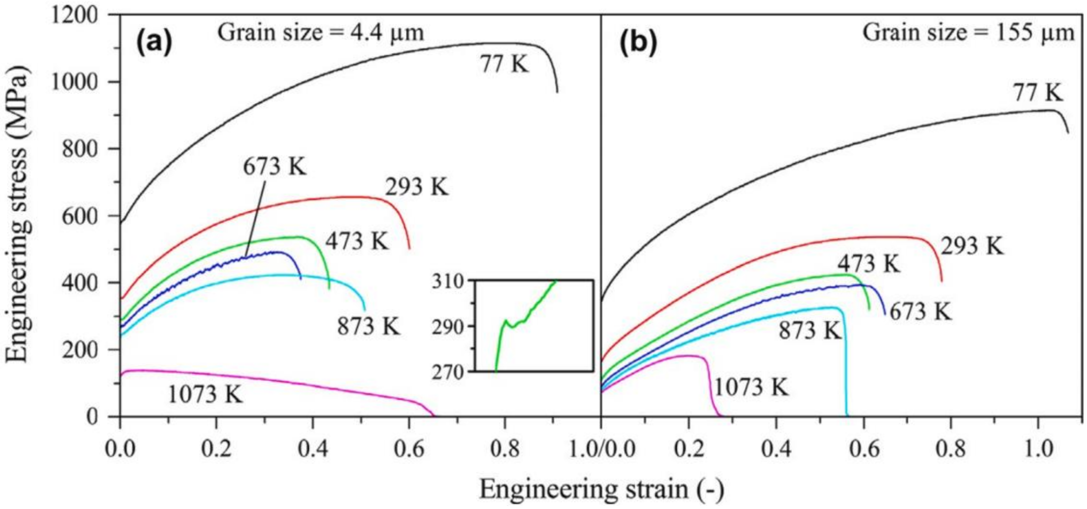

Figure 2.8 Typical tensile curves of the homogeneous equiaxed CoCrFeMnNi HEAs with grain sizes of (a) 4.4 μm and (b) 155 μm, measured at the temperatures from –196 to 800 °C (77 to 1073 K) [33].

Table 2.1 Values of friction stress σ_0 and the Hall-Petch coefficient k in the Hall-Petch relationship at different temperatures [33].

T (K)	σ_0 (MPa)	k (MPa/μm$^{1/2}$)
77	310	538
293	125	494
473	83	425
673	57	436
873	43	421
1073	69	127

The dislocation accumulation during deformation has been further analysed by transmission electron microscopy (TEM). At the early stage of plastic deformation, the planar glide of 1/2<110> dislocations on (111) planes occurs exclusively. Then the dislocations split into

1/6<112> Shockley partials with stacking faults and finally pile up, forming cell structures at high strain [33]. The multiplication and interaction of dislocations lead to the Taylor work hardening during deformation, which can be expressed as follows [35]:

$$\sigma_{dis}=\alpha MGb\sqrt{\rho_{dis}} \tag{2.4}$$

where σ_{dis} denotes the Taylor work hardening induced via dislocations, α is a constant, M is the Taylor factor, G is the shear modulus, b is the Burgers vector, and ρ_{dis} is the density of dislocation. In addition, nano-twinning was observed in the CoCrFeMnNi HEAs deformed at room temperature or above. However, it was initiated close to the necking and rarely contributed to work hardening [33].

Regarding the deformation at the cryogenic temperature, the strength and ductility are significantly improved due to the intensive nano-twinning initiated at the early stage of deformation, which introduces an additional deformation mechanism, namely the twinning-induced plasticity (TWIP) [36]. Compared with other FCC alloys, the twinning ability of the CoCrFeMnNi HEA is improved significantly due to the reduction of stacking fault energy (SFE) at the cryogenic temperature, which lowers the critical stress required by the formation of twinning [12, 37-39]. Consequently, the alloy is strengthened by the increased grain boundaries due to the dynamic Hall-Petch effect. In general, the CoCrFeMnNi HEA possesses outstanding mechanical properties at the cryogenic temperature [33, 36]. Moreover, a reduction variation of the CoCrFeMnNi HEA, the CrCoNi medium entropy alloy (MEA), was reported as one of the toughest materials (270 MPa·m$^{1/2}$), as shown in Figure 2.9 [40].

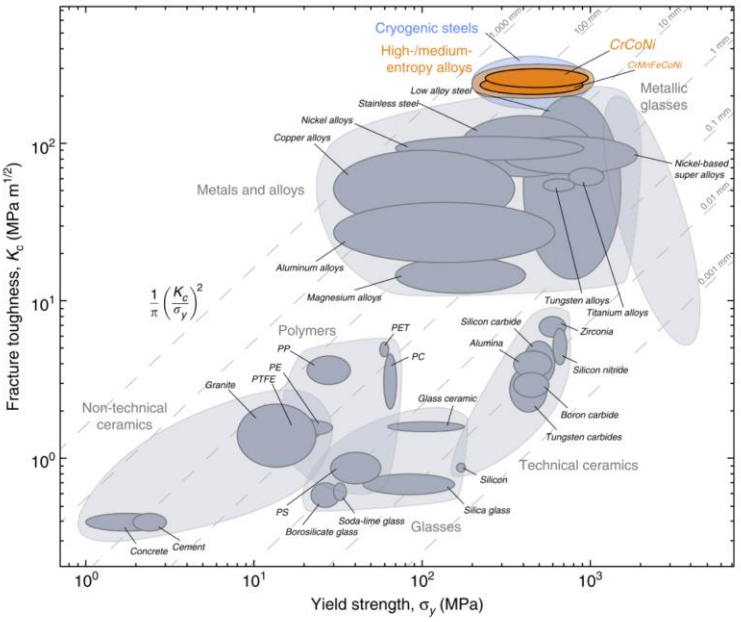

Figure 2.9 Ashby map showing the fracture toughness and yield strength of different materials, indicating the CrCoNi medium entropy alloy (MEA) as one of the toughest materials [40].

In conclusion, the deformation mechanisms of CoCrFeMnNi HEA share similarities with pure FCC metals. But the strength and work hardening rate are improved due to the local lattice distortions in the HEA matrix [12]. However, at the cryogenic temperature, its mechanical properties are distinct from pure FCC metals and can be comparable to some best cryogenic alloys [36]. More importantly, different mechanisms could be tuned to develop new alloys based on the vast compositional space of the HEA system [37, 41, 42]. For example, an oxide-dispersion-strengthened (ODS) CoCrFeMnNi HEA was fabricated via mechanical alloying, and its strength was improved by 30% and 70%, respectively, at room temperature and 800 °C, showing effective dispersion strengthening [43].

2.1.3 Al_xCoCrFeNi HEA system

By replacing the Mn in the CoCrFeMnNi HEA with Al, and further varying the content of Al from 0 to equiatomic or more, the Al_xCoCrFeNi HEA system can transform from FCC single-phase to FCC + BCC dual-phase, and finally, BCC single-phase, as shown in Figure 2.10(a) [17, 44-46]. The BCC transformation starts from $x = 0.3$ and the full BCC transformation can be realised at $x = 0.85$ in the Al_xCoCrFeNi HEAs fabricated via directed laser deposition (DLD) [44]. The lattice parameter changes from 0.359 nm of the FCC phase to 0.288 nm of the BCC phase [45]. The FCC-to-BCC transformation is attributed to the lattice distortion induced by Al. Since Al has a significantly larger atomic size than the rest elements, the alloy tends to form a BCC phase with a relatively low atomic-packing efficiency instead of a close-packed FCC structure as the Al content increases [17]. It is also observed that an ordered B2 phase enriched in Al-Ni coexists with the disordered BCC matrix [47]. Furthermore, the formation of BCC and B2 phases favours cooling conditions such as water quenching and air cooling, while FCC and σ phases can precipitate in the BCC matrix at a low cooling rate (1 K/s), as shown in Figure 2.10(b) [48]. In general, for the CoCrFeMnNi and AlCoCrFeNi HEAs, the equiatomic FCC and BCC phases are meta-stable at room temperature. However, the formation of single-phase solid solutions is still expected at the high cooling rates of AM techniques.

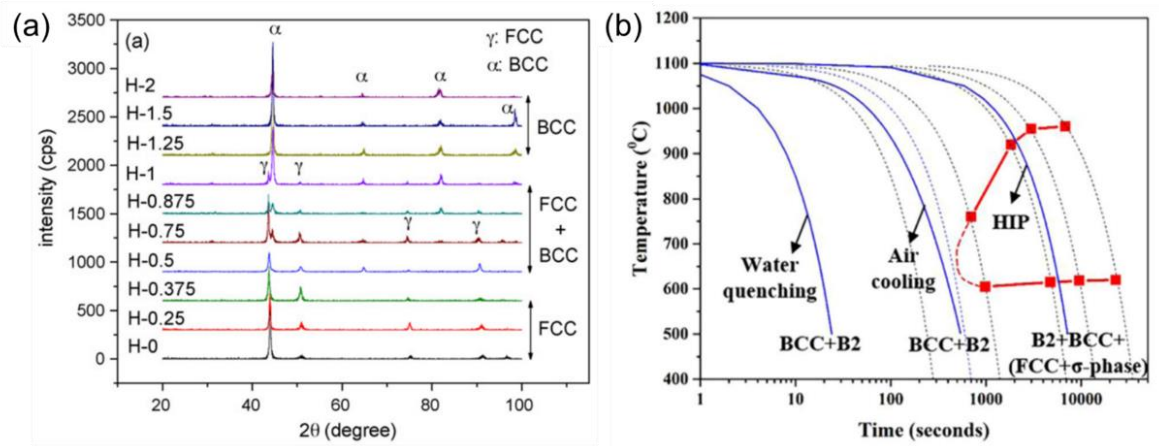

Figure 2.10 (a) XRD spectra of arc melted $Al_xCoCrFeNi$ HEAs with x (H) varies from 0 to 2, and (b) continuous cooling transformation (CCT) diagram of arc melted $Al_{0.85}CoCrFeNi$ HEA [45, 48].

Along with the phase transformation, the mechanical properties of the $Al_xCoCrFeNi$ HEAs also change dramatically. Microhardness increases gradually from 113 to 517 HV as the phase transforms from FCC to BCC, see Figure 2.11(a) [47]. In tensile testing, as shown in Figure 2.11(b), the FCC-dominated $Al_{0.3}CoCrFeNi$ HEA shows a yield strength of 210 MPa and outstanding ductility with a fracture elongation of 97%. With increasing Al content, the content of the BCC phase (36%) in the $Al_{0.7}CoCrFeNi$ HEA increases and the yield strength improves to 600 MPa, but the fracture elongation decreases to 8%, indicating poor ductility [46]. In general, the $Al_xCoCrFeNi$ HEA system transforms from ductile to brittle as the dominant phase in the matrix changes from FCC to BCC.

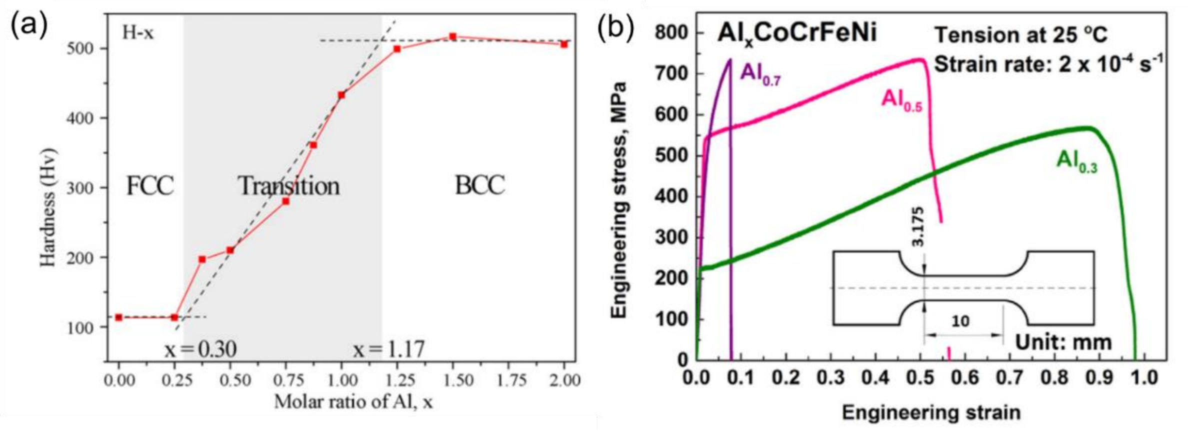

Figure 2.11 (a) Microhardness and (b) tensile curves of arc-melted Al$_x$CoCrFeNi HEAs [46, 47].

2.2 Additive Manufacturing of Metallic Materials

2.2.1 General introduction

Additive manufacturing (AM), also referred to as 3D printing, is a collective name to describe the techniques that produce 3D components from computer-aided design (CAD) models by progressively adding materials. Without the limits of machining capabilities and requirements of moulds, AM techniques provide advantages of rapid prototyping, customisation, and structural optimisation [49-51]. Powder bed fusion (PBF) and directed energy deposition (DED) are the two mainstream categories of AM techniques for metallic materials, and the techniques can be further classified regarding the heat sources employed by the processes, e.g., laser, electron beam, and plasma arc [49]. The laser-based PBF technique is also known as laser powder bed fusion (LPBF), or selective laser melting (SLM). Meanwhile, the laser-based DED technique is also referred to as DED-L or directed laser deposition (DLD) [52]. Figure 2.12 provides the illustrations of LPBF and DLD processes that employ powders as feedstock. The main distinction shown in the illustrations is the manner of powder delivery: LPBF creates a whole powder bed for layer-by-layer scanning (Figure 2.12(a)), whilst DLD delivers powder by nozzles to the meltpool for deposition (Figure 2.12(b)). Since multiple nozzles can be equipped by DLD devices to deliver different powders simultaneously, DLD has more compositional flexibility compared with the powder bed used by LPBF, even though some approaches have been carried out to create multi-material powder beds [52-54]. However, the laser spot size used by LPBF (10s μm) is much finer than DLD (10^3s μm). Hence, delicate meltpools can be produced by LPBF to fabricate complex parts with relatively high forming accuracy [50].

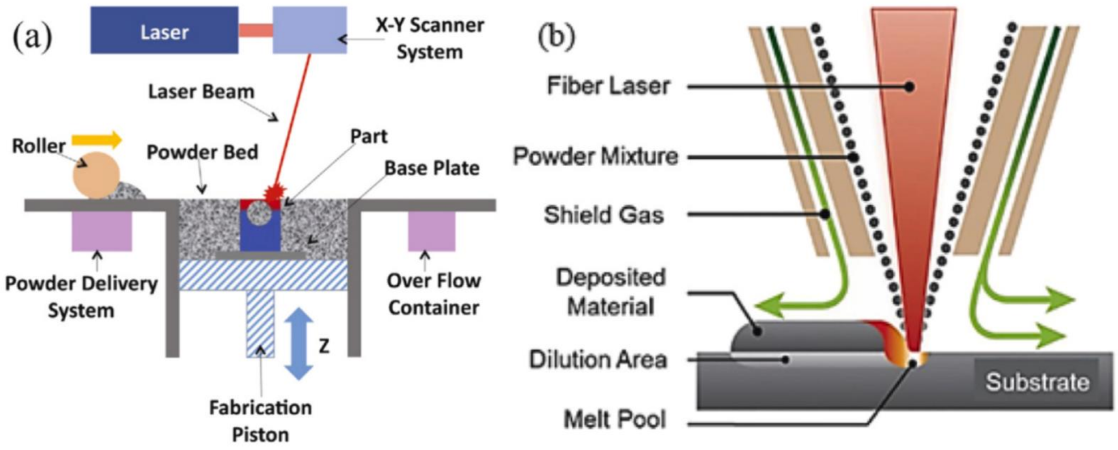

Figure 2.12 Schematic illustrating the (a) laser powder bed fusion (LPBF) and (b) directed laser deposition (DLD) processes [52].

2.2.2 Laser powder bed fusion

In the LPBF process, the powder bed is scanned to form meltpools of 10^2s-μm sizes; the single-track meltpools solidify track-by-track (1D), and then layer-by-layer (2D) to form 3D objects. Complicate thermal cycles are experienced by the materials involved in the process. This section provides the physical aspects of LPBF and correlated phenomena.

2.2.2.1 *Laser absorption and meltpool mode*

In most modern LPBF facilities, the laser power sources are Nb: YAG or Yb-fibre lasers with wavelengths of ~1 μm [55, 56]. The laser absorption of powder layers is affected by the material, powder morphology, layer thickness, laser beam size, etc. [49]. However, during the actual LPBF processes, the powder layer is immediately melted by the laser beam, and materials mainly interact with the laser in the form of liquid [57]. Therefore, the meltpool structure becomes the critical factor in the laser absorption of LPBF.

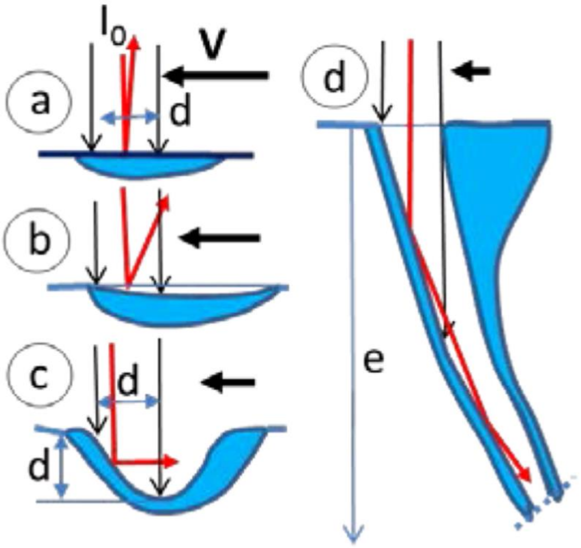

Figure 2.13 Schematic illustrating the meltpool structures of (a) conduction mode, (b, c) transition mode, and then (d) keyhole mode. Red arrows imply the laser path [58].

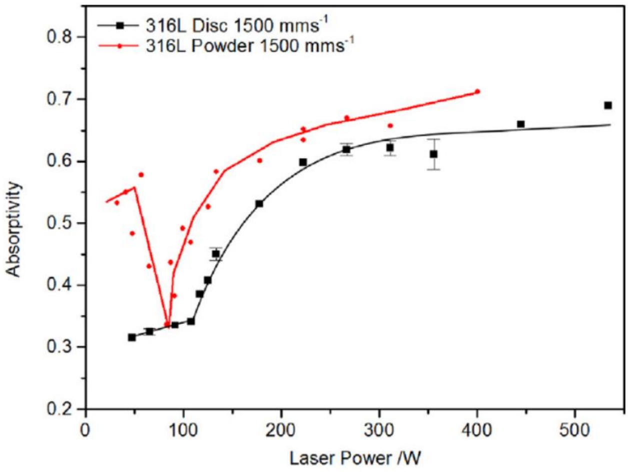

Figure 2.14 Absorptivity of 316L steel with/without a 100-µm powder layer at the laser scanning speed of 1500 mm/s [59].

Figure 2.13 illustrates the development of meltpool structures in LPBF processes, together with the measured laser absorptivity results shown in Figure 2.14. The results from Figures 2.13 & 14 show the following characteristics for trends in absorptivity [58, 59]:

- Before melting, the powder bed used in LPBF possesses a higher laser absorptivity than bare metal substrates because of the multiple reflections in the gaps between the powders [55].
- The absorptivity decreases significantly as the powder bed melts and forms a flat liquid surface, resulting in a conduction meltpool, see Figure 2.13(a).
- Because the liquid vaporises at the meltpool surface when the laser power increases (Figure 2.13(b)), the recoil pressure depresses the flat meltpool surface. Consequently, the laser beam starts to reflect between the liquid surfaces, resulting in higher laser absorptivity (Figure 2.13(c)).

- Once a deep keyhole forms owing to the recoil pressure, the laser beam is trapped inside, and the absorptivity stabilises within a steady range, as shown in Figure 2.13(d).

Ye et al. [56] further investigated the scaling law of laser absorption of different materials, including Inconel 625 superalloy, Ti-64 alloy and 316L steel. The results showed that the absorptivity of different materials is ~0.3 in the conduction mode, while the steady absorptivity of keyhole meltpools was in a range between 0.6 and 0.8.

2.2.2.2 Thermal history and solidification

The actual thermal field inside an LPBF meltpool is hard to measure due to the rapid movement of heat sources and the resolution of available techniques [49, 60]. Most thermal profiles of LPBF meltpool are acquired by modelling and simulation. Due to the rapid scanning of laser, the cooling rate of LPBF can reach 10^5–10^6 K/s [60-63], which is two orders of magnitude higher than the 10^3–10^4 K/s of DLD [64, 65] or the 10–10^2 K/s of casting [66]. Figure 2.15 shows the simulated thermal field of an LPBFed 316L meltpool in the conduction mode. The shape of LPBFed meltpools is similar to welding meltpools but with relatively small dimensions. In actual processes, the centre temperature can exceed the boiling point of the material in meltpools, resulting in radical thermal gradients and cooling rates.

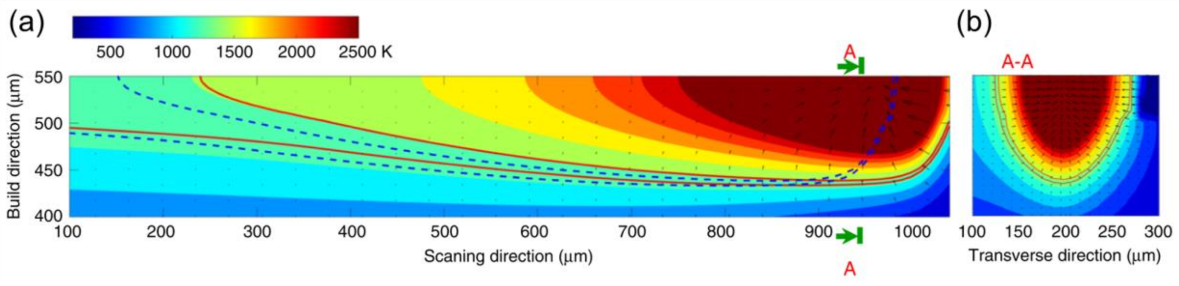

Figure 2.15 (a) Side view and (b) front view of a simulated thermal field during the LPBF process of 316L steel. Dash lines and solid lines indicate two consecutive meltpools, while inner and outer lines denote the solidus and liquidus temperatures; black arrows show the local thermal gradient [63].

The solidification in LPBFed meltpools is also similar to that in welding meltpools. Because LPBFed meltpools are normally scanned on previous layers of the same material, epitaxial growth is preferred owing to its low energy barrier. During solidification, the atoms in the liquid attach to the liquid/solid interface at the meltpool boundaries and form sub-structures. Figure 2.16 illustrates the sub-structures formed with different thermal gradients (G) and growth rates (R). The growth mode can be maintained as planar when constitutional supercooling is avoided, which is determined by the following relationship [67]:

$$\frac{G}{R} \geq \frac{\Delta T}{D_L} \tag{2.5}$$

where ΔT is the solidification range, and D_L is the diffusion coefficient in the liquid. If the thermal gradient decreases while the growth rate increases, constitutional supercooling occurs, and the planar growth changes to the cellular mode, columnar dendritic mode, or ultimately equiaxed dendritic mode. Mixed sub-structures may co-exist in a welding meltpool because of the spatial distribution of the thermal gradient [67]. These sub-structures become finer as the cooling rate ($G \times R$) increases. With rapid cooling during LPBF processes, the grain growth is often observed to be fine cellular structures with sizes of ~1 μm [63, 68]. Although columnar/equiaxed dendritic structures may occur near the surface of the welding meltpools, only the sub-structures near the bottom of the LPBFed meltpools can be reserved in the final parts because of the occasional layer-by-layer remelting. At the same time, the growth mode may also vary with the composition of materials: The cellular-to-dendritic transition was observed in LPBFed maraging steel parts with increasing SiC content [69]; While an equiaxed-columnar bimodal grain structure was observed in an Al-Mn-Sc alloy whose composition was tuned for LPBF processing [70].

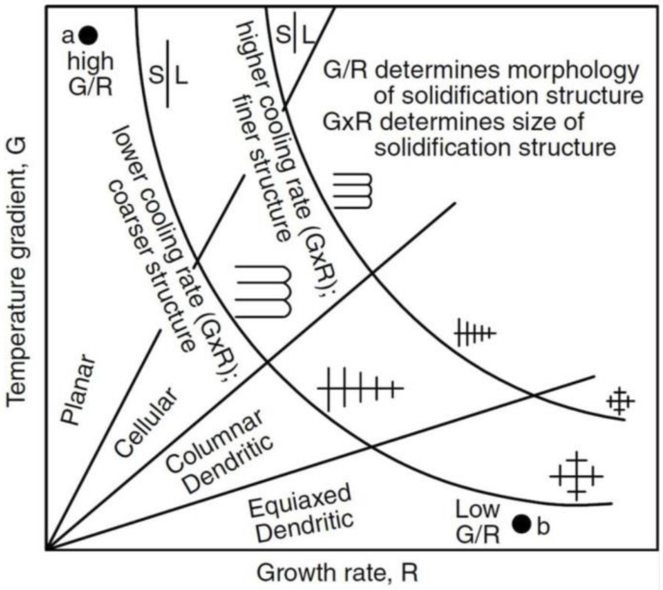

Figure 2.16 Plot showing the microstructural dependence on the thermal/temperature gradient (*G*) and growth rate (*R*). The crystal growth mode changes from planar to cellular, then columnar, and finally equiaxed dendritic as *G*/*R* decreases, while the resulting structures become finer at higher cooling rates (*G* × *R*) [67].

The rapid heating and cooling process of the first laser scanning is one significant stage in the thermal history of LPBF processes. After the first scanning, as-solidified tracks will experience the heat input from other tracks in the same layer, then the laser scanning in the following layers [71, 72]. As shown in Figure 2.17, the temperature of the printed material can exceed its melting point twice or more during the LPBF process, indicating that as-solidified parts will be partially or fully melted more than once in the whole process. In addition, the heat accumulation in the process also increases the temperature near the bottom and substrate. In prolonged building, the different thermal histories of layers could result in spatial-dependent microstructures, e.g., different grain and cell sizes [73, 74]. Moreover, the local thermal history is also affected by the scanning strategy and part geometry [75].

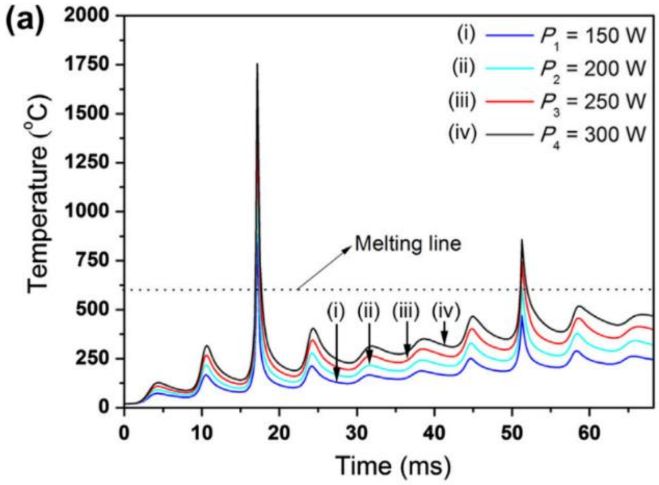

Figure 2.17 Simulated thermal history at the centre of the first layer during the LPBF process of Al alloy, showing the temperature of the as-built part could exceed its melting point once again during the process. [62].

2.2.2.3 Meltpool flows

Similar to the thermal field, modelling methods also play an essential role in understanding the fluid motion inside LPBFed meltpools [49]. Meanwhile, in-situ methods have been employed to monitor the contours and spatters of meltpools [76-78]. The internal flow affects the heat and mass transfer in LPBF meltpools, as well as the defect formation and spatters. Firstly, due to the thermal gradient, the local surface tension gradient drives the liquid from the area with low surface tension to the area with high surface tension, and creates the Marangoni flow, as shown in Figure 2.18 [79]. The Marangoni effect has been considered as the main driving force in conduction meltpools, and its flow speed ranges from 10 to 10^2 mm/s [57, 79-81].

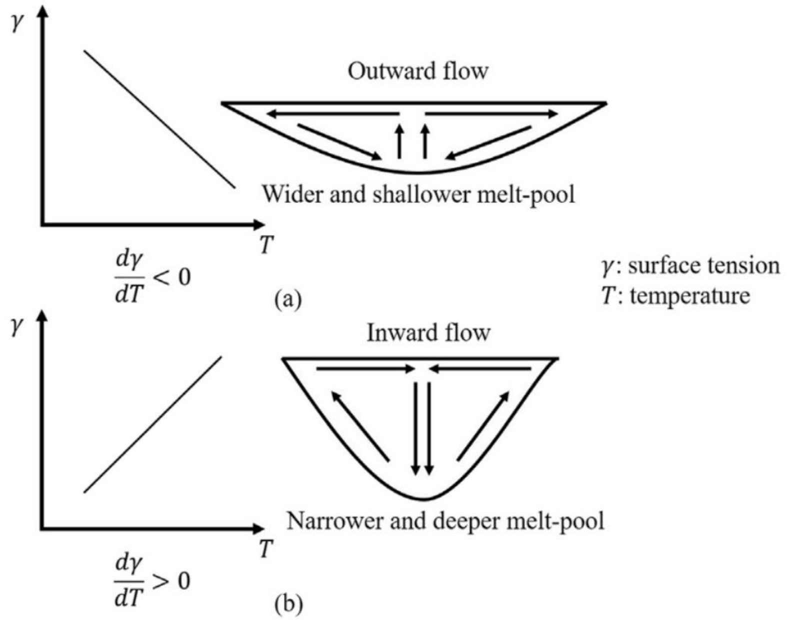

Figure 2.18 Front-view schematics illustrating the Marangoni flow in the meltpools of liquid with (a) negative ($d\gamma/dT < 0$) and (b) positive ($d\gamma/dT > 0$) surface tension gradients [79].

In the keyhole mode, the liquid metal vaporises at the meltpool surface and results in a recoil pressure that depresses the liquid (~10^3 mm/s) away from the laser spot, as shown in Figure 2.19. The recoil pressure (10^5–10^6 Pa) acting on the keyhole wall is around two orders of magnitude higher than the Marangoni force (10^3–10^4 Pa) [80]. Consequently, the internal flow is dominated by the recoil pressure in keyhole meltpools, coupled with the Marangoni flow at the rear meltpool and other minor driven forces [57, 80]. As the meltpool moves forward, the liquid pressed away from the keyhole turns back to the keyhole at its rear wall. Figure 2.19(a) illustrates scenarios where the liquid at the keyhole rear wall reaches close to the front wall with a low scanning speed. Thus, an unstable chamber occurs at the bottom of the meltpool, and its collapse could result in keyhole porosity during solidification. However, such porosity can be avoided by improving the scanning speed to maintain a relatively stable spacing between the front and back walls, like the scenario shown in Figure 2.19(c). Recent in-situ monitoring studies observed stable keyhole meltpools and suggested that the keyhole porosity was evitable in keyhole meltpools [80, 82].

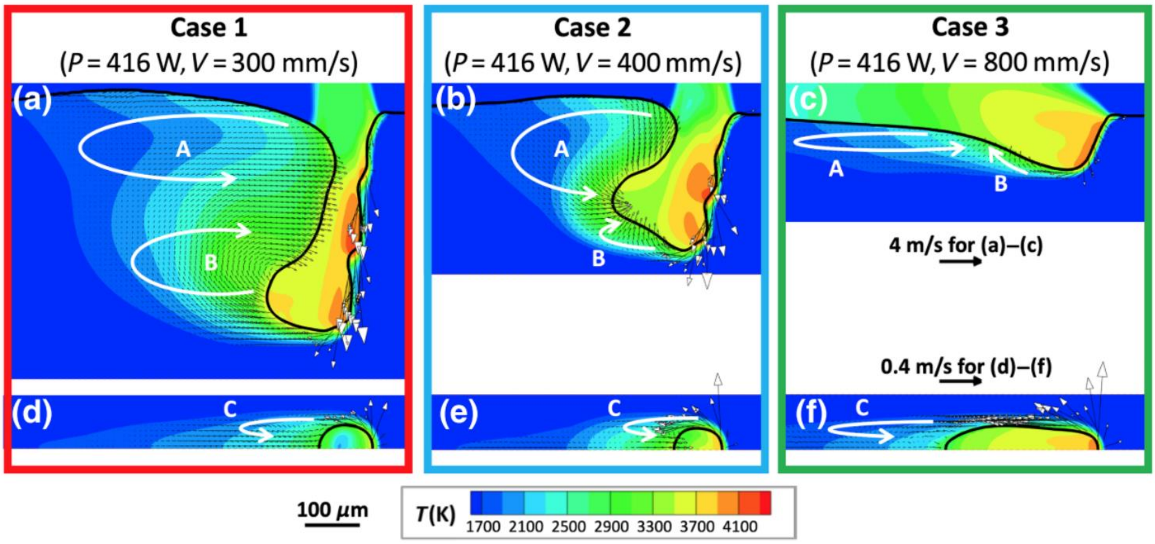

Figure 2.19 (a)-(c) Side-views and (d)-(f) top-views of thermal fields and fluid motions in LPBFed meltpools with different laser parameters [80].

2.2.2.4 Track-based structure and printability

As shown in Figure 2.20(a), single tracks are the fundamental units of LPBFed parts. The width and depth of a single track are mainly determined by laser power (*P*) and scanning speed (*v*). These two parameters can be integrated as the linear energy density (*LED*) to describe the energy input during the single-track scanning [83], as given below:

$$LED = \frac{P}{v} \tag{2.5}$$

The *LED* only determines the size of single tracks. Layer thickness (*t*) and hatch spacing (*h*) further determine the vertical and horizontal spacing between tracks, i.e., the spatial density of tracks. Therefore, the volumetric energy density (*VED*) is introduced to describe the overall energy input to the LPBFed parts composed of multiple tracks [49], as given below:

$$VED = \frac{P}{vht} \tag{2.6}$$

The *LED* and *VED* have been extensively employed by researchers to summarise the parameter-microstructure correlations, especially the densification of as-built samples [10, 81, 84, 85]. Regarding the densification of LPBF parts, it is essential to obtain adequate meltpools to fully melt the raw powder layers. Meanwhile, the hatch spacing between meltpools needs to be modified to ensure enough overlapping. In other words, a minimum energy density is always required to achieve good densification. Figure 2.20(b) shows the meltpool distribution in a well-densified LPBFed sample.

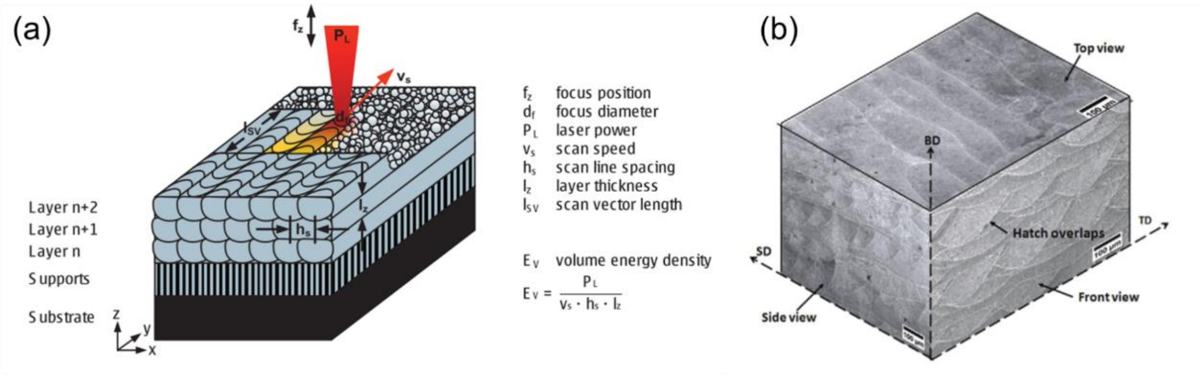

Figure 2.20 (a) Schematic illustrating the tracks-to-bulk process of LPBF. (b) Typical meltpool distribution in an as-built part (Al alloy) [86, 87].

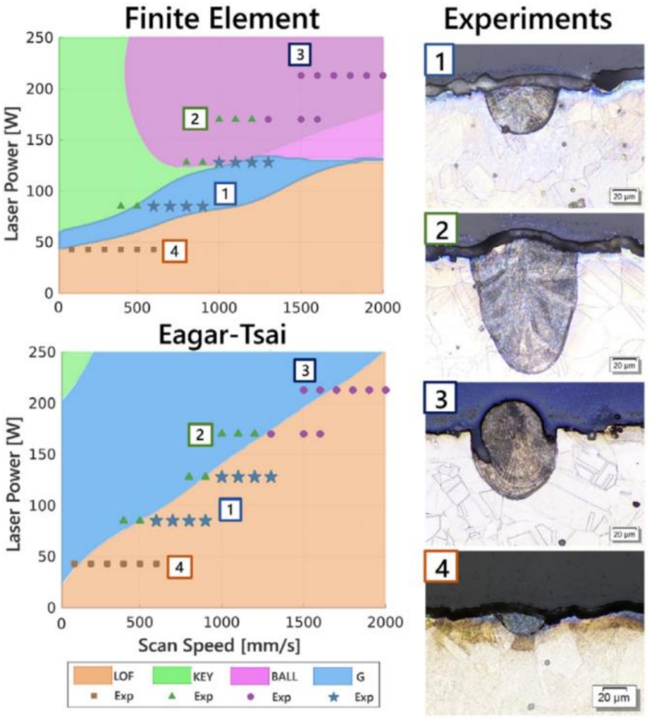

Figure 2.21 Predicted processing maps using different modelling methods (Finite Element and Eagar-Tsar) and experimental results, with corresponding cross-sections of single tracks (CoCrFeMnNi HEA) representing: (1) good printability, (2) keyhole, (3) balling, and (4) lack of fusion [88]

Based on single-track morphology, many approaches have been carried out to predict the processing window of materials, i.e., the processing parameters of well-densified samples [88-93]. A principle of such methods is to acquire the processing parameters of meltpools with sufficient dimensions but without keyhole formation, either through modelling or experimental measurement. Johnson et al. [88] employed a Finite Element (FE) model and the Eagar-Tsai model [94] to predict the printability of Ni-5wt.%Nb alloy and CoCrFeMnNi HEA. The processing widows predicted by the FE model were in agreement with the experimental results in their study, as shown in Figure 2.21. Tang et al. [89] predicted the formation of lack-of-fusion porosity via simulating meltpool dimensions based on the Rosenthal equation, and revealed close correspondences between their predicted processing maps and experimental data [95].

Nevertheless, it should be noted that the Eagar-Tsai model employed via Johnson et al. is also a derivation from the Rosenthal equation, but with a modified Gaussian heat source [94, 95]. Furthermore, the Rosenthal equation provides a convenient approach to the estimation of thermal fields in welding processes, but keyhole formation is neglected. Thereby, several bulletins can be raised from current single-track studies:

- Assessing LPBF printability through single tracks has shown the potential for shortening the processing development and predicting possible defects in as-built LPBF parts. Moreover, modelling methods can be advanced by comprehensive thermal-physical understanding and advanced computational resources [53, 84, 96].
- The applicability of modelling methods in the literature was limited by specific scenarios. Predicted meltpool dimensions could deviate from actual values when different materials and parameter ranges were engaged [92, 97, 98].
- The conduction-keyhole threshold was hard to determine by modelling methods, especially considering a wide transition range could exist between the two modes [99-101].
- Single-track experiments were mostly carried out on bare substrates or substrates coated with the initial powder layer, which differed from the powder layer coated on as-built surfaces during actual processes [90-92, 102, 103].

In addition, although single-track experiments were carried out to understand the grain development and surface morphology of LPBFed parts [104, 105], the elemental distribution in single-track meltpools has rarely been revealed and correlated to the overall homogenisation in bulk samples.

2.2.2.5 Residual stress and cracking

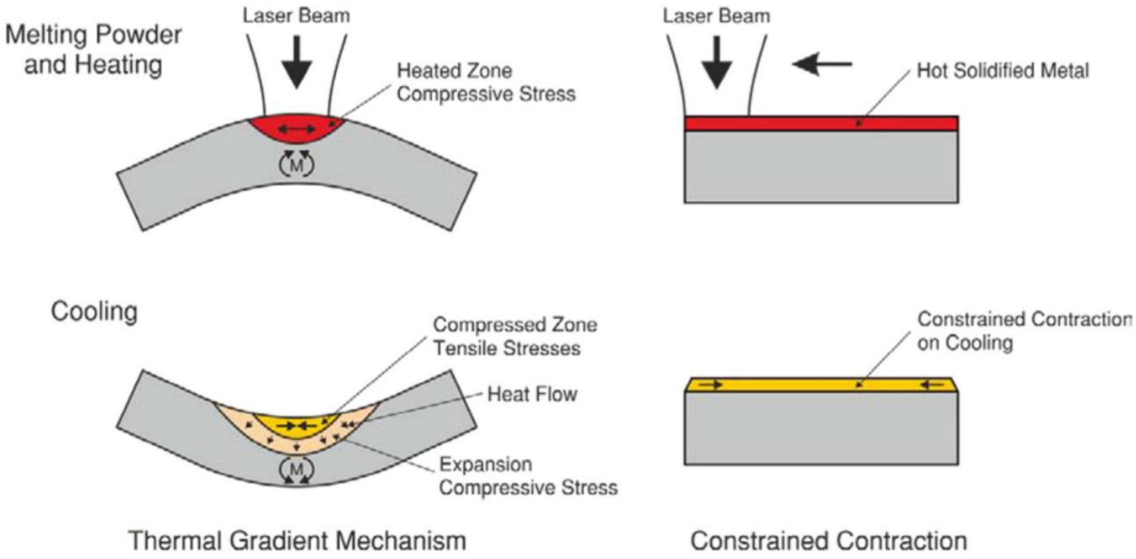

Figure 2.22 Schematic illustrating the thermal gradient and constrained contraction mechanisms of residual stress in as-built LPBFed parts [106].

Due to the delicate laser spots used by LPBF, the residual stress tends to accumulate to a high level (10^2–10^3 MPa) and could result in cracking during LPBF processes [107]. Figure 2.22 illustrates the origins of residual stress: (a) The solidification of meltpools leads to local expansion and contraction; (b) Fast heating and cooling cycles lead to a steep thermal gradient near the upper part, resulting in mismatched contraction [108]. Besides the local thermal factors, the incompatible thermal strain of heterogeneous microstructures could also accumulate residual stress during LPBF processes [49].

Cracking is hence a major category of defects in LPBFed parts due to the inevitable residual stress. The cracking behaviours in LPBFed parts can be categorised into three types [49, 54]: (a) Solidification cracking, namely hot cracking, initiated at the grain boundaries due to the shrinkage of previously solidified parts and inadequate liquid at the final stage of solidification; (b) Liquation cracking initiated at the mushy zones, because low-melting-point phases are affected by subsequent heat input; (c) Cold cracking (delamination) formed due to the accumulated residual stress, which leads to the failure of solidified materials, especially brittle materials. Severe cracking could lead to macro cracking between layers, which is fatal to the formability of LPBFed parts. Regarding the LPBF printability, it is essential to employ proper scanning strategies and pre-heating. Thereby, the accumulation of residual stress can be partially restrained [107-109].

2.3 LPBF of CoCrFeNi-Based High Entropy Alloys

2.3.1 LPBF of FCC CoCrFeMnNi HEA

The fabrication of HEAs via LPBF was firstly reported by Brif et al. in 2014 [9]. A pre-alloyed, gas-atomised CoCrFeNi HEA powder was employed to fabricate cuboid and tensile samples via LPBF. The as-built CoCrFeNi samples were well densified and possessed an FCC single phase with good chemical homogeneity (Figure 2.23), implying the good LPBF printability of the CoCrFeNi HEA powder. Furthermore, the study also showed that the tensile strength and microhardness of the as-built HEA were significantly improved compared with the CoCrFeNi HEA fabricated via arc melting. Brif et al. attributed the reinforcement of mechanical properties to the refined grain structure resulting from LPBF.

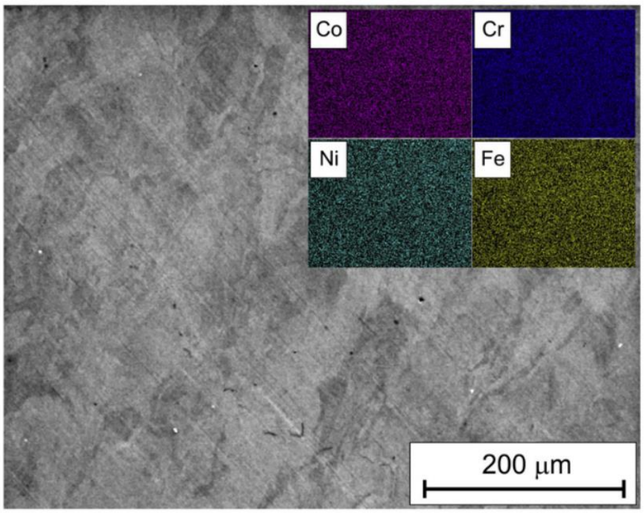

Figure 2.23 SEM image and EDS mapping results of LPBFed CoCrFeNi HEA [9].

After the early approach to the quaternary CoCrFeNi HEA from Birf et al., more studies on the printability of quinary CoCrFeMnNi HEA have been conducted. Li et al. [10] correlated the densification of as-built HEAs to the *VED*, and the highest relative density, 98.2%, was obtained at the *VED* of 74 J/mm^3. As shown in Figure 2.24, the results also suggested that bulk CoCrFeMnNi HEA was printable in a wide *VED* range. Moreover, well-densified, crack-free CoCrFeMnNi HEAs have been provided using pre-alloyed powders by worldwide researchers [10, 110-113]. Relative details are summarised in Table 2.2. Although the *VED* range for the highest relative density is close to 80 J/mm^3, the other specific laser parameters, however, distribute in broad ranges. Furthermore, the raw CoCrFeMnNi powders were from different suppliers and processed by different LPBF facilities. It can be concluded that the CoCrFeMnNi HEA possesses good LPBF printability. A wide processing window also implies that the microstructural tailoring of as-built parts could be reached by parametrical study.

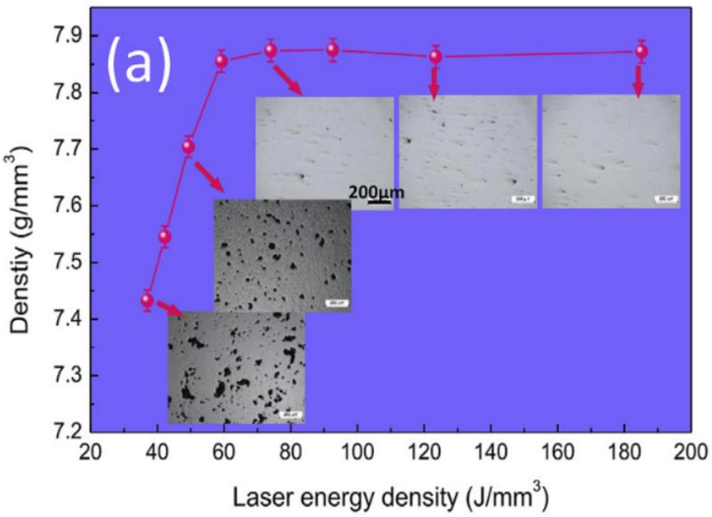

Figure 2.24 Density of LPBFed CoCrFeMnNi HEA verse volumetric energy density, with embedded images of porosity [10].

Table 2.2 Processing parameters of CoCrFeMnNi HEAs fabricated via LPBF using pre-alloyed powders.

Refs	Machine	Relative density (%)	*VED* (J/mm^3)	*LED* (J/mm)	*P* (W)	*v* (mm/s)	*h* (μm)	*t* (μm)
Li [10]	Farsoon FS271M	98.2	74	0.20	400	2000	90	30
Zhu [110]	3D system ProX300	99.2	60	0.12	240	2000	50	40
Piglione [111]	Renishaw AM250	99.3	N/A	0.27	200	~750	125	N/A
Kim [112]	Concept LaserMlab	N/A	75	0.15	90	600	80	25
Ren [113]	EOS M290	99.5	78	0.25	370	1500	80	40
Xu [114]	Hanbang HBD-100	N/A	100	0.3	150	500	50	60
Wang [115]	BLT-S200	N/A	89	0.32	280	870	90	40
Zhang [116]	HanBang HBD-100	N/A	89	0.13	160	1200	50	30

2.3.1.1 Defects in LPBFed CoCrFeMnNi HEAs

Cracking and porosity are the two main defect categories to focus on when assessing the printability of materials. Although micro-cracks (Figure 2.25) were recognised in some LPBFed CoCrFeMnNi HEAs [10, 116, 117], their effects on the densification were relatively minor and could be eliminated by hot isostatic pressing (HIP) [118]. Inevitable cracking that led to the failure during LPBF processes was barely reported in the literature. Zhang et al. [116] specifically investigated the relations between micro-cracks and scanning strategies. The results suggested that the cracking tendency in LPBFed CoCrFeMnNi HEAs could be effectively inhibited via modifying the rotation angle between layers. Because CoCrFeMnNi HEAs can be processed in a wide processing window, the porosity, including lack-of-fusion pores and keyhole pores, was extensively observed in as-built samples. At the low *VED*, the overlaps between adjacent tracks and layers are insufficient to fulfil the gaps, resulting in lack-of-fusion pores after solidification, as shown in Figure 2.24. The size of such lack-of-fusion pores can be 10s μm or larger, whilst unmelted or partially melted powder often occurs inside such pores. Lack-of-fusion pores can be eliminated by enlarging meltpools or narrowing the spacing between tracks or layers [57].

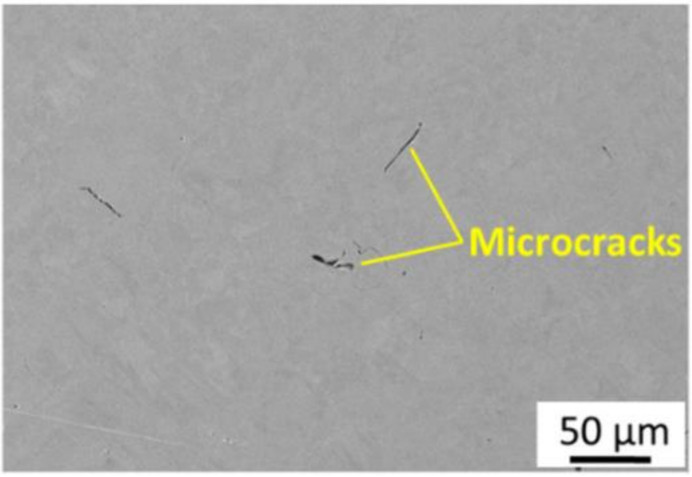

Figure 2.25 SEM image showing micro-cracks in as-built CoCrFeMnNi HEA [117].

The LPBF approaches also showed that the densification of LPBFed CoCrFeMnNi HEA reached the maximum in a *VED* range close to 80 J/mm^3. Then the relative density of as-built samples stopped increasing or slightly dropped when the *VED* exceeded the range [10, 13, 110], because keyhole porosity became the main defect inside the as-built samples built with the excessive energy input. As the energy input increases, the molten material starts to vaporise and create gas pores. Such gas pores could be trapped in the meltpools during solidification, as illustrated by Guo et al. [119] in Figure 2.26. To eliminate the keyhole porosity, the laser power and scanning speed should be tuned to form sufficient but stable meltpools. The available energy density reported in the literature indicates that the available processing window of CoCrFeMnNi HEA is adequate to avoid both lack-of-fusion and keyhole porosity.

There is also another type of gas porosity that exists in LPBFed components [120]. Gas can be trapped inside raw powders or dissolved into the materials during gas-atomisation processes. The trapped gas can be released into the atmosphere during LPBF processes, but some gas gets trapped as bubbles after solidification and leaves gas porosity. The content of such gas pores is often minor and depends on the quality of raw powders.

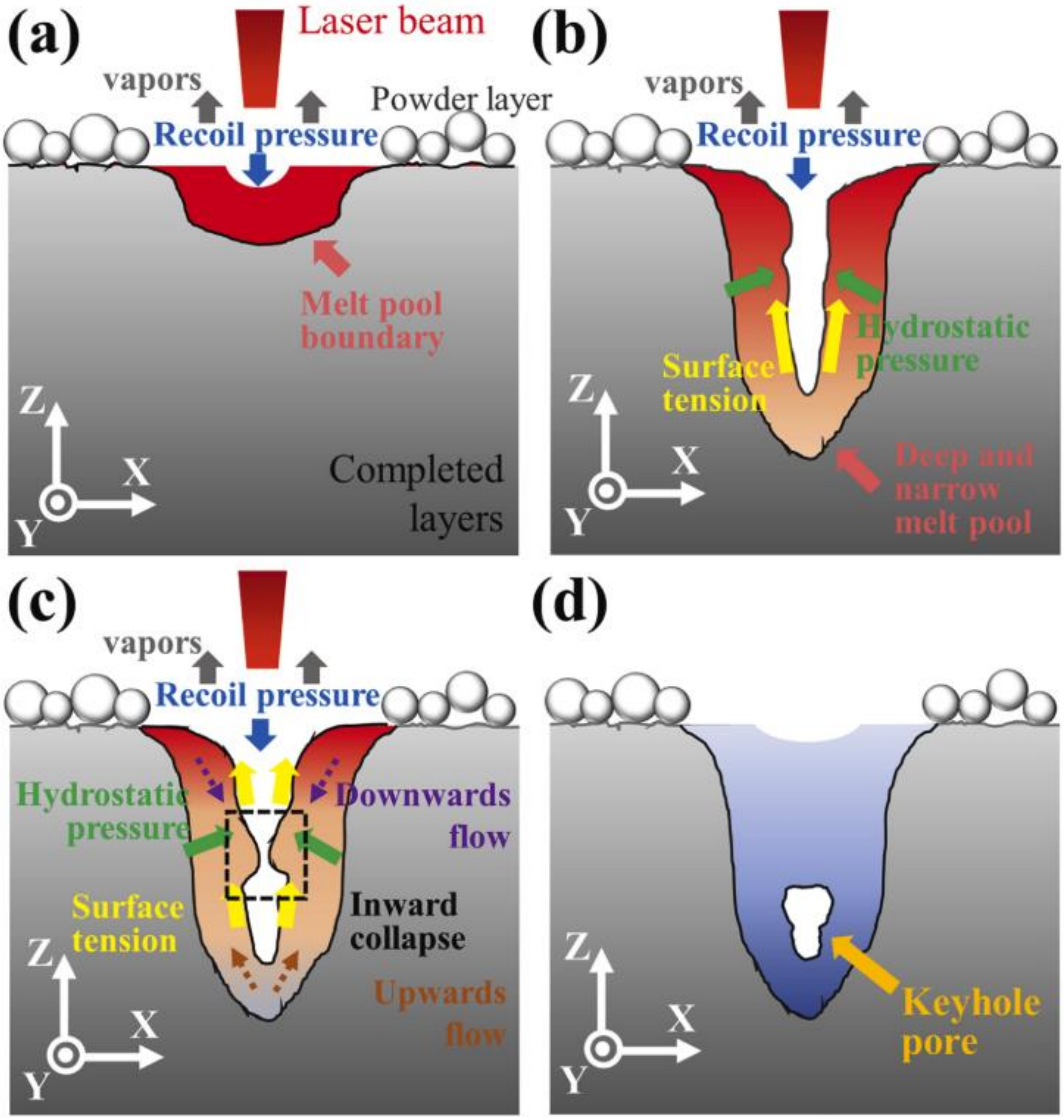

Figure 2.26 Schematics illustrating the formation of keyhole pores in a meltpool (Inconel 738) [119]. (a) The recoil pressure form at the meltpool surface (b) and creates a deep keyhole. (c) The internal cavity of the keyhole meltpool is unstable and leaves (d) a keyhole pore after solidification.

2.3.1.2 Grain structures in LPBFed CoCrFeMnNi HEAs

The literature on LPBFed CoCrFeMnNi HEAs agreed that the grain growth possessed a strong <001> preference along the thermal gradient during solidification, coinciding with the preferred growth direction of FCC alloys [121]. During the continuous growth of cubic crystals, the atoms in the liquid tend to attach to the planes with low planar density and high interplanar spacing, i.e., the growth of (001) planes in the <001> orientation [122]. Hence, the <001> orientation possesses the highest growth rate compared with other orientations and dominates the building direction (horizontal plane) in many reports [10, 110, 111, 123]. An aggregation of <101> orientations (Figure 2.27 (a)) was also observed in the horizontal plane of the CoCrFeMnNi HEA fabricated via Kim et al. [112]. On the other hand, in vertical planes parallel to the building direction, the dominant orientation varied with the different scanning strategies and processing parameters.

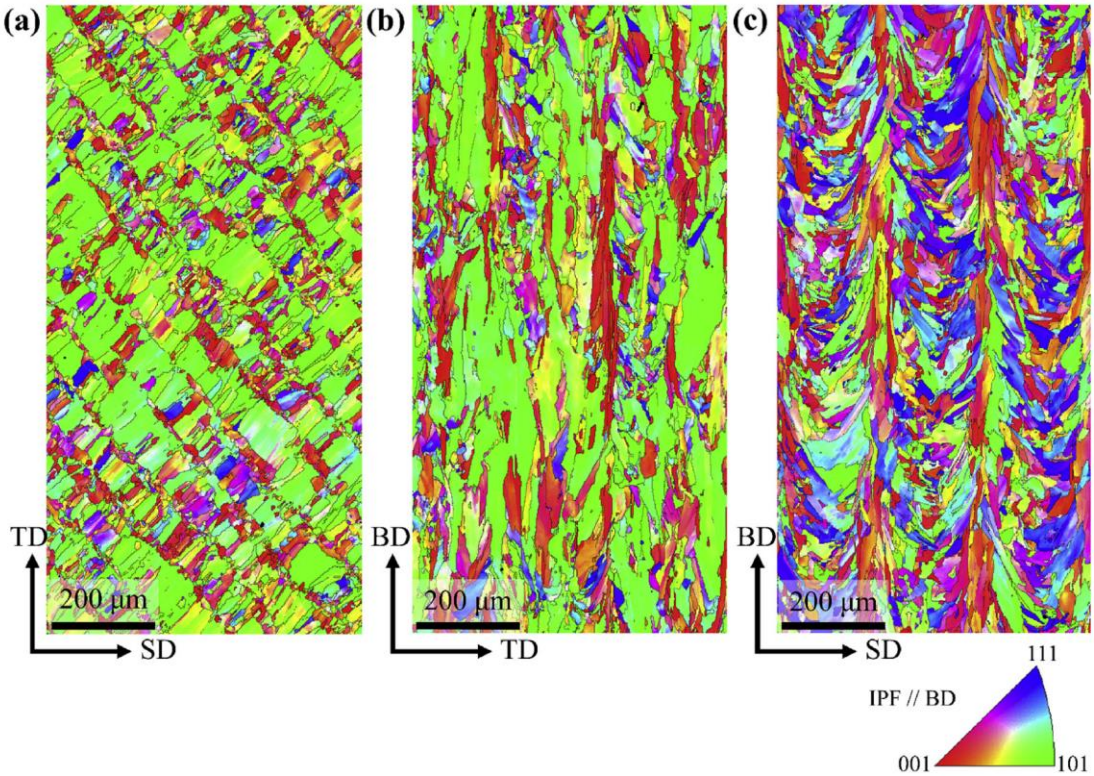

Figure 2.27 Inverse pole figure (IPF) mapping results of (a) the horizontal plane (TD-SD), and (b) (c) vertical planes (BD-TD/SD) of LPBFed CoCrFeMnNi HEA [112].

The grain sizes of LPBFed CoCrFeMnNi HEAs also vary with processing parameters: Kim et al. [112] reported an average grain size of 5.98 μm in the horizontal plane, while 15.66 and

12.93 μm in the vertical planes, as shown in Figure 2.27; Zhu et al. [110] reported a similar average gain size of 12.9 μm in the vertical plane; Niu et al. [120] provided samples with average grain sizes from 18.8 to 44.6 μm in vertical planes with *VED* from 59.3 to 185.2 J/mm^3. In general, the average grain size of LPBFed CoCrFeMnNi HEA is ~10s μm, while the grain sizes in the vertical planes are overall coarser than horizontal planes due to the large columnar grains growing along the building direction. Grain sizes around 1 μm were reported by Xu et al. [114] and Li et al. [10]. However, according to the electron back-scattered diffraction (EBSD) results in their reports, the values should be the sizes of cellular sub-structures instead of grain sizes.

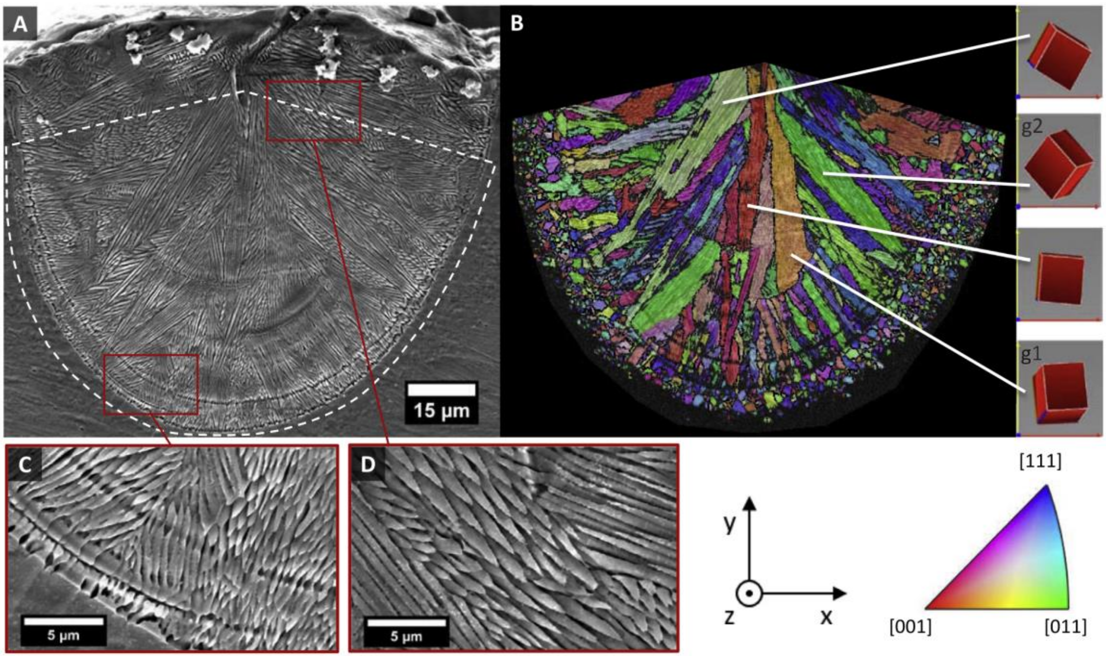

Figure 2.28 (a) SEM and (b) IPF mapping results showing the fine cellular structures and grain growth in a LPBFed CoCrFeMnNi single track. SEM results of (c) fine structures near the meltpool boundary and coarse structures near the meltpool centre [111].

Further investigation of the microstructural development showed that the fine cellular structures formed owing to rapid cooling were dominant in the as-built CoCrFeMnNi HEAs from multiple reports. By characterising single tracks, Piglione et al. [111] revealed that the grain growth of CoCrFeMnNi HEAs consisted of fine cellular structures that grow epitaxially from the meltpool boundaries toward the centre surface, see Figure 2.28. At the beginning of epitaxial growth, the cellular structures with <001> orientations aligned closer to the direction of the heat gradient overgrew the others, and therefore, the <001> orientations tended to converge at the surface centre of the meltpools. Such growth preference was further confirmed in their following study on bulk building [63]. Kim et al. [112] used electron channelling contrast imaging (ECCI) to characterise the cellular structures and revealed that abundant dislocation networks were stored in their boundaries, see Figure 2.29. Zhu et al. [110] employed scanning transmission electron microscopy (STEM) to characterise the dislocation networks, and the corresponding EDS results suggested homogeneous elemental distribution, as given in Figure 2.30. Similar cellular structures were also found in the 316L steel fabricated by LPBF, and its formation was attributed to the ultrahigh cooling rate during the LPBF process and the slight misalignment between adjacent cells [124]. The size of cellular structures varied with processing parameters, and the average cell size was between 0.3 and 0.6 μm in the reports on LPBFed CoCrFeMnNi HEAs [110-112]. Such cellular structures were found to be thermodynamically metastable and could be eliminated after heat treatment [10, 110].

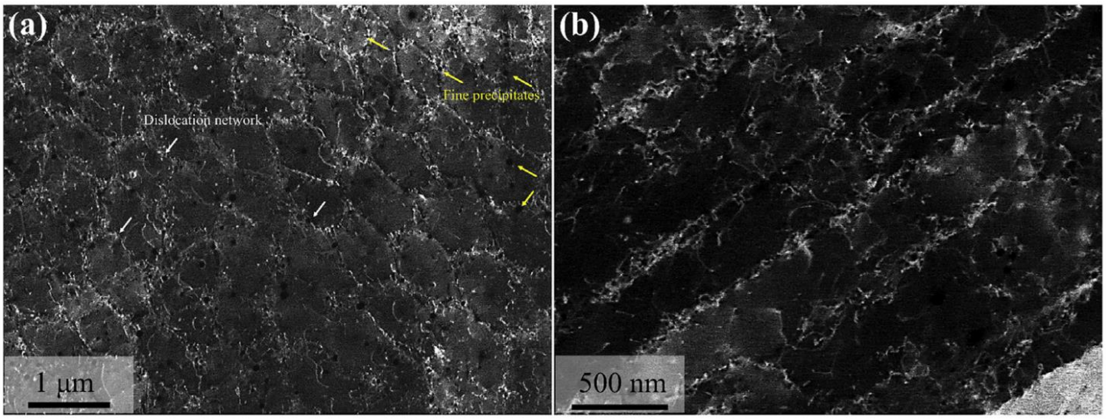

Figure 2.29 ECCI images of (a) cellular and (b) columnar structures (side view of cells) consisting of dislocation networks in LPBFed CoCrFeMnNi HEA [112].

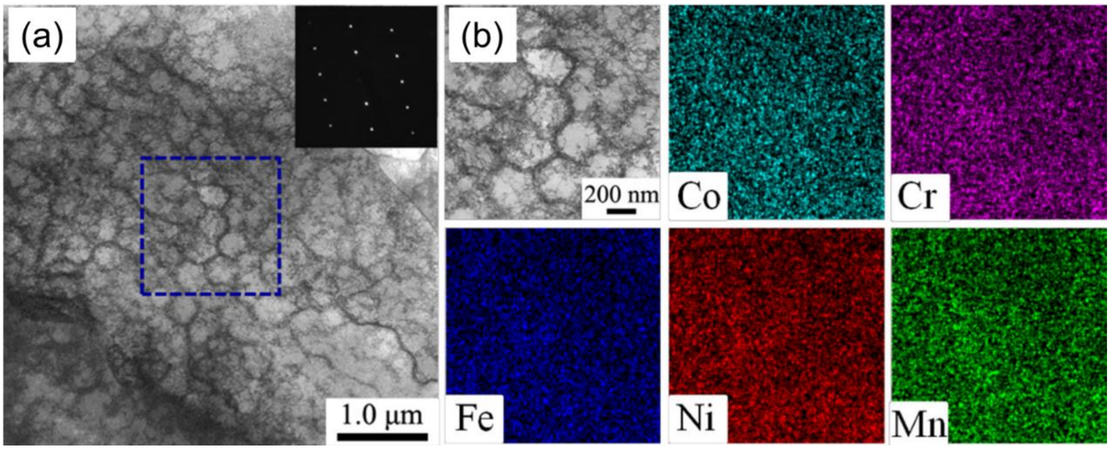

Figure 2.30 (a) Bright-field STEM image of the cellular structures and (b) corresponding EDS mapping results showing homogeneous elemental distribution in LPBFed CoCrFeMnNi HEA [110].

In general, LPBFed CoCrFeMnNi HEAs possess hierarchical microstructures, including grains, meltpools and cellular structures. It is noted that grains can grow epitaxially between adjacent meltpools, e.g., in Figures 2.27(b) and (c), the columnar grains are much larger than the layer thickness (25 μm) in the building direction. Microstructural anisotropy is significant in the LPBFed HEAs, especially between building and transverse directions. The variant grain structures reported from different studies also suggest the potential for processing optimisation.

2.3.1.3 Phase formation and elemental distribution

The X-ray diffraction (XRD) results in different studies have agreed that the LPBFed CoCrFeMnNi HEAs possess an FCC single-phase matrix in the as-built state, while secondary phases have not been recognised by XRD. The peaks in XRD spectra tend to shift to high degrees with improving energy input, indicating a reduction of the lattice parameter, as shown in Figure 2.31. Li et al. [10] suggested that the reduction was due to the burning loss of Mn. Because Mn possesses the lowest boiling point and vaporisation heat, meanwhile, the highest vapour pressure of the five composing elements, the vaporisation of Mn is thus thermodynamically favoured compared with the rest elements at high temperatures. Moreover, Mn also possesses a relatively large atomic size. Consequently, the burning loss of Mn results in reduced lattice parameters. Besides the lattice parameter, Kim et al. [112] claimed that the broadened full-width at half-maximum (FWHM) in their XRD results indicated that more lattice distortions and defects were stored in the LPBFed CoCrFeMnNi HEA than casted ones, which was corresponding to the abundant dislocation networks.

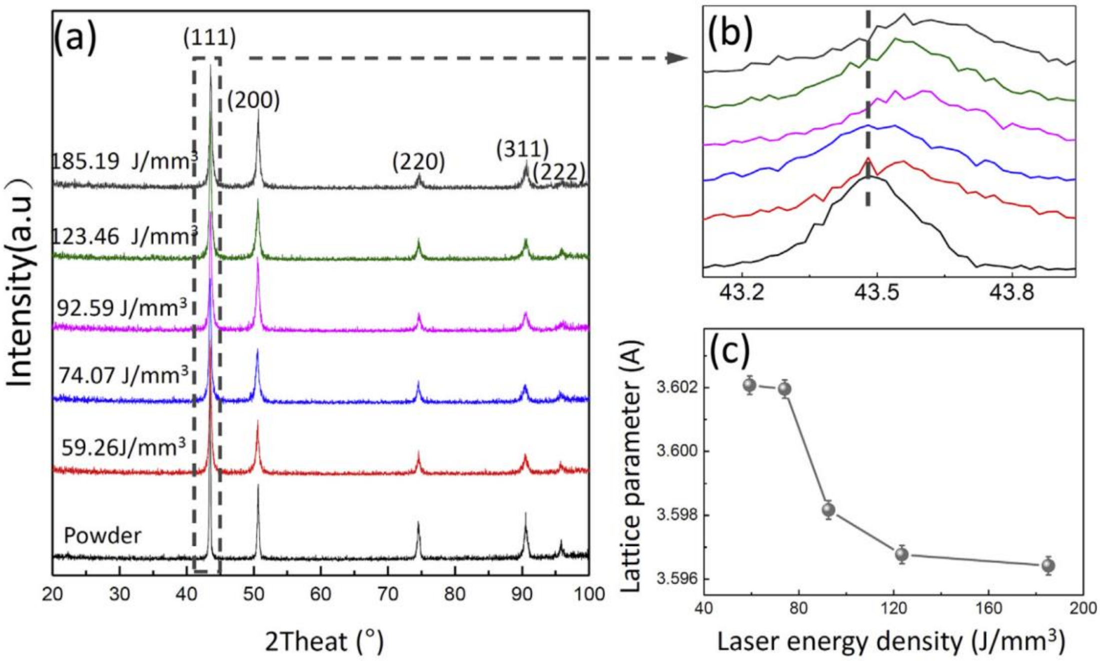

Figure 2.31 XRD spectra of (a) pre-alloyed CoCrFeMnNi powder and LPBFed samples, and (b) individual comparison of the peak (111). (c) Corresponding lattice parameters calculated from the XRD spectra [10].

EDS showed the elemental distribution in as-built CoCrFeMnNi HEAs was overall homogeneous, indicating the rapid solidification could restrain the elemental segregation [110-112, 114]. Slight Mn segregations at the meltpool boundaries were observed by Li et al. [10] using an electron probe micro analyser (EPMA). Such segregations could be homogenised by HIP treatment. Moreover, the meltpool and cellular structures were also neutralised by the HIP treatment as well, which led to coarsened microstructures.

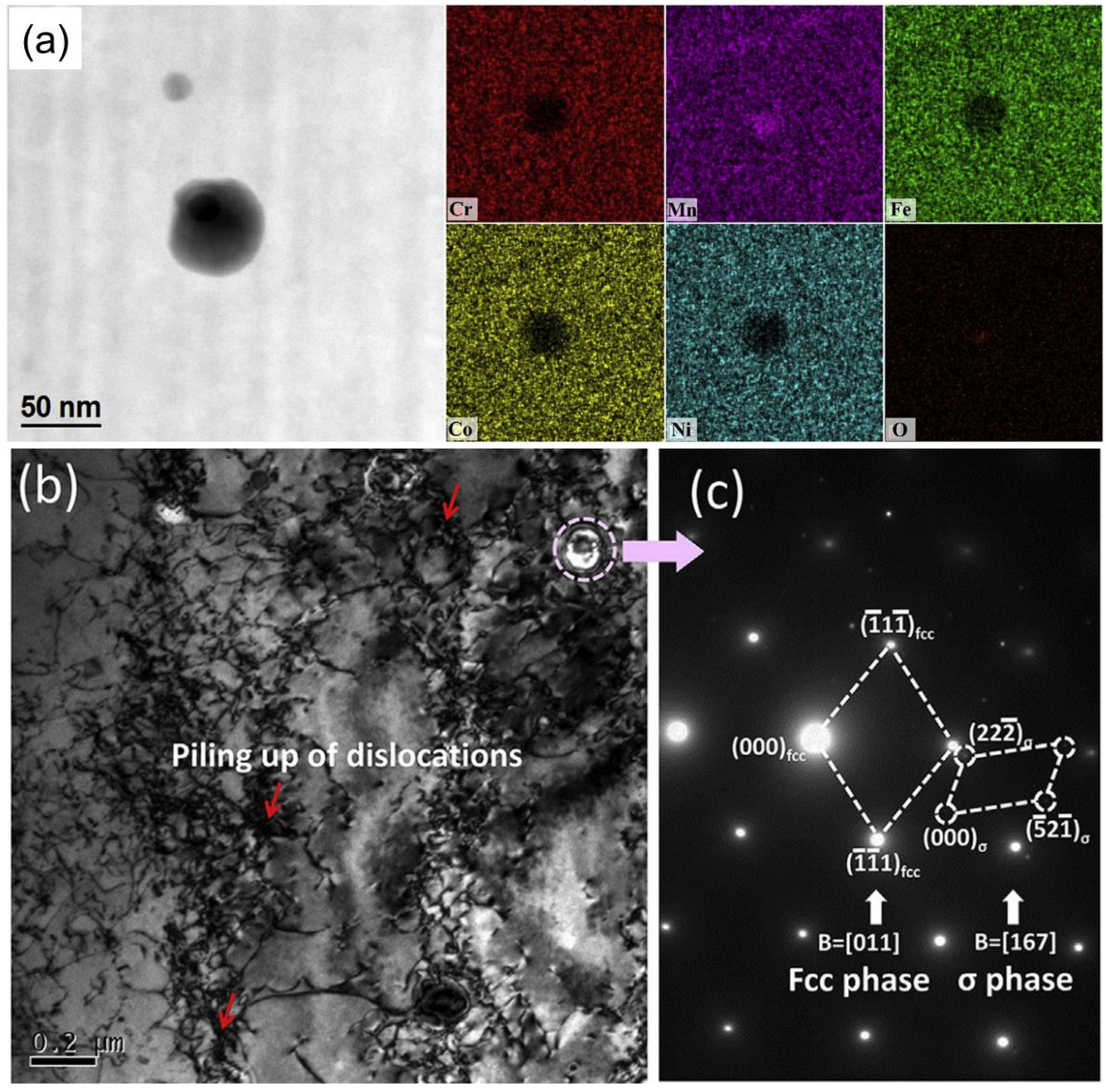

Figure 2.32 (a) STEM image of Mn_2O_3 particle in LPBFed CoCrFeMnNi HEA and corresponding EDS mapping results [112]. (b) Bright-field TEM image of precipitation and (c) correlated SAED pattern in LPBFed CoCrFeMnNi HEA [10].

Secondary phases, including Cr-rich σ phase and Mn_2O_3, have been found in LPBFed CoCrFeMnNi HEAs via TEM, see Figure 2.32 [10, 112]. The particle sizes of the secondary phases were below 100 nm, and their contents were too low to be distinguished by the resolution of regular XRD. The formation of the σ phase was due to the metastable nature of the CoCrFeMnNi matrix. The prolonged heat input during LPBF processes and abundant dislocation stored in the matrix can lead to the precipitation of the σ phase. On the other hand, the formation of the Mn_2O_3 particles has not been investigated by the literature. In-situ oxidation during the process or inheritance from the raw powder could be possible sources.

2.3.1.4 Mechanical properties

Table 2.3 Comparison of mechanical properties of LPBFed CoCrFeMnNi HEAs at room temperature.

Refs	Hardness (HV)	σ_y (MPa)	σ_{uts} (MPa)	ε_f (%)
Rolling [33]	N/A	365	650	60
Casting [110, 125]	176	205 ± 5	493 ± 2	55 ± 3
DLD [126]	~200	246	566	~27
Li [10]	N/A	519	601	35
Zhu [110, 117]	~200	510 ± 10	609 ± 10	34 ± 3
Zhang [116]	N/A	~550	~650	~23
Wang [115]	N/A	583 ± 11	680 ± 13	23.8 ± 1.4
Piglione [111]	212	N/A	N/A	N/A
Kim [127]	N/A	774.8	923.3	30.8

The mechanical properties of LPBFed CoCrFeMnNi HEAs were significantly affected by the rapid solidification of LPBF processes. Microhardness and tensile properties were the main mechanical assessments in the literature.

As given in Table 2.3, the LPBFed CoCrFeMnNi HEAs possess improved microhardness and tensile strength, but compromised tensile ductility compared with the casted and DLDed HEAs. Such strength-ductility trade-off was recognised in other LPBFed alloys like 316L steel due to the high dislocation density and defects formed during LPBF processes [49]. Compression properties were investigated by a few studies [112, 120]. A significant tensile-compression asymmetry of ductility was recognised in LPBFed CoCrFeMnNi HEAs, because the LPBFed defects were less sensitive during the compressive deformation. Therefore, the failure in compression tests occurred at a much higher strain (77.6%) than in tensile tests. Moreover, the ultimate strength also increased to 2448 MPa due to the prolonged work hardening during tensile deformation [120].

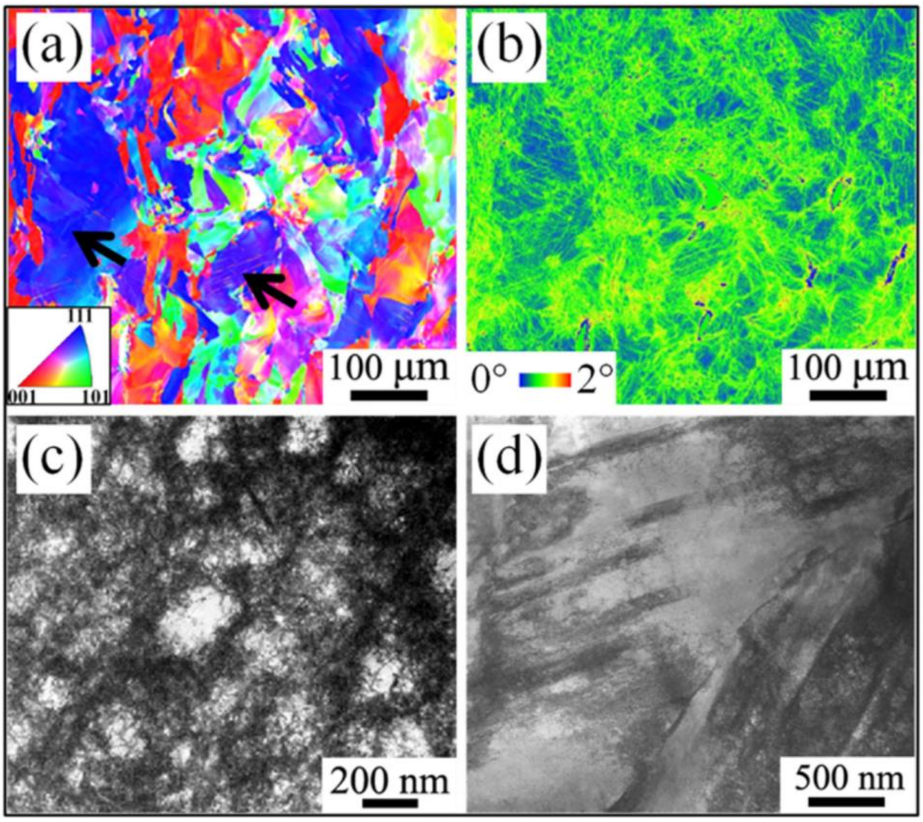

Figure 2.33 (a) IPF mapping, (b) KAM mapping and (c, d) Bright-field STEM results of a deformed CoCrFeMnNi sample. Black arrows show the deformation twinning [110].

Despite the Hall-Petch relation contributed by grain boundaries [33], dislocation strengthening has been considered a primary strengthening mechanism in LPBFed CoCrFeMnNi HEAs [110, 112]. During the deformation, dislocations are trapped by the pre-existing dislocation networks, and their motions are further hindered [124]. Figure 2.33 shows the sophisticated dislocation configuration after the tensile fracture. Limited deformation twinning was observed by Li et al. [10] and Zhu et al. [110] in their tensile-deformed specimens (Figure 2.33(a)).

Kim et al. [112, 127] systematically investigated the mechanical properties of the LPBFed CoCrFeMnNi HEA, and further suggested that the Orowan strengthening could be an essential strengthening mechanism because nano-size Mn oxides were observed in their approach (Figure 2.32(a)). The tensile strength reported by Kim et al. [127] was about 50% higher than the values from other studies that also employed pre-alloyed CoCrFeMnNi powders, while the tensile ductility remained comparable. It implies that a further understanding of the oxide formation during powder preparation and LPBF processes could be meaningful to the final performance. The mechanical properties of LPBFed HEAs also showed anisotropy as microstructural anisotropy was already revealed (Figure 2.27). In compression testing, the yield strength in the building direction (728 MPa) was lower than in the transverse direction (772 MPa), and the work hardening was more significant and evenly in the building direction [112]. In tensile testing carried out by Wang et al. [115], the yield strength and ultimate strength in the transverse direction were improved compared with the building direction; however, the ductility was compromised in the transverse direction.

In general, the hardness and strength of the CoCrFeMnNi HEA can be reinforced by the LPBF process, yet the tensile ductility decays to a moderate level (~30%). The results from different studies also suggest an available processing window for the modification of mechanical properties. Furthermore, different strengthening mechanisms such as the oxide-dispersion-strengthening can be introduced by LPBF, and promising performance has been realised by existing reports.

2.3.2 AM approaches to BCC AlCoCrFeNi HEA

Compared with the extensive reports on the CoCrFeMnNi HEA, the reports on LPBFed AlCoCrFeNi HEAs were relatively limited. Selective electron beam melting (SEBM) was employed to build block samples using pre-alloyed AlCoCrFeNi powder, and the products were compared with casted samples [128]. In Figure 2.34, XRD showed that instead of forming a BCC phase as the pre-alloyed powder and casted samples, the FCC phase was also detected at the bottom of SEBMed samples. Further EBSD results showed that the phase contents of the FCC phase were 19% near the bottom and 7% near the top of the SEBMed AlCoCrFeNi HEA. The precipitation of the FCC phase was due to the prolonged heating above 900 ℃ during the SEBM process [48]. In compression testing, cracks tended to initiate and grow along the BCC-FCC boundaries during deformation. However, the BCC + FCC dual-phase SEBMed sample still possessed better ductility than the casted sample which had a BCC single phase.

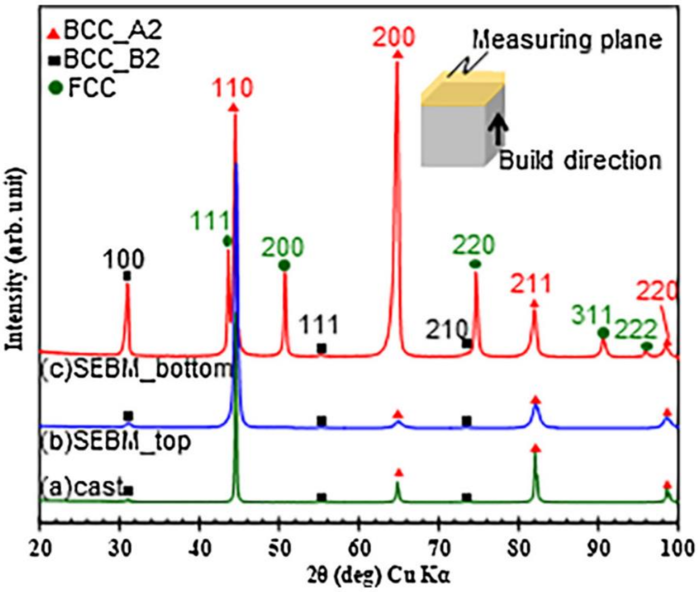

Figure 2.34 XRD spectra of casted and SEBMed AlCoCrFeNi samples.

By using the blends of gas-atomised elemental powders of Co, Cr, Fe, Ni and Al, Joseph et al. [44] in-situ fabricated $Al_xCoCrFeNi$ (x = 0.3, 0.6 and 0.85) HEAs via DLD successfully. As the Al content increased from 0.3 to 0.85, the phase formation in as-deposited HEAs transformed from FCC to FCC + BCC, and finally BCC. This approach was the first report on in-situ alloying HEAs via a laser-based AM technique, especially considering the brittleness of BCC HEAs. However, the laser spot used by LPBF is much smaller than that used by DLD. The resultant meltpools are therefore much smaller while the cooling rates are higher than DLD. Moreover, the high-temperature pre-heating used by SEBM has not yet been adopted by LPBF [49]. Considering the steep thermal gradient during LPBF processes, the printability of the AlCoCrFeNi HEA could be rather challenging.

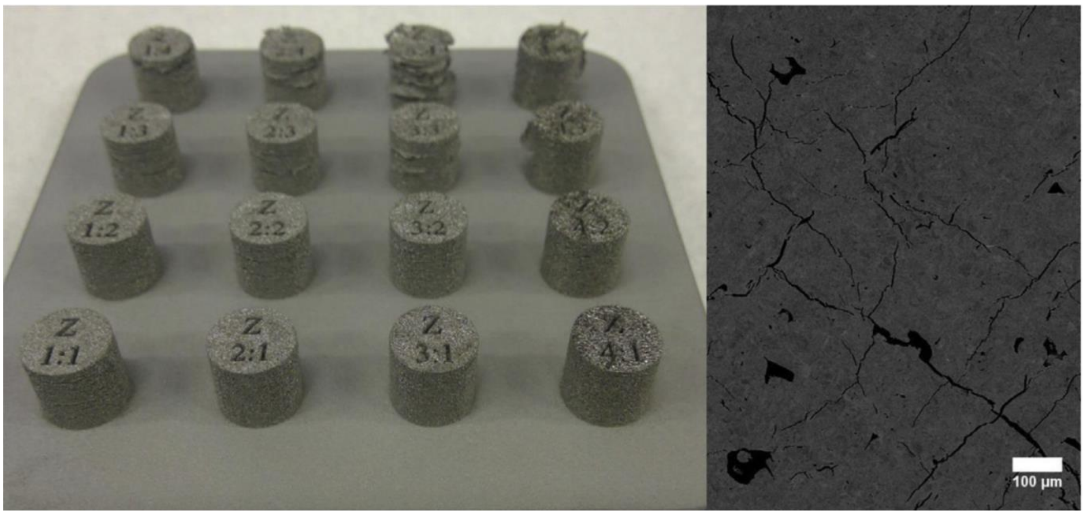

Figure 2.35 LPBFed samples fabricated using pre-alloyed AlCoCrFeNi powder and a BSE image of the cross-section of an as-built sample [129].

Karlsson et al. [129] investigated the feasibility of the LPBF printability of AlCoCrFeNi HEA using pre-alloyed powder. However, they failed to produce samples free of cracking/porosity despite trying a broad processing map with laser power, scanning speed, hatch spacing, defocus and layer thickness in wide ranges [129]. Figure 2.35 shows the as-built AlCoCrFeNi HEAs on a substrate. Macro-cracks can be observed on the surface of some samples. Meanwhile, in the samples with relative better surface quality, abundant pores and cracks can still be observed in cross-sections. A cracking-porosity trade-off was summarised by the study: By increasing the energy input, the cracking tendency was aggravated and led to the failure of building; By decreasing the energy input, more porosity occurred due to the insufficient fusion of powder. Karlsson et al. suggested that the main reason for the inevitable cracking was the cycling thermal stresses and phase transformation during the process. As shown in Figure 2.36, the content of the FCC phase could increase to about 40 % when the AlCoCrFeNi powder was heated to 900 °C. It was also suggested in the study that a pre-heating stage at elevated temperatures or compositional modifications could improve the building quality of the AlCoCrFeNi HEA.

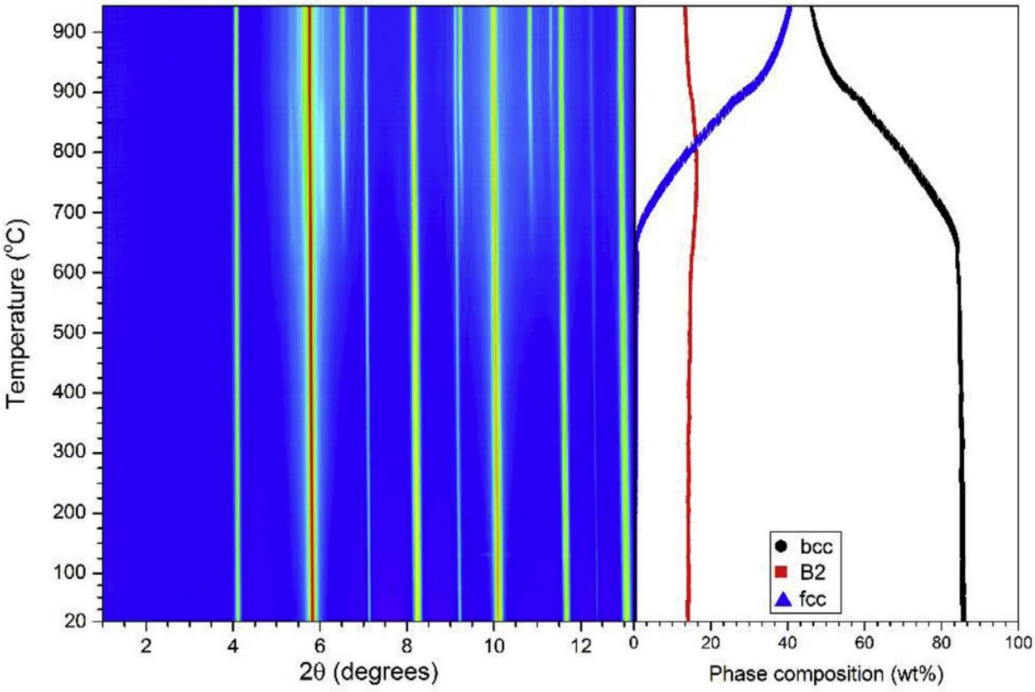

Figure 2.36 In-situ XRD results from 20 to 900 °C showing the phase composition of pre-alloyed AlCoCrFeNi powder [129].

Niu et al. [130] also carried out LPBF fabrication by using pre-alloyed AlCoCrFeNi powder. The substrate was pre-heated to 100 ℃ for the building, and the *VED* in a range from 69.4 to 111.1 J/mm^3 was investigated by the study. A maximum relative density of 98.4% was achieved at the highest *VED*. The as-built AlCoCrFeNi HEAs consisted of disordered A2 and ordered B2 BCC phases. Meanwhile, the hardness of LPBFed samples was improved compared with the DLDed and SEBMed ones. However, only microstructures and microhardness results were produced by the study, but the overall formability of as-built samples was not presented.

The LPBF printability of Al$_x$CoCrFeNi HEA variations has also been investigated by using pre-alloyed powders. Peyrouzet et al. [131] fabricated the FCC Al$_{0.3}$CoCrFeNi HEA with near fully densification via LPBF. Similarly, the FCC Al$_{0.5}$CoCrFeNi HEA also possessed good LPBF printability with pre-alloyed powder [132]. These approaches further suggested that the brittle BCC phase restricted the printability of BCC Al$_x$CoCrFeNi HEAs. Otherwise, FCC Al$_x$CoCrFeNi HEAs still possessed the good printability similar to other FCC CoCrFeNi-based HEAs.

By comparing the results of different AM approaches to the AlCoCrFeNi HEA, it can be concluded that the LPBF printability of the BCC AlCoCrFeNi HEA is limited. The BCC matrix is not as ductile as the FCC matrix, and the phase transformation caused by heating cycles further introduces unstable phase interfaces. Therefore, the AlCoCrFeNi HEA lacks resistance to the thermal stress during LPBF processes. Since pre-heating at elevated temperatures was not conducted by the available reports, it could be a possible processing route to produce the AlCoCrFeNi HEA without cracking.

2.4 LPBF In-Situ Alloying

LPBF was initially developed as a net-shape technique to produce complex components. Therefore, the pre-alloyed powder is the preferred feedstock for LPBF. The gas atomisation of commercial alloys, such as 316L steel, Inconel 625, Ti-6Al-4V and AlSi10Mg, etc., has been well established by worldwide suppliers [49, 51]. However, LPBF's potential for in-situ alloying has been gradually recognised by researchers over the past few years [52, 54]. LPBF has shown the capability of in-situ alloying minor contents of elemental powders or secondary particles [81, 123, 133, 134]. However, regarding the alloy development of HEAs, the modification of compositions is often on an equiatomic scale, which further challenges the capability of in-situ homogenisation.

Zhang et al. [135, 136] carried out LPBF in-situ alloying to produce shape memory Ti-Ni and magnetic Fe-Ni alloys, by using Ti-Ni (1:1 at. %) and Fe-Ni (7:3 at. %) blended powders, respectively. Bulk samples were successfully fabricated using the blended powders, and the Ti-Ni approach reached a relative density higher than 99%. Meanwhile, the by-product intermetallics such as Ti_2Ni and Fe_7Ni_3, and elemental homogeneity were also observed in the as-built samples. Although the approaches demonstrated that bulk samples could be fabricated by LPBF using the blended elemental powders, the expected phase formation was not achieved.

Grigoriev and Polozov et al. [134, 137] used blended elemental powder to produce Ti-5Al and Ti-22Al-25Nb alloys. The as-built Ti-5Al samples had an HCP single phase with elemental homogeneity. Moreover, the mechanical properties of the in-situ alloyed Ti-5Al were comparable to the casted Ti-5Al. On the other hand, the as-built samples of Ti-22Al-25Nb, which had a concentrated composition like HEAs, also achieved a high relative density of 99.55%. But the as-built Ti-22Al-25Nb samples showed a complex phase composition in the

XRD results, and further scanning electron microscopy (SEM) characterisation revealed that the Nb was barely dissolved into the matrix, see Figure 2.37. Polozov et al. claimed that the poor homogenisation of Nb was due to its incompatible melting point. The results implied that the elemental homogenisation of concentrated compositions could be challenging to LPBF.

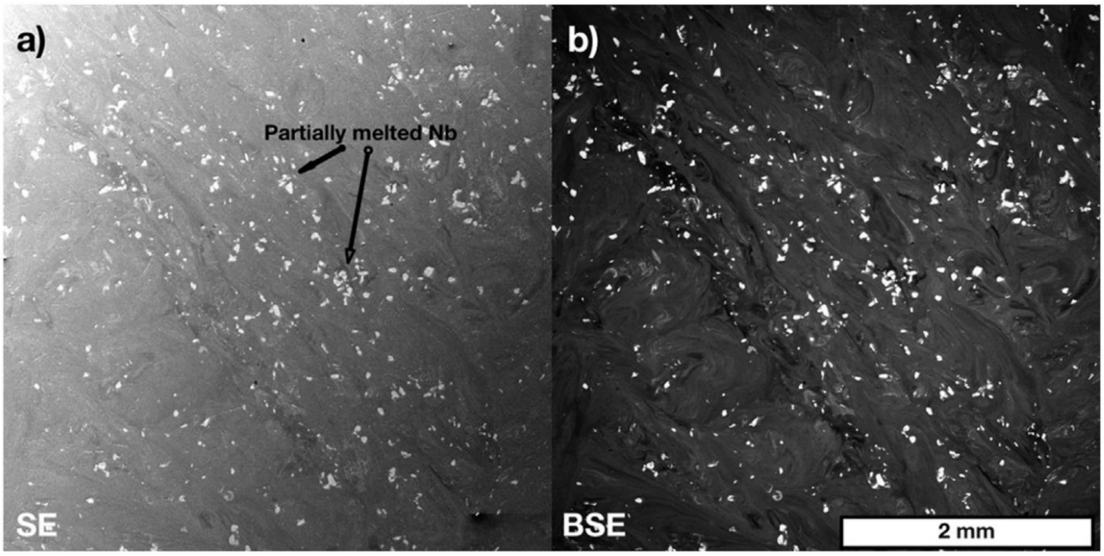

Figure 2.37 (a) SE and (b) BSE images of LPBF in-situ alloyed Ti-22Al-25Nb.

As learnt from the early in-situ alloying attempts, besides the general metallurgical defects initiated by the LPBF process, the elemental homogeneity and complications raised by the incompatible thermal-physical properties are foreseeable when carrying out the in-situ alloying of HEAs [54].

2.4.1 In-situ alloying approaches to HEAs

AM techniques, including DLD and SEBM, have shown the capability of fabricating HEAs from elemental powders [44, 138, 139]. The $Al_xCoCrFeNi$ and CoCrFeMnNi HEAs in-situ fabricated by DLD possessed uniform elemental distribution and good densification. It was verified by the studies that the use of blended powders could advance the compositional flexibility of HEAs. Moreover, the rapid prototyping capability of AM can validate the performance of new compositions efficiently. Considering the forming accuracy and emerging industrial applications of LPBF, in-situ alloying via LPBF can further improve the efficiency from compositional design to component validation [140]. Most LPBF studies have used pre-alloyed powders as feedstock, especially notable HEAs like the Cantor alloy have been studied by worldwide researchers. The reports on LPBF in-situ alloying, nevertheless, was much limited compared with the vast compositions of HEAs. It should be noted that there has not been any previous publication on LPBF in-situ alloying of HEAs before the establishment of this study.

2.4.1.1 Approaches using elemental powders

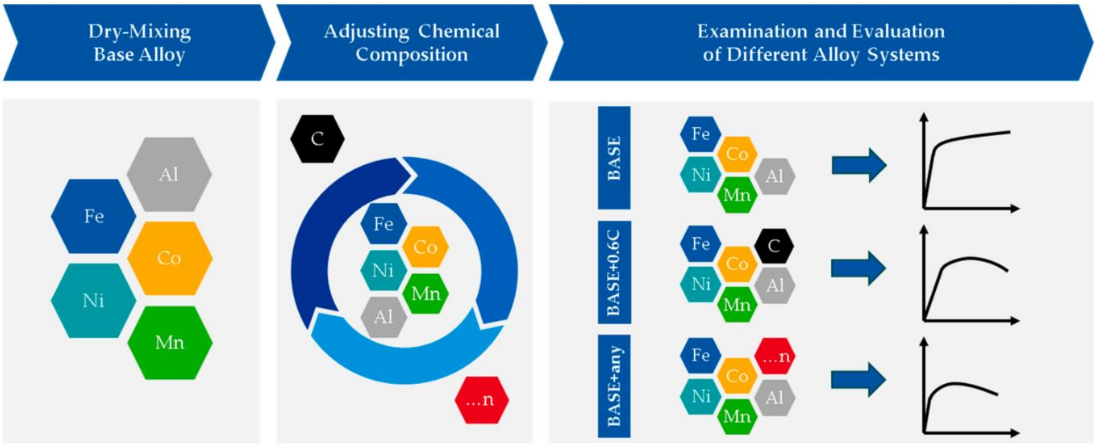

Figure 2.38 Illustration of the rapid alloy development via LPBF in-situ alloying [141].

Ewald et al. [141] introduced a rapid alloy development methodology using LPBF, which was inspired by a previous study using DLD [139]. The illustration in Figure 2.38 presents the route from mixing elemental powders to validating the mechanical properties of HEAs with different compositions. In this study, the $Al_{0.26}CoFeMnNi$ HEAs with/without 0.6 wt. % of C was fabricated from elemental powders to evaluate the feasibility of in-situ alloying. As shown in

Figure 2.39, the elemental powders had distinct morphology and size distribution. A relative density above 99.5% was achieved with both compositions. More importantly, an FCC structure and homogeneous elemental distribution with minor Al segregations were obtained with the high *VED*, as shown in Figure 2.40. The additional C dramatically improved the tensile strength and ductility of the HEA. This study verified the feasibility of using elemental powders to in-situ fabricate and modify HEAs by LPBF. It was also emphasised that the application of the high *VED* (247 J/mm^3) was critical to elemental homogenisation since more elemental powder could be melted. The study also claimed that burning loss could happen due to the incompatible physical properties of the elements. However, the chemical compositions of the as-built samples were not presented in their results.

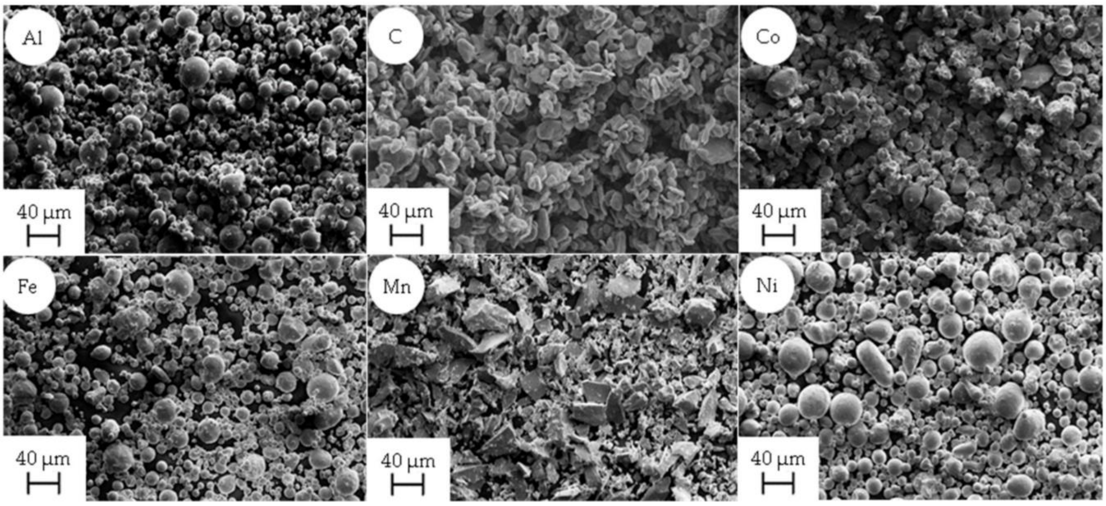

Figure 2.39 SEM images of elemental powders used to produce the Al$_{0.26}$CoFeMnNi HEA [141].

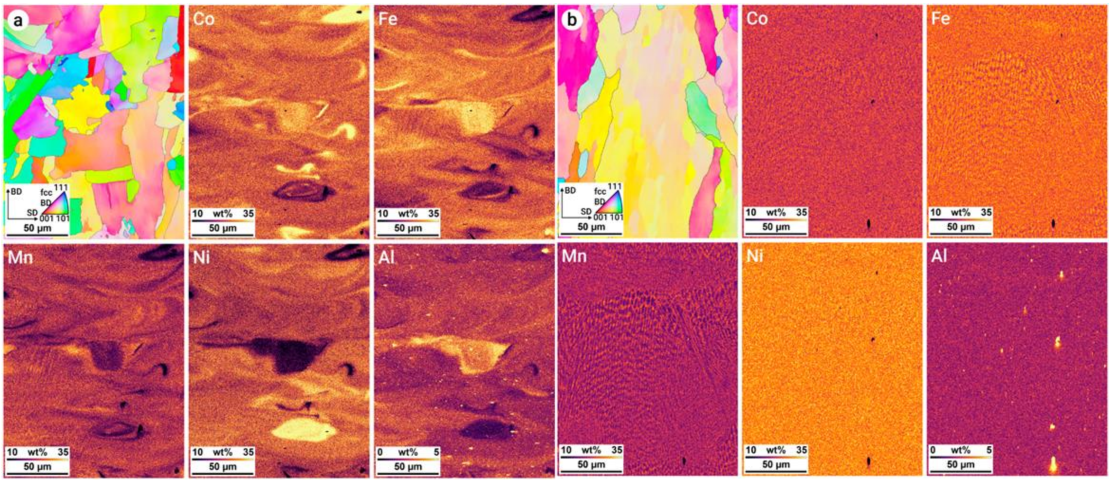

Figure 2.40 IPF and EDS mapping results of the in-situ alloyed $Al_{0.26}$CoFeMnNi HEAs fabricated with the *VED* of (a) 143 and (b) 247 J/mm^3 [141].

Hou et al. [142] comparatively studied the FCC CoCrFeNi HEAs fabricated using pre-alloyed powder and elemental powders, respectively. The as-built samples showed an FCC structure in XRD spectra. However, the densification and mechanical properties were not identical, although the same parameters were applied, as given in Figure 2.41. The lack of strength at the low *VED* was correlated with the abundant lack-of-fusion defects in the in-situ alloyed samples. Nevertheless, the mechanical properties of the in-situ alloyed samples were even improved compared with the pre-alloyed ones when the high *VED* was applied. The elemental homogenisation was found to be more effective at the highest *VED* of 223 J/mm^3, but still with minor segregations at meltpool boundaries. The complete homogenisation of elements required heat treatment (1200 °C, 20 h). The incompatible melting points and size distribution of alloying elements were considered the main reasons for the segregations.

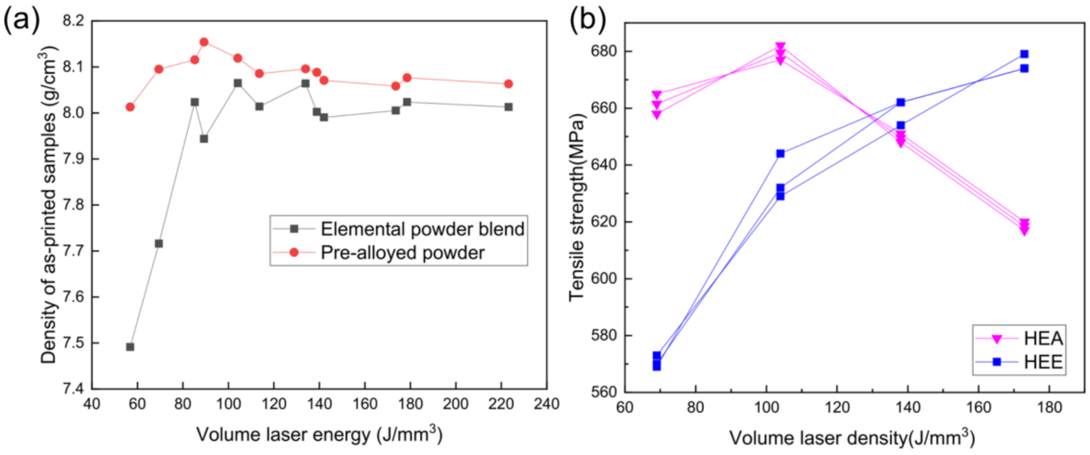

Figure 2.41 (a) Density and (b) tensile strength of CoCrFeNi HEAs built using pre-alloyed (HEA) and elemental powders (HEE) [142].

A BCC refractory HEA, VNbMoTaW, was prepared using elemental powders by Huber et al. [143]. Although extreme parameters such as the laser power of 600 W and scanning speed of 100 mm/s were employed to produce an excessive *VED* of 889 J/mm^3, unmelted W particles and cracking were hard to be eliminated during the LPBF process. Hence, high-temperature pre-heating was recommended by the study to avoid cracking, because the ductility of the BCC VNbMoTaW HEA was limited at room temperature. Moreover, refractory elements like W and Mo, which had very high melting points, were not recommended in terms of LPBF in-situ alloying.

In-situ alloying approach to the $Al_{0.5}CoCrFeNi$ HEA was carried out by Sun et al. [144] using blended elemental powders. Cracks and pores were observed in the samples built with the low *VED*. The relative density was improved to 99.92% as the energy input increased to 150 J/mm^3, as shown in Figure 2.42(a). The in-situ alloyed samples using the optimised parameters also had a good surface finish (Figure 2.42(b)). Although the XRD results indicated the resultant samples consisted of FCC and BCC phases, the tensile performance was still similar to the FCC HEAs, instead of showing the brittleness of the BCC phase. Elemental heterogeneity was evident in the as-built samples, implying the difficulty of fully homogenising concentrated elemental powders.

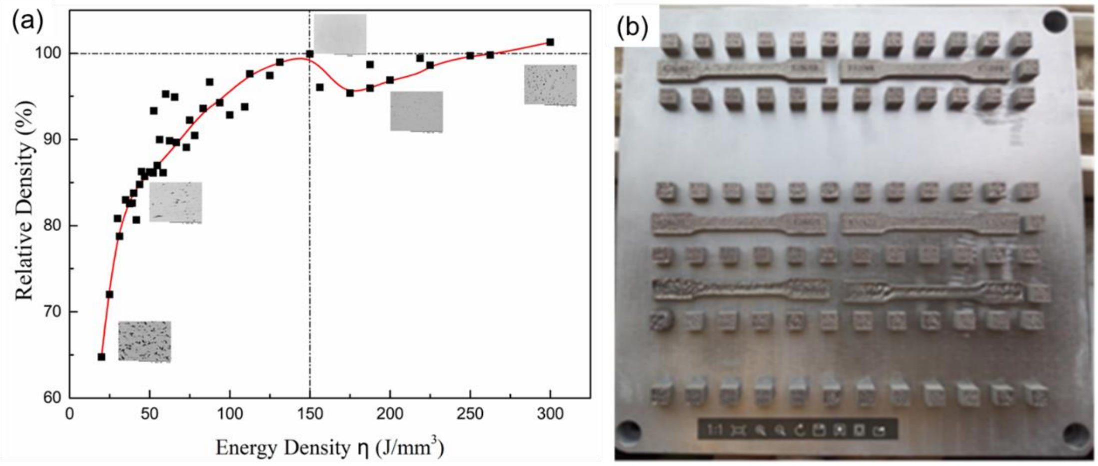

Figure 2.42 (a) Relative density verse volumetric energy density and (b) top-view of in-situ alloyed $Al_{0.5}CoCrFeNi$ samples [144].

2.4.1.2 Approaches using pre-alloyed powders as the base

Besides using the blends of individual elemental powders, the blends of pre-alloyed powders and additional elemental powders have been employed by LPBF in-situ alloying as well [145-148]. Since many HEA systems share common principal elements, the vast space in phase diagrams can be explored by varying the contents of one or two elements. The pre-alloyed powders of some common principal elements, e.g., Fe, Ni, and Cr, in the 3d-transition HEAs, can improve the elemental homogeneity in blended powders and thus promote homogenisation.

By using the blends of pre-alloyed AlCrCuFeNi powder and elemental Ni powder, the $AlCrCuFeNi_x$ ($2 \leq x \leq 3$) HEA system with BCC + FCC dual-phase structures was in-situ fabricated by Luo et al. [145]. The increment of Ni contents could promote the BCC-to-FCC transformation in the HEA system. And the cracking tendency was restrained when the highest Ni/FCC content was adopted. The as-built $AlCrCuFeNi_3$ samples possessed an FCC + B2 dual-phase structure. Meanwhile, coherent A2 nano-precipitates were found embedded in the B2 phase. The formation of B2/A2 interfaces stimulated twinning and phase transformation in the B2 phase during tension, which was recognised as a new deforming mechanism in HEAs.

Lin et al. [146] used elemental Fe, Co, Ni, and pre-alloyed $Ni_{47}Cr_{50}Si_3$ powders to fabricate the CoCrFeNi HEA with 1.5 at. % of Si. The study implemented extra scanning in each layer with a relatively low energy input after the first scanning. Then the influences of remelting on elemental homogenisation and mechanical properties were compared with the samples without remelting. The elemental homogenisation was significantly improved by the remelting, and Liu et al. attributed it to the extra internal flows introduced during the process, as illustrated in Figure 2.43. The strength and ductility of the remelted samples were both meliorated due to the microstructural optimisation, i.e., finer grain size, higher densification, and improved homogeneity.

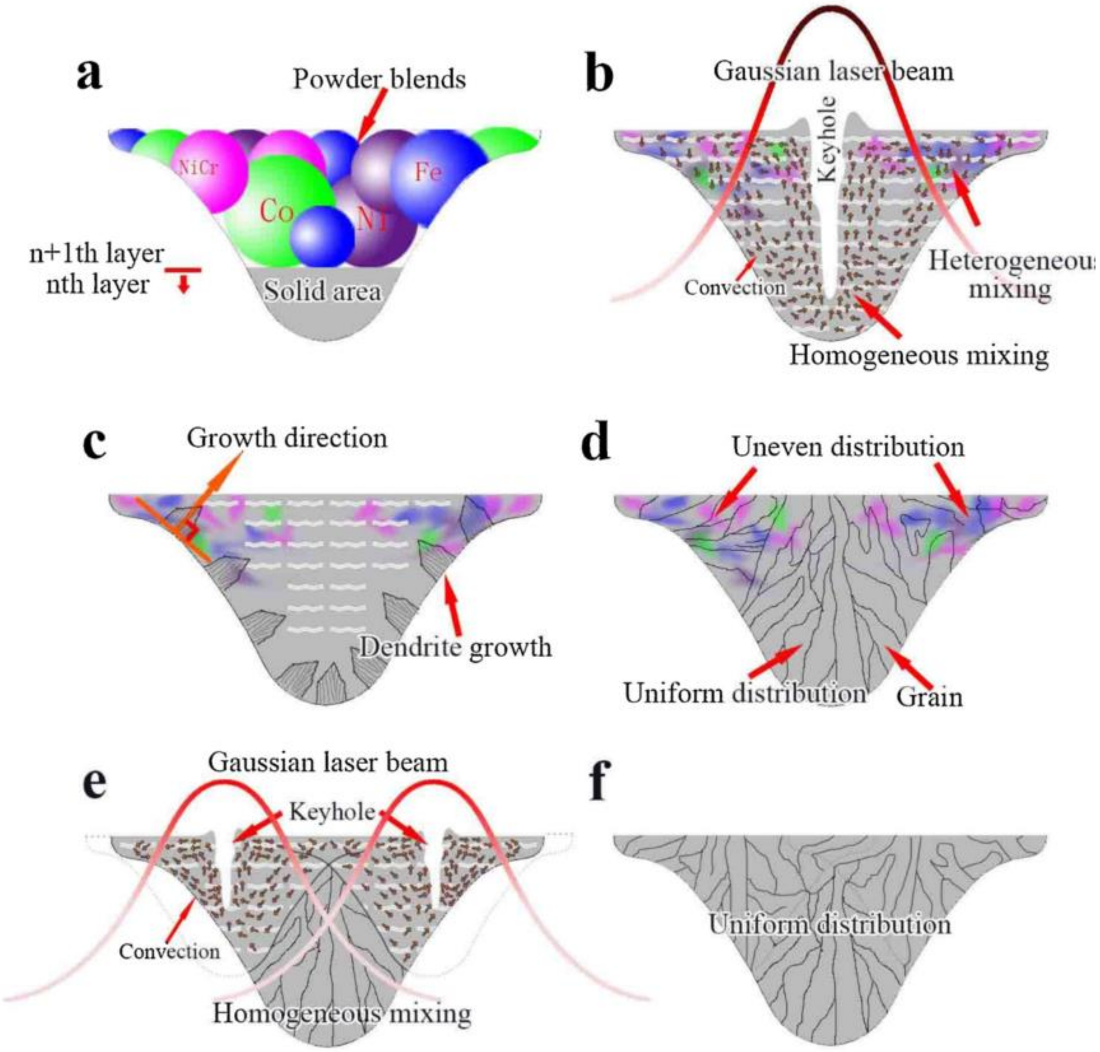

Figure 2.43 Schematic illustrating the microstructural development with the extra scanning in each layer of in-situ alloyed CoCrFeNi HEA [146]. (a) Blended powder is firstly scanned by (b) a high-power laser and forms a keyhole meltpool. (c) The meltpool solidification with (d) heterogeneous elemental distribution. (e) The as-solidified layer is then scanned by a low-power laser and achieves uniform elemental distribution.

Kuzminova et al. [147] and Gao et al. [148] used powder blends composed of pre-alloyed CoCrFeNi powders and elemental powders to fabricate $Al_xCoCrFeNi$ ($0 \leq x \leq 0.1$) and CoCrCuFeNi HEAs, respectively. In both studies, the in-situ alloyed HEAs appeared an FCC single phase in XRD spectra, and without fatal defects. However, with the similar *VED* applied by the two studies, the homogenisation of the Al was not as ideal as the Cu, whose content was even higher. A small amount of BCC phase also formed in the $Al_{0.1}$CoCrFeNi samples, and the content of Al dropped from 3.0 wt. % in the blended powder to 1.67 wt. % in the as-built sample, indicating near 50% of Al burning loss.

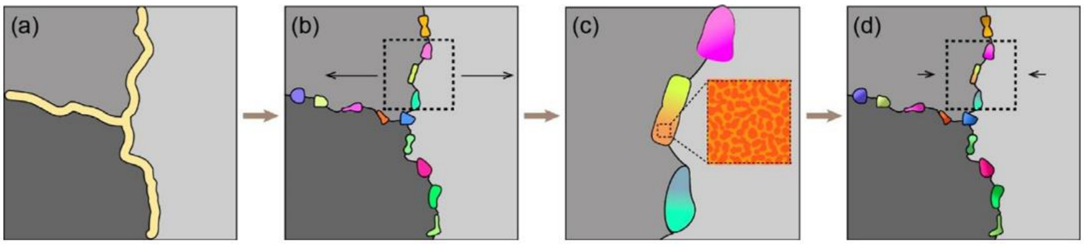

Figure 2.44 Schematic illustrating the minimisation of residual stress in the in-situ alloyed $Al_{0.5}$CoCrFeNi HEA. (a) Al segregates at the dendrite/grain boundaries of the FCC matrix and forms (b) BCC/B2 grains at the boundaries. (c) Tensile stress at grain boundaries is neutralised by the molar volume expansion of BCC/B2 grains. (d) The tensile residual stress is tuned into relatively minor compressive residual stress, and therefore cracking is restrained [149].

Sun et al. [149] analysed the cracking tendency of in-situ alloyed Al_xCoCrFeNi ($0 \leq x \leq 1$) HEAs, which were fabricated using the blends of elemental Al and pre-alloyed CoCrFeNi powders. This study showed that cold cracking was the dominant cracking mechanism in the equiatomic AlCoCrFeNi samples with the brittle BCC phase, which was consistent with the pre-alloyed approaches [129]. Furthermore, compared with the pre-alloyed CoCrFeNi samples, liquation cracking increased significantly in $Al_{0.1}$CoCrFeNi samples due to an enlarged solidification range. However, it should be noted that the $Al_{0.1}$CoCrFeNi HEA provided via Kuzminova et al. [147] was without evident cracking, indicating the cracking could be inhibited by optimising parameters. On the other hand, Sun et al. recognised that cracking was restrained in the $Al_{0.5}$CoCrFeNi samples fabricated with the identical processing parameters, and further investigated the mechanism of cracking inhibition. A grain boundary engineering theory was raised by the study: After the solidification of FCC grains, BCC/B2 grains formed at interdendritic boundaries due to the segregation of Al; The tensile residual stress was hence neutralised by the expansion of the BCC/B2 phase, as illustrated in Figure 2.44. Although such grain boundary segregation engineering demands precise compositional control during in-situ alloying processes when extended to other alloy systems, this study still provides a possible route to improve the printability of LPBFed parts.

2.4.2 Summary of LPBF in-situ alloyed HEAs to date

Table 2.4 summarises the printability of LPBFed in-situ alloyed HEAs to date. Since the first report from Ewald et al. [141] in 2019, several in-situ alloying approaches have been carried out by different groups using powder blends over the recent years. Most of these approaches have managed to produce bulk HEAs with a relative density above 99% and free of cracking. By summarising the in-situ alloying approaches and comparing them with the pre-alloyed ones, some features of LPBF in-situ alloyed HEAs are presented as follows:

- In-situ alloying processes favours parameters producing relative higher *VED* (> 150 J/mm^3) than pre-alloyed approaches (~70 J/mm^3). Besides eliminating the lack-of-fusion porosity, the high *VED* is crucial to elemental homogenisation.
- The printability of FCC-dominated HEAs is overall better than the BCC-dominated HEAs in terms of the resistance to cracking.
- Although overall elemental distribution can be homogenised by using the high *VED* and XRD spectra show HEA phases only, by-product secondary phases tend to form during the in-situ alloying process, especially when introducing active elements such as Al and Mn.

- The microstructures of the in-situ alloyed HEAs are more complicated than the pre-alloyed ones due to local heterogeneity on the nanoscale. However, such heterogeneous structures could result in the reinforcement of hardness and strength.
- The chemical compositions of the in-situ alloyed HEAs always deviate from their nominal compositions. A compromise between the burning loss and insufficient homogenisation of alloying elements due to incompatible thermal-physical properties is therefore raised.

Table 2.4 Comparison of LPBF in-situ alloyed HEAs

HEA	Powders	Relative density (%)	Optimised VED (J/mm^3)	Phase	Homogeneity	notes
$Al_{0.26}$CoFeMnNi [141]	elemental	99.98	247	FCC + Al oxides	good	N/A
$Al_{0.5}$CoCrFeNi [144]	elemental	99.92	150	FCC + BCC	insufficient	Al burning loss
Al_xCoCrFeNi ($0 \leq x \leq 0.1$) [147]	CoCrFeNi + Al	99.85	156	FCC + BCC	insufficient	Al burning loss
Al_xCoCrFeNi ($0 \leq x \leq 1$) [149]	CoCrFeNi + Al	N/A	111	FCC + BCC	pure Al particles	crack-free, x = 0.5
AlCrCuFeNi_x ($2.0 \leq x \leq 3.0$) [145]	AlCrCuFeNi + Ni	> 99.7	312	FCC + BCC	good	crack-free, x = 3
CoCrFeNi + 1.5 at. % Si [146]	$Ni_{47}Cr_{50}Si_3$ + Fe, Co,Ni	99.85	remelting	FCC	good	N/A
CoCrFeNi [142]	elemental	> 99	223	FCC	regional deviation	N/A
CoCrCuFeNi [148]	CoCrFeNi + Cu	>99.5	100	FCC	good	N/A
VNbMoTaW [143]	elemental	> 99.8	889	BCC	unmelted W	severe cracking
WTaMoNb [150]	elemental	< 90	remelting	BCC	N/A	delamination

2.5 ODS Alloys In-Situ Fabricated by LPBF

Oxide-dispersion-strengthened (ODS) alloys are potential for elevated-temperature applications such as the nuclear industry, due to the thermal stability and strengthening effect of oxide particles [151-153]. However, the production of ODS parts with homogeneous oxide distribution is challenging: The nano-size oxides tend to agglomerate when handled via ingot metallurgy methods such as casting; Powder metallurgy methods such as HIP or spark plasma sintering (SPS) lack geometric flexibility [152]. Hence, AM techniques with rapid solidification have been employed to produce ODS alloys with homogeneous oxide distribution, as well as complex structures.

Through AM processes, oxide particles can be introduced into base alloys from two sources, either pre-added oxide particles or in-situ oxidation. Boegelein et al. [152] fabricated ODS steels via LPBF using a mechanically alloyed powder. A fine dispersion of nano-size Y(Al, Ti) oxide particles was retained in the as-built samples, indicating the agglomerate of particles could be inhibited by rapid solidification. However, Hunt et al. [154] claimed that the dispersion of yttria oxide particles was damaged in their LPBF approach using similar mechanically alloyed powder. It was noted that the laser power applied (360 W) by Hunt et al. was significantly higher than that used by Boegelein et al. (50 W), indicating that the oxide particles could be unstable due to the high energy input. Besides mechanically alloyed powder, pre-alloyed powders coated with oxide particles (Y_2O_3, La_2O_3) have been recently employed to fabricate ODS alloys as well [155-158], see the schematic in Figure 2.45. The ODS CP-Ti, and steels fabricated using the oxide-coated powders possessed fine dispersion of oxide particles with average sizes between 10 and 100 nm, as well as improved mechanical properties. The results from these studies suggest that, with proper processing optimisation, oxide particles can be retained and further dispersed in the LPBFed parts, leading to the improvement of mechanical properties.

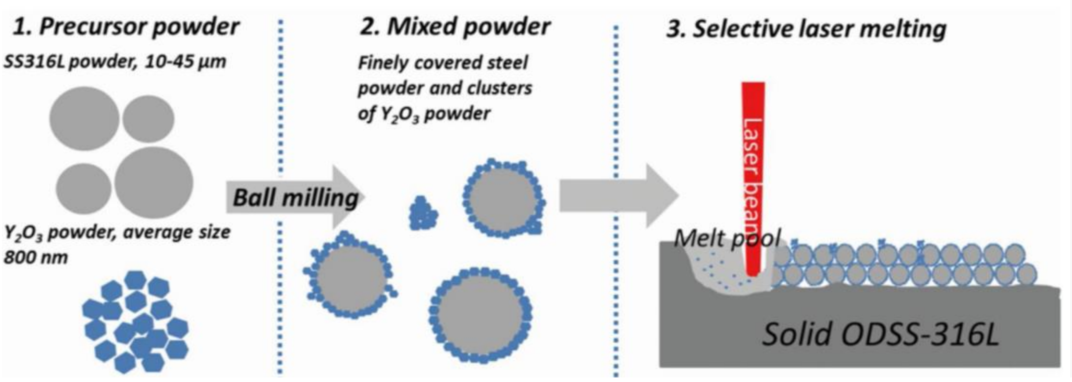

Figure 2.45 Schematic illustrating the LPBF process of ODS 316L steel using oxide-coated powder [157].

In-situ oxidation is another way to introduce oxides into AM parts. Springer et al. [159] removed the gas shield on purpose during the laser deposition of 316L powder. Consequently, $MnCr_2O_4$ particles with an average size of 400 nm were found in the as-deposited samples. More recently, the dispersed oxide particles formed due to in-situ oxidation have also been recognised in LPBFed products fabricated with Ar protection [127, 160-163]. The oxygen could originate from the building atmosphere, and raw powders, e.g., the Fe-Ni (Invar 36) powder with an oxygen content of 3000 ppm was used by Chunlei [161]. In most cases, the in-situ formed particles lead to the reinforcement of hardness and strength as extrinsic oxide particles, e.g., in-situ formed Mn_2O_3 particles (average size = 27.3 nm) dramatically improved the tensile strength whilst maintaining comparable ductility of an LPBFed CoCrFeMnNi HEA [127]. However, Lou et al. [160] also stated that micro-voids could be induced by oxide particles and decay the toughness of LPBFed parts, where the average particle size was 300 nm. Regarding the Orowan strengthening, its strengthening effect increases with the decreasing size and increasing volume fraction of particles; meanwhile, below100 nm is suggested as the effective size range of increasing reinforcement [164, 165]. In general, the mechanical performance of the in-situ alloyed ODS alloys depends on the final distribution of particles, while the reported particle sizes and contents vary in wide ranges, especially those approaches of in-situ oxidation. It is reasonable to conclude that the in-situ formation of oxides is not as ideal as the mechanically alloyed or coated powders at the current stage.

2.6 Gaps in the Literature

In this literature review, an overview of CoCrFeNi-based HEAs and their fabrication through LPBF is provided. The HEAs produced via AM in-situ alloying are summarised. Furthermore, the investigations of ODS approaches and LPBFed meltpools are included.

Based on the review, it can be summarised that HEAs are of growing interest in the LPBF community. Over recent years, LPBF in-situ alloying approaches have been conducted to accelerate the alloy development of HEAs. The gaps in the literature and their corresponding investigations in this research are given as follows:

- HEAs, especially the FCC HEAs, have shown outstanding formability via LPBF. However, the reported approaches were mostly using pre-alloyed powders. Lack of research assessed the in-situ fabrication of HEAs using LPBF.
- The 3d-transition HEAs were the most extensively studied HEA family, including the notable FCC CoCrFeMnNi and BCC AlCoCrFeNi HEAs. Therefore, in-situ alloying using the quaternary CoCrFeNi HEA as the base alloy can be a promising composition to start with.

LPBF processing development using the powder blends of pre-alloyed CoCrFeNi and elemental powders to produce quinary HEAs is investigated.

- ODS HEAs were fabricated via methods such as SPS. However, there was limited research that investigated the feasibility of the fabrication of ODS HEAs via AM techniques.

Mechanical properties of the in-situ alloyed CoCrFeMnNi HEA are examined. ODS effect and the formation of oxides are analysed.

- The building quality of LPBF in-situ alloying was mainly assessed via experimental bulk building. No previous research focused on the microstructural development in the single-track meltpools.
- Single tracks have been studied via abundant attempts. However, limited studies investigated the influences of remelting.

Systematic experiments based on single tracks are designed in this research. The microstructural development during the in-situ alloying processes is revealed.

2.7 References

[1] J.W. Yeh, S.K. Chen, S.J. Lin, J.Y. Gan, T.S. Chin, T.T. Shun, C.H. Tsau, S.Y. Chang, Nanostructured high-entropy alloys with multiple principal elements: Novel alloy design concepts and outcomes, Advanced Engineering Materials 6(5) (2004) 299-303. http://doi.org/10.1002/adem.200300567.

[2] B. Cantor, I.T.H. Chang, P. Knight, A.J.B. Vincent, Microstructural development in equiatomic multicomponent alloys, Materials Science and Engineering: A 375-377 (2004) 213-218. http://doi.org/10.1016/j.msea.2003.10.257.

[3] B. Cantor, Multicomponent and High Entropy Alloys, Entropy 16(9) (2014) 4749-4768. http://doi.org/10.3390/e16094749.

[4] Y. Zhang, T.T. Zuo, Z. Tang, M.C. Gao, K.A. Dahmen, P.K. Liaw, Z.P. Lu, Microstructures and properties of high-entropy alloys, Progress in Materials Science 61 (2014) 1-93. http://doi.org/10.1016/j.pmatsci.2013.10.001.

[5] D.B. Miracle, O.N. Senkov, A critical review of high entropy alloys and related concepts, Acta Materialia 122 (2017) 448-511. http://doi.org/10.1016/j.actamat.2016.08.081.

[6] E.P. George, D. Raabe, R.O. Ritchie, High-entropy alloys, Nature Reviews Materials 4(8) (2019) 515-534. http://doi.org/10.1038/s41578-019-0121-4.

[7] X. Li, Additive manufacturing of advanced multi-component alloys: Bulk metallic glasses and high entropy alloys, Advanced Engineering Materials 20(5) (2017) 1700874. http://doi.org/10.1002/adem.201700874.

[8] C. Han, Q. Fang, Y. Shi, S.B. Tor, C.K. Chua, K. Zhou, Recent advances on high-entropy alloys for 3D printing, Advanced Materials 32(26) (2020) 1903855. http://doi.org/10.1002/adma.201903855.

[9] Y. Brif, M. Thomas, I. Todd, The use of high-entropy alloys in additive manufacturing, Scripta Materialia 99 (2015) 93-96. http://doi.org/10.1016/j.scriptamat.2014.11.037.

[10] R. Li, P. Niu, T. Yuan, P. Cao, C. Chen, K. Zhou, Selective laser melting of an equiatomic CoCrFeMnNi high-entropy alloy: Processability, non-equilibrium microstructure and mechanical property, Journal of Alloys and Compounds 746 (2018) 125-134. http://doi.org/10.1016/j.jallcom.2018.02.298.

[11] M.J. Yao, K.G. Pradeep, C.C. Tasan, D. Raabe, A novel, single phase, non-equiatomic FeMnNiCoCr high-entropy alloy with exceptional phase stability and tensile ductility, Scripta Materialia 72-73 (2014) 5-8. http://doi.org/10.1016/j.scriptamat.2013.09.030.

[12] B. Cantor, Multicomponent high-entropy Cantor alloys, Progress in Materials Science 120 (2021) 100754. http://doi.org/10.1016/j.pmatsci.2020.100754.

[13] R. Zhou, Y. Liu, C. Zhou, S. Li, W. Wu, M. Song, B. Liu, X. Liang, P.K. Liaw, Microstructures and mechanical properties of C-containing FeCoCrNi high-entropy alloy fabricated by selective laser melting, Intermetallics 94 (2018) 165-171. http://doi.org/10.1016/j.intermet.2018.01.002.

[14] Z.G. Zhu, K.H. Ma, Q. Wang, C.H. Shek, Compositional dependence of phase formation and mechanical properties in three CoCrFeNi-(Mn/Al/Cu) high entropy alloys, Intermetallics 79 (2016) 1-11. http://doi.org/10.1016/j.intermet.2016.09.003.

[15] H. Shiratori, T. Fujieda, K. Yamanaka, Y. Koizumi, K. Kuwabara, T. Kato, A. Chiba, Relationship between the microstructure and mechanical properties of an equiatomic AlCoCrFeNi high-entropy alloy fabricated by selective electron beam melting, Materials Science and Engineering: A 656 (2016) 39-46. http://doi.org/10.1016/j.msea.2016.01.019.

[16] B. Jia, X. Liu, H. Wang, Y. Wu, Z. Lu, Microstructure and mechanical properties of FeCoNiCr high-entropy alloy strengthened by nano-Y2O3 dispersion, Science China Technological Sciences 61 (2017) 179-183. http://doi.org/10.1007/s11431-017-9115-5.
[17] M. Ogura, T. Fukushima, R. Zeller, P.H. Dederichs, Structure of the high-entropy alloy Al x CrFeCoNi: fcc versus bcc, Journal of Alloys and Compounds 715 (2017) 454-459. http://doi.org/10.1016/j.jallcom.2017.04.318.
[18] H. Jiang, K. Han, D. Qiao, Y. Lu, Z. Cao, T. Li, Effects of Ta addition on the microstructures and mechanical properties of CoCrFeNi high entropy alloy, Materials Chemistry and Physics 210 (2017) 43-48. http://doi.org/10.1016/j.matchemphys.2017.05.056.
[19] W.H. Liu, J.Y. He, H.L. Huang, H. Wang, Z.P. Lu, C.T. Liu, Effects of Nb additions on the microstructure and mechanical property of CoCrFeNi high-entropy alloys, Intermetallics 60 (2015) 1-8. http://doi.org/10.1016/j.intermet.2015.01.004.
[20] Z. Lei, X. Liu, Y. Wu, H. Wang, S. Jiang, S. Wang, X. Hui, Y. Wu, B. Gault, P. Kontis, D. Raabe, L. Gu, Q. Zhang, H. Chen, H. Wang, J. Liu, K. An, Q. Zeng, T.G. Nieh, Z. Lu, Enhanced strength and ductility in a high-entropy alloy via ordered oxygen complexes, Nature 563(7732) (2018) 546-550. http://doi.org/10.1038/s41586-018-0685-y.
[21] J.W. Yeh, Recent progress in high-entropy alloys, Annales De Chimie-Science Des Materiaux 31(6) (2006) 633-648. http://doi.org/DOI 10.3166/acsm.31.633-648.
[22] E.J. Pickering, R. Muñoz-Moreno, H.J. Stone, N.G. Jones, Precipitation in the equiatomic high-entropy alloy CrMnFeCoNi, Scripta Materialia 113 (2016) 106-109. http://doi.org/10.1016/j.scriptamat.2015.10.025.
[23] B. Schuh, F. Mendez-Martin, B. Völker, E.P. George, H. Clemens, R. Pippan, A. Hohenwarter, Mechanical properties, microstructure and thermal stability of a nanocrystalline CoCrFeMnNi high-entropy alloy after severe plastic deformation, Acta Materialia 96 (2015) 258-268. http://doi.org/10.1016/j.actamat.2015.06.025.
[24] N.D. Stepanov, N.Y. Yurchenko, S.V. Zherebtsov, M.A. Tikhonovsky, G.A. Salishchev, Aging behavior of the HfNbTaTiZr high entropy alloy, Materials Letters 211 (2018) 87-90. http://doi.org/10.1016/j.matlet.2017.09.094.
[25] B. Schuh, B. Völker, J. Todt, N. Schell, L. Perrière, J. Li, J.P. Couzinié, A. Hohenwarter, Thermodynamic instability of a nanocrystalline, single-phase TiZrNbHfTa alloy and its impact on the mechanical properties, Acta Materialia 142 (2018) 201-212. http://doi.org/10.1016/j.actamat.2017.09.035.
[26] H. Yao, J.W. Qiao, M. Gao, J. Hawk, S.G. Ma, H. Zhou, MoNbTaV medium-entropy alloy, Entropy 18(5) (2016) 189. http://doi.org/10.3390/e18050189.
[27] Z. Li, Interstitial equiatomic CoCrFeMnNi high-entropy alloys: carbon content, microstructure, and compositional homogeneity effects on deformation behavior, Acta Materialia 164 (2019) 400-412. http://doi.org/10.1016/j.actamat.2018.10.050.
[28] Z. Li, D. Raabe, Strong and ductile non-equiatomic high-entropy alloys: Design, processing, microstructure, and mechanical properties, JOM 69(11) (2017) 2099-2106. http://doi.org/10.1007/s11837-017-2540-2.
[29] M. Laurent-Brocq, A. Akhatova, L. Perrière, S. Chebini, X. Sauvage, E. Leroy, Y. Champion, Insights into the phase diagram of the CrMnFeCoNi high entropy alloy, Acta Materialia 88 (2015) 355-365. http://doi.org/10.1016/j.actamat.2015.01.068.
[30] G. Bracq, M. Laurent-Brocq, C. Varvenne, L. Perrière, W.A. Curtin, J.M. Joubert, I. Guillot, Combining experiments and modeling to explore the solid solution strengthening of high and medium entropy alloys, Acta Materialia 177 (2019) 266-279. http://doi.org/10.1016/j.actamat.2019.06.050.

[31] M. Laurent-Brocq, L. Perrière, R. Pirès, F. Prima, P. Vermaut, Y. Champion, From diluted solid solutions to high entropy alloys: On the evolution of properties with composition of multi-components alloys, Materials Science and Engineering: A 696 (2017) 228-235. http://doi.org/10.1016/j.msea.2017.04.079.

[32] F. Otto, A. Dlouhý, K.G. Pradeep, M. Kuběnová, D. Raabe, G. Eggeler, E.P. George, Decomposition of the single-phase high-entropy alloy CrMnFeCoNi after prolonged anneals at intermediate temperatures, Acta Materialia 112 (2016) 40-52. http://doi.org/10.1016/j.actamat.2016.04.005.

[33] F. Otto, A. Dlouhý, C. Somsen, H. Bei, G. Eggeler, E.P. George, The influences of temperature and microstructure on the tensile properties of a CoCrFeMnNi high-entropy alloy, Acta Materialia 61(15) (2013) 5743-5755. http://doi.org/10.1016/j.actamat.2013.06.018.

[34] S.J. Sun, Y.Z. Tian, H.R. Lin, X.G. Dong, Y.H. Wang, Z.J. Zhang, Z.F. Zhang, Enhanced strength and ductility of bulk CoCrFeMnNi high entropy alloy having fully recrystallized ultrafine-grained structure, Materials & Design 133 (2017) 122-127. http://doi.org/10.1016/j.matdes.2017.07.054.

[35] Z. Li, S. Zhao, R.O. Ritchie, M.A. Meyers, Mechanical properties of high-entropy alloys with emphasis on face-centered cubic alloys, Progress in Materials Science 102 (2019) 296-345. http://doi.org/10.1016/j.pmatsci.2018.12.003.

[36] B. Gludovatz, A. Hohenwarter, D. Catoor, E.H. Chang, E.P. George, R.O. Ritchie, A fracture-resistant high-entropy alloy for cryogenic applications, Science 345(6201) (2014) 1153-1158. http://doi.org/10.1126/science.1254581.

[37] E.P. George, W.A. Curtin, C.C. Tasan, High entropy alloys: A focused review of mechanical properties and deformation mechanisms, Acta Materialia 188 (2020) 435-474. http://doi.org/10.1016/j.actamat.2019.12.015.

[38] A.J. Zaddach, C. Niu, C.C. Koch, D.L. Irving, Mechanical properties and stacking fault energies of NiFeCrCoMn high-entropy alloy, JOM 65(12) (2013) 1780-1789. http://doi.org/10.1007/s11837-013-0771-4.

[39] S. Huang, W. Li, S. Lu, F. Tian, J. Shen, E. Holmström, L. Vitos, Temperature dependent stacking fault energy of FeCrCoNiMn high entropy alloy, Scripta Materialia 108 (2015) 44-47. http://doi.org/10.1016/j.scriptamat.2015.05.041.

[40] B. Gludovatz, A. Hohenwarter, K.V. Thurston, H. Bei, Z. Wu, E.P. George, R.O. Ritchie, Exceptional damage-tolerance of a medium-entropy alloy CrCoNi at cryogenic temperatures, Nature Communications 7 (2016) 10602. http://doi.org/10.1038/ncomms10602.

[41] C. Varvenne, A. Luque, W.A. Curtin, Theory of strengthening in fcc high entropy alloys, Acta Materialia 118 (2016) 164-176. http://doi.org/10.1016/j.actamat.2016.07.040.

[42] P. Sathiyamoorthi, H.S. Kim, High-entropy alloys with heterogeneous microstructure: Processing and mechanical properties, Progress in Materials Science 123 (2020) 100709. http://doi.org/10.1016/j.pmatsci.2020.100709.

[43] H. Hadraba, Z. Chlup, A. Dlouhy, F. Dobes, P. Roupcova, M. Vilemova, J. Matejicek, Oxide dispersion strengthened CoCrFeNiMn high-entropy alloy, Materials Science and Engineering: A 689 (2017) 252-256. http://doi.org/10.1016/j.msea.2017.02.068.

[44] J. Joseph, T. Jarvis, X. Wu, N. Stanford, P. Hodgson, D.M. Fabijanic, Comparative study of the microstructures and mechanical properties of direct laser fabricated and arc-melted AlxCoCrFeNi high entropy alloys, Materials Science and Engineering: A 633 (2015) 184-193. http://doi.org/10.1016/j.msea.2015.02.072.

[45] H.P. Chou, Y.S. Chang, SK. Chen, J.W. Yeh, Microstructure, thermophysical and electrical properties in AlxCoCrFeNi (0≤x≤2) high-entropy alloys, Materials Science and Engineering: B 163(3) (2009) 184-189. http://doi.org/10.1016/j.mseb.2009.05.024.

[46] J.C. Rao, H.Y. Diao, V. Ocelík, D. Vainchtein, C. Zhang, C. Kuo, Z. Tang, W. Guo, J.D. Poplawsky, Y. Zhou, P.K. Liaw, J.T.M. De Hosson, Secondary phases in Al x CoCrFeNi high-entropy alloys: An in-situ TEM heating study and thermodynamic appraisal, Acta Materialia 131 (2017) 206-220. http://doi.org/10.1016/j.actamat.2017.03.066.

[47] Y.F. Kao, T.J. Chen, S.K. Chen, J.W. Yeh, Microstructure and mechanical property of as-cast, -homogenized, and -deformed AlxCoCrFeNi (0≤x≤2) high-entropy alloys, Journal of Alloys and Compounds 488(1) (2009) 57-64. http://doi.org/10.1016/j.jallcom.2009.08.090.

[48] J. Joseph, P. Hodgson, T. Jarvis, X. Wu, N. Stanford, D.M. Fabijanic, Effect of hot isostatic pressing on the microstructure and mechanical properties of additive manufactured Al x CoCrFeNi high entropy alloys, Materials Science and Engineering: A 733 (2018) 59-70. http://doi.org/10.1016/j.msea.2018.07.036.

[49] T. DebRoy, H.L. Wei, J.S. Zuback, T. Mukherjee, J.W. Elmer, J.O. Milewski, A.M. Beese, A. Wilson-Heid, A. De, W. Zhang, Additive manufacturing of metallic components – Process, structure and properties, Progress in Materials Science 92 (2018) 112-224. http://doi.org/10.1016/j.pmatsci.2017.10.001.

[50] C. Tan, F. Weng, S. Sui, Y. Chew, G. Bi, Progress and perspectives in laser additive manufacturing of key aeroengine materials, International Journal of Machine Tools and Manufacture 170 (2021) 103804. http://doi.org/10.1016/j.ijmachtools.2021.103804.

[51] D. Zhang, S. Sun, D. Qiu, M.A. Gibson, M.S. Dargusch, M. Brandt, M. Qian, M. Easton, Metal alloys for fusion-based additive manufacturing, Advanced Engineering Materials 20(5) (2018) 1700952. http://doi.org/10.1002/adem.201700952.

[52] M.H. Mosallanejad, B. Niroumand, A. Aversa, A. Saboori, In-situ alloying in laser-based additive manufacturing processes: A critical review, Journal of Alloys and Compounds 872 (2021) 159567. http://doi.org/10.1016/j.jallcom.2021.159567.

[53] C. Wei, L. Li, Recent progress and scientific challenges in multi-material additive manufacturing via laser-based powder bed fusion, Virtual and Physical Prototyping 16(3) (2021) 347-371. http://doi.org/10.1080/17452759.2021.1928520.

[54] S.L. Sing, S. Huang, G.D. Goh, G.L. Goh, C.F. Tey, J.H.K. Tan, W.Y. Yeong, Emerging metallic systems for additive manufacturing: In-situ alloying and multi-metal processing in laser powder bed fusion, Progress in Materials Science 119 (2021) 100795. http://doi.org/10.1016/j.pmatsci.2021.100795.

[55] C.Y. Yap, C.K. Chua, Z.L. Dong, Z.H. Liu, D.Q. Zhang, L.E. Loh, S.L. Sing, Review of selective laser melting: Materials and applications, Applied Physics Reviews 2(4) (2015) 041101. http://doi.org/10.1063/1.4935926.

[56] J. Ye, S.A. Khairallah, A.M. Rubenchik, M.F. Crumb, G. Guss, J. Belak, M.J. Matthews, Energy coupling mechanisms and scaling behavior associated with laser powder bed fusion additive manufacturing, Advanced Engineering Materials 21(7) (2019) 1900185. http://doi.org/10.1002/adem.201900185.

[57] S.A. Khairallah, A.T. Anderson, A. Rubenchik, W.E. King, Laser powder-bed fusion additive manufacturing: Physics of complex melt flow and formation mechanisms of pores, spatter, and denudation zones, Acta Materialia 108 (2016) 36-45. http://doi.org/10.1016/j.actamat.2016.02.014.

[58] R. Fabbro, M. Dal, P. Peyre, F. Coste, M. Schneider, V. Gunenthiram, Analysis and possible estimation of keyhole depths evolution, using laser operating parameters and material properties, Journal of Laser Applications 30(3) (2018) 032410. http://doi.org/10.2351/1.5040624.

[59] J. Trapp, A.M. Rubenchik, G. Guss, M.J. Matthews, In situ absorptivity measurements of metallic powders during laser powder-bed fusion additive manufacturing, Applied Materials Today 9 (2017) 341-349. http://doi.org/10.1016/j.apmt.2017.08.006.
[60] P.A. Hooper, Melt pool temperature and cooling rates in laser powder bed fusion, Additive Manufacturing 22 (2018) 548-559. http://doi.org/10.1016/j.addma.2018.05.032.
[61] I.A. Roberts, C.J. Wang, R. Esterlein, M. Stanford, D.J. Mynors, A three-dimensional finite element analysis of the temperature field during laser melting of metal powders in additive layer manufacturing, International Journal of Machine Tools and Manufacture 49(12-13) (2009) 916-923. http://doi.org/10.1016/j.ijmachtools.2009.07.004.
[62] Y. Li, D. Gu, Parametric analysis of thermal behavior during selective laser melting additive manufacturing of aluminum alloy powder, Materials & Design 63 (2014) 856-867. http://doi.org/10.1016/j.matdes.2014.07.006.
[63] M.S. Pham, B. Dovgyy, P.A. Hooper, C.M. Gourlay, A. Piglione, The role of side-branching in microstructure development in laser powder-bed fusion, Nature Communications 11(1) (2020) 749. http://doi.org/10.1038/s41467-020-14453-3.
[64] T. Mukherjee, V. Manvatkar, A. De, T. DebRoy, Dimensionless numbers in additive manufacturing, Journal of Applied Physics 121(6) (2017) 064904. http://doi.org/10.1063/1.4976006.
[65] N.A. Kistler, A.R. Nassar, E.W. Reutzel, D.J. Corbin, A.M. Beese, Effect of directed energy deposition processing parameters on laser deposited Inconel®718: Microstructure, fusion zone morphology, and hardness, Journal of Laser Applications 29(2) (2017) 022005. http://doi.org/10.2351/1.4979702.
[66] J.W. Elmer, S.M. Allen, T.W. Eagar, Microstructural development during solidification of stainless steel alloys, Metallurgical Transactions A 20(10) (1989) 2117-2131. http://doi.org/10.1007/BF02650298.
[67] S. Kou, Welding Metallurgy 2nd edn, John Wiley & Sons, New Jersey, 2003.
[68] R. Casati, J. Lemke, M. Vedani, Microstructure and fracture behavior of 316L austenitic stainless steel produced by selective laser melting, Journal of Materials Science & Technology 32(8) (2016) 738-744. http://doi.org/10.1016/j.jmst.2016.06.016.
[69] C. Tan, J. Zou, D. Wang, W. Ma, K. Zhou, Duplex strengthening via SiC addition and in-situ precipitation in additively manufactured composite materials, Composites Part B: Engineering 236 (2022) 109820. http://doi.org/10.1016/j.compositesb.2022.109820.
[70] Q. Jia, P. Rometsch, S. Cao, K. Zhang, X. Wu, Towards a high strength aluminium alloy development methodology for selective laser melting, Materials & Design 174 (2019) 107775. http://doi.org/10.1016/j.matdes.2019.107775.
[71] A.K. Mishra, A. Kumar, Numerical and experimental analysis of the effect of volumetric energy absorption in powder layer on thermal-fluidic transport in selective laser melting of Ti6Al4V, Optics & Laser Technology 111 (2019) 227-239. http://doi.org/10.1016/j.optlastec.2018.09.054.
[72] Y. Liu, J. Zhang, Z. Pang, Numerical and experimental investigation into the subsequent thermal cycling during selective laser melting of multi-layer 316L stainless steel, Optics & Laser Technology 98 (2018) 23-32. http://doi.org/10.1016/j.optlastec.2017.07.034.
[73] S. Holland, X. Wang, J. Chen, W. Cai, F. Yan, L. Li, Multiscale characterization of microstructures and mechanical properties of Inconel 718 fabricated by selective laser melting, Journal of Alloys and Compounds 784 (2019) 182-194. http://doi.org/10.1016/j.jallcom.2018.12.380.
[74] P. Kontis, E. Chauvet, Z. Peng, J. He, A.K. da Silva, D. Raabe, C. Tassin, J.-J. Blandin, S. Abed, R. Dendievel, B. Gault, G. Martin, Atomic-scale grain boundary engineering to

overcome hot-cracking in additively-manufactured superalloys, Acta Materialia 177 (2019) 209-221. http://doi.org/10.1016/j.actamat.2019.07.041.

[75] B. Attard, S. Cruchley, C. Beetz, M. Megahed, Y.L. Chiu, M.M. Attallah, Microstructural control during laser powder fusion to create graded microstructure Ni-superalloy components, Additive Manufacturing 36 (2020) 101432. http://doi.org/10.1016/j.addma.2020.101432.

[76] C. Zhao, K. Fezzaa, R.W. Cunningham, H. Wen, F. De Carlo, L. Chen, A.D. Rollett, T. Sun, Real-time monitoring of laser powder bed fusion process using high-speed X-ray imaging and diffraction, Scientific Reports 7 (2017) 3602. http://doi.org/10.1038/s41598-017-03761-2.

[77] V. Gunenthiram, P. Peyre, M. Schneider, M. Dal, F. Coste, I. Koutiri, R. Fabbro, Experimental analysis of spatter generation and melt-pool behavior during the powder bed laser beam melting process, Journal of Materials Processing Technology 251 (2018) 376-386. http://doi.org/10.1016/j.jmatprotec.2017.08.012.

[78] Q. Guo, C. Zhao, M. Qu, L. Xiong, L.I. Escano, S.M.H. Hojjatzadeh, N.D. Parab, K. Fezzaa, W. Everhart, T. Sun, L. Chen, In-situ characterization and quantification of melt pool variation under constant input energy density in laser powder bed fusion additive manufacturing process, Additive Manufacturing 28 (2019) 600-609. http://doi.org/10.1016/j.addma.2019.04.021.

[79] T.-N. Le, Y.-L. Lo, Effects of sulfur concentration and Marangoni convection on melt-pool formation in transition mode of selective laser melting process, Materials & Design 179 (2019) 107866. http://doi.org/10.1016/j.matdes.2019.107866.

[80] N. Kouraytem, X. Li, R. Cunningham, C. Zhao, N. Parab, T. Sun, A.D. Rollett, A.D. Spear, W. Tan, Effect of laser-matter interaction on molten pool flow and keyhole dynamics, Physical Review Applied 11(6) (2019) 064054. http://doi.org/10.1103/PhysRevApplied.11.064054.

[81] P. Yuan, D. Gu, Molten pool behaviour and its physical mechanism during selective laser melting of TiC/AlSi10Mg nanocomposites: simulation and experiments, Journal of Physics D: Applied Physics 48(3) (2015) 035303. http://doi.org/10.1088/0022-3727/48/3/035303.

[82] Z. Gan, O.L. Kafka, N. Parab, C. Zhao, L. Fang, O. Heinonen, T. Sun, W.K. Liu, Universal scaling laws of keyhole stability and porosity in 3D printing of metals, Nature Communications 12(1) (2021) 2379. http://doi.org/10.1038/s41467-021-22704-0.

[83] H. Gu, H. Gong, D. Pal, K. Rafi, T. Starr, B. Stucker, Influences of energy density on porosity and microstructure of selective laser melted 17-4PH stainless steel, 24th International SFF Symposium - An Additive Manufacturing Conference, SFF 2013, 2013, pp. 474-489.

[84] J.P. Oliveira, T.G. Santos, R.M. Miranda, Revisiting fundamental welding concepts to improve additive manufacturing: From theory to practice, Progress in Materials Science 107 (2020) 100590. http://doi.org/10.1016/j.pmatsci.2019.100590.

[85] Y. Ren, L. Liang, Q. Shan, A. Cai, J. Du, Q. Huang, S. Liu, X. Yang, Y. Tian, H. Wu, Effect of volumetric energy density on microstructure and tribological properties of FeCoNiCuAl high-entropy alloy produced by laser powder bed fusion, Virtual and Physical Prototyping 15(sup1) (2020) 543-554. http://doi.org/10.1080/17452759.2020.1848284.

[86] J. Suryawanshi, K.G. Prashanth, S. Scudino, J. Eckert, O. Prakash, U. Ramamurty, Simultaneous enhancements of strength and toughness in an Al-12Si alloy synthesized using selective laser melting, Acta Materialia 115 (2016) 285-294. http://doi.org/10.1016/j.actamat.2016.06.009.

[87] E. Uhlmann, A. Bergmann, W. Gridin, Investigation on Additive Manufacturing of Tungsten Carbide-cobalt by Selective Laser Melting, Procedia CIRP 35 (2015) 8-15. http://doi.org/10.1016/j.procir.2015.08.060.

[88] L. Johnson, M. Mahmoudi, B. Zhang, R. Seede, X. Huang, J.T. Maier, H.J. Maier, I. Karaman, A. Elwany, R. Arróyave, Assessing printability maps in additive manufacturing of

metal alloys, Acta Materialia 176 (2019) 199-210. http://doi.org/10.1016/j.actamat.2019.07.005.

[89] M. Tang, P.C. Pistorius, J.L. Beuth, Prediction of lack-of-fusion porosity for powder bed fusion, Additive Manufacturing 14 (2017) 39-48. http://doi.org/10.1016/j.addma.2016.12.001.

[90] Y. He, M. Zhong, J. Beuth, B. Webler, A study of microstructure and cracking behavior of H13 tool steel produced by laser powder bed fusion using single-tracks, multi-track pads, and 3D cubes, Journal of Materials Processing Technology 286 (2020) 116802. http://doi.org/10.1016/j.jmatprotec.2020.116802.

[91] S. Ghosh, L. Ma, L.E. Levine, R.E. Ricker, M.R. Stoudt, J.C. Heigel, J.E. Guyer, Single-track melt-pool measurements and microstructures in Inconel 625, JOM 70(6) (2018) 1011-1016. http://doi.org/10.1007/s11837-018-2771-x.

[92] C. Bruna-Rosso, A.G. Demir, B. Previtali, Selective laser melting finite element modeling: Validation with high-speed imaging and lack of fusion defects prediction, Materials & Design 156 (2018) 143-153. http://doi.org/10.1016/j.matdes.2018.06.037.

[93] H.J. Willy, X. Li, Z. Chen, T.S. Herng, S. Chang, C.Y.A. Ong, C. Li, J. Ding, Model of laser energy absorption adjusted to optical measurements with effective use in finite element simulation of selective laser melting, Materials & Design 157 (2018) 24-34. http://doi.org/10.1016/j.matdes.2018.07.029.

[94] T.W. Eagar, N.S. Tsai, Temperature-fields produced by traveling distributed heat-sources, Welding Journal 62(12) (1983) 346-355.

[95] D. Rosenthal, Mathematical theory of heat distribution during welding and cutting, Welding Journal 20(5) (1941) 220-234.

[96] J.H.K. Tan, S.L. Sing, W.Y. Yeong, Microstructure modelling for metallic additive manufacturing: a review, Virtual and Physical Prototyping 15(1) (2019) 87-105. http://doi.org/10.1080/17452759.2019.1677345.

[97] P. Promoppatum, S.-C. Yao, P.C. Pistorius, A.D. Rollett, A comprehensive comparison of the analytical and numerical prediction of the thermal history and solidification microstructure of Inconel 718 products made by laser powder-bed fusion, Engineering 3(5) (2017) 685-694. http://doi.org/10.1016/j.Eng.2017.05.023.

[98] A.M. Rubenchik, W.E. King, S.S. Wu, Scaling laws for the additive manufacturing, Journal of Materials Processing Technology 257 (2018) 234-243. http://doi.org/10.1016/j.jmatprotec.2018.02.034.

[99] S. Patel, M. Vlasea, Melting modes in laser powder bed fusion, Materialia 9 (2020) 100591. http://doi.org/10.1016/j.mtla.2020.100591.

[100] D.B. Hann, J. Iammi, J. Folkes, Keyholing or conduction – Prediction of laser penetration depth, in: S. Hinduja, L. Li (Eds.) Proceedings of the 36th International MATADOR Conference, Springer London, London, 2010, pp. 275-278.

[101] H. Ghasemi-Tabasi, J. Jhabvala, E. Boillat, T. Ivas, R. Drissi-Daoudi, R.E. Logé, An effective rule for translating optimal selective laser melting processing parameters from one material to another, Additive Manufacturing 36 (2020) 101496. http://doi.org/10.1016/j.addma.2020.101496.

[102] J. Yang, J. Han, H. Yu, J. Yin, M. Gao, Z. Wang, X. Zeng, Role of molten pool mode on formability, microstructure and mechanical properties of selective laser melted Ti-6Al-4V alloy, Materials & Design 110 (2016) 558-570. http://doi.org/10.1016/j.matdes.2016.08.036.

[103] W.E. King, H.D. Barth, V.M. Castillo, G.F. Gallegos, J.W. Gibbs, D.E. Hahn, C. Kamath, A.M. Rubenchik, Observation of keyhole-mode laser melting in laser powder-bed fusion additive manufacturing, Journal of Materials Processing Technology 214(12) (2014) 2915-2925. http://doi.org/10.1016/j.jmatprotec.2014.06.005.

[104] C. Panwisawas, C. Qiu, M.J. Anderson, Y. Sovani, R.P. Turner, M.M. Attallah, J.W. Brooks, H.C. Basoalto, Mesoscale modelling of selective laser melting: Thermal fluid dynamics and microstructural evolution, Computational Materials Science 126 (2017) 479-490. http://doi.org/10.1016/j.commatsci.2016.10.011.

[105] C. Qiu, C. Panwisawas, M. Ward, H.C. Basoalto, J.W. Brooks, M.M. Attallah, On the role of melt flow into the surface structure and porosity development during selective laser melting, Acta Materialia 96 (2015) 72-79. http://doi.org/10.1016/j.actamat.2015.06.004.

[106] J.H. Robinson, I.R.T. Ashton, E. Jones, P. Fox, C. Sutcliffe, The effect of hatch angle rotation on parts manufactured using selective laser melting, Rapid Prototyping Journal 25(2) (2019) 289-298. http://doi.org/10.1108/rpj-06-2017-0111.

[107] J.L. Bartlett, X. Li, An overview of residual stresses in metal powder bed fusion, Additive Manufacturing 27 (2019) 131-149. http://doi.org/10.1016/j.addma.2019.02.020.

[108] J. Robinson, I. Ashton, P. Fox, E. Jones, C. Sutcliffe, Determination of the effect of scan strategy on residual stress in laser powder bed fusion additive manufacturing, Additive Manufacturing 23 (2018) 13-24. http://doi.org/10.1016/j.addma.2018.07.001.

[109] S.Z. Uddin, L.E. Murr, C.A. Terrazas, P. Morton, D.A. Roberson, R.B. Wicker, Processing and characterization of crack-free aluminum 6061 using high-temperature heating in laser powder bed fusion additive manufacturing, Additive Manufacturing 22 (2018) 405-415. http://doi.org/10.1016/j.addma.2018.05.047.

[110] Z.G. Zhu, Q.B. Nguyen, F.L. Ng, X.H. An, X.Z. Liao, P.K. Liaw, S.M.L. Nai, J. Wei, Hierarchical microstructure and strengthening mechanisms of a CoCrFeNiMn high entropy alloy additively manufactured by selective laser melting, Scripta Materialia 154 (2018) 20-24. http://doi.org/10.1016/j.scriptamat.2018.05.015.

[111] A. Piglione, B. Dovgyy, C. Liu, C.M. Gourlay, P.A. Hooper, M.S. Pham, Printability and microstructure of the CoCrFeMnNi high-entropy alloy fabricated by laser powder bed fusion, Materials Letters 224 (2018) 22-25. http://doi.org/10.1016/j.matlet.2018.04.052.

[112] Y.K. Kim, J. Choe, K.A. Lee, Selective laser melted equiatomic CoCrFeMnNi high-entropy alloy: Microstructure, anisotropic mechanical response, and multiple strengthening mechanism, Journal of Alloys and Compounds 805 (2019) 680-691. http://doi.org/10.1016/j.jallcom.2019.07.106.

[113] J. Ren, C. Mahajan, L. Liu, D. Follette, W. Chen, S. Mukherjee, Corrosion behavior of selectively laser melted CoCrFeMnNi high entropy alloy, Metals 9(10) (2019) 1029. http://doi.org/10.3390/met9101029.

[114] Z. Xu, H. Zhang, W. Li, A. Mao, L. Wang, G. Song, Y. He, Microstructure and nanoindentation creep behavior of CoCrFeMnNi high-entropy alloy fabricated by selective laser melting, Additive Manufacturing 28 (2019) 766-771. http://doi.org/10.1016/j.addma.2019.06.012.

[115] B. Wang, M. Sun, B. Li, L. Zhang, B. Lu, Anisotropic response of CoCrFeMnNi high-entropy alloy fabricated by selective laser melting, Materials (Basel) 13(24) (2020) 5687. http://doi.org/10.3390/ma13245687.

[116] C. Zhang, K. Feng, H. Kokawa, B. Han, Z. Li, Cracking mechanism and mechanical properties of selective laser melted CoCrFeMnNi high entropy alloy using different scanning strategies, Materials Science and Engineering: A 789 (2020) 139672. http://doi.org/10.1016/j.msea.2020.139672.

[117] J. Guo, M. Goh, Z. Zhu, X. Lee, M.L.S. Nai, J. Wei, On the machining of selective laser melting CoCrFeMnNi high-entropy alloy, Materials & Design 153 (2018) 211-220. http://doi.org/10.1016/j.matdes.2018.05.012.

[118] X. Zhao, X. Lin, J. Chen, L. Xue, W. Huang, The effect of hot isostatic pressing on crack healing, microstructure, mechanical properties of Rene88DT superalloy prepared by laser solid forming, Materials Science and Engineering: A 504(1-2) (2009) 129-134. http://doi.org/10.1016/j.msea.2008.12.024.

[119] C. Guo, Z. Xu, Y. Zhou, S. Shi, G. Li, H. Lu, Q. Zhu, R.M. Ward, Single-track investigation of IN738LC superalloy fabricated by laser powder bed fusion: Track morphology, bead characteristics and part quality, Journal of Materials Processing Technology 290 (2021) 117000. http://doi.org/10.1016/j.jmatprotec.2020.117000.

[120] P. Niu, R. Li, S. Zhu, M. Wang, C. Chen, T. Yuan, Hot cracking, crystal orientation and compressive strength of an equimolar CoCrFeMnNi high-entropy alloy printed by selective laser melting, Optics & Laser Technology 127 (2020). http://doi.org/10.1016/j.optlastec.2020.106147.

[121] X. Zhou, K. Li, D. Zhang, X. Liu, J. Ma, W. Liu, Z. Shen, Textures formed in a CoCrMo alloy by selective laser melting, Journal of Alloys and Compounds 631 (2015) 153-164. https://doi.org/10.1016/j.jallcom.2015.01.096.

[122] C. Chattopadhyay, S. Sangal, K. Mondal, A relook at the preferred growth direction of the solid–liquid interface during solidification of pure metals, Acta Materialia 58(16) (2010) 5342-5353. http://doi.org/10.1016/j.actamat.2010.06.009.

[123] B. Zhang, G. Bi, S. Nai, C.-n. Sun, J. Wei, Microhardness and microstructure evolution of TiB2 reinforced Inconel 625/TiB2 composite produced by selective laser melting, Optics & Laser Technology 80 (2016) 186-195. http://doi.org/10.1016/j.optlastec.2016.01.010.

[124] L. Liu, Q. Ding, Y. Zhong, J. Zou, J. Wu, Y.-L. Chiu, J. Li, Z. Zhang, Q. Yu, Z. Shen, Dislocation network in additive manufactured steel breaks strength–ductility trade-off, Materials Today 21(4) (2017) 354-361. http://doi.org/10.1016/j.mattod.2017.11.004.

[125] J.Y. He, W.H. Liu, H. Wang, Y. Wu, X.J. Liu, T.G. Nieh, Z.P. Lu, Effects of Al addition on structural evolution and tensile properties of the FeCoNiCrMn high-entropy alloy system, Acta Materialia 62 (2014) 105-113. http://doi.org/10.1016/j.actamat.2013.09.037.

[126] Z. Tong, X. Ren, J. Jiao, W. Zhou, Y. Ren, Y. Ye, E.A. Larson, J. Gu, Laser additive manufacturing of FeCrCoMnNi high-entropy alloy: Effect of heat treatment on microstructure, residual stress and mechanical property, Journal of Alloys and Compounds 785 (2019) 1144-1159. http://doi.org/10.1016/j.jallcom.2019.01.213.

[127] Y.K. Kim, M.S. Baek, S. Yang, K.A. Lee, In-situ formed oxide enables extraordinary high-cycle fatigue resistance in additively manufactured CoCrFeMnNi high-entropy alloy, Additive Manufacturing 38 (2021) 101832. http://doi.org/10.1016/j.addma.2020.101832.

[128] K. Kuwabara, H. Shiratori, T. Fujieda, K. Yamanaka, Y. Koizumi, A. Chiba, Mechanical and corrosion properties of AlCoCrFeNi high-entropy alloy fabricated with selective electron beam melting, Additive Manufacturing 23 (2018) 264-271. http://doi.org/10.1016/j.addma.2018.06.006.

[129] D. Karlsson, A. Marshal, F. Johansson, M. Schuisky, M. Sahlberg, J.M. Schneider, U. Jansson, Elemental segregation in an AlCoCrFeNi high-entropy alloy – A comparison between selective laser melting and induction melting, Journal of Alloys and Compounds 784 (2019) 195-203. http://doi.org/10.1016/j.jallcom.2018.12.267.

[130] P.D. Niu, R.D. Li, T.C. Yuan, S.Y. Zhu, C. Chen, M.B. Wang, L. Huang, Microstructures and properties of an equimolar AlCoCrFeNi high entropy alloy printed by selective laser melting, Intermetallics 104 (2019) 24-32. http://doi.org/10.1016/j.intermet.2018.10.018.

[131] F. Peyrouzet, D. Hachet, R. Soulas, C. Navone, S. Godet, S. Gorsse, Selective laser melting of Al0.3CoCrFeNi high-entropy alloy: printability, microstructure, and mechanical properties, JOM 71 (2019) 3443-3451. http://doi.org/10.1007/s11837-019-03715-1.

[132] P.F. Zhou, D.H. Xiao, Z. Wu, X.Q. Ou, Al0.5FeCoCrNi high entropy alloy prepared by selective laser melting with gas-atomized pre-alloy powders, Materials Science and Engineering: A 739 (2019) 86-89. http://doi.org/10.1016/j.msea.2018.10.035.

[133] Z.H. Zhang, Y.H. Zhou, S.Y. Zhou, L. Zhang, M. Yan, Mechanically blended Al: Simple but effective approach to improving mechanical property and thermal stability of selective laser-melted Inconel 718, Metallurgical and Materials Transactions A 50a(8) (2019) 3922-3936. http://doi.org/10.1007/s11661-019-05299-6.

[134] I. Polozov, V. Sufiiarov, A. Popovich, D. Masaylo, A. Grigoriev, Synthesis of Ti-5Al, Ti-6Al-7Nb, and Ti-22Al-25Nb alloys from elemental powders using powder-bed fusion additive manufacturing, Journal of Alloys and Compounds 763 (2018) 436-445. http://doi.org/10.1016/j.jallcom.2018.05.325.

[135] B. Zhang, J. Chen, C. Coddet, Microstructure and transformation behavior of in-situ shape memory alloys by selective laser melting Ti–Ni mixed powder, Journal of Materials Science & Technology 29(9) (2013) 863-867. http://doi.org/10.1016/j.jmst.2013.05.006.

[136] B. Zhang, N.-E. Fenineche, H. Liao, C. Coddet, Microstructure and magnetic properties of Fe–Ni alloy fabricated by selective laser melting Fe/Ni mixed powders, Journal of Materials Science & Technology 29(8) (2013) 757-760. http://doi.org/10.1016/j.jmst.2013.05.001.

[137] A. Grigoriev, I. Polozov, V. Sufiiarov, A. Popovich, In-situ synthesis of Ti2AlNb-based intermetallic alloy by selective laser melting, Journal of Alloys and Compounds 704 (2017) 434-442. http://doi.org/10.1016/j.jallcom.2017.02.086.

[138] V.V. Popov, A. Katz-Demyanetz, A. Koptyug, M. Bamberger, Selective electron beam melting of Al0.5CrMoNbTa0.5 high entropy alloys using elemental powder blend, Heliyon 5(2) (2019) e01188. http://doi.org/10.1016/j.heliyon.2019.e01188.

[139] C. Haase, F. Tang, M.B. Wilms, A. Weisheit, B. Hallstedt, Combining thermodynamic modeling and 3D printing of elemental powder blends for high-throughput investigation of high-entropy alloys – Towards rapid alloy screening and design, Materials Science and Engineering: A 688 (2017) 180-189. http://doi.org/10.1016/j.msea.2017.01.099.

[140] Z. Li, A. Ludwig, A. Savan, H. Springer, D. Raabe, Combinatorial metallurgical synthesis and processing of high-entropy alloys, Journal of Materials Research 33 (2018) 3156-3169. http://doi.org/10.1557/jmr.2018.214.

[141] S. Ewald, F. Kies, S. Hermsen, M. Voshage, C. Haase, J.H. Schleifenbaum, Rapid alloy development of extremely high-alloyed metals using powder blends in laser powder bed fusion, Materials (Basel) 12(10) (2019) 1706. http://doi.org/10.3390/ma12101706.

[142] Y. Hou, H. Su, H. Zhang, X. Wang, C. Wang, Fabricating homogeneous FeCoCrNi high-entropy alloys via slm in situ alloying, Metals 11(6) (2021) 942. http://doi.org/10.3390/met11060942.

[143] F. Huber, D. Bartels, M. Schmidt, In-situ alloy formation of a WMoTaNbV refractory metal high entropy alloy by laser powder bed fusion (PBF-LB/M), Materials (Basel) 14(11) (2021) 3095. http://doi.org/10.3390/ma14113095.

[144] K. Sun, W. Peng, L. Yang, L. Fang, Effect of SLM processing parameters on microstructures and mechanical properties of Al0.5CoCrFeNi high entropy alloys, Metals 10(2) (2020) 292. http://doi.org/10.3390/met10020292.

[145] S. Luo, C. Zhao, H. Yang, Q. Liu, Z. Wang, X. Zeng, Selective laser melting of dual phase AlCrCuFeNix high entropy alloys: formability, heterogeneous microstructures and deformation mechanisms, Additive Manufacturing 31 (2019) 100925. http://doi.org/10.1016/j.addma.2019.100925.

[146] D. Lin, L. Xu, X. Li, H. Jing, G. Qin, H. Pang, F. Minami, A Si-containing FeCoCrNi high-entropy alloy with high strength and ductility synthesized in situ via selective laser melting, Additive Manufacturing 35 (2020) 101340. http://doi.org/10.1016/j.addma.2020.101340.
[147] Y. Kuzminova, A. Shibalova, S. Evlashin, I. Shishkovsky, P. Krakhmalev, Structural effect of low Al content in the in-situ additive manufactured CrFeCoNiAlx high-entropy alloy, Materials Letters 303 (2021) 130487. http://doi.org/10.1016/j.matlet.2021.130487.
[148] J. Gao, Y. Jin, Y. Fan, D. Xu, L. Meng, C. Wang, Y. Yu, D. Zhang, F. Wang, Fabricating antibacterial CoCrCuFeNi high-entropy alloy via selective laser melting and in-situ alloying, Journal of Materials Science & Technology 102 (2022) 159-165. http://doi.org/10.1016/j.jmst.2021.07.002.
[149] Z. Sun, X. Tan, C. Wang, M. Descoins, D. Mangelinck, S.B. Tor, E.A. Jägle, S. Zaefferer, D. Raabe, Reducing hot tearing by grain boundary segregation engineering in additive manufacturing: example of an AlxCoCrFeNi high-entropy alloy, Acta Materialia 204 (2021) 116505. http://doi.org/10.1016/j.actamat.2020.116505.
[150] H. Zhang, W. Xu, Y. Xu, Z. Lu, D. Li, The thermal-mechanical behavior of WTaMoNb high-entropy alloy via selective laser melting (SLM): Experiment and simulation, The International Journal of Advanced Manufacturing Technology 96 (2018) 461-474. http://doi.org/10.1007/s00170-017-1331-9.
[151] C.A. Williams, P. Unifantowicz, N. Baluc, G.D.W. Smith, E.A. Marquis, The formation and evolution of oxide particles in oxide-dispersion-strengthened ferritic steels during processing, Acta Materialia 61(6) (2013) 2219-2235. http://doi.org/10.1016/j.actamat.2012.12.042.
[152] T. Boegelein, S.N. Dryepondt, A. Pandey, K. Dawson, G.J. Tatlock, Mechanical response and deformation mechanisms of ferritic oxide dispersion strengthened steel structures produced by selective laser melting, Acta Materialia 87 (2015) 201-215. http://doi.org/10.1016/j.actamat.2014.12.047.
[153] Y. Miao, K. Mo, Z. Zhou, X. Liu, K.-C. Lan, G. Zhang, M.K. Miller, K.A. Powers, Z.-G. Mei, J.-S. Park, J. Almer, J.F. Stubbins, On the microstructure and strengthening mechanism in oxide dispersion-strengthened 316 steel: A coordinated electron microscopy, atom probe tomography and in situ synchrotron tensile investigation, Materials Science and Engineering: A 639 (2015) 585-596. http://doi.org/10.1016/j.msea.2015.05.064.
[154] R.M. Hunt, K.J. Kramer, B. El-Dasher, Selective laser sintering of MA956 oxide dispersion strengthened steel, Journal of Nuclear Materials 464 (2015) 80-85. http://doi.org/10.1016/j.jnucmat.2015.04.011.
[155] Q. Wang, K. Zhang, D. Qiu, W. Niu, Additive manufacturing of high-strength commercially pure titanium through lanthanum oxide addition, Materials Characterization 176 (2021) 111074. http://doi.org/10.1016/j.matchar.2021.111074.
[156] C. Doñate-Buendia, P. Kürnsteiner, F. Stern, M.B. Wilms, R. Streubel, I.M. Kusoglu, J. Tenkamp, E. Bruder, N. Pirch, S. Barcikowski, K. Durst, J.H. Schleifenbaum, F. Walther, B. Gault, B. Gökce, Microstructure formation and mechanical properties of ODS steels built by laser additive manufacturing of nanoparticle coated iron-chromium powders, Acta Materialia 206 (2021) 116566. http://doi.org/10.1016/j.actamat.2020.116566.
[157] Y. Zhong, L. Liu, J. Zou, X. Li, D. Cui, Z. Shen, Oxide dispersion strengthened stainless steel 316L with superior strength and ductility by selective laser melting, Journal of Materials Science & Technology 42 (2020) 97-105. http://doi.org/10.1016/j.jmst.2019.11.004.
[158] M. Ghayoor, K. Lee, Y. He, C.H. Chang, B.K. Paul, S. Pasebani, Selective laser melting of austenitic oxide dispersion strengthened steel: Processing, microstructural evolution and

strengthening mechanisms, Materials Science and Engineering: A 788 (2020) 139532. http://doi.org/10.1016/j.msea.2020.139532.

[159] H. Springer, C. Baron, A. Szczepaniak, E.A. Jägle, M.B. Wilms, A. Weisheit, D. Raabe, Efficient additive manufacturing production of oxide- and nitride-dispersion-strengthened materials through atmospheric reactions in liquid metal deposition, Materials & Design 111 (2016) 60-69. http://doi.org/10.1016/j.matdes.2016.08.084.

[160] X. Lou, P.L. Andresen, R.B. Rebak, Oxide inclusions in laser additive manufactured stainless steel and their effects on impact toughness and stress corrosion cracking behavior, Journal of Nuclear Materials 499 (2018) 182-190. http://doi.org/10.1016/j.jnucmat.2017.11.036.

[161] C. Qiu, A new approach to synthesise high strength nano-oxide dispersion strengthened alloys, Journal of Alloys and Compounds 790 (2019) 1023-1033. http://doi.org/10.1016/j.jallcom.2019.03.221.

[162] S. Mirzababaei, M. Ghayoor, R.P. Doyle, S. Pasebani, In-situ manufacturing of ODS FeCrAlY alloy via laser powder bed fusion, Materials Letters 284 (2021) 129046. http://doi.org/10.1016/j.matlet.2020.129046.

[163] K. Saeidi, X. Gao, Y. Zhong, Z.J. Shen, Hardened austenite steel with columnar sub-grain structure formed by laser melting, Materials Science and Engineering: A 625 (2015) 221-229. http://doi.org/10.1016/j.msea.2014.12.018.

[164] Z. Zhang, D. Chen, Consideration of Orowan strengthening effect in particulate-reinforced metal matrix nanocomposites: A model for predicting their yield strength, Scripta Materialia 54(7) (2006) 1321-1326. http://doi.org/10.1016/j.scriptamat.2005.12.017.

[165] Z. Zhang, D.L. Chen, Contribution of Orowan strengthening effect in particulate-reinforced metal matrix nanocomposites, Materials Science and Engineering: A 483-484 (2008) 148-152. http://doi.org/10.1016/j.msea.2006.10.184.

Chapter 3: Materials and Experimental Methods

This chapter details the materials and methods used in the thesis. The LPBF experiments were carried out at the UoB and SUSTech using different facilities and powders. The processing development of cuboid samples (CoCrFeMnNi and AlCoCrFeNi) and preparation of tensile samples (CoCrFeMnNi) were conducted at the UoB, namely bulk building (Chapters 4 to 6). The experiments of single tracks (CoCrFeMnNi) were conducted at the SUSTech, namely track building (Chapter 7). Microstructural characterisation and mechanical testing were mainly carried out at the SUSTech.

3.1 Materials

The feedstock included pre-alloyed CoCrFeNi powders as the base alloy, and elemental Mn/Al powders as the alloying elements. For the bulk building at the UoB, the pre-alloyed CoCrFeNi powder (Figure 3.1(a)) was fabricated using gas atomisation by TLS Technik. The elemental Al powder (99.9 purity, Figure 3.1(b)) and elemental Mn powder (99% purity, Figure 3.1(c)) were provided by LPW and Sigma-Aldrich, respectively. For the track building at the SUSTech, the pre-alloyed CoCrFeNi powder (Figure 3.2(a)) from Zhongyuan Advanced Materials was also fabricated via gas atomisation, and the elemental Mn powder (99.9% purity, Figure 3.2(b)) was provided by Aladdin. As shown in the SEM images, the pre-alloyed CoCrFeNi and elemental Al powders fabricated via gas atomisation were mostly spherical, while the elemental Mn powders were in irregular shapes with sharp edges.

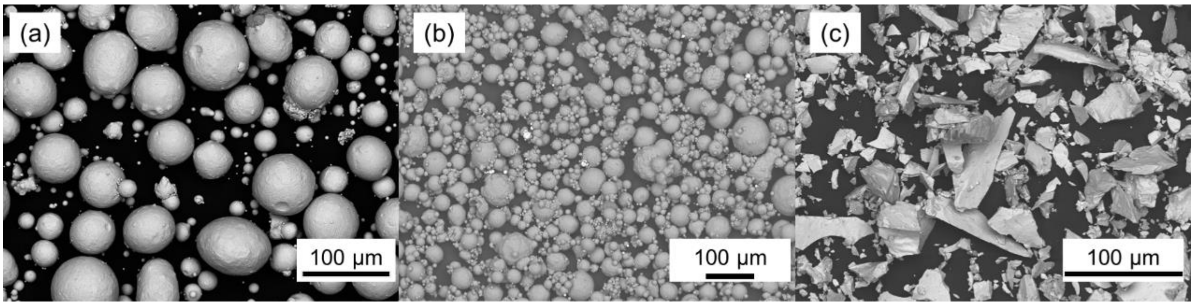

Figure 3.1 Scanning electron microscopy (SEM) images of (a) the pre-alloyed CoCrFeNi, elemental (b) Al and (c) Mn powders used for the bulk building.

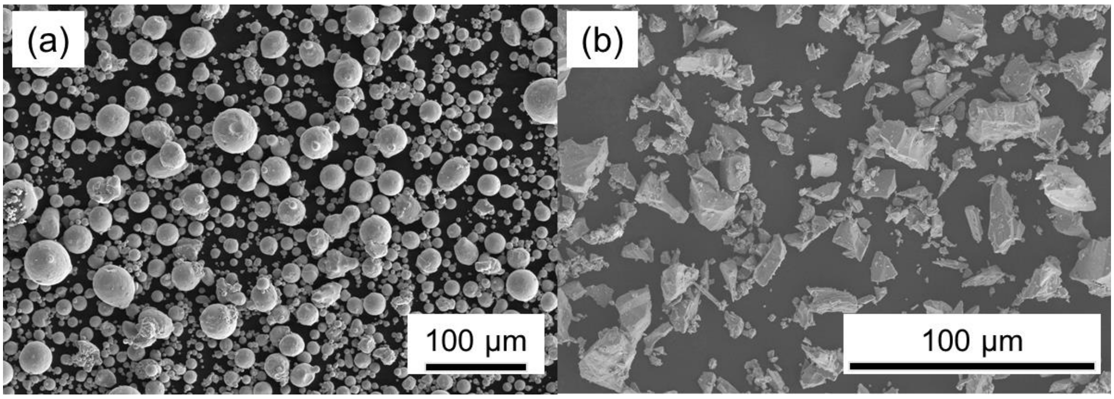

Figure 3.2 SEM images of (a) the pre-alloyed CoCrFeNi and (b) elemental Mn powders used for the track building.

3.1.1 Powder size distribution

The size distribution of pre-alloyed CoCrFeNi powders was analysed using a Malvern Mastersizer 3000 following the ASTM method of laser scattering (ASTM B822-17 [1]). The tested powders were dispersed in water for wet dispersion, and the Fraunhofer model was employed to analyse the results.

3.1.2 Powder chemistry

The pre-alloyed CoCrFeNi powders were sent to local analytical service suppliers to measure the contents of principal elements. Different testing methods were adopted by technicians. The pre-alloyed powder supplied by TLS was analysed via AMG Superalloys (South Yorkshire, UK) using X-ray fluorescence (XRF). The pre-alloyed powder from Zhongyuan was tested via inductively coupled plasma-optical emission spectrometry (ICP-OES) at 863 New Material and Technology (Shenzhen, China).

3.1.3 Summary

The size distribution and chemical compositions of pre-alloyed CoCrFeNi powders are provided in Table 3.1. Although both powders were spherical and quasi-equiatomic, the powder for bulk building was in the ideal size range (10–60 μm) for LPBF [2], while the powder for track building was relatively finer. Such fine powder lacked flowability and could not be delivered by the recoating system used at the SUSTech. An alternative recoating process was thus designed instead of using the default recoating system. Relative details are provided in the following part of LPBF experiments (3.2).

Table 3.1 Size distribution and contents of principal elements of the pre-alloyed CoCrFeNi powders used for bulk and track building.

Building	Dv 10 (μm)	Dv 50 (μm)	Dv 90 (μm)	Co (at. %)	Cr (at. %)	Fe (at. %)	Ni (at. %)
Bulk	17.7	32.4	59.9	25.4	27.6	23.7	23.3
Track	6.25	18.1	40.3	23.9	25.7	25.8	24.6

3.1.4 Powder blend

All the pre-alloyed and elemental powders were sieved by 73-μm sieves to remove oversized particles before weighing and mixing. 79 wt. % of pre-alloyed CoCrFeNi powder and 21 wt. %

of elemental Mn powder were weighed to obtain a quasi-equiatomic composition of the CoCrFeMnNi HEA. The blend used to produce AlCoCrFeNi HEAs consisted of 89 wt. % of pre-alloyed CoCrFeNi powder and 11 wt. % of elemental Al powder. At the UoB, 800 g of blended powders were mixed by a horizontal mixing machine for at least 12 h each time. A schematic of the horizontal mixing machine is provided in Figure 3.3.

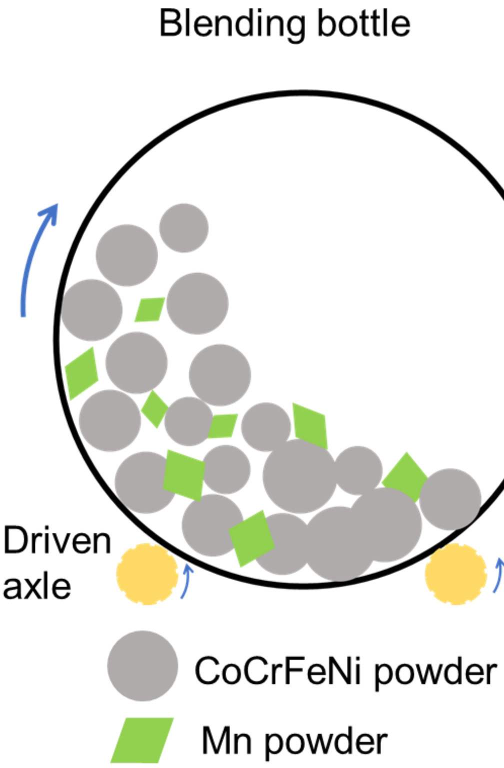

Figure 3.3 Schematic of the horizontal blending machine at the UoB.

At the SUSTech, the blended powder was mixed for 4 h using a WAB Turbula T2F mixer, and 100 g of powder was mixed each time. The SEM images of blended powders are provided in Figure 3.4 & 5, and the nominal contents of blended powders are listed in Table 3.2.

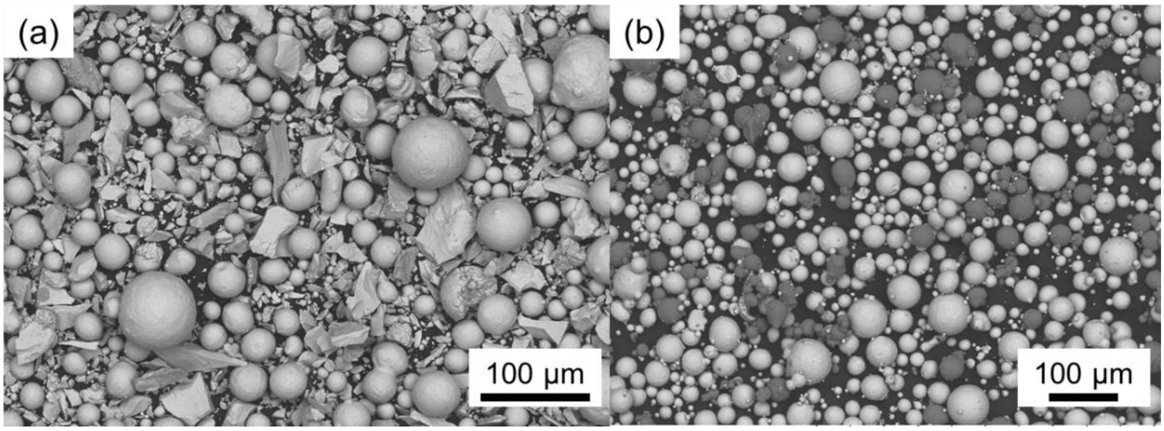

Figure 3.4 Blended powders for the bulk building of (a) CoCrFeMnNi and (b) AlCoCrFeNi HEAs at the UoB.

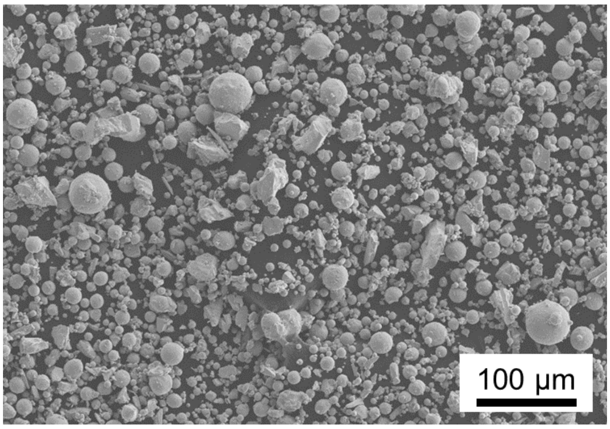

Figure 3.5 Blended powder for the track building of CoCrFeMnNi HEA at the SUSTech.

Table 3.2 Nominal contents of principal elements in the blended powders.

Building	Co (at. %)	Cr (at. %)	Fe (at. %)	Ni (at. %)	Mn (at. %)	Al (at. %)
Bulk-Mn	19.9	21.7	18.6	18.3	21.5	N/A
Bulk-Al	20.2	21.9	18.8	18.6	N/A	20.5
Track-Mn	18.8	20.1	20.4	19.3	21.4	N/A

3.2 Laser Powder Bed Fusion

Two LPBF facilities were employed in this study. The bulk building of CoCrFeMnNi and AlCoCrFeNi HEAs was carried out using a Concept Laser M2 at the UoB. An SLM Solutions SLM125HL at the SUSTech was used for track building of CoCrFeMnNi HEA. Details of the two facilities are provided in Table 3.3.

Table 3.3 Technical specifications of the Concept Laser M2 [3] and SLM Solutions SLM125HL [4].

LPBF facilities	M2	SLM125HL
Laser type	Yb-fibre continuous	Yb-fibre continuous
Laser spot size (μm)	~70	~67
Laser powder (W)	Up to 400	Up to 400
Layer thickness (μm)	20–50	20–75
Scanning speed (mm/s)	Up to 7000	Up to 10000
Recoating system	Powder bed delivery	Upper delivery
Regular substrate size (mm^2)	250 × 250	125 × 125
Reduced substrate size (mm^2)	100 × 100	50 × 50
Built height (mm)	280	125
Protective atmosphere	Ar (<0.1 wt. % O_2)	Ar (<0.2 wt. % O_2)
Pre-heating temperature (K)	Up to 973	Up to 473
Substrate	316L stainless steel	316L stainless steel

Despite the differences in technical specs, the two facilities delivered powders in different manners. Figure 3.6 illustrates the structure of the processing chamber of the M2. For each new layer, a fixed thickness of powder was lifted by the feedstock chamber, and then the lifted powder was spread to the building chamber by a recoater. This recoating system was capable of spreading powders effectively.

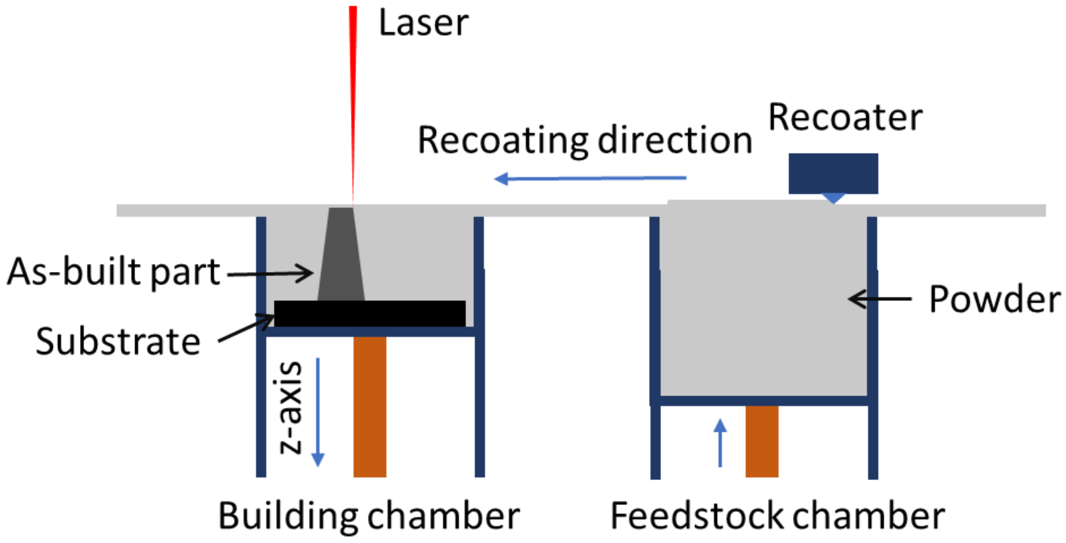

Figure 3.6 Schematic (front view) of the processing chamber of the Concept Laser M2.

The powder delivery system and building chamber of the SLM125HL are illustrated in Figure 3.7. The powder was stored in a feedstock can fixed upon the machine and delivered to the building chamber by gravity. A feedstock controller managed the amount of powder sent into the recoater each time. However, powders with poor flowability cannot be delivered to the building chamber in this manner, i.e., the fine pre-alloyed CoCrFeNi powder used for track building.

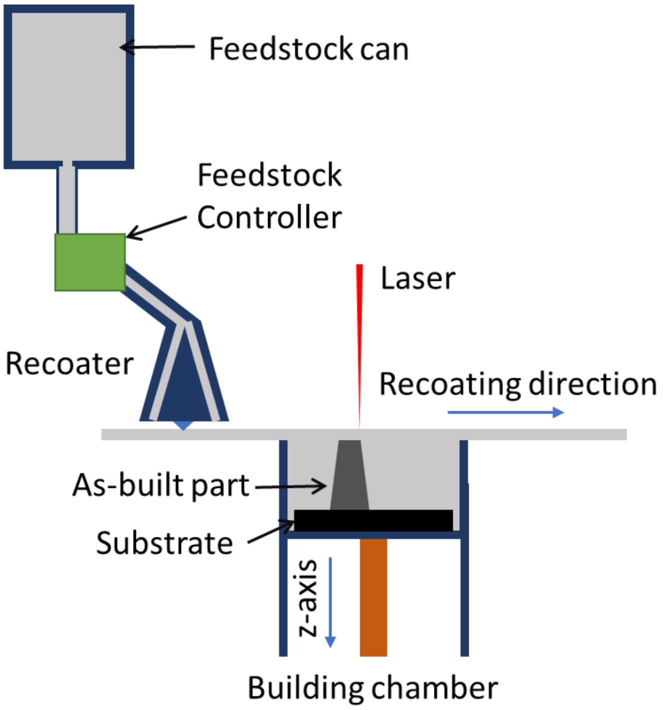

Figure 3.7 Schematic (side view) of the processing chamber of SLM125HL.

Reduced substrates were used on both machines instead of regular-size substrates. For the bulk building of the CoCrFeMnNi HEA, a reduced kit was installed into the original building and feedstock chambers of the M2, as shown in Figure 3.8(a). Meanwhile, a heated bed module was employed in the building of the AlCoCrFeNi HEA, because the M2 was without an original pre-heating module. A 3D model of the module is provided in Figure 3.8(b). The heated bed module was fixed in the reduced building chamber. Moreover, the size of heated substrates was 60 × 60 mm^2, which was even smaller than the reduced one.

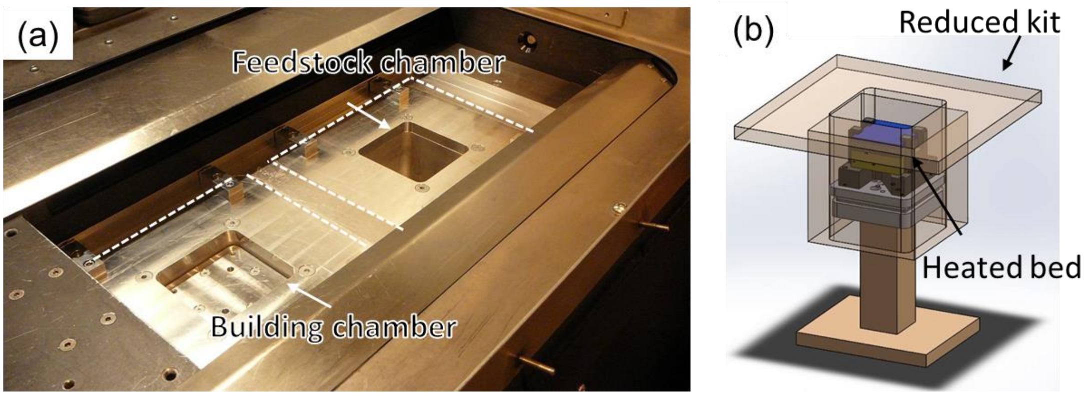

Figure 3.8. (a) Image showing the reduced kit installed in the processing chamber of the M2. White dashed lines mark the original building and feedstock chambers. (b) 3D model of the heated bed module for the M2.

Regarding the track building using the SLM125HL, the original upper delivery system was abandoned due to the poor flowability of powders. The powders were recoated manually on a reduced substrate (Figure 3.9(a)). The reduced substrate was fixed on a regular substrate by tapes, and surrounded by the pre-alloyed CoCrFeNi powder to imitate the powder bed of the M2. During the LPBF process, the powder was manually reloaded using a spoon on the position marked in Figure 3.9(b) and then spread to the substrate by the original recoater. The recoater only worked as a spreading blade without the function of loading powder. Moreover, different powders could be loaded for each layer manually. However, the complicated procedures made this method not suitable for the bulk building that required prolonged recoating.

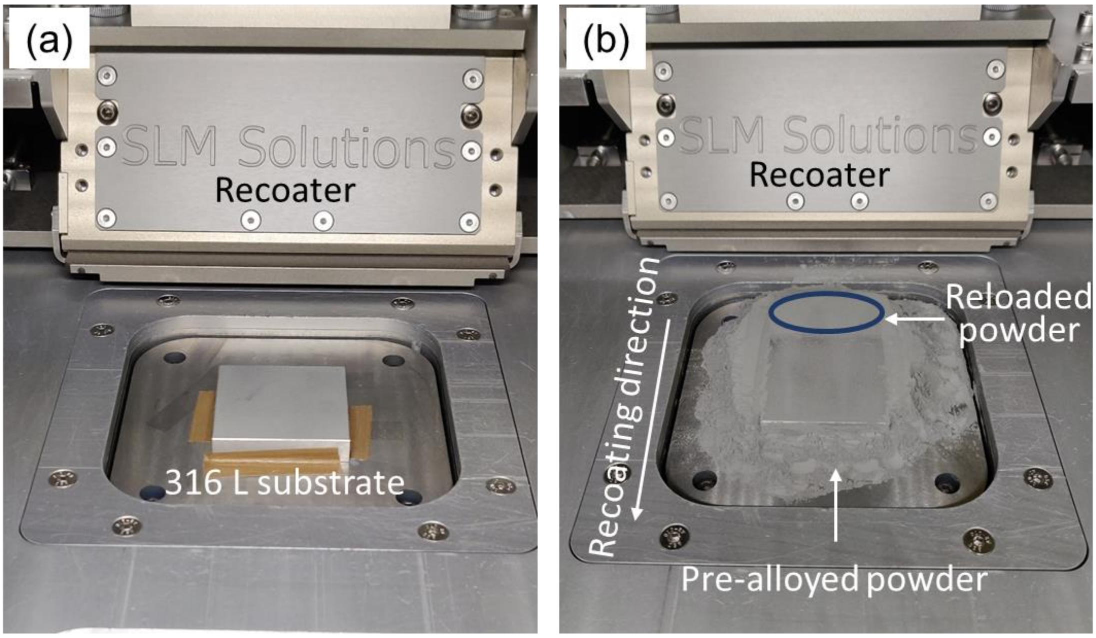

Figure 3.9 (a) Image of a reduced 316L substrate fixed on a regular substrate in SLM125HL, and (b) illustration of the recoating process via the powder bed.

3.2.1 Model preparation

For all the experiments using the M2 and SLM125HL, models were prepared and sliced by the software Materialise Magics [5] without any support structures. Regarding the models prepared in this thesis, the z-axis denotes the building direction (BD), while the x and y-axes are parallel or normal to the laser scanning direction (SD) in each layer. And thus the xy-plane denotes the cross-section normal to the BD, meanwhile, xz/yz-planes stand for the cross-section parallel to the BD.

3.2.1.1 Bulk building

9 mm × 9 mm × 12 mm cuboids were created for the experimental bulk building using the M2. The model used to produce flat tensile parts is provided in Figure 3.10. The scanning strategy was 5 mm × 5 mm chessboard scanning, as shown in Figure 3.11(a). Each layer was separated into 5 mm × 5 mm blocks, whose internal scanning routes were normal to their neighbours.

Every block was rotated 90 ° and shifted 1 mm along both x and y-axes in the next layer. The edges of cuboids were tilted 45 ° toward the recoating direction, as shown in Figure 3.11(b), in order to protect the recoating blade from any sudden impacts.

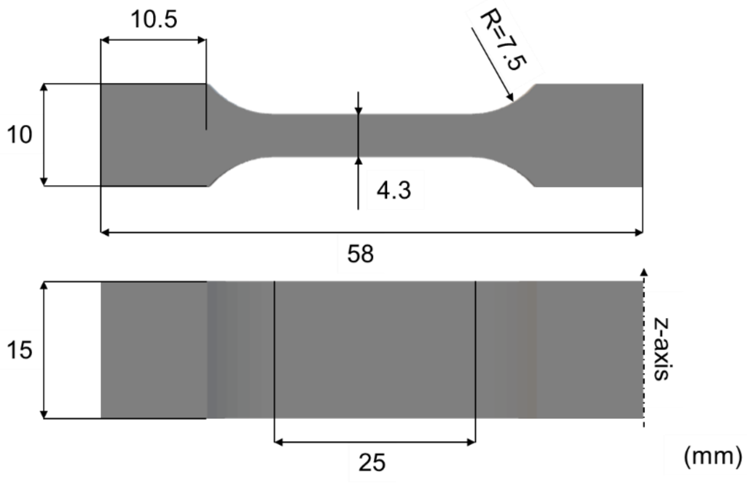

Figure 3.10 Diagram illustrating the flat tensile models used in bulk building.

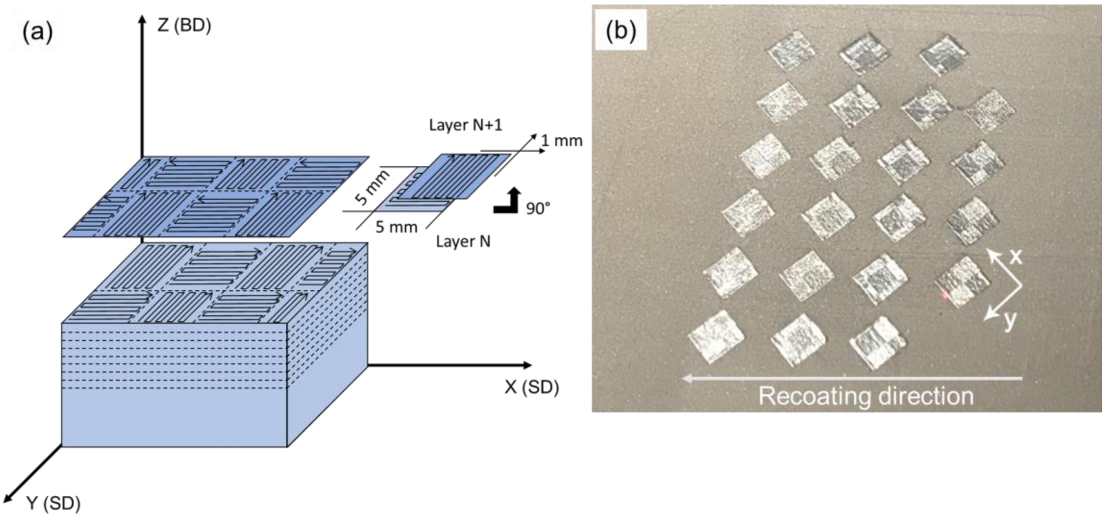

Figure 3.11 (a) Diagram of the chessboard scanning strategy used for bulk building, and (b) image showing cuboid samples built in the M2.

3.2.1.2 Track building

Single-track, single-layer, and three-layer experiments were designed to investigate the single track, which was the fundamental unit of LPBFed parts. By using the manual recoating process on the SLM125HL, models were designed explicitly for the track building.

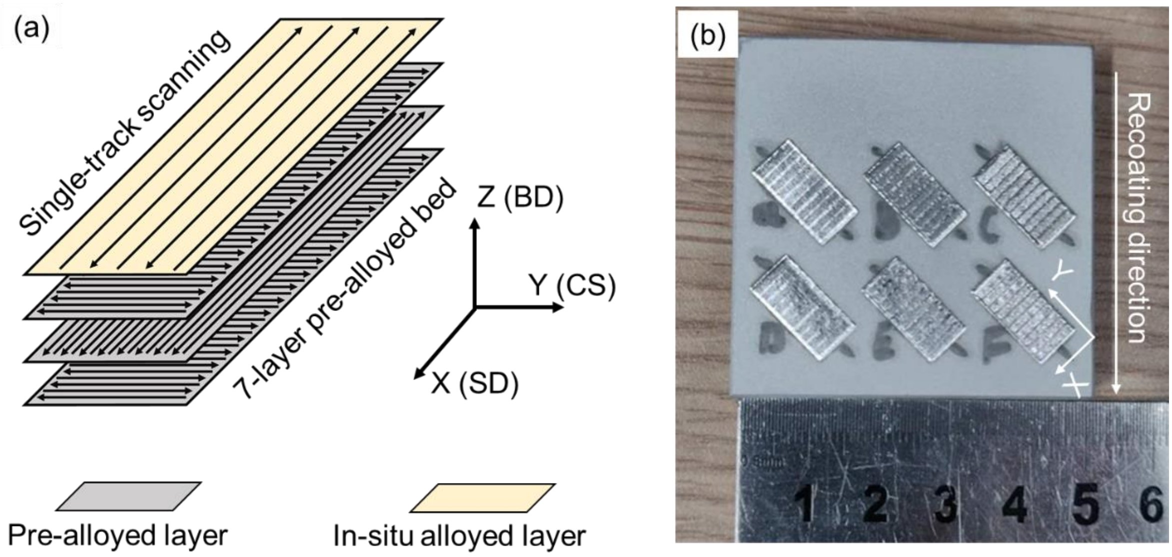

Figure 3.12 (a) Diagram of a single-track model used in track building, and (b) as-built single-track samples on a reduced substrate.

Figure 3.12(a) illustrates the model used in the single-track experiment. 7 layers of pre-alloyed powder were scanned on a 316L substrate prior to the in-situ alloyed layers for the following purposes: (1) To avoid the contamination from substrate materials, so the distribution of Mn could be clearly distinguished from the pre-alloyed CoCrFeNi layers; (2) Powder layers were recoated more evenly after the first few layers during the LPBF process; (3) Recoating on an LPBFed surface was close to the actual situation of normal building. The blended powder was then spread on the pre-alloyed beds to print the single-track, single-layer, and three-layer samples.

The scanning strategy for pre-alloyed beds was simple scanning. Scanning routes were anti-parallel to each other in the same layer, meanwhile, normal to those in adjacent layers. The scanning routes in the in-situ alloyed layer were normal to the previous pre-alloyed layer to distinguish single-tack meltpools clearly. In the three-layer experiments, the scanning routes in the medium layer were normal to those in the bottom and top layers. A substrate holding as-built single-track samples is shown in Figure 3.12(b).

3.2.2 LPBF parameters

Table 3.4 lists the parameters involved in this study, including laser power (P), scanning speed (v), hatch spacing (h), pre-heating temperature (T_0), and layer thickness (t). 873-K pre-heating was employed in the bulk building of the AlCoCrFeNi HEA to reduce thermal stress. 373-K pre-heating was applied in the track building to improve the flowability of powders. The parameters for track building were selected according to the processing window of the bulk building.

After the LPBF process, as-built parts were removed from substrates via electrical discharge machining (EDM). About 1 mm of the bottom material were consumed via EDM. Regarding the samples fabricated in the single-track experiments, a thin layer (~0.5 mm) of 316L substrate was cut with the samples to retain the meltpool structures.

Table 3.4 Processing parameters used in the in-situ alloying experiments.

Building	Sample	Facility	P (W)	v (mm/s)	h (μm)	t (μm)	T_0 (K)
AlCoCrFeNi Bulk	Cuboid	Concept Laser M2	80–300	100–2400	30–135	20–60	RT, 873
CoCrFeMnNi Bulk	Cuboid		100–300	600–2000	30–75	30	RT
	Miniature tensile		200	800	45	30	RT
	Flat tensile		280	800	60	30	RT
CoCrFeMnNi Track	pre-alloyed bed	SLM Solution SLM125HL	220	600	60	30	373
	Single-track		150–300	600–1000	N/A	30	373
	Single-layer		150–300	600, 1000	60–100	30	373
	Three-layer		150–300	600–1000	60, 100	30	373

3.3 Density Measurement

The density of cuboid samples was measured according to the Archimedes method (ASTM B962-17 [6]), without vacuum at room temperature. Each sample was measured at least three times, and then the average was taken. Regarding the AlCoCrFeNi samples with open cracking and porosity, Micro-CT was carried out by an external testing supplier, ND Inspection & Control Solution (Shanghai, China), using a Diondo D2 to analyse the defect distribution and relative density in the samples.

3.4 Metallurgical Sample Preparation

The as-built cuboid samples were cut by EDM along their horizontal and vertical planes, and then hot mounted using conductive bakelite. The single-track samples were cut perpendicularly to the scanning directions and mounted. Then the exposed cross-sections were ground by grit papers from p240 till p2000, and polished with diamond suspensions from 9 μm to 3 μm. A Buehler VibroMet 2 vibratory polisher was employed for the final finish of samples.

The meltpool structures of CoCrFeMnNi samples were revealed using a 10% oxalic acid solution. The polished samples were electrochemically etched in the solution for 100–120 s at 2.5 V, then rinsed with ethanol and dried.

3.5 Optical Microscopy

A Leica DM2700 optical microscope (OM) was employed to check the cross-sections of polished and etched surfaces. The software Leica Application Suite was used to measure the meltpool dimensions from OM images. Width (W), depth (D), and height (H) were measured from etched samples, as illustrated in Figure 3.13, and five individual meltpools were measured for each parameter set.

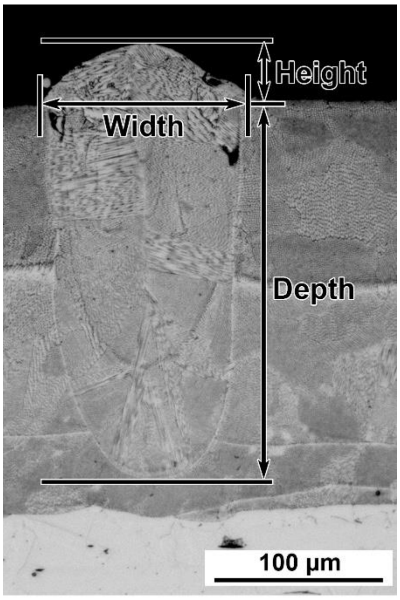

Figure 3.13 Diagram illustrating the measurement of single-track meltpools.

3.6 X-Ray Diffraction

X-ray diffraction (XRD) was conducted by different facilities at the UoB and SUSTech. The AlCoCrFeNi samples were characterised at the UoB, using a Bruker D2 Phaser equipped with a Co radiation source (Co Kα, λ = 1.7890 nm). A Rigaku Smartlab equipped with a Cu radiation source (Cu Kα, λ = 1.5418 nm) was employed to characterise the CoCrFeMnNi samples at the SUSTech. XRD was performed on polished surfaces, and the XRD results were analysed using the software Match! [7].

3.7 Oxygen Content Measurement

The oxygen contents of powders and as-built CoCrFeMnNi samples were measured using a LECO 836 Elemental Analyser following the ASTM method (ASTM E1019-18 [8]). ~0.5 g of material was handled by an aluminium crucible and measured as a steel-type material by the equipment.

3.8 Electron Microscopy

A Hitachi TM 3000 desktop selective electron microscope (SEM) equipped with an energy dispersive spectroscopy (EDS) detector was employed to characterise the powders and AlCoCrFeNi samples at the UoB. A ZEISS Merlin field emission SEM equipped with an EDS detector and an electron back-scattered diffraction (EBSD) system was employed to acquire secondary electron (SE), back-scattered electron (BSE), and electron channelling contrast imaging (ECCI) results of the CoCrFeMnNi samples at the SUSTech. To observe powder morphology, LPBF defects, fracture surfaces, and meltpool morphology, the Merlin SEM was operated at 10 kV, and images were acquired by the SE detector. The BSE images were acquired at 25 kV to reveal the distribution of oxide particles. With 5 BSE images taken at 5000X magnification, the oxide particles were quantified following the particle analyse process of ImageJ [9]. ECCI was also conducted in the BSE mode at 30 kV, with the working distance down to 3 mm, and the sample holder tilted between 2 and 5 ° [10]. ECCI revealed the distribution of dislocation and oxide particles. EDS was operated at 25 kV, and the results were analysed using the TEAM [11]. The elemental distribution in bulk samples was assessed via EDS mapping. In single-layer samples, EDS line scanning was performed 30 μm beneath surfaces, which was one layer thickness. EBSD was conducted to characterise the grain structures and operated at 20 kV on polished or etched surfaces. The EBSD results were identified using an austenite profile whose lattice parameter was modified to 0.36 nm. The TSL OIM Analysis [12] was used to analyse EBSD results.

An FEI Talos F200X transmission electron microscope (TEM) equipped with an EDS detector was operated at 200 kV to acquire bright-field (BF), dark-field (DF), scanning transmission electron microscopy (STEM), and selected area electron diffraction (SAED) results. TEM samples were prepared in two manners, i.e., ion milling and focused ion beam (FIB). A GANTA PIPS II 695 was employed for ion milling. Φ 3-mm disc samples were ground to a thickness of 30–60 μm before ion milling. The ion milling was operated from 5 to 1 keV, 7 to 3 ° to punch holes, thin and remove the amorphous layer. FIB was performed by an FEI Helios Nanolab 600i. A 10 μm × 8 μm × 2 μm sample was cut with Pt coating and fixed on an FIB grid, then thinned by the ion beam from 30 to 2 kV. The TEM samples were further cleaned via a Fischione 1040 NanoMill before characterisation. SAED patterns were analysed by the Gatan Microscopy Suite [13] to identify the phases in CoCrFeMnNi samples. BF and DF images were acquired from the deformed samples to analyse the interaction between the oxide particles and the HEA matrix.

3.9 X-Ray Photoelectron Spectroscopy

A PHI 5000 Versaprobe III was used to analyse the surface of elemental Mn powder via X-ray photoelectron spectroscopy (XPS). A survey scanning was carried out in the bonding energy range from 0 to 800 eV, followed by a narrow scanning from 635 to 660 eV specifically for the peaks of Mn.

3.10 Mechanical Testing

The mechanical properties of the in-situ alloyed HEAs were assessed via hardness, tensile, compression, and nano-indentation tests. All the tests were carried out at room temperature.

3.10.1 Hardness

The measurement of Vickers hardness followed the ASTM method E92-17 [14]. The AlCoCrFeNi samples were tested by a Struers DuraScan tester at the UoB, and the method HV 0.5 with a load of 500 gf and a dwell time of 10 s was applied. The Vickers hardness of the

CoCrFeMnNi samples was tested with a load of 300 gf and a dwell time of 10 s, using a Shanghai Optical Instrument Factory HX1000TM/LCD hardness tester at the SUSTech. All tested surfaces were polished prior to the tests, and 10 points were tested for each sample.

3.10.2 Tensile properties

Two kinds of specimens were used for the tensile testing of the CoCrFeMnNi samples. The Miniature specimen illustrated in Figure 3.14 was EDM cut from cuboid samples at the processing development stage. After the optimisation of parameters, the flat tensile model in Figure 3.10 was fabricated and separated into 2-mm thickness via EDM to provide reduced tensile specimens according to the ASTM E8 method [15]. The surfaces of tested specimens were ground with p800 grit papers, and three specimens were tested for each parameter set.

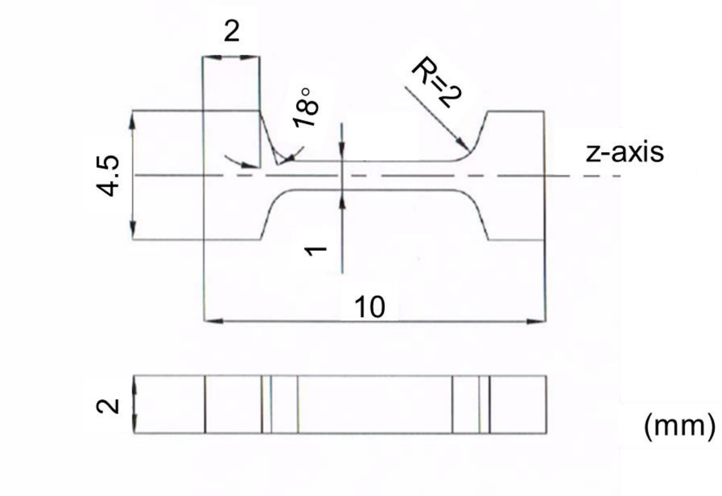

Figure 3.14 Illustration of the miniature tensile specimen.

The miniature specimens were tested by a Wance ETM universal testing machine at a fixed cross-head speed of 0.21 mm/min, without using an extensometer. The tensile direction was along the z-axis, which was the building direction of bulk samples. The flat specimens were tested using an Instron 3382 universal testing machine according to the ASTM E8 method [15].

A 10-mm extensometer was fixed on the tested flat specimens, and the strain rate was controlled at 10^{-3}/s [16]. The tensile direction was normal to the building direction.

3.10.3 Compression properties

Φ 6 mm × 9 mm cylinder specimens were EDM cut from the CoCrFeMnNi cuboids for compression testing. The sample surfaces were ground via p800 grit papers. The tests were operated at a strain rate of 10^{-3}/s [16], using the Instron 3382 universal testing machine according to the ASTM method ASTM E9 [17]. The compression direction was normal to the building direction.

3.10.4 Nano-indentation

Nano-indentation was carried out to assess the hardness distribution in single-track meltpools. A Hysitron TI-950 equipped with a Berkovich indenter was used for nano-indentation mapping. The height and width of tested arrays were set according to the meltpool dimensions, and the indentations were separated by 10 μm in rows and columns. A tested array and its corresponding single-track meltpool are shown in Figure 3.15. The maximum load was set as 8000 μN, while the load time, dwell time and unload time were set as 5, 2, and 5 s, respectively.

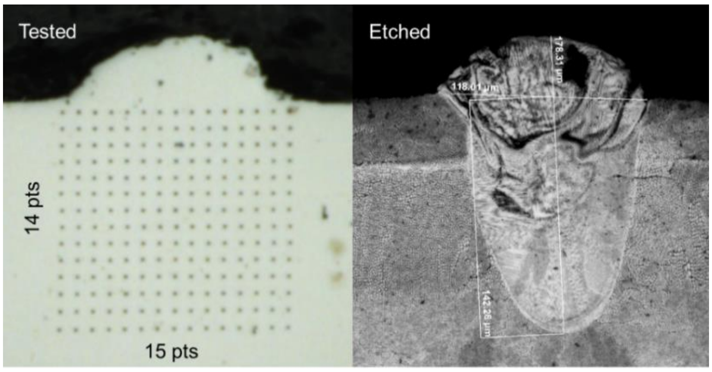

Figure 3.15 OM images of a nano-indentation array on a single-track meltpool.

3.11 References

[1] ASTM B822-20, Standard Test Method for Particle Size Distribution of Metal Powders and Related Compounds by Light Scattering, ASTM International, West Conshohocken, PA, 2020.
[2] T. DebRoy, H.L. Wei, J.S. Zuback, T. Mukherjee, J.W. Elmer, J.O. Milewski, A.M. Beese, A. Wilson-Heid, A. De, W. Zhang, Additive manufacturing of metallic components – process, structure and properties, Progress in Materials Science 92 (2018) 112-224. http://doi.org/10.1016/j.pmatsci.2017.10.001.
[3] GE Additive, GE Additive – Concept Laser – Machines (https://www.ge.com/additive/additive-manufacturing/machines). 2021.
[4] SLM Solutions, SLM Solutions – Machines (https://www.slm-solutions.com/products-and-solutions/machines/slm-125/). 2021.
[5] Materialise, Materialise – Software (https://www.materialise.com/en/software/magics). 2021.
[6] ASTM B962-17, Standard Test Methods for Density of Compacted or Sintered Powder Metallurgy (PM) Products Using Archimedes' Principle, ASTM International, West Conshohocken, PA, 2017.
[7] Crystal Impact, Crystal Impact – Match! (https://www.crystalimpact.com/match/Default.htm). 2021.
[8] ASTM E1019-18, Standard Test Methods for Determination of Carbon, Sulfur, Nitrogen, and Oxygen in Steel, Iron, Nickel, and Cobalt Alloys by Various Combustion and Inert Gas Fusion Techniques, ASTM International, West Conshohocken, PA, 2018.
[9] ImageJ - Analyse Particles, ImageJ – Documentation (https://imagej.nih.gov/ij/docs/guide/index.html). 2021.
[10] Y.-K. Kim, J. Choe, K.-A. Lee, Selective laser melted equiatomic CoCrFeMnNi high-entropy alloy: Microstructure, anisotropic mechanical response, and multiple strengthening mechanism, Journal of Alloys and Compounds 805 (2019) 680-691. http://doi.org/10.1016/j.jallcom.2019.07.106.
[11] EDAX, EDAX – TEAM (http://www.edax.com/Products/Integrated/TEAM-Pegasus-Integrated-EDS-and-EBSD-Analysis-System.aspx). 2016.
[12] EDAX, EDAX – OIM Analysis (https://www.edax.com/products/ebsd/oim-analysis). 2021.
[13] Gatan , Gatan – Gatan Microscopy Suite Software (https://www.gatan.com/products/tem-analysis/gatan-microscopy-suite-software). 2021.
[14] ASTM E92-17, Standard Test Methods for Vickers Hardness and Knoop Hardness of Metallic Materials, ASTM International, West Conshohocken, PA, 2017
[15] ASTM E8 / E8M-16a, Standard Test Methods for Tension Testing of Metallic Materials, ASTM International, West Conshohocken, PA, 2016
[16] Z.G. Zhu, Q.B. Nguyen, F.L. Ng, X.H. An, X.Z. Liao, P.K. Liaw, S.M.L. Nai, J. Wei, Hierarchical microstructure and strengthening mechanisms of a CoCrFeNiMn high entropy alloy additively manufactured by selective laser melting, Scripta Materialia 154 (2018) 20-24. http://doi.org/10.1016/j.scriptamat.2018.05.015.
[17] ASTM E9-19, Standard Test Methods of Compression Testing of Metallic Materials at Room Temperature, ASTM International, West Conshohocken, PA, 2019

Chapter 4: Fabricating CoCrFeMnNi High Entropy Alloy via Selective Laser Melting In-Situ Alloying

To develop an additive manufacturing route for high entropy alloys, the processing development starts with the in-situ alloying of CoCrFeNi & Mn blended powder. The printability of the powder is assessed in this chapter, along with the preliminary mechanical properties of the as-built CoCrFeMnNi samples.

Published article

Peng Chen[a, b], Sheng Li[a], Yinghao Zhou[b], Ming Yan[b], Moataz M. Attallah[a]

Journal of Materials Science & Technology, 43 (2020) 40-43.

[a] Advanced Materials Processing Laboratory, University of Birmingham, Birmingham B15 2TT, UK

[b] Department of Materials Science and Engineering, and Shenzhen Key Laboratory for Additive Manufacturing of High Performance Materials, Southern University of Science and Technology, Shenzhen 518055, China

Abstract

Quasi-equiatomic CoCrFeMnNi high entropy alloy (HEA) has been in-situ alloyed by selective laser melting (SLM) from a blend of pre-alloyed CoCrFeNi powder and elemental Mn powder. The blended powder shows good printability with various SLM parameters and the as-built HEA samples achieve a reliable forming quality. Despite the slight evaporation of Mn, energy dispersive spectrometer mapping and X-ray diffraction results show that the as-built HEA has a homogeneous chemical distribution and presents a single face-centred-cubic (FCC) phase, indicating successful in-situ alloying. The study has verified the feasibility of using blended powder to prepare high-quality HEA by SLM.

Keywords: High entropy alloys; Laser processing; Selective laser melting; In-situ alloying; CoCrFeMnNi; Crystal structure

4.1 Introduction

High entropy alloys (HEAs) have drawn attention from both academia and industries because of their unique microstructural features and outstanding mechanical properties. The initial definition of HEAs is solid solutions consisting of no less than 5 elements, each concentration between 5 and 35 at. % [1]. Arc melting is the most widely used technique to fabricate HEAs in laboratories due to its compositional flexibility and capability of homogenising microstructure, but the geometry and size of produced parts are normally restricted. Additive manufacturing (AM) techniques including directed laser deposition (DLD), selective laser melting (SLM), and selective electron beam melting (SEBM) have been employed to fabricate HEAs [2-4] for their capability to manufacture complex geometry, as well as the associated high cooling rate which restrains segregation.

Among various HEAs, CoCrFeNi and CoCrFeMnNi HEAs have been fabricated by SLM using pre-alloyed powder, and the as-built HEAs possess chemical homogenisation and outstanding mechanical properties [5, 6]. However, in order to further explore HEAs, the existing pre-alloyed powder approach, which often relies on gas atomisation to provide the powder, seems rigid and time-consuming and largely compromises the compositional flexibility of HEAs. As such, $Al_xCoCrFeNi$ HEAs have been in-situ alloyed by DLD using elemental powders [2]. DLD can mix several elemental powders in a large molten pool but this also results in low forming accuracy which requires considerable post-processing. It would bypass preparing pre-alloyed powder and post-machining if HEAs could be in-situ alloyed by SLM, which has higher geometry accuracy and better surface finish. SLM has been employed to fabricate Ti alloys and Ni-based superalloys using blended powders. In-situ alloying can be achieved when the fraction of the additional element is less than 5 at. % [7, 8]. When the fraction is too high, the additional elements tend to stay unalloyed after the SLM process [9]. The use of SLM in-situ alloying for manufacturing HEAs has not been reported yet. Its feasibility and the underlying mechanism are still to be investigated, particularly considering that as much as 20 at. % of additional alloying elements is going to be involved in HEAs.

This research employed CoCrFeNi pre-alloyed powder as a base alloy. Mn was chosen as the additional metal since the printability of CoCrFeMnNi has been proved, useful as a reference for comparison. SLM experiments were carried out to verify the printability of the blended powder. The microstructures and chemistry of the in-situ alloyed HEA were studied to understand the feasibility of the SLM in-situ alloying.

4.2 Experiment

Pre-alloyed CoCrFeNi powder was fabricated by TLS Technik GmbH and its composition is listed in Table 4.1. Elemental Mn powder (99% purity) was provided by Sigma-Aldrich. 79 wt. % of the pre-alloyed CoCrFeNi powder and 21 wt. % of the elemental Mn powder were weighed for quasi-equiatomic composition. Powders were blended for 24 h by a horizontal blending machine. 9 mm × 9 mm × 12 mm blocks were manufactured by a Concept Laser M2 SLM printer on steel substrates with a laser spot size of 90 µm, and layer thickness (t) of 30 µm. A processing map including laser power (P: 110–280 W), scanning speed (v: 800–2000 mm/s), and hatch spacing (h: 45–75 µm) was designed to optimise SLM parameters. The density of samples was measured according to the Archimedes method. X-ray diffraction (XRD) was performed to investigate the phase of powder and the as-built HEA on a Rigaku Smartlab equipped with Cu K_α radiation. A Zeiss Merlin field emission scanning electron microscope (SEM) with electron back-scattered diffraction (EBSD) detector and energy dispersive spectrometer (EDS) was employed to analyse the microstructures and chemistry of samples. Prior to EBSD and XRD analyses, vibratory polishing was conducted to provide stress-free samples. The Vickers hardness was tested with a load of 300 gf and dwell time of 10 s on polished sample cross-sections. Miniature tensile specimens with gauge dimensions of 1 mm × 2 mm × 3.4 mm were machined from as-built HEA blocks. Tensile tests were performed on a Wance ETM universal testing machine at a cross-head speed of 0.21 mm/min.

Table 4.1 Chemical analysis and various properties of the raw materials used in this study.

	Fe	Ni	Cr	Co	Mn
Pre-alloyed powder (at. %)	23.69	23.34	27.57	25.40	N/A
Blended powder (at. %)	18.59	18.31	21.64	19.93	21.53
SLM 259.3 (at. %)	20.14	19.72	21.88	21.59	16.67
T_B (K)	3134	3003	2944	3200	2334
ΔH_{vap} (kJ/mol)	340	379	347	377	221
Atomic radius (pm)	126	124	128	125	127

4.3 Results and Discussion

Figures 4.1(a) and (b) show the SEM images of the pre-alloyed CoCrFeNi powder and the elemental Mn powder. The pre-alloyed powder is gas-atomised spherical powder while the Mn powder is irregular. They can be easily distinguished in the blended powder by their appearances (Figure 4.1(c)). The as-built CoCrFeMnNi HEA samples in Figure 4.1(d) are free of cracking or delamination on their surfaces.

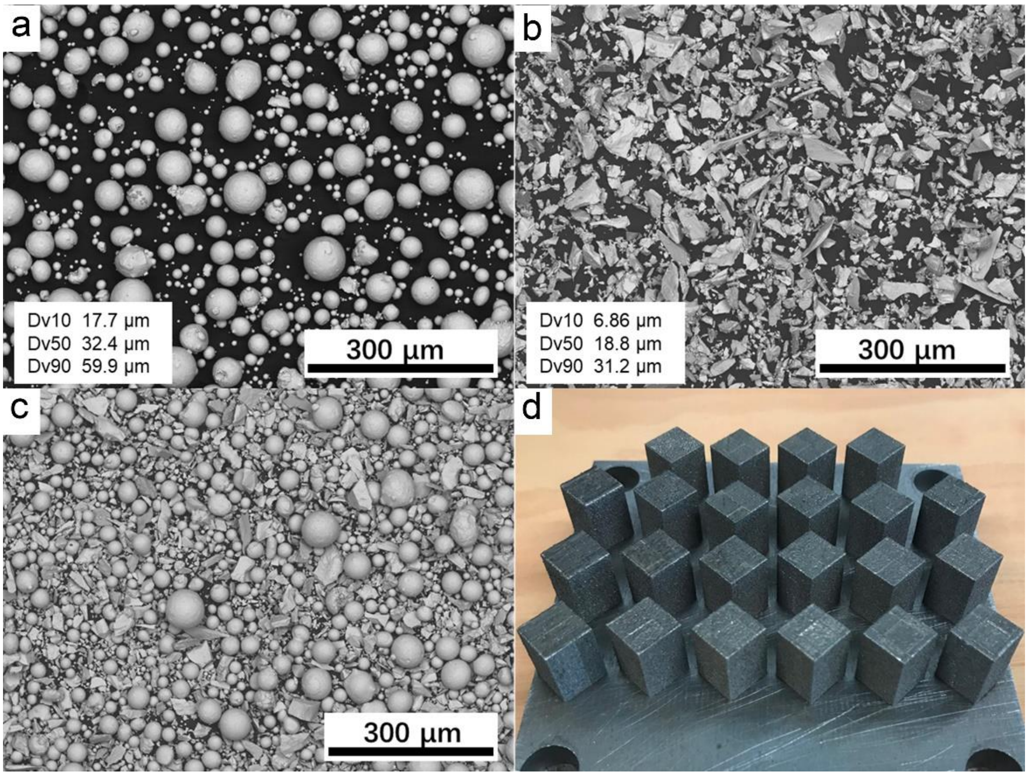

Figure 4.1 SEM images of (a) pre-alloyed CoCrFeNi powder, (b) elemental Mn powder and (c) blended powder. (d) As-built CoCrFeMnNi HEA blocks.

In Figure 4.2(a), the density of as-built samples, including CoCrFeNi HEA built using pre-alloyed powder, is plotted verse laser volumetric energy density (*VED*) which is calculated by $VED = P/(vht)$ [10]. It shows that the density of the in-situ alloyed CoCrFeMnNi HEA keeps increasing till the maximum *VED* of 259.3 J/mm^3 and reaches 7.89 g/cm^3 (the sample is denoted as SLM 259.3). The porosity observed in the cross-sections matches the trend of increasing density as well, see the figure inset in Figure 4.2(a). Without the elemental Mn powder, the highest density of CoCrFeNi HEA occurs at the *VED* of 104.3 J/mm^3. In the former research using pre-alloyed powder, the density of SLMed CoCrFeMnNi HEA reaches the maximum when the *VED* is 60 J/mm^3 or 74 J/mm^3 [5, 6], while excessive energy input generates defects and therefore decreases the density [11]. Thus, the addition of elemental Mn powder somehow helps to restrain the defect in SLMed parts at higher *VED* values. Mn has the lowest heat of vaporisation and the lowest boiling point among the five composing elements (Table 4.1). It has also been found that Mn evaporates more than the other elements during the SLM process [5], and hence its loss is expectable, particularly as an elemental powder. According to Table 4.1, the Mn content drops to 16.67 at. % in the SLM 259.3. Besides the energy consumed by Mn evaporation, the irregular shape of powder and the spatter may also reduce the laser absorption during the SLM process, so the samples could maintain well densified with high *VED* [12, 13].

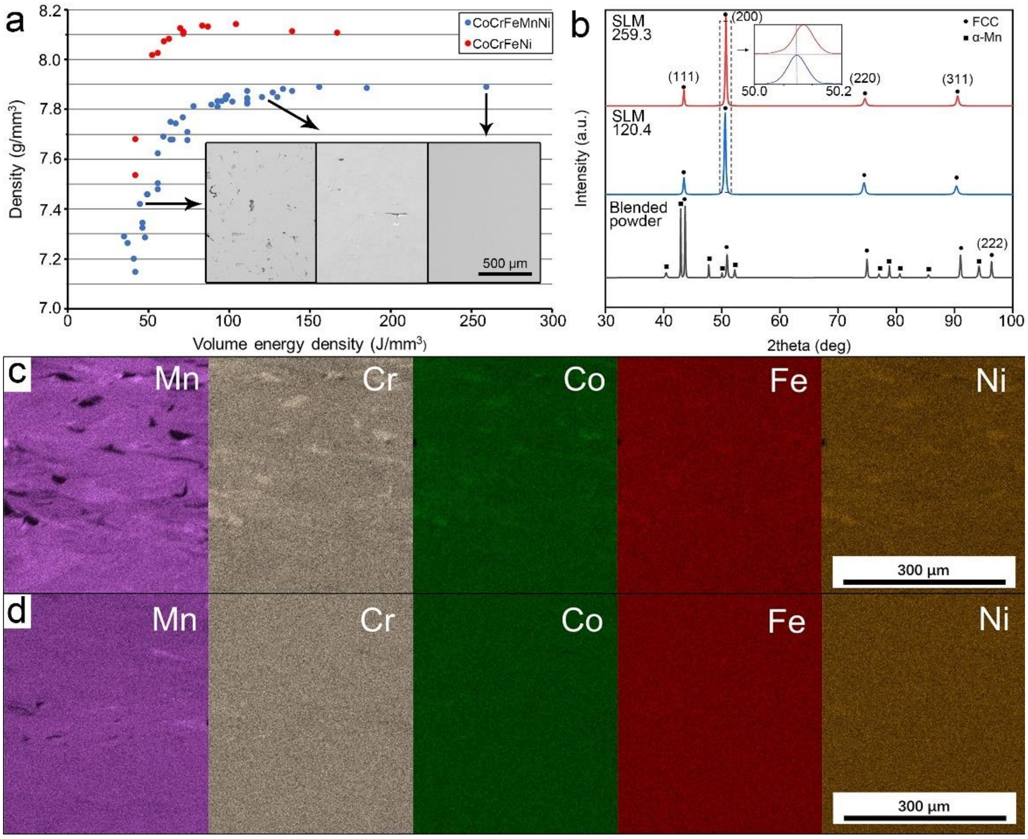

Figure 4.2 (a) Dependence of density on the *VED*, with embedded SEM images of cross-sections. (b) XRD results of the blended powder and as-built CoCrFeMnNi HEA samples. EDS mapping of (c) the SLM 120.4 and (d) the SLM 259.3.

XRD results are illustrated in Figure 4.2(b). Face-centred-cubic (FCC) structure from the pre-alloyed CoCrFeNi powder and α-Mn are both detected in the blended powder. After the SLM process, peaks of the α-Mn disappear and the as-built CoCrFeMnNi HEA samples possess an FCC single phase, revealing that *VED* of 120.4 J/mm^3 can in-situ alloy most of the elemental Mn powder and form a desirable HEA microstructure. The lattice parameter of the as-built CoCrFeMnNi HEA calculated from the XRD spectrums is approximately 3.60 Å, which matches the values of this HEA fabricated by arc melting (~3.59 Å) and SLM (~3.60 Å) using pre-alloyed powder [6, 10]. This lattice parameter is larger than 3.57 Å of the pre-alloyed CoCrFeNi powder since the atomic radius of Mn is the second largest among constituent elements (Table 4.1), and hence the alloying of Mn leads to a larger lattice parameter. The shifting of (200) peaks in the spectrum also proves this point: The sample built with higher *VED* has lower Mn content due to evaporation, and therefore its lattice parameter is smaller. Figure 4.2(c) shows the EDS mapping of the SLM 120.4. The depletion of Mn and segregation of the pre-alloyed elements occur extensively, indicating poor elemental homogeneity. As the *VED* increases to 259.3 J/mm^3, the pre-alloyed elements distribute uniformly in Figure 4.2(d), and the distribution of Mn is mostly homogeneous. High *VED* can increase the temperature in the meltpool, enlarge the size of it, and promote internal flows [14, 15]. The larger meltpool allows more powder to be molten and mixed by the internal flow, meanwhile; it remelts previously solidified part, leading to better homogenisation and in-situ alloying [16].

EBSD was performed on the planes parallel and perpendicular to the building direction of the SLM 259.3 HEA. In Figure 4.3, the z-axis represents the building direction while the x and y-axes represent the directions parallel to scanning directions. The inverse pole figure (IPF) map of the yz-plane shown in Figure 4.3(a) illustrates that coarse columnar grains can grow through more than 10 layers in the building direction. In the xy-plane (Figure 4.3(b)), grains are not typically equiaxed and the average grain size is 53.1 µm. Figure 4.3(c) shows the pole figure (PF) and IPF of the xy-plane. The IPF reveals a strong <001> texture because <001>

orientation is the preferred growth direction in FCC crystals along the heat gradient, which is overall parallel to the building direction during SLM processes [17]. Besides the building direction, <001> orientation also gathers along x and y-axes in the PF, indicating crystal growth is affected by scanning directions during the SLM process.

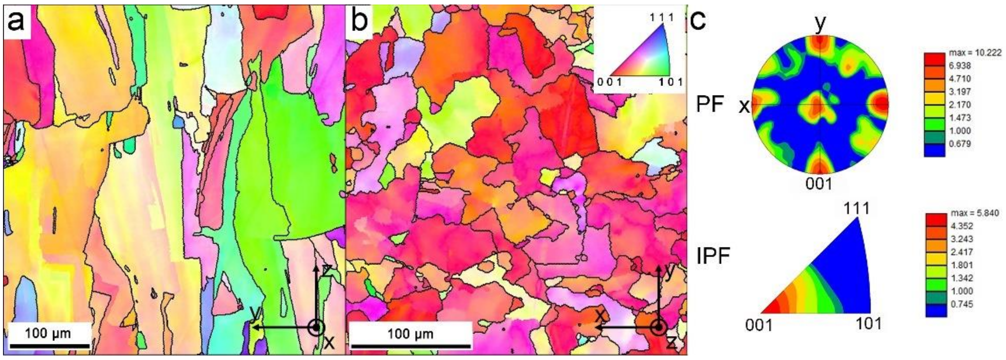

Figure 4.3 IPF maps of (a) the perpendicular (yz) plane and (b) the horizontal (xy) plane of the SLM 259.3. (c) PF and IPF of the horizontal plane.

The tensile properties and microhardness of the SLM in-situ alloyed CoCrFeMnNi HEA are provided in Table 4.2. The in-situ alloyed HEA possesses higher hardness and ultimate tensile strength (σ_{uts}) than the HEAs fabricated using pre-alloyed powder, whereas its elongation at break (ε_f) is lower. It is noted that the oxygen content of the in-situ alloyed HEA (= 3300 ppm) is higher than that in the literature [5]. Since Mn is a reactive element, oxygen could be introduced by the Mn powder during the in-situ alloying process. It has been reported that the strength of SLMed HEAs can be enhanced by nano-size Mn oxides [18], which is likely the reason for the higher hardness and tensile strength value measured by this study.

Table 4.2 Comparison of microhardness and tensile properties of CoCrFeMnNi HEAs fabricated by SLM using blended powder and pre-alloyed powder.

Materials	Microhardness (HV)	σ_{uts} (MPa)	ε_f (%)
Present blended powder	261 ± 7	681 ± 14	12.5 ± 0.5
Pre-alloyed powder [5]	N/A	609 ± 10	34 ± 3
Pre-alloyed powder [6]	N/A	601	35
Pre-alloyed powder [17]	212	N/A	N/A

A brief comment on the above results is made as follows: In-situ alloying using blended powders has realised the fabrication of segregation-free, high-density and good mechanical property CoCrFeMnNi HEA through careful process optimisation. The approach holds the potential for further exploring HEAs such as those consisting of senary or even more composing elements and maximising the compositional flexibility of HEAs.

4.4 Conclusions

Bulk CoCrFeMnNi HEA has been in-situ alloyed from the blend of pre-alloyed CoCrFeNi powder and elemental Mn powder. XRD results showing a single FCC phase indicate that the Mn has been alloyed during the SLM process. High *VED* helps to homogenise Mn in the as-built parts, and Mn distributes almost uniformly at the *VED* of 259.3 J/mm^3. Based on the wide permissible *VED* range and good printability of the blended powder, it is possible that the current approach can be applied to other CoCrFeNi-based HEAs as well by SLM in-situ alloying.

4.5 Acknowledgements

This research is supported by Shenzhen Science and Technology Innovation Commission [ZDSYS201703031748354 and JCYJ20170817110358927]; Science and Technology Planning Project of Guangdong Province of China [2017B090911003], Natural Science Foundation of Guangdong Province [2016A030313756]. Dr. M. Yan appreciates the support of Humboldt Research Fellowship for Experienced Researchers.

4.6 References

[1] Y. Zhang, T.T. Zuo, Z. Tang, M.C. Gao, K.A. Dahmen, P.K. Liaw, Z.P. Lu, Microstructures and properties of high-entropy alloys, Progress in Materials Science 61 (2014) 1-93. http://doi.org/10.1016/j.pmatsci.2013.10.001.

[2] J. Joseph, T. Jarvis, X. Wu, N. Stanford, P. Hodgson, D.M. Fabijanic, Comparative study of the microstructures and mechanical properties of direct laser fabricated and arc-melted AlxCoCrFeNi high entropy alloys, Materials Science and Engineering: A 633 (2015) 184-193. http://doi.org/10.1016/j.msea.2015.02.072.

[3] Y. Brif, M. Thomas, I. Todd, The use of high-entropy alloys in additive manufacturing, Scripta Materialia 99 (2015) 93-96. http://doi.org/10.1016/j.scriptamat.2014.11.037.

[4] T. Fujieda, H. Shiratori, K. Kuwabara, T. Kato, K. Yamanaka, Y. Koizumi, A. Chiba, First demonstration of promising selective electron beam melting method for utilizing high-entropy alloys as engineering materials, Materials Letters 159 (2015) 12-15. http://doi.org/10.1016/j.matlet.2015.06.046.

[5] Z.G. Zhu, Q.B. Nguyen, F.L. Ng, X.H. An, X.Z. Liao, P.K. Liaw, S.M.L. Nai, J. Wei, Hierarchical microstructure and strengthening mechanisms of a CoCrFeNiMn high entropy alloy additively manufactured by selective laser melting, Scripta Materialia 154 (2018) 20-24. http://doi.org/10.1016/j.scriptamat.2018.05.015.

[6] R. Li, P. Niu, T. Yuan, P. Cao, C. Chen, K. Zhou, Selective laser melting of an equiatomic CoCrFeMnNi high-entropy alloy: Processability, non-equilibrium microstructure and mechanical property, Journal of Alloys and Compounds 746 (2018) 125-134. http://doi.org/10.1016/j.jallcom.2018.02.298.

[7] Z.H. Zhang, Y.H. Zhou, S.Y. Zhou, L. Zhang, M. Yan, Mechanically blended Al: Simple but effective approach to improving mechanical property and thermal stability of selective laser-melted Inconel 718, Metallurgical and Materials Transactions A 50a(8) (2019) 3922-3936. http://doi.org/10.1007/s11661-019-05299-6.

[8] I. Polozov, V. Sufiiarov, A. Popovich, D. Masaylo, A. Grigoriev, Synthesis of Ti-5Al, Ti-6Al-7Nb, and Ti-22Al-25Nb alloys from elemental powders using powder-bed fusion additive manufacturing, Journal of Alloys and Compounds 763 (2018) 436-445. http://doi.org/10.1016/j.jallcom.2018.05.325.

[9] A. Grigoriev, I. Polozov, V. Sufiiarov, A. Popovich, In-situ synthesis of Ti2AlNb-based intermetallic alloy by selective laser melting, Journal of Alloys and Compounds 704 (2017) 434-442. http://doi.org/10.1016/j.jallcom.2017.02.086.

[10] A. Simchi, Direct laser sintering of metal powders: Mechanism, kinetics and microstructural features, Materials Science and Engineering: A 428(1-2) (2006) 148-158. http://doi.org/10.1016/j.msea.2006.04.117.

[11] Q.B. Nguyen, Z. Zhu, F.L. Ng, B.W. Chua, S.M.L. Nai, J. Wei, High mechanical strengths and ductility of stainless steel 304L fabricated using selective laser melting, Journal of Materials Science & Technology 35(2) (2019) 388-394. http://doi.org/10.1016/j.jmst.2018.10.013.

[12] L.-z. Wang, J.-j. Wu, D.-j. Zhang, Properties evolution of additive manufacture used tungsten powders prepared by radio frequency induction plasma, International Journal of Refractory Metals and Hard Materials 67 (2017) 90-97. http://doi.org/10.1016/j.ijrmhm.2017.05.007.

[13] Y.H. Zhou, Z.H. Zhang, Y.P. Wang, G. Liu, S.Y. Zhou, Y.L. Li, J. Shen, M. Yan, Selective laser melting of typical metallic materials: An effective process prediction model developed by energy absorption and consumption analysis, Additive Manufacturing 25 (2019) 204-217. http://doi.org/10.1016/j.addma.2018.10.046.

[14] A.M. Rubenchik, W.E. King, S.S. Wu, Scaling laws for the additive manufacturing, Journal of Materials Processing Technology 257 (2018) 234-243. http://doi.org/10.1016/j.jmatprotec.2018.02.034.

[15] B. AlMangour, D. Grzesiak, J. Cheng, Y. Ertas, Thermal behavior of the molten pool, microstructural evolution, and tribological performance during selective laser melting of TiC/316L stainless steel nanocomposites: Experimental and simulation methods, Journal of Materials Processing Technology 257 (2018) 288-301. http://doi.org/10.1016/j.jmatprotec.2018.01.028.

[16] B. Zhang, N.-E. Fenineche, H. Liao, C. Coddet, Microstructure and Magnetic Properties of Fe–Ni Alloy Fabricated by Selective Laser Melting Fe/Ni Mixed Powders, Journal of Materials Science & Technology 29(8) (2013) 757-760. http://doi.org/10.1016/j.jmst.2013.05.001.

[17] A. Piglione, B. Dovgyy, C. Liu, C.M. Gourlay, P.A. Hooper, M.S. Pham, Printability and microstructure of the CoCrFeMnNi high-entropy alloy fabricated by laser powder bed fusion, Materials Letters 224 (2018) 22-25. http://doi.org/10.1016/j.matlet.2018.04.052.

[18] Y.K. Kim, J. Choe, K.A. Lee, Selective laser melted equiatomic CoCrFeMnNi high-entropy alloy: Microstructure, anisotropic mechanical response, and multiple strengthening mechanism, Journal of Alloys and Compounds 805 (2019) 680-691. http://doi.org/10.1016/j.jallcom.2019.07.106.

Chapter 5: In-Situ Alloying of AlCoCrFeNi High Entropy Alloy via Laser Powder Bed Fusion with Pre-Heating

In the last chapter, the in-situ alloying of a representative FCC HEA, CoCrFeMnNi was demonstrated. To further explore the compositional flexibility of the current in-situ alloying approach, the CoCrFeNi & Al blended powder is adopted in this chapter to produce a BCC AlCoCrFeNi HEA. Moreover, high-temperature pre-heating is performed to restrain cracking.

Under review

Peng Chen[a, b], Sheng Li[a], Ming Yan[b], Moataz M. Attallah[a]

Additive Manufacturing Letters

[a] Advanced Materials Processing Laboratory, University of Birmingham, Birmingham B15 2TT, UK

[b] Department of Materials Science and Engineering, and Shenzhen Key Laboratory for Additive Manufacturing of High Performance Materials, Southern University of Science and Technology, Shenzhen 518055, China

Abstract

The in-situ alloying printability of body-centred-cubic (BCC) AlCoCrFeNi high entropy alloy (HEA) was assessed via laser powder bed fusion (LPBF) using a blend of pre-alloyed CoCrFeNi powder and elemental Al powder. However, despite searching a wide range of parameters and using a heated bed at 600 °C, defect-free samples could not be prepared using these approaches, indicating poor printability of the blended powder. Elemental mapping results showed the in-situ alloyed Al was heterogeneously distributed and with significant loss by evaporation. X-ray diffraction (XRD) results implied that the BCC and face-centred-cubic (FCC) phases co-existed in the as-built samples, rather than a single BCC phase of the nominal composition. Defect distribution in the as-built samples was further analysed using Micro-CT, and its forming mechanisms were discussed. It appeared that cracking occurred via solidification cracking due to the heterogeneous Al-distribution, which was inevitable in the in-situ alloyed AlCoCrFeNi HEAs. Since LPBF in-situ alloying has become an emerging technique for rapid validation of new HEAs, the printability of FCC and BCC HEAs via both pre-alloyed and in-situ alloyed powders are discussed to assist future alloy development.

Keywords: High entropy alloys; Laser powder bed fusion; In-situ alloying; AlCoCrFeNi

5.1 Introduction

High entropy alloys (HEAs) have become one of the most significant research areas during the past decade. More studies are being carried out by researchers due to the unique microstructures and superior mechanical properties of HEAs, and, more importantly, the vast space unleashed for alloy development [1-4]. An early composition-based definition of HEAs was alloy composing 5 or more principal elements with each concentration between 5 and 35 at. %, meanwhile forming single-phase solid solutions, e.g., face-centred-cubic (FCC) or body-centred-cubic (BCC) [5]. Based on their great compositional flexibility, HEAs with dual-phase structures, precipitation strengthening, and minor alloying elements have also been developed in recent years [6, 7]. In order to validate the microstructures and properties of different HEA compositions, conventional methods such as arc melting, and coating have been widely used because of their convenience of compositional modification [4]. However, the geometrical flexibility of such methods is limited when complex components are required for testing.

Laser powder bed fusion (LPBF) is an additive manufacturing technique capable of fabricating net-shape components with outstanding forming accuracy. Normally, pre-alloyed powders are used as feedstock. Recently, the in-situ alloying potential of LPBF has been explored by researchers, because the cost and time of customising pre-alloyed powders can be considerable, especially for HEAs with great compositional flexibility [8, 9]. Over the past few years, various approaches to the fabrication of HEAs via LPBF in-situ alloying have been carried out worldwide by different groups, using powder blends of either elemental powders or pre-alloyed powders and elemental powders [10-19]. Near full-dense (relative density > 99.5%) HEAs with good elemental homogeneity could be successfully achieved, including CoCrFeNi, CoCrFeMnNi, and $Al_xCoCrFeNi$, etc. However, these LPBF in-situ alloyed HEAs were mostly FCC or FCC-dominated, while successful fabrication of BCC single-phase HEAs was not reported. Cracking was found to be the major flaw that was detrimental to the printability of in-situ alloyed BCC HEAs [18, 19].

$Al_xCoCrFeNi$ is an HEA system whose phase formation can change from FCC to FCC + BCC dual-phase, then BCC as the content of Al increases from 0 to equiatomic [20]. With the use of blended elemental powders, $Al_xCoCrFeNi$ ($x = 0.3$–0.8) HEAs were in-situ fabricated via directed laser deposition (DLD), and the as-built $Al_{0.8}CoCrFeNi$ HEA possessed a BCC single phase without fatal cracking [21]. Sun et al. [14] in-situ fabricated $Al_xCoCrFeNi$ ($x = 0$–1) HEAs using LPBF, but the crack-free sample could only be produced with an FCC-dominated structure when $x = 0.5$. Although the equiatomic AlCoCrFeNi HEA can be fabricated via selective electron beam melting (SEBM) using blended powder [22], LPBF approaches using pre-alloyed powder still suggested poor printability of the BCC AlCoCrFeNi HEA. Karlsson et al. [23] claimed that it was impossible to build cracking/porosity-free samples after a wide processing window was investigated, and further suggested using a high-temperature stage to reduce thermal stress. The best relative density of as-built AlCoCrFeNi HEA fabricated by Niu et al. was also lower than 99%, implying the lack of densification [24].

The in-situ alloying approaches using pre-alloyed CoCrFeNi powder with extra elemental powders have shown their feasibility of the fabrication of near full-dense defect-free FCC HEAs [15-17]. By exploring a wide range of processing parameters, including using a heated substrate to restrain residual stress [25], this study assessed the feasibility of using a blend of pre-alloyed CoCrFeNi powder and elemental Al powder to fabricate BCC AlCoCrFeNi HEA. Densification, elemental homogenisation, and phase formation in as-built samples, were revealed. The results of this study will provide a useful guide for the design of compositions when employing LPBF in-situ alloyed for rapid validation of HEAs.

5.2 Experiment

Pre-alloyed CoCrFeNi and elemental Al spherical powders were fabricated by argon gas atomisation, with Dv 50 of 32.4 μm and 40.1 μm, respectively. 89 wt. % of the pre-alloyed CoCrFeNi powder and 11 wt. % of the elemental Al powder were weighed for a quasi-equiatomic composition, as shown in Table 5.1, and then blended for 24 h using a horizontal blending machine. The blended powder is shown in Figure 5.1.

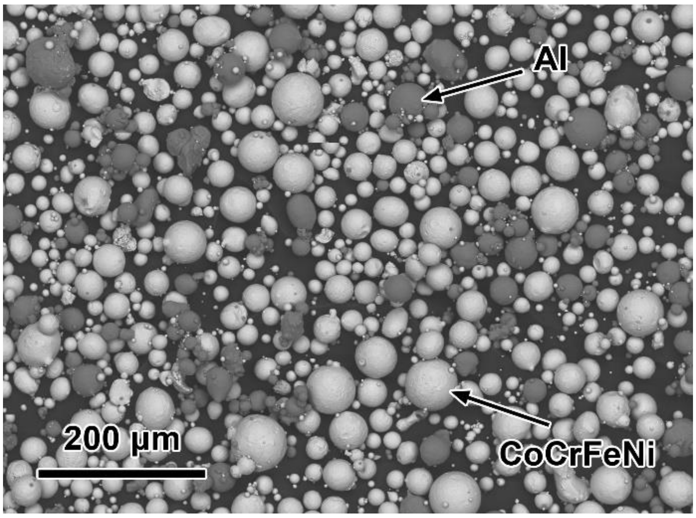

Figure 5.1 The blend of pre-alloyed CoCrFeNi powder and elemental Al powder.

Table 5.1 Chemical analysis and physical properties of the raw powders.

	Fe	Ni	Cr	Co	Al
Pre-alloyed powder (at. %)	23.7	23.3	27.6	25.4	\
Blended powder (at. %)	18.8	18.6	21.9	20.2	20.5
T_{melting} (K)	1812	1728	2180	1766	933
T_{boiling} (K)	3134	3003	2944	3200	2792
ΔH_{vap} (kJ/mol)	340	379	347	377	285
Atomic radius (pm)	126	124	128	125	143

9 mm × 9 mm × 12 mm blocks were manufactured using a Concept Laser M2 with a laser spot size of 90 µm on steel substrates. The 5 mm × 5 mm chessboard scanning strategy was applied during slicing [17]. All the LPBF experiments were carried out with argon protection controlled down to 1000-ppm oxygen content. The processing parameters, including laser power (P), scanning speed (v), hatch spacing (h), layer thickness, and pre-heating temperature (T_0), are listed in Table 5.2. Linear energy density ($LED = P/v$ [26]) and volumetric energy density ($VED = P/vht$ [17]) were used to describe the energy input of the different parameter sets. As-built samples were removed from the substrate using electrical discharge machining (EDM).

Table 5.2 Processing parameters used in this study.

Powder	P (W)	v (mm/s)	h (µm)	t (µm)	T_0 (°C)
Pre-alloyed	150–350	800–2000	30–120	30	RT
In-situ alloyed	80–300	100–2400	30–135	20–60	RT, 600

The densification of the pre-alloyed samples was assessed via ASTM B962 Archimedes method. Meanwhile, A Diondo D2 Micro-CT was used to characterise in-situ alloyed samples. A Hitachi TM 3000 desktop selective electron microscope (SEM) operated at 15 kV and equipped with a Bruker energy dispersive X-ray spectroscope (EDS) was used to analyse defects and elemental distribution in LPBFed parts. To confirm the in-situ alloying and phase formation in as-built samples, X-ray diffraction (XRD) was performed on a Bruker D2 Phaser (Co Kα). The microhardness of the samples was tested by a Struers DuraScan using the method HV 0.5 (500 gf, 10 s).

5.3 Results and Discussion

5.3.1 LPBF of the pre-alloyed CoCrFeNi

The purpose of pre-alloyed building is to determine the possible processing window of the blended powder, because the pre-alloyed powder forms the majority of the blend. Figure 5.2(a) shows the measured density of the as-built CoCrFeNi samples. The density increases to a maximum of 8.14 g/cm^3 with a *VED* of 104 J/mm^3, and then slightly decreases as the energy input increases. Pores, caused either by lack-of-fusion or keyhole, tend to occur when the *VED* is insufficient or excessive, which reduces the density of as-built parts [27]. Figure 5.2(b) provides a representative optical micrograph for the cross-section of the as-built CoCrFeNi sample with high density, showing good densification without severe cracking or porosity. Generally, the pre-alloyed CoCrFeNi powder possesses good LPBF printability that allows high-quality parts to be fabricated in a wide *VED* processing window [28]. In this study, a *VED* range from 70 to 150 J/mm^3 is determined as the optimum processing window of the pre-alloyed powder.

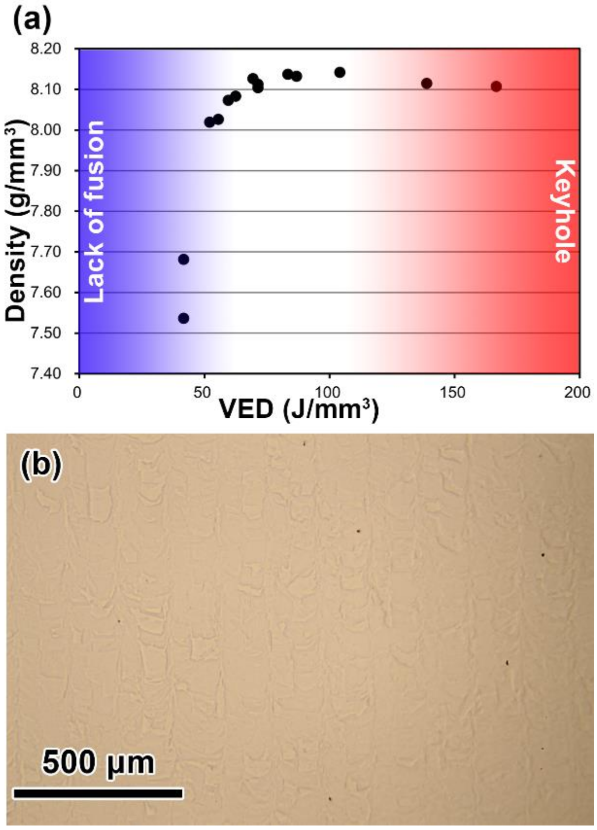

Figure 5.2 (a) Density of LPBFed CoCrFeNi HEA. (b) Optical micrograph showing the cross-section of CoCrFeNi HEA fabricated using the pre-alloyed powder.

5.3.2 LPBF of the in-situ alloyed AlCoCrFeNi

In-situ alloying experiments were carried out based on the optimised processing window of the pre-alloyed powder. However, the blended powder cannot be processed effectively with the optimum parameters for the pre-alloyed CoCrFeNi powder due to the severe delimitation which occurred in the processing. By further exploration of the processing map, bulk samples can be fabricated using a relatively low energy input (*LED* < 0.12 J/mm), as shown in Figure 5.3(a). In-situ alloyed AlCoCrFeNi samples using optimised parameters are shown in Figure 5.3(b). As indicated by the processing map, although bulks were fabricated by LPBF, cracking and porosity were inevitable. Severe delimitation can be observed at the sample surfaces, indicating poor printability of the blended powder, which is in agreement with the approach using pre-alloyed powder [23].

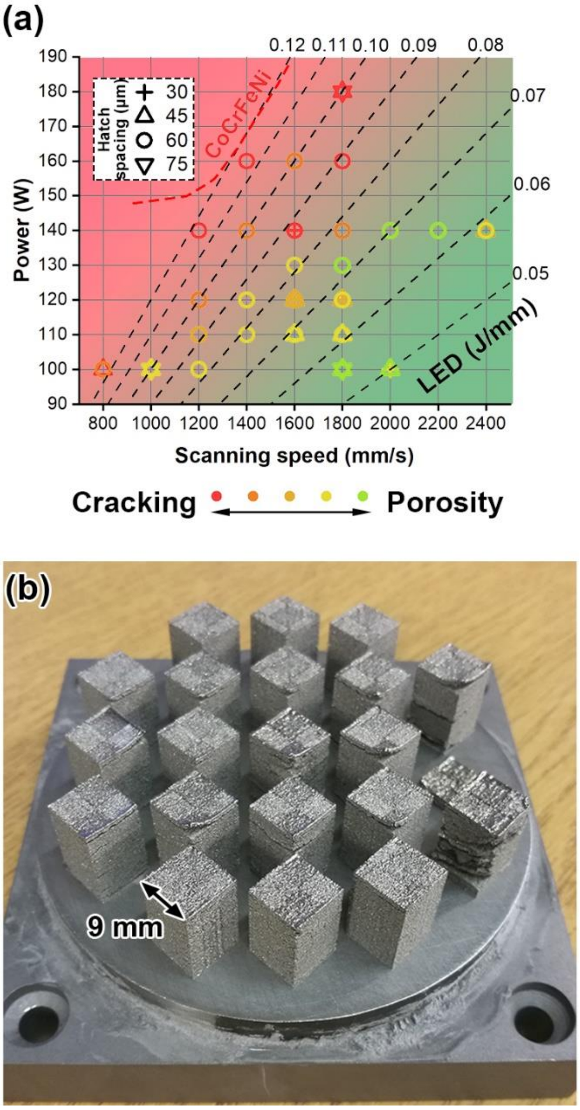

Figure 5.3 (a) Processing map of the in-situ alloyed AlCoCrFeNi HEA. The red dashed line illustrates the processing window of the pre-alloyed CoCrFeNi HEA. (b) As-built AlCoCrFeNi samples obtained using optimised parameters.

5.3.3 Phase formation of the in-situ alloyed AlCoCrFeNi

XRD was performed to confirm the phases in the pre-alloyed CoCrFeNi and in-situ alloyed AlCoCrFeNi samples, Figure 5.4. The CoCrFeNi sample possessed an FCC single phase, while the FCC + BCC dual phases were revealed in the in-situ alloyed AlCoCrFeNi samples, implying that most of the Al powder dissolved during the LPBF process. The relative intensity of the BCC phase was more significant in the sample fabricated using a higher *LED* of 0.125 J/mm. Because the high *LED* can improve the dissolution of Al [17]; meanwhile, Al is a BCC stabiliser to the Al_xCoCrFeNi HEA system [29]. The FCC-to-BCC transition was therefore promoted in the in-situ alloyed samples with the high energy input. It was also noted that a BCC single-phase structure was not obtained by in-situ alloying, despite an equiatomic nominal composition in the blended powder.

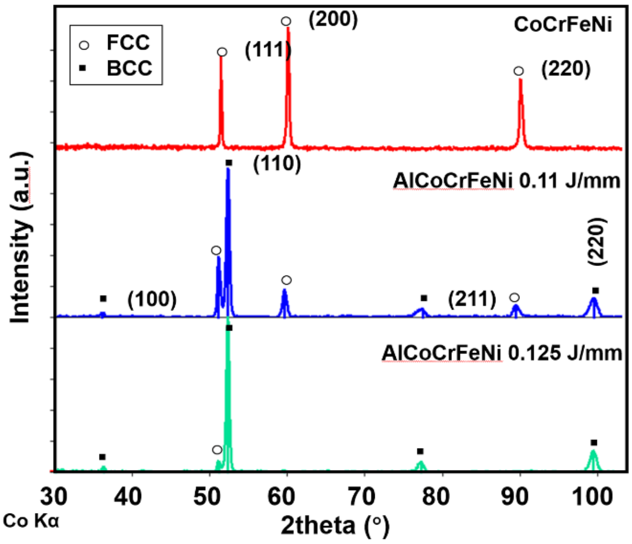

Figure 5.4 XRD spectra of CoCrFeNi and AlCoCrFeNi samples.

5.3.4 In-situ homogenisation of Al

Figure 5.5 provides EDS mapping results of the in-situ AlCoCrFeNi HEA. Although the mapping results indicate that the Al has dissolved into the HEA matrix, the Al distribution is still heterogeneous with obvious segregations. In previous in-situ alloying studies on other HEAs, the homogenisation of the alloying elements can be improved by applying excessive *LED*, e.g., 0.25 J/mm for $Al_{0.1}$CoCrFeNi [15] and 0.35 J/mm for CoCrFeMnNi [17]. Regarding the equiatomic blended powder used in this study, bulk samples can only be produced using an *LED* below 0.1 J/mm^3, while a higher *VED* would lead to failure of the parts. Consequently, the in-situ homogenisation is restrained.

Although a relatively low energy input was applied to build the bulk samples, the burning loss of Al was still significant in as-built samples. The EDS results showed that the Al content of the samples fabricated using *LED* of 0.11 and 0.125 J/mm dropped from equiatomic to 11.2 and 10.0 at. %, respectively. As given in Table 5.1, both the boiling point (T_b) and latent heat of vaporisation (ΔH_{vap}) of Al were the lowest of the five alloying elements, and its burning loss was to be expected. Burning loss was also observed in the in-situ alloying approach with a minor $Al_{0.1}$ addition [15]. Meanwhile, the sample built with the high energy input (0.125 J/mm) had a relatively lower Al content but a higher intensity of the BCC peaks (Figure 5.4), implying that the alloying Al was more effectively homogenised in the HEA matrix to induce the BCC transition, despite its relatively high burning loss.

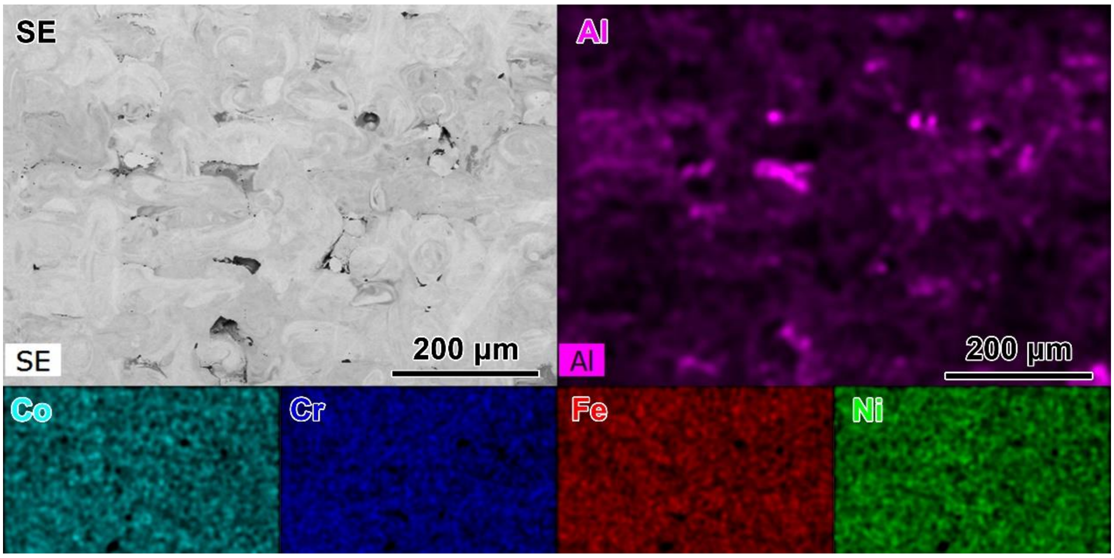

Figure 5.5 Elemental distribution of in-situ alloyed AlCoCrFeNi.

5.3.5 Microhardness of the as-built HEAs

The microhardness results of the pre-alloyed and in-situ alloyed HEAs in this study are listed in Table 5.3. The hardness of the pre-alloyed CoCrFeNi is 286 ± 15 HV, consistent with the reported values [30]. In the in-situ alloyed AlCoCrFeNi samples, the hardness results were distributed in a broad range from 270 to 568 HV, located between the FCC and BCC hardness values. With an increasing Al content, the hardness of the $Al_xCoCrFeNi$ system increased gradually as the matrix transformed from ductile FCC to brittle BCC phase [20]. The variation of hardness can thus be correlated to the heterogeneity of Al.

Table 5.3 Comparison of microhardness of LPBFed CoCrFeNi and AlCoCrFeNi HEAs.

HEA	Method	Phase	Microhardness (HV)
CoCrFeNi	LPBF pre-alloyed	FCC	286±15
CoCrFeNi [30]	LPBF pre-alloyed	FCC	238
AlCoCrFeNi	LPBF in-situ alloyed	FCC + BCC	270–568
AlCoCrFeNi [24]	LPBF pre-alloyed	BCC	633

5.3.6 Defects in the in-situ alloyed AlCoCrFeNi

As previously mentioned, defect-free samples cannot be produced using the in-situ alloyed approach. The processing map revealed a trade-off between cracking and porosity. This cracking tendency increases with energy input and leads to delimitation during the process. Furthermore, the porosity becomes more severe when the energy input is set lower in order to restrain cracking, which is likely to be assisted by the residual stresses at higher heat input conditions. SEM cross-sections showed that abundant defects existed inside the in-situ alloyed samples, either dominated by cracking (Figure 5.6(a)) or porosity (Figure 5.6(b)). The EDS mapping results in Figure 5.6(c) revealed that cracks tend to appear within the regions with Al segregation. The heterogeneity of Al can lead to severe local distortion of lattice and abundant FCC/BCC interfaces.

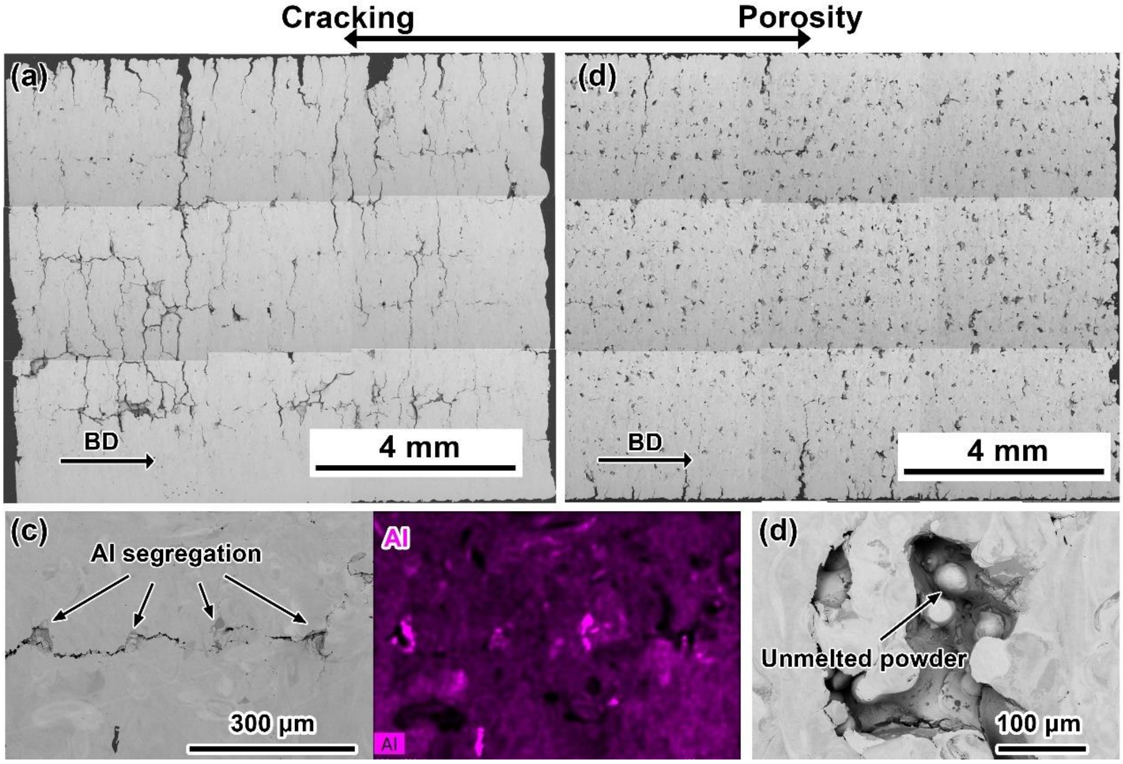

Figure 5.6 SEM vertical cross-sections of in-situ alloyed AlCoCrFeNi HEAs with (a) cracking and (b) porosity. (c) Detailed SEM image of a crack and corresponding EDS mapping result of Al. (d) SEM image showing unmelted powders in a lack-of-fusion pore.

Since the thermal history of the LPBF process consists of many cycles of rapid heating and cooling, thermal stress in such heterogeneous areas is more critical due to the expansion and contraction of lattices [23]. The phase interfaces are also likely to become sources of cracks because liquid/mushy zones can form locally with the segregation of low-melting-point Al, leading to either solidification or liquation cracking [14, 27]. The porosity in samples is dominated by lack-of-fusion pores, as shown in Figure 5.6(d), where some partially melted powder remained. The energy density used for in-situ alloying experiments was much lower than that required to fully densify the pre-alloyed CoCrFeNi powder, see Figure 5.2(a) and Figure 5.3(a). Consequently, the meltpool was insufficient to melt all the powder and to form an adequate overlap with each other [31]. Generally, a cracking-porosity trade-off was found in the in-situ alloyed approach using the current blended powder, leaving a poor processing window for defect-free samples. Therefore, further optimisation of the process and the material composition should be attempted to improve the printability of the BCC HEA.

5.3.7 Pre-heating effects on the printability of the in-situ alloyed AlCoCrFeNi

Pre-heating was employed to improve the build quality during in-situ alloying. Previous work showed that it lowered the thermal gradient to restrain thermal stress and enlarge meltpools to eliminate lack-of-fusion porosity [25, 31]. In this study, the substrate was heated at 600 °C before laser scanning, which was slightly lower than the melting point of Al (660 °C).

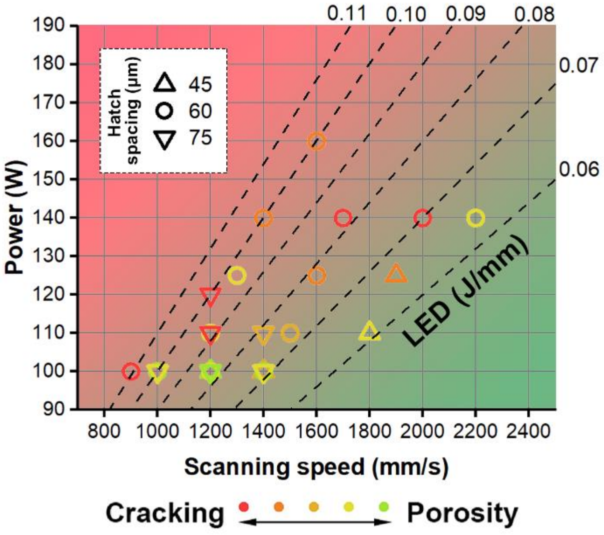

Figure 5.7 Processing map of the in-situ alloyed AlCoCrFeNi HEA pre-heated at 600 °C.

However, even when pre-heated at 600 ℃, the printability of the blended powder did not show noticeable improvement, see Figure 5.7. Defect distribution in the samples built using identical laser parameters was further analysed via Micro-CT (Figure 5.8), indicating porosity and cracking cannot be eliminated, and cracking is still the critical factor in building quality. There was even a minor drop in relative density, from 97.8% of the RT sample to 97.3% of the pre-heated sample,

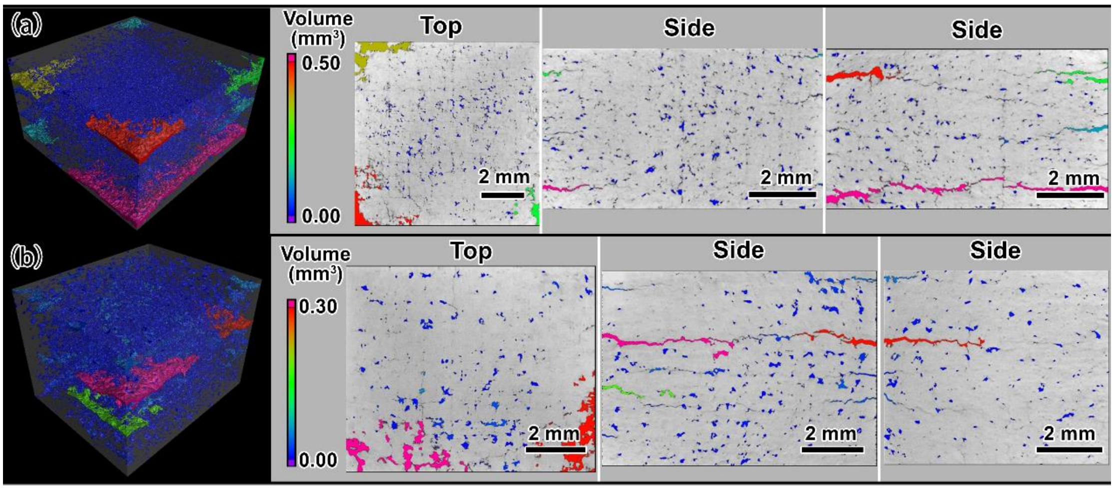

Figure 5.8 Micro-CT results showing defect distribution in AlCoCrFeNi samples fabricated on substrates at (a) RT and (b) 600 ℃.

Pre-heating is, without doubt, an effective method to reduce the thermal stresses [25]. Therefore, Therefore, solidification cracking is likely to be the primary cracking initiation in the in-situ alloyed AlCoCrFeNi samples. Furthermore, liquation/mushy zones are even more likely to occur because of the high temperature. Such cracking cannot be eliminated by further increasing the pre-heating temperature as it will not eliminate the Al segregation. DLD can provide millimetre-size meltpools to melt and homogenise elemental powders, while the cooling rate is much lower [27]. Therefore, in-situ alloying of BCC AlCoCrFeNi HEA can be achieved by DLD using elemental powders [21]. On the contrary, even with the application of pre-alloyed powder with ideal elemental homogenisation, cracking was still inevitable in the LPBF approach [23]. It is reasonable to conclude that in-situ alloying of AlCoCrFeNi HEA cannot be satisfactorily realised by LPBF.

In addition, some important indications about in-situ alloying have been raised by this study and by the results of previous research into in-situ alloying approaches. Most successful in-situ alloying approaches have been carried out on HEAs dominated by an FCC matrix [10-17]. A ductile FCC matrix can withstand the high energy input required to homogenise alloying elements, while BCC HEAs should not be recommended for LPBF in-situ alloying due to their brittle nature. Furthermore, the alloy should be carefully designed so that such liquid-phase regions can be avoided. Otherwise, solidification cracking because of elemental segregation in the liquid phase regions will occur.

5.4 Conclusions

Compared with the pre-alloyed CoCrFeNi powder, the blended Al & CoCrFeNi powder lacked LPBF printability despite pre-heating at 600 °C. Although bulk samples could be prepared by applying a low energy input, lack-of-fusion porosity and Al heterogeneity could not be eliminated with such a low energy input. Moreover, the burning loss of Al was significant. Solidification cracking along the Al segregation areas was responsible for the failure of in-situ alloying.

For future research on in-situ alloyed HEAs, the choice of FCC systems with elements possessing similar liquidation phase regions is recommended to ensure printability and elemental homogenisation.

5.5 Acknowledgements

This research is supported by Science and Technology Planning Project of Guangdong Province of China [grant number 2019B010943001], Shenzhen Science and Technology Innovation Commission [JCYJ20180504165824643], and National Natural Science Foundation of Guangdong Province [2020A1515011373]. The authors acknowledge the assistance of SUSTech Core Research Facilities.

5.6 References

[1] D.B. Miracle, O.N. Senkov, A critical review of high entropy alloys and related concepts, Acta Materialia 122 (2017) 448-511. http://doi.org/10.1016/j.actamat.2016.08.081.

[2] I. Basu, J.T.M. De Hosson, Strengthening mechanisms in high entropy alloys: Fundamental issues, Scripta Materialia 187 (2020) 148-156. http://doi.org/10.1016/j.scriptamat.2020.06.019.

[3] B. Cantor, Multicomponent high-entropy Cantor alloys, Progress in Materials Science 120 (2021) 100754. http://doi.org/10.1016/j.pmatsci.2020.100754.

[4] K. Li, W. Chen, Recent progress in high-entropy alloys for catalysts: synthesis, applications, and prospects, Materials Today Energy 20 (2021) 100638. http://doi.org/10.1016/j.mtener.2021.100638.

[5] J.W. Yeh, Recent progress in high-entropy alloys, Annales De Chimie-Science Des Materiaux 31(6) (2006) 633-648. http://doi.org/10.3166/acsm.31.633-648.

[6] Y.F. Ye, Q. Wang, J. Lu, C.T. Liu, Y. Yang, High-entropy alloy: challenges and prospects, Materials Today 19(6) (2016) 349-362. http://doi.org/10.1016/j.mattod.2015.11.026.

[7] E.P. George, D. Raabe, R.O. Ritchie, High-entropy alloys, Nature Reviews Materials 4(8) (2019) 515-534. http://doi.org/10.1038/s41578-019-0121-4.

[8] S.L. Sing, S. Huang, G.D. Goh, G.L. Goh, C.F. Tey, J.H.K. Tan, W.Y. Yeong, Emerging metallic systems for additive manufacturing: In-situ alloying and multi-metal processing in laser powder bed fusion, Progress in Materials Science 119 (2021) 100795. http://doi.org/10.1016/j.pmatsci.2021.100795.

[9] M.H. Mosallanejad, B. Niroumand, A. Aversa, A. Saboori, In-situ alloying in laser-based additive manufacturing processes: A critical review, Journal of Alloys and Compounds 872 (2021) 159567. http://doi.org/10.1016/j.jallcom.2021.159567.

[10] S. Ewald, F. Kies, S. Hermsen, M. Voshage, C. Haase, J.H. Schleifenbaum, Rapid alloy development of extremely high-alloyed metals using powder blends in laser powder bed fusion, Materials (Basel) 12(10) (2019) 1706. http://doi.org/10.3390/ma12101706.

[11] D. Lin, L. Xu, X. Li, H. Jing, G. Qin, H. Pang, F. Minami, A Si-containing FeCoCrNi high-entropy alloy with high strength and ductility synthesized in situ via selective laser melting, Additive Manufacturing 35 (2020) 101340. http://doi.org/10.1016/j.addma.2020.101340.

[12] K. Sun, W. Peng, L. Yang, L. Fang, Effect of SLM processing parameters on microstructures and mechanical properties of Al0.5CoCrFeNi high entropy alloys, Metals 10(2) (2020) 292. http://doi.org/10.3390/met10020292.

[13] Y. Hou, H. Su, H. Zhang, X. Wang, C. Wang, Fabricating homogeneous FeCoCrNi High-entropy alloys via SLM in situ alloying, Metals 11(6) (2021) 942. http://doi.org/10.3390/met11060942.

[14] Z. Sun, X. Tan, C. Wang, M. Descoins, D. Mangelinck, S.B. Tor, E.A. Jägle, S. Zaefferer, D. Raabe, Reducing hot tearing by grain boundary segregation engineering in additive manufacturing: example of an AlxCoCrFeNi high-entropy alloy, Acta Materialia 204 (2021) 116505. http://doi.org/10.1016/j.actamat.2020.116505.

[15] Y. Kuzminova, A. Shibalova, S. Evlashin, I. Shishkovsky, P. Krakhmalev, Structural effect of low Al content in the in-situ additive manufactured CrFeCoNiAlx high-entropy alloy, Materials Letters 303 (2021) 130487. http://doi.org/10.1016/j.matlet.2021.130487.

[16] J. Gao, Y. Jin, Y. Fan, D. Xu, L. Meng, C. Wang, Y. Yu, D. Zhang, F. Wang, Fabricating antibacterial CoCrCuFeNi high-entropy alloy via selective laser melting and in-situ alloying, Journal of Materials Science & Technology 102 (2022) 159-165. http://doi.org/10.1016/j.jmst.2021.07.002.

[17] P. Chen, S. Li, Y. Zhou, M. Yan, M.M. Attallah, Fabricating CoCrFeMnNi high entropy alloy via selective laser melting in-situ alloying, Journal of Materials Science & Technology 43 (2020) 40-43. http://doi.org/10.1016/j.jmst.2020.01.002.

[18] F. Huber, D. Bartels, M. Schmidt, In-situ alloy formation of a WMoTaNbV refractory metal high entropy alloy by laser powder bed fusion (PBF-LB/M), Materials (Basel) 14(11) (2021) 3095. http://doi.org/10.3390/ma14113095.

[19] S. Luo, C. Zhao, H. Yang, Q. Liu, Z. Wang, X. Zeng, Selective laser melting of dual phase AlCrCuFeNix high entropy alloys: formability, heterogeneous microstructures and deformation mechanisms, Additive Manufacturing 31 (2019) 100925. http://doi.org/10.1016/j.addma.2019.100925.

[20] Y.-F. Kao, T.-J. Chen, S.-K. Chen, J.-W. Yeh, Microstructure and mechanical property of as-cast, -homogenized, and -deformed AlxCoCrFeNi (0≤x≤2) high-entropy alloys, Journal of Alloys and Compounds 488(1) (2009) 57-64. http://doi.org/10.1016/j.jallcom.2009.08.090.

[21] J. Joseph, T. Jarvis, X. Wu, N. Stanford, P. Hodgson, D.M. Fabijanic, Comparative study of the microstructures and mechanical properties of direct laser fabricated and arc-melted AlxCoCrFeNi high entropy alloys, Materials Science and Engineering: A 633 (2015) 184-193. http://doi.org/10.1016/j.msea.2015.02.072.

[22] H. Shiratori, T. Fujieda, K. Yamanaka, Y. Koizumi, K. Kuwabara, T. Kato, A. Chiba, Relationship between the microstructure and mechanical properties of an equiatomic AlCoCrFeNi high-entropy alloy fabricated by selective electron beam melting, Materials Science and Engineering: A 656 (2016) 39-46. http://doi.org/10.1016/j.msea.2016.01.019.

[23] D. Karlsson, A. Marshal, F. Johansson, M. Schuisky, M. Sahlberg, J.M. Schneider, U. Jansson, Elemental segregation in an AlCoCrFeNi high-entropy alloy – A comparison between selective laser melting and induction melting, Journal of Alloys and Compounds 784 (2019) 195-203. http://doi.org/10.1016/j.jallcom.2018.12.267.

[24] P.D. Niu, R.D. Li, T.C. Yuan, S.Y. Zhu, C. Chen, M.B. Wang, L. Huang, Microstructures and properties of an equimolar AlCoCrFeNi high entropy alloy printed by selective laser melting, Intermetallics 104 (2019) 24-32. http://doi.org/10.1016/j.intermet.2018.10.018.

[25] S.Z. Uddin, L.E. Murr, C.A. Terrazas, P. Morton, D.A. Roberson, R.B. Wicker, Processing and characterization of crack-free aluminum 6061 using high-temperature heating in laser powder bed fusion additive manufacturing, Additive Manufacturing 22 (2018) 405-415. http://doi.org/10.1016/j.addma.2018.05.047.

[26] H. Gu, H. Gong, D. Pal, K. Rafi, T. Starr, B. Stucker, Influences of energy density on porosity and microstructure of selective laser melted 17-4PH stainless steel, 24th International SFF Symposium - An Additive Manufacturing Conference, SFF 2013, 2013, pp. 474-489.

[27] T. DebRoy, H.L. Wei, J.S. Zuback, T. Mukherjee, J.W. Elmer, J.O. Milewski, A.M. Beese, A. Wilson-Heid, A. De, W. Zhang, Additive manufacturing of metallic components – Process, structure and properties, Progress in Materials Science 92 (2018) 112-224. http://doi.org/10.1016/j.pmatsci.2017.10.001.

[28] R. Zhou, Y. Liu, C. Zhou, S. Li, W. Wu, M. Song, B. Liu, X. Liang, P.K. Liaw, Microstructures and mechanical properties of C-containing FeCoCrNi high-entropy alloy fabricated by selective laser melting, Intermetallics 94 (2018) 165-171. http://doi.org/10.1016/j.intermet.2018.01.002.

[29] H.P. Chou, Y.S. Chang, S.K. Chen, J.W. Yeh, Microstructure, thermophysical and electrical properties in AlxCoCrFeNi (0≤x≤2) high-entropy alloys, Materials Science and Engineering: B 163(3) (2009) 184-189. http://doi.org/10.1016/j.mseb.2009.05.024.

[30] Y. Brif, M. Thomas, I. Todd, The use of high-entropy alloys in additive manufacturing, Scripta Materialia 99 (2015) 93-96. http://doi.org/10.1016/j.scriptamat.2014.11.037.

[31] M. Tang, P.C. Pistorius, J.L. Beuth, Prediction of lack-of-fusion porosity for powder bed fusion, Additive Manufacturing 14 (2017) 39-48. http://doi.org/10.1016/j.addma.2016.12.001.

Chapter 6: In-Situ Alloyed, Oxide-Dispersion-Strengthened CoCrFeMnNi High Entropy Alloy Fabricated via Laser Powder Bed Fusion

After the processing development of blended powders in Chapters 4 & 5, this chapter investigates the mechanical properties of high-quality CoCrFeMnNi samples, and the microstructural evolution during deformation. The strengthening effect produced by in-situ formed oxide particles is highlighted.

Published article

Peng Chen[a, b], Chao Yang[c], Sheng Li[b], Moataz M. Attallah[b], Ming Yan[a]

Materials & Design, 194 (2020) 108966.

[a] Department of Materials Science and Engineering, Southern University of Science and Technology, Shenzhen 518055, China

[b] School of Metallurgy and Materials, University of Birmingham, Birmingham B15 2TT, UK

[c] School of Mechanical and Automotive Engineering, South China University of Technology, Guangzhou 510641, China

Abstract

By using a blend of pre-alloyed CoCrFeNi powder and elemental Mn powder, quasi equiatomic CoCrFeMnNi high entropy alloy (HEA) has been in-situ alloyed via laser powder bed fusion (LPBF). Besides being homogeneously dissolved into the HEA matrix, Mn also forms oxide particles with oxygen originating from both powder feedstock and printing atmosphere, resulting in an in-situ alloyed, oxide-dispersion-strengthened (ODS) HEA. The tensile strength of the ODS HEA is significantly improved to a yield strength of 620 MPa and tensile strength of 730 MPa. The tensile ductility of the ODS HEA is lower than the ones prepared by using fully pre-alloyed powders, but an outstanding compression ductility maintains for the ODS HEA. The deforming behaviour of the alloy has been revealed, and the contribution of Orowan strengthening has been quantified along with other mechanisms. The study provides an approach to developing advanced HEAs with high strength and moderate ductility by LPBF.

Keywords: High entropy alloys; Powder bed fusion; Additive manufacturing; Deformation behaviour; Orowan strengthening

6.1 Introduction

The discovery of high entropy alloys (HEAs) is one of the most significant developments in the field of metallic materials. The concept of HEA allows researchers to choose multi-principal elements in one HEA system, each concentration between 5 and 35 at. %, which composition locates at the normally unexplored central area of a phase diagram [1-3]. At the initial stage of the alloy development, HEAs are requested to form single-phase solid solutions with five or more principal elements at an equiatomic ratio [4]. The definition of HEAs has evolved with time. For instances, dual-phase solid solution HEAs like $Al_xCoCrFeNi$ are accepted, whose microstructure gradually transforms from ductile face-centred-cubic (FCC) phase to brittle body-centred-cubic (BCC) phase as the content of Al increases; precipitation-strengthened HEAs such as FCC-CoCrFeNi reinforced by $L1_2$-Ni_3(Ti, Al) also emerge [5-7]. The great compositional flexibility endows HEAs with the possibility to cover most property maps of knowing alloy systems and even extend to those previously unattainable areas.

HEAs have shown application potential due to their outstanding properties. Conventionally, HEAs are mostly fabricated by arc melting or coating methods to avoid segregation during solidification [3]. But the products fabricated via those techniques can hardly accomplish the requirements of various applications [8]. Manufacturing of HEA parts with chemistry homogeneity, geometry flexibility and excellent mechanical properties is still in the beginning stage.

Laser powder bed fusion (LPBF), also known as selective laser melting (SLM), is a laser-based additive manufacturing (AM) technique that has been widely employed to fabricate metallic parts with complex geometry for many important industries [9, 10]. As for HEAs, single-phase FCC HEAs such as CoCrFeNi, CoCrFeMnNi, and $Al_{0.5}$FeCoCrNi possess good LPBF printability, when using pre-alloyed powder [11-13]. Heterogeneous pre-alloyed HEA powders have also been developed for LPBF, e.g., CoCrFeNiTi-based HEA, AlCrCuFeNi$_x$ and C-containing CoCrFeNi HEAs [14-18]. Shortcomings of the pre-alloyed powder approach include that the compositional flexibility is restricted, and the production circle can be quite time-consuming. Directed laser deposition (DLD) is another laser-based AM technique, which can deliver different elemental powders simultaneously and melt them in a large molten pool to achieve in-situ alloying. Al$_x$CoCrFeNi HEA has been in-situ alloyed by DLD, and all the compositional elements can be dissolved and homogenised [19]. In this way, the composition of HEAs can be more flexible than using pre-alloyed powder, yet the forming accuracy of DLD is much lower than that of LPBF, which means that considerable secondary processing is inevitable to produce a qualified part via DLD in-situ alloying.

To produce HEA parts with both complex geometry and compositional flexibility by AM, a potential solution is the in-situ alloying by LPBF using blended powder rather than pre-alloyed powder. In previous studies, LPBF in-situ alloying has shown its feasibility of introducing a minor amount of elemental powder into conventional alloy systems, e.g., 2 at. % of elemental Al powder has been in-situ alloyed with pre-alloyed In718 powder to precipitate more sigma phase and enhance the mechanical properties; Ti2AlNb has also been in-situ alloyed from a blend of elemental powders [20, 21]. However, the small molten pool in the LPBF process encounters problems like segregation of the introduced element and the high cracking tendency due to the generation of secondary phases, when the amount of elemental powder increases to a higher level [22]. In this regard, the feasibility of in-situ fabricating HEAs using blended elemental powders via LPBF needs to be further testified.

Based on this consideration, a CoCrFeMnNi HEA has been in-situ alloyed from a blend of pre-alloyed CoCrFeNi powder and elemental Mn powder in our previous research as a pilot study [23]. It shows that the HEA matrix can maintain an FCC structure as the content of dissolved Mn is up to 20 at. %, which is considerably compositional feasibility achieved via the LPBF in-situ alloying. Aside from good densification and homogeneity, the in-situ alloyed HEA has also shown improved microhardness and oxygen content. More interestingly, a much-enhanced strength has been discovered in the in-situ alloyed HEA, the detailed mechanism for which needs to be clarified. In this study, the structure-property correlation of the in-situ alloyed HEA is thoroughly analysed. Mn oxide particles are found dispersed extensively in the HEA matrix, resulting in an oxide-dispersion-strengthened (ODS) HEA. Although ODS HEAs have been produced using spark plasma sintering (SPS) via adding yttria or alumina particles to HEA powder [24, 25], ODS HEAs fabricated using in-situ AM techniques have rarely been reported [26, 27]. Hence, this study investigates the oxides formation mechanism of the in-situ alloyed HEA, which is essential for offering a time and cost-efficient LPBF route to fabricate advanced ODS parts with excellent mechanical properties, particularly in terms of strength.

6.2 Material and Methods

6.2.1 Powder and LPBF process

A powder blend of pre-alloyed CoCrFeNi powder (TLS Technik GmbH) and elemental Mn powder (Sigma-Aldrich) was used as raw material to fabricate the in-situ alloyed CoCrFeMnNi HEA. The two powders were weighed to ensure quasi-equiatomic composition (Table 6.1), and then mixed by a horizontal mixing machine for 12 h to pre-homogenise before the LPBF process (Figure 6.1(a)). The original atomic percentage of Mn was higher than the nominal 20 at. %, since the selective evaporation of Mn was expected during printing, and the extra amount of Mn may help to compensate for the elemental loss. A Concept Laser M2 was employed to fabricate bulk HEA parts from the blended powder. All the samples were fabricated on 316L stainless steel substrates with argon protection. A schematic of the scanning strategy used in this study is shown in Figure 6.1(b). Each layer was separated into chessboard patterns composed of 5 mm × 5 mm blocks, with internal scanning routes normal to those in neighbouring blocks. Every block rotated 90 ° and shifted 1 mm along both x and y-axes in the following layer. The scanning patterns are revealed in Figure 6.1(c). The y-axis was marked as the gauge length of tensile specimens as well. The layer thickness (*t*) was 30 µm for the blended powder. An optimised laser parameter set, including laser power (*P*) of 280 W, scanning speed (*v*) of 800 mm/s, and hatch spacing (*h*) of 60 µm, was applied in the LPBF process, achieving a high relative density [23]. The volumetric energy density (*VED*) applied in the LPBF process was calculated by $VED = P/(vht)$ [23].

Table 6.1 Chemistry of the blended powder and as-built sample in this study.

		Co	Cr	Fe	Ni	Mn
Blended powder	wt. %	79 (pre-alloyed)				21 (elemental)
	at. %	19.93	21.64	18.59	18.31	21.53
As-built HEA (at. %)		21.59	21.88	20.14	19.72	16.67

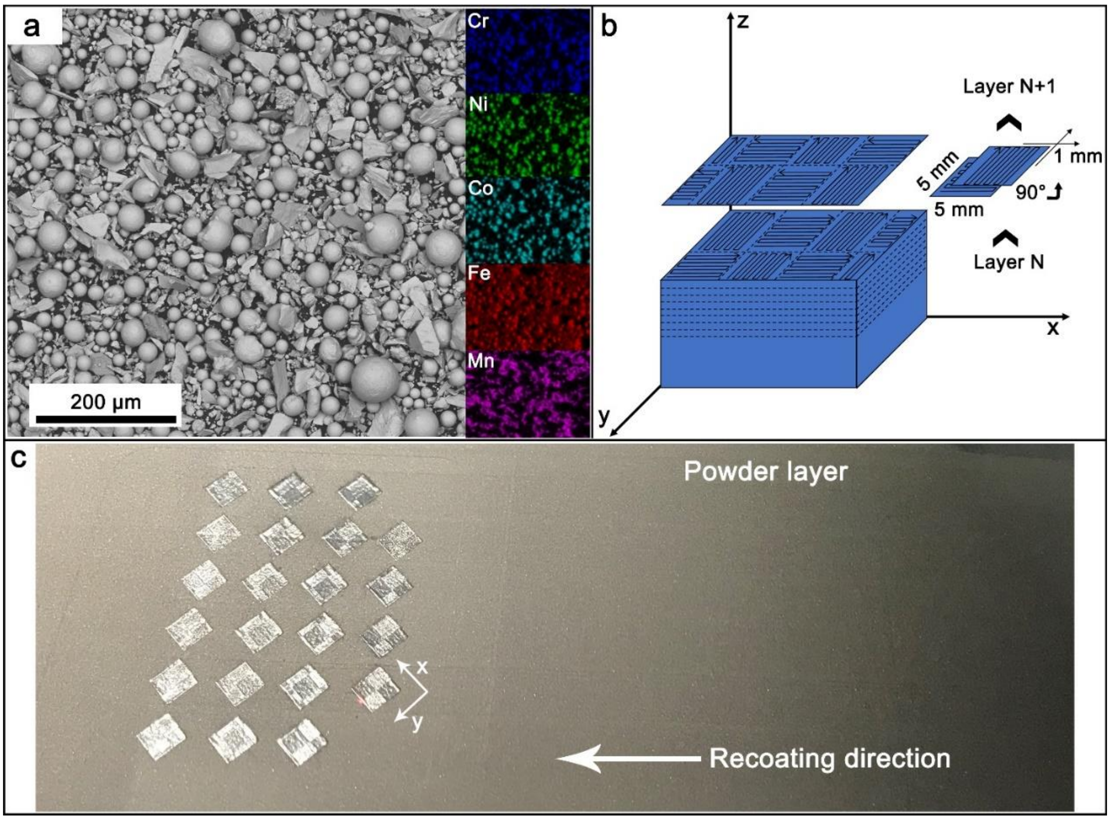

Figure 6.1 (a) An SEM image of the blended powder including spherical pre-alloyed powder and irregular-shaped elemental Mn powder, with EDS mapping results of elemental distribution which is similar to the powder layer before scanning. (b) A Schematic of the chessboard scanning strategy and (c) a layer scanned by laser in the LPBF process.

6.2.2 Microstructural characterisation

Phase formation of the blended powder and LPBFed samples was characterised by X-ray diffraction (XRD) on a Rigaku Smartlab with Cu radiation. To reveal the microstructure of the in-situ alloyed HEA, samples were grounded and then finished by a Buehler VibroMet 2 Vibratory Polisher. A Zeiss Merlin field emission scanning electron microscope (SEM) equipped with electron back-scattered diffraction (EBSD) and back-scattered electron (BSE) detectors was employed to reveal the microstructure. Electron channelling contrast imaging (ECCI) was also performed through the BSE detector operated at 30 kV, and the sample holder tilted between 2 and 5 °. Samples for transmission electron microscopy (TEM) were prepared via focused ion beam (FIB) using an FEI Helios Nanolab 600i, and then analysed by an FEI Talos F200X equipped with an energy dispersive spectrometer (EDS). The surface of the elemental Mn powder was characterised by X-ray photoelectron spectroscopy (XPS) via a PHI 5000 Versaprobe III. A LECO ON736 elemental analyser was employed to measure the oxygen content.

6.2.3 Mechanical testing

Tensile parts were fabricated according to the model illustrated in Figure 6.2(a), and then separated into tensile specimens with gauge dimensions of 25 mm × 4.3 mm × 2 mm by electrical discharge machining (EDM). Tensile tests were carried out on an Instron 3382 universal testing machine with an extensometer and controlled at a strain rate of 10^{-3}/s. For compression tests, cylinder specimens with a diameter of 6 mm and a height of 9 mm were produced by EDM from bulk samples. The compression tests were operated at a strain rate of 10^{-3}/s without an extensometer.

6.3 Results

6.3.1 Mechanical properties of the in-situ alloyed HEA

A representative tensile curve of the in-situ alloyed HEA is plotted in Figure 6.2(a). Details of the tensile properties are listed in Table 6.2, which is compared with results from using pre-alloyed powder to print the CoCrFeMnNi HEA. In comparison, the strength of the in-situ alloyed HEA is significantly improved, but the fracture elongation (ε_f) drops to ~12%, which seems to be a strength-ductility trade-off. The work hardening rate and true stress-strain curves are illustrated in Figure 6.2(b). It is recognised that the work hardening rate drops dramatically after the yield point. In contrast, the work hardening effect is considerable in CoCrFeMnNi HEAs fabricated using DLD, casting or forging [28-30]. Both the strain-hardening ability and ductility of the CoCrFeMnNi HEA are mainly attributed to the planar dislocation slip of the HEA matrix [28, 31]. The lack of tensile ductility and work hardening effect in this alloy will be discussed in detail later.

On the other hand, the in-situ alloyed sample performs outstandingly in compression ductility, which origins from the ductile nature of the CoCrFeMnNi HEA. A compression curve is partially provided in Figure 6.2(c), as the tested sample did not fail during the test even though the true strain exceeded 100%.

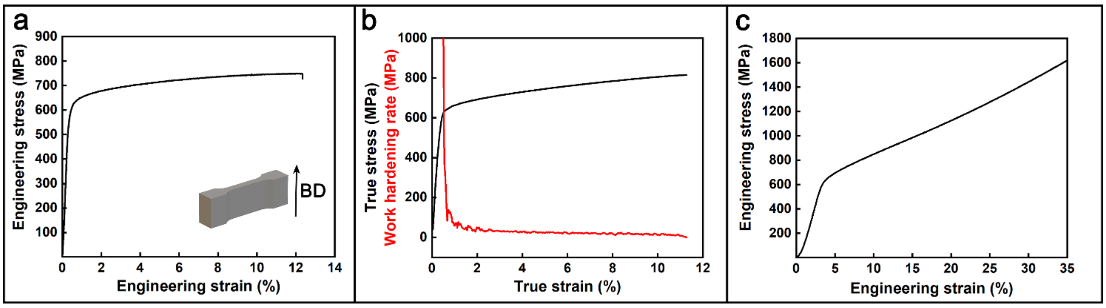

Figure 6.2 (a) The tensile curve of the in-situ alloyed HEA, with an embedded demonstration of the tensile model used for the LPBF process. (b) The true stress-strain curve specimen and work hardening rate curve of the tensile specimen. (c) A partial compression curve of the in-situ alloyed HEA.

Table 6.2 Comparison of tensile properties between CoCrFeMnNi HEAs fabricated using blended powder and pre-alloyed powder.

CoCrFeMnNi	*VED* (J/mm^3)	$\sigma_{0.2}$ (MPa)	σ_{uts} (MPa)	ε_f (%)	d (μm)
In-situ alloyed	194	624 ± 4	747 ± 2	12.3 ± 0.2	42.9
Z. Zhu [32]	60	510 ± 10	609 ± 10	34 ± 3	12.9
R. Liu [12]	123	519	601	34	/

6.3.2 Microstructure and deformational behaviour

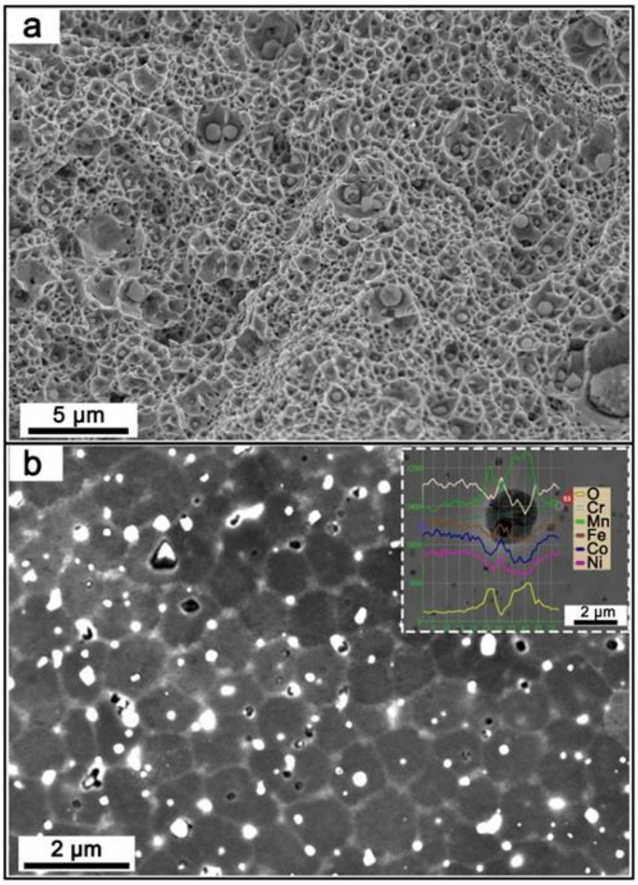

Figure 6.3 (a) The SEM fracture surface of a tensile specimen. (b) BSE-ECCI image of as-built HEA revealing bright oxide particles and cellular structure, embedded with an EDS line scanning of an oxide particle.

The SEM fractography of a tensile specimen is provided in Figure 6.3(a). Besides typical micro-dimples similar to other CoCrFeMnNi HEAs fabricated via LPBF, plenty of microparticles can be observed inside those dimples, which is abnormal for this material [12, 32]. The extensive occurrence of microparticles might be responsible for the premature failure of the material during tensile testing. In Figure 6.3(b), a BSE image with inverse contrast also reveals the distribution of secondary particles in the HEA substrate, as well as a cellular structure that is typical in the LPBFed HEA. The EDS line scan results indicate that the concentration of Mn and O is evidently higher in the particle compared with other alloying elements. The volumetric fraction of the particles should be small. Otherwise, the corresponding XRD spectrum (Figure 6.4) should have shown its presence rather than the currently revealed single FCC phase. ImageJ analysis suggests the volumetric fraction of the oxide particles is around 7%.

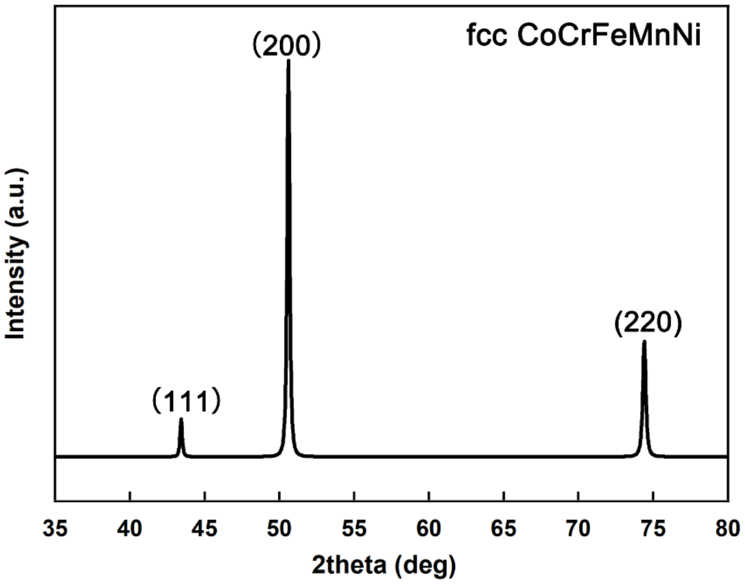

Figure 6.4 The XRD spectrum of the in-situ alloyed CoCrFeMnNi HEA, showing a single-phase FCC structure.

TEM has been employed to further identify these particles. Figure 6.5(a) and Figure 6.3 reveal a homogeneous distribution of near-spherical particles, with an average size of ~100 nm. Irregularly shaped particles of a few micrometres in size were occasionally observed as well. Since the elemental Mn powder has a much larger Dv10 of ~7 µm, these particles were in-situ formed during the LPBF process, rather than being from the original powder. To investigate the crystal structure, selected area electron diffraction (SAED) was conducted on the spherical particles. SAED patterns and EDS mapping results of a particle-containing area are shown in Figure 6.5(b). The FCC HEA matrix contains homogeneous distributions of all the alloying elements including Mn. The particles were rich in Mn and oxygen as expected. The electron diffraction information indicated the particle was Mn_2O_3 phase. Such phase has also been found in an LPBFed CoCrFeMnNi HEA fabricated using pre-alloyed powder [33]. The distribution of the ceramic Mn_2O_3 material in the current alloy is, however, extensive, which should have influenced the deforming behaviour and mechanical properties dramatically.

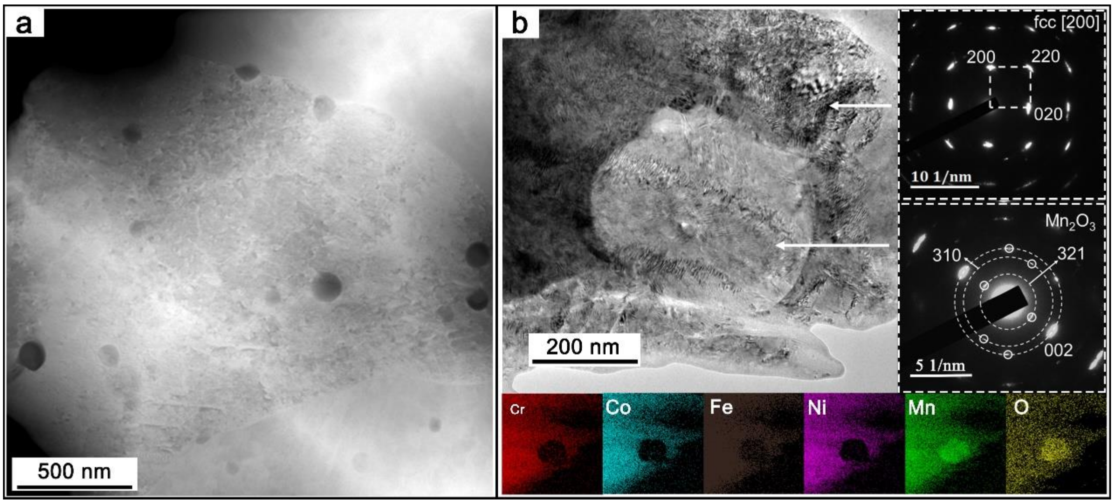

Figure 6.5 (a) A scanning transmission electron microscopy (STEM) image showing the distribution of particles in the HEA, and (b) TEM EDS mapping results with embedded SAED patterns of the HEA matrix and a particle.

In order to investigate the influence of oxide particles on deformation behaviours, the microstructures of the samples in the as-built and deformed states were characterised. The inverse pole figure (IPF) maps of cross-sections normal to the building direction (z-axis) are shown in Figures 6.6(a, e). Most of the coarse grains align along x and y-axes, which are scanning directions. Meanwhile, finer grains fill in gaps between the array of coarse grains. This characteristic grain geometry in the xy-planes is a consequence of the scanning route and can vary according to scanning strategies. In comparison, there is no obvious change in grain geometry after tensile deformation, and mechanical twins have not been found. Although the twinning effect is considered responsible for both the deformability and work hardening tendency in the CoCrFeMnNi HEA, the initiation of twins normally requires a high strain rate as well as cryogenic temperature [28, 30]. As for the CoCrFeMnNi HEA fabricated via LPBF, the occurrence of nano-twins has been observed in samples with tensile strain higher than 20% [12]. It is deduced that twins have not occurred in this study because the failure happens within 15% strain. By comparing kernel average misorientation (KAM) maps before and after deformation, the accumulation of misorientations occurs not only at the grain boundaries but also around oxide particles, as shown in the embedded pictures (Figures 6.6(b, f)), hence the in-situ alloyed HEA can be strengthened by the extra dislocations. Pole Figures (PFs) are provided in Figures 6.6(c, g). The <001> orientation, which is the preferred growth direction of the FCC HEA along the heat gradient, gathers at either the building direction or the scanning directions, indicating the heat gradient is affected by scanning strategy as well [34]. After tensile deformation in the y-direction, the distortion of grain is also reflected as stretches along the y-axis. Besides that, the <001> texture is weaker due to the distortion according to the IPFs in Figures 6.6(d, h).

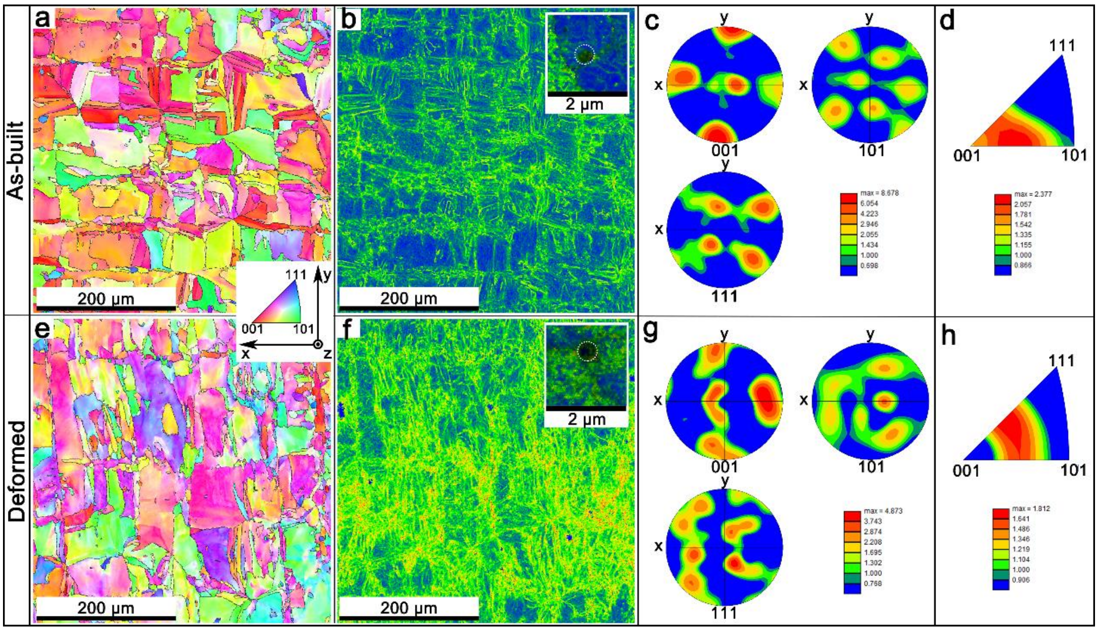

Figure 6.6 (a, e) IPF maps, (b, f) KAM maps with embedded pictures showing areas around oxide particles, (c, g) PFs, and (d, h) IPFs of as-built and deformed HEA samples.

As the deformational behaviour of the in-situ alloyed HEA is most likely related to the oxide particles, the morphology of the oxide particles and dislocations are revealed by ECCI. In the as-built status (Figure 6.7(a)), oxide particles are mostly round and rarely surrounded by massive dislocations. After deformation (Figure 6.7(b)), besides the occurrence of slip bands, dislocations have grown obviously inside grains, especially in areas around oxide particles. Several oxide particles are pointed out in the deformed sample by arrows. These particles locate inside slip bands, and their contour profile has been stretched along the slip direction, therefore transforming into spindle shapes.

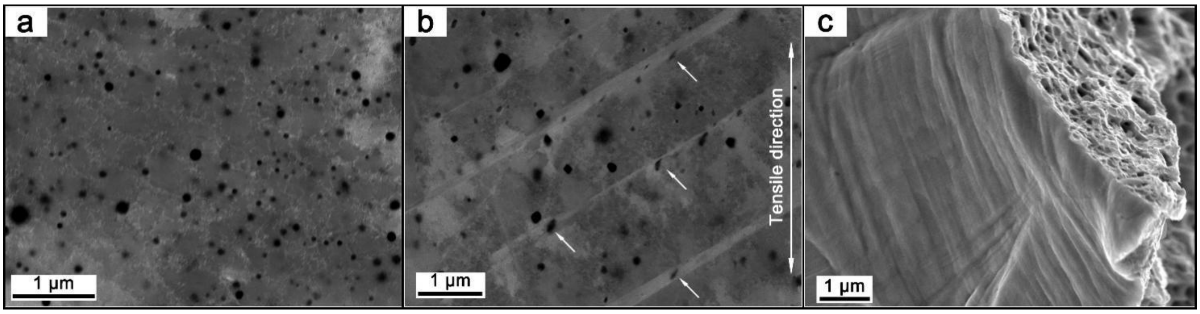

Figure 6.7 The distribution of dislocations and oxide particles are revealed in ECCI images of (a) the as-built HEA, and (b) a tested tensile specimen. (c) An SEM image of the slide lines in the fracture surface.

TEM has been performed to investigate the transformation in these regions. Figure 6.8(a) shows an oxide particle crossed by a slip band. Two gaps are observed on symmetrical sides of the particles. Meanwhile, they are also located on opposite sides of the slip band. Figure 6.8(b) shows a spindle structure consisting of an oxide particle and two enlarged triangular spacings, which corresponds to those spindle areas observed in the ECCI image at the lower magnification. The SAED patterns embedded in Figure 6.8(c) show that there are MnO particles in the matrix other than Mn_2O_3.

Although TEM images were not taken in in-situ tensile tests, the deformation behaviour can still be deduced that when the HEA matrix moves towards opposite directions as arrows marked in Figures 6.8(a, b), gaps occur due to the weak bonding and difference in stiffness between oxide particles and the HEA matrix [35]. As the displacement increases, they gradually grow into larger voids and lead to the failure of the material. There have been reports on LPBFed CoCrFeMnNi HEAs strengthened via introducing secondary phases particles such as TiN and carbide, but the dynamic interaction between the particles and the matrix remains absent [14, 36]. The abundance of oxide particles in the in-situ alloyed HEA creates a much higher density of sub-micron voids that result in early fracture during the tensile deformation, which also explains those oxide particles present in dimples. On the other hand, dispersed oxide particles hinder the plastic deformation, reinforcing the in-situ alloyed HEA and making it a kind of oxide-dispersion-strengthened (ODS) HEA.

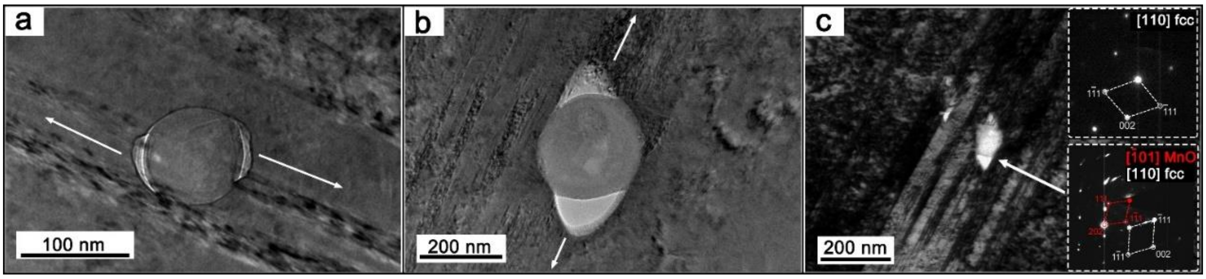

Figure 6.8 (a, b) TEM bright-field images of oxide particles and micro-voids formed around them after deformation. (c) A TEM dark-field image with SAED patterns of the HEA matrix and an oxide particle.

6.4 Discussion

Along with the results of a previous study [23], the above experimental results demonstrate that as long as an appropriate powder mixing procedure and optimised printing parameters are adopted, a crack-free CoCrFeMnNi HEA with compositional homogeneity can be realised by the powder-mixture and then laser in-situ alloying approach, and by using Mn as a secondary powder to add into the quaternary, pre-alloyed CoCrFeNi HEA powder. It is important to add that cracks may still form if the heat input parameters are too excessive, leading to solidification cracking or cracking due to residual stresses. Still, the process parameters need to be optimised to ensure achieving chemical homogeneity during in-situ alloying with Mn-doping.

A few important phenomena involved in the approach, however, need to be clarified, which are discussed as follows.

6.4.1 Strengthening mechanism

For the CoCrFeMnNi HEA fabricated via LPBF, grain boundary strengthening and dislocation strengthening (σ_{dis}) are considered as the two major strengthening mechanisms. The deformation behaviours observed in this study indicate the oxide particles act as strong obstacles despite their difference in size (see Figures 6.7 & 8), which is non-shearable for dislocations [14, 37]. The Orowan strengthening (σ_O) is therefore also applied to understand the mechanical performance of the in-situ alloyed HEA. The overall estimated yield strength can be expressed as follows:

$$\sigma_y=\sigma_{HP}+\sigma_{dis}+\sigma_O \tag{6.1}$$

The term σ_{HP} summarises the grain boundary strengthening by the Hall-Petch relationship [28]:

$$\sigma_{HP}=\sigma_0+kd^{-1/2} \tag{6.2}$$

where σ_0 is the friction stress, k is the Hall-Petch coefficient and d is the grain size which is 42.9 µm in this study. Based on the σ_0 of 194 MPa and k of 490 MPa/µm$^{1/2,}$ which are typically applied to the CoCrFeMnNi HEA [38], σ_{HP} is calculated to be ~269 MPa.

The term dislocation strengthening is expressed as follows [32]:

$$\sigma_{dis}=\alpha MGb\sqrt{\rho_{dis}} \tag{6.3}$$

where α is a constant. M, G and b denote the Taylor factor (3.06 for FCC HEA), the shear modulus (80 GPa [39]), and the Burgers vector (0.255 nm [30]), respectively. In the CoCrFeMnNi HEA fabricated via LPBF, most of the dislocations are stored in the cellular walls of the sub-grain structure (Figure 6.3(a)). Therefore, the dislocation density (ρ_{dis}) can be estimated according to the correlation below [40]:

$$\sqrt{\rho_{dis}}=c/\lambda \tag{6.4}$$

where λ stands for the cell size 0.89 µm in this study. c is a constant as well as the α, and their product is near one [40]. In addition, the contribution of dislocation strengthening is calculated to be ~70 MPa in the in-situ alloyed HEA.

The Orowan strengthening is an untypical strengthening mechanism for the single-phase CoCrFeMnNi HEA. Although nano-precipitates have been observed in some LPBFed HEAs, their reinforcement to the strength is negligible due to their low volumetric fraction. In the in-situ alloyed HEA, the Orowan strengthening is considerable because those oxide particles are widely dispersed into the HEA matrix, and its impact can be further expressed as follows [33]:

$$\sigma_O=\frac{0.4M}{\pi\sqrt{1-v_P}}\frac{Gb}{L}\ln\left(\sqrt{\frac{2}{3}}d_o/b\right) \tag{6.5}$$

where v_P denotes the Poisson's ratio (0.26 [14]). L and d_o represent the inter-particle spacing and mean particle diameter of oxide particles. L can be calculated via the equation shown below:

$$L=\sqrt{\frac{2}{3}}d_o\sqrt{\frac{\pi}{4f}-1} \tag{6.6}$$

where f is the volumetric fraction of oxide particles.

In this study, the d_o (87 nm) and f (0.068) are measured via particle counting on cross-sections (ImageJ). By using Eq. 6.5 and Eq. 6.6, the estimated strengthening contribution from the Orowan strengthening is ~263 MPa. In addition, the theoretical yield strength calculated from Eq. 6.1 is ~602 MPa, which is close to the experimental result (624 MPa). Because high volumetric energy density has been employed to homogenise the Mn distribution (Table 6.2, [23]), microstructures (grain size and cell size) are coarsened by the extra energy input, while coarse microstructures could lead to a reduction in grain boundary strengthening and dislocation strengthening. Figure 6.9(a) illustrates that the in-situ alloyed HEA still has an advantage over those fabricated using pre-alloy powder due to the considerable Orowan strengthening (~44% of contributions to the strength), where the contributions from all the three mechanisms are summarised in Figure 6.9(b). On the other hand, embrittlement due to the oxides is also noticeable in the study that employs SPS to fabricate ODS CoCrFeMnNi HEA. A similar mechanism has been observed in the LPBFed stainless steel that was fabricated using a blend of pre-alloyed powder and Y_2O_3 powder; the appearance of micro-voids causes a sudden drop in strain-hardening rate and limits the elongation of the material [35]. Nevertheless, Figure 6.9(a) indicates that the presently developed material has a combination of high yield strength and moderate tensile elongation, compared with the same material but produced by different approaches. The current in-situ alloying approach is efficient to produce oxide particles but with a coarse average size. It is possible to achieve a better combination of strength and ductility by tailoring the size distribution, for instance, applying a partially reductive atmosphere (H_2 + Ar gas mixture) in the LPBF process.

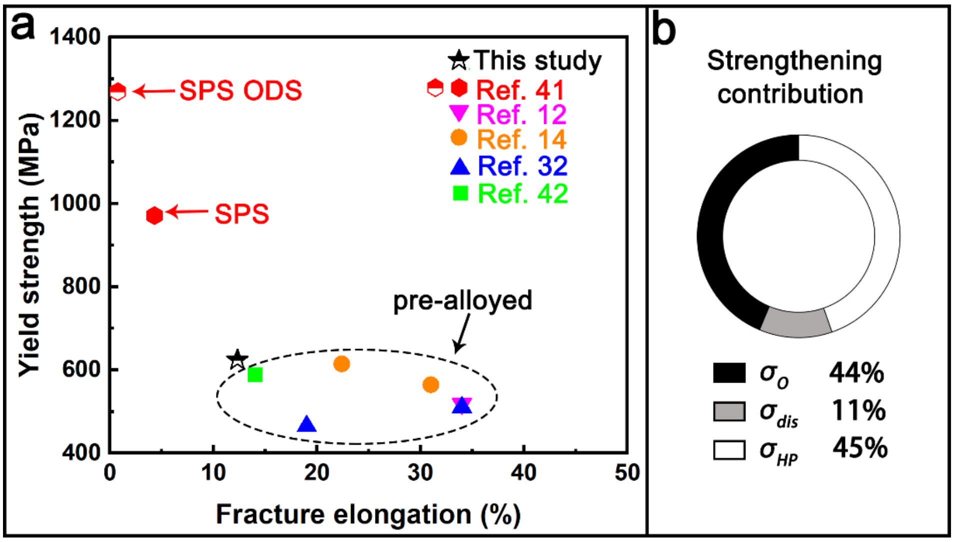

Figure 6.9 (a) Comparison of tensile properties of CoCrFeMnNi HEAs fabricated via LPBF using pre-alloyed powder, and ODS CoCrFeMnNi HEA fabricated via SPS [12, 14, 32, 41, 42]. (b) Illustration of estimated contribution from each strengthening mechanism.

6.4.2 Formation of the Mn oxides during the LPBF process

Two types of Mn oxides, MnO and Mn_2O_3, have been observed in the in-situ alloyed HEA. They could either exist in the raw powder or form due to in-situ oxidation. Regarding the mechanism, the following discussion can be made. Firstly, Mn is a reactive element and hence the surface of the Mn powder can be oxidised after fabrication, resulting in a shell of surface oxide. The outermost surface of the elemental Mn powder used in this study is therefore analysed via XPS to confirm this, and the spectra are provided in Figure 6.10. As expected, Mn and O are both detected in the survey spectrum (Figure 6.10(a)), where the peaks of C used for calibration are shown as well. To determine the Mn oxidation states, a fine scan is operated near Mn2p, which is the primary XPS region of Mn (binding energy of Mn2$p_{3/2}$, ~638.7 eV). Although Mn^{2+} possesses the same Mn2$p_{3/2}$ peak at 641.4 eV as Mn^{3+}, its characteristic satellite feature (~647 eV) does not appear in Figure 6.10(b). The results imply that the oxide covering the original elemental Mn powder is identified as Mn_2O_3, which matches the TEM result in Figure 6.5(b). The Mn_2O_3 layer can be melted and subsequently mixed into the matrix during the LPBF process, remaining as Mn_2O_3 particles in the in-situ alloyed HEA [43]. It is known that Mn_2O_3 can deoxygenate to form Mn_3O_4 in either oxidising or non-oxidising atmosphere (~1050 °C), but Mn_3O_4 particle has not been observed in this study. Furthermore, its change to MnO requires a reducing atmosphere (e.g., H_2) [44], which is not the case in the present study.

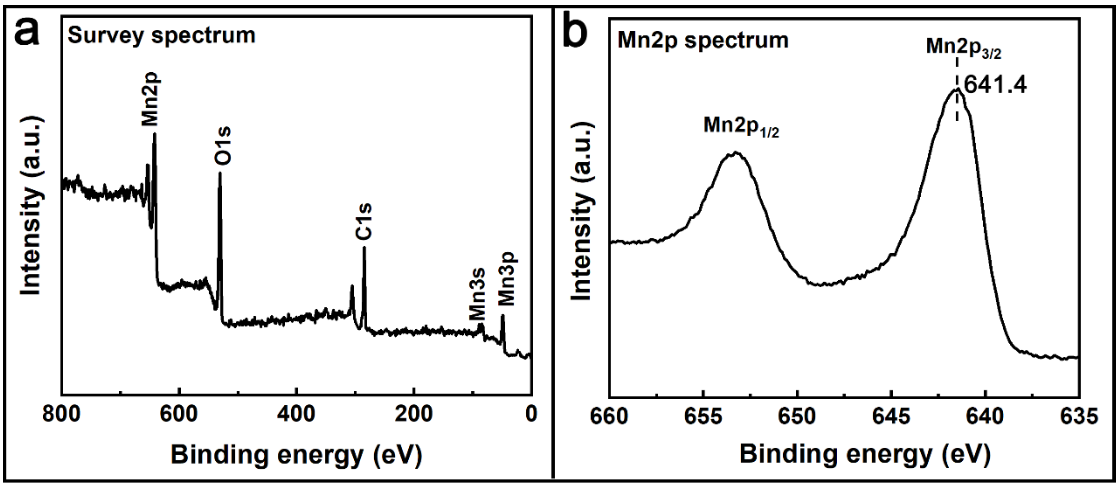

Figure 6.10 The Mn2p XPS spectra measured from the surface of the elemental Mn powder, (a) survey scan and (b) fine scan on the Mn2p peaks.

Besides the remnant from the elemental Mn powder, in-situ oxidation is hardly evitable during the LPBF process due to the high chemical reactivity of Mn for oxygen, which can be another source of the oxides. This can be argued as follows: Although the atmospheric oxygen level in the building chamber is normally lowered down to 0.2% before printing, there is still residual oxygen in powder as well as the atmosphere that can react with the Mn [26, 27]. The oxygen content increases from ~3051 ppm in the blended powder, to ~3310 ppm in the as-built sample, indicating in-situ oxidation during the LPBF process. In this study, MnO is found in the as-built

HEA other than the Mn_2O_3 as mentioned above. The Gibbs energy of formation (ΔG_f^0) for MnO is lower than that for Cr_2O_3 (e.g., at 1100 K: MnO –610 kJ/mol [45] vs. Cr_2O_3 –565 kJ/mol [26]), which is the most stable binary oxide among the elements from the pre-alloyed powder [46]. A study on the oxidation of $CoCrFeNiAl_{0.1}$ HEA indicated that this HEA system possesses better resistance to oxidation compared with some conventional alloys. Meanwhile, it was pointed out by the study that the oxides were primarily Cr_2O_3, alongside Al_2O_3 [47]. As Cr_2O_3 has not been observed in the present HEA, the formation of other binary oxides (e.g., NiO, Fe_2O_3) is further less possible. Moreover, although some ternary oxides such as $(Mn, Cr)_3O_4$ system can be thermodynamically favourable, their formation requires a long holding time at elevated temperatures, which is not the case in the present LPBF process [26, 48]. Hence, the in-situ reaction of the elemental Mn powder is illustrated in Figure 6.11(a) to explain the occurrence of MnO and Mn_2O_3 particles in the in-situ alloyed HEA. Figure 6.11(b) shows the process of laser scanning over the powder bed of the blended powder.

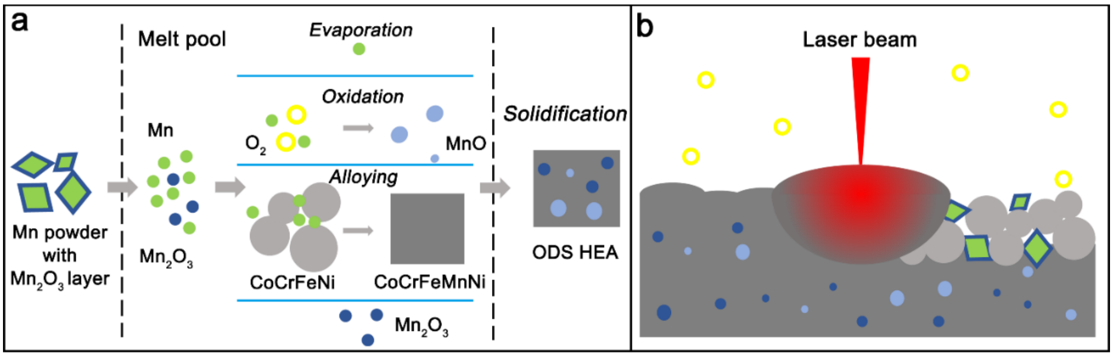

Figure 6.11 The in-situ reaction of the elemental Mn powder. (b) A schematic showing the transformation of materials in the LPBF process.

6.5 Conclusions

By combining the novelty of HEA and compositional flexibility of LPBF in-situ alloying, this research reveals the possibility of developing LPBFed high-performance HEAs. Conclusions can be made as follows.

- A blend of pre-alloyed CoCrFeNi powder and elemental Mn powder has been used to in-situ fabricate CoCrFeMnNi HEA via LPBF. The process results in an ODS HEA that consists of an FCC CoCrFeMnNi matrix with ~7% volumetric fraction of Mn oxide particles. A combination of the high tensile strength (630/730 as yield/fracture strengths) and moderate tensile ductility (~12%) has been achieved by the LPBFed, oxide-dispersion-strengthened CoCrFeMnNi HEA. The developed HEA also maintained high compression ductility.
- The strength of the in-situ alloyed HEA is mainly reinforced by the Orowan strengthening compared with those CoCrFeMnNi HEAs fabricated using pre-alloyed powder. Sub-micron oxide particles hinder the plastic deformation of the matrix, generating voids along the slip directions and reducing the tensile ductility to a certain degree.
- Oxide particles in the ODS HEA are recognised to be Mn_2O_3 and MnO. The Mn_2O_3 phase is most likely resulted from remelting of the oxide surface of elemental Mn powder, while the MnO particles should be due to the in-situ oxidation reaction between Mn and oxygen during the LPBF process.

6.6 Acknowledgements

This research is supported by Shenzhen Science and Technology Innovation Commission [ZDSYS201703031748354 and JCYJ20170817110358927]; Science and Technology Planning Project of Guangdong Province of China [grant number 2017B090911003], Natural Science Foundation of Guangdong Province [2016A030313756]. Dr. M. Yan appreciates the support of Humboldt Research Fellowship for Experienced Researchers. The authors acknowledge the assistance of SUSTech Core Research Facilities. The authors also acknowledge the facilities, and the scientific and technical assistance of the RMIT University's Microscopy & Microanalysis Facility, a linked laboratory of the Microscopy Australia.

6.7 References

[1] Y. Zhang, T.T. Zuo, Z. Tang, M.C. Gao, K.A. Dahmen, P.K. Liaw, Z.P. Lu, Microstructures and properties of high-entropy alloys, Progress in Materials Science 61 (2014) 1-93. http://doi.org/10.1016/j.pmatsci.2013.10.001.

[2] J.W. Yeh, Recent progress in high-entropy alloys, Annales De Chimie-Science Des Materiaux 31(6) (2006) 633-648. http://doi.org/10.3166/acsm.31.633-648.

[3] D.B. Miracle, O.N. Senkov, A critical review of high entropy alloys and related concepts, Acta Materialia 122 (2017) 448-511. http://doi.org/10.1016/j.actamat.2016.08.081.

[4] J.W. Yeh, S.K. Chen, S.J. Lin, J.Y. Gan, T.S. Chin, T.T. Shun, C.H. Tsau, S.Y. Chang, Nanostructured high-entropy alloys with multiple principal elements: Novel alloy design concepts and outcomes, Advanced Engineering Materials 6(5) (2004) 299-303. http://doi.org/10.1002/adem.200300567.

[5] J.Y. He, W.H. Liu, H. Wang, Y. Wu, X.J. Liu, T.G. Nieh, Z.P. Lu, Effects of Al addition on structural evolution and tensile properties of the FeCoNiCrMn high-entropy alloy system, Acta Materialia 62 (2014) 105-113. http://doi.org/10.1016/j.actamat.2013.09.037.

[6] Z. Li, K.G. Pradeep, Y. Deng, D. Raabe, C.C. Tasan, Metastable high-entropy dual-phase alloys overcome the strength-ductility trade-off, Nature 534(7606) (2016) 227-230. http://doi.org/10.1038/nature17981.

[7] J.Y. He, H. Wang, H.L. Huang, X.D. Xu, M.W. Chen, Y. Wu, X.J. Liu, T.G. Nieh, K. An, Z.P. Lu, A precipitation-hardened high-entropy alloy with outstanding tensile properties, Acta Materialia 102 (2016) 187-196. http://doi.org/10.1016/j.actamat.2015.08.076.

[8] S. Singh, N. Wanderka, B.S. Murty, U. Glatzel, J. Banhart, Decomposition in multi-component AlCoCrCuFeNi high-entropy alloy, Acta Materialia 59(1) (2011) 182-190. https://doi.org/10.1016/j.actamat.2010.09.023.

[9] D. Zhang, S. Sun, D. Qiu, M.A. Gibson, M.S. Dargusch, M. Brandt, M. Qian, M. Easton, Metal alloys for fusion-based additive manufacturing, Advanced Engineering Materials 20(5) (2018) 1799962. http://doi.org/10.1002/adem.201700952.

[10] T. DebRoy, H.L. Wei, J.S. Zuback, T. Mukherjee, J.W. Elmer, J.O. Milewski, A.M. Beese, A. Wilson-Heid, A. De, W. Zhang, Additive manufacturing of metallic components – process, structure and properties, Progress in Materials Science 92 (2018) 112-224. http://doi.org/10.1016/j.pmatsci.2017.10.001.

[11] Y. Brif, M. Thomas, I. Todd, The use of high-entropy alloys in additive manufacturing, Scripta Materialia 99 (2015) 93-96. http://doi.org/10.1016/j.scriptamat.2014.11.037.

[12] R. Li, P. Niu, T. Yuan, P. Cao, C. Chen, K. Zhou, Selective laser melting of an equiatomic CoCrFeMnNi high-entropy alloy: Processability, non-equilibrium microstructure and mechanical property, Journal of Alloys and Compounds 746 (2018) 125-134. http://doi.org/10.1016/j.jallcom.2018.02.298.

[13] P.F. Zhou, D.H. Xiao, Z. Wu, X.Q. Ou, Al0.5FeCoCrNi high entropy alloy prepared by selective laser melting with gas-atomized pre-alloy powders, Materials Science and Engineering: A 739 (2019) 86-89. http://doi.org/10.1016/j.msea.2018.10.035.

[14] J.M. Park, J. Choe, J.G. Kim, J.W. Bae, J. Moon, S. Yang, K.T. Kim, J.-H. Yu, H.S. Kim, Superior tensile properties of 1%C-CoCrFeMnNi high-entropy alloy additively manufactured by selective laser melting, Materials Research Letters 8(1) (2019) 1-7. http://doi.org/10.1080/21663831.2019.1638844.

[15] T. Fujieda, M. Chen, H. Shiratori, K. Kuwabara, K. Yamanaka, Y. Koizumi, A. Chiba, S. Watanabe, Mechanical and corrosion properties of CoCrFeNiTi-based high-entropy alloy

additive manufactured using selective laser melting, Additive Manufacturing 25 (2019) 412-420. http://doi.org/10.1016/j.addma.2018.10.023.

[16] S. Luo, C. Zhao, Y. Su, Q. Liu, Z. Wang, Selective laser melting of dual phase AlCrCuFeNix high entropy alloys: Formability, heterogeneous microstructures and deformation mechanisms, Additive Manufacturing 31 (2020) 100925. https://doi.org/10.1016/j.addma.2019.100925.

[17] R. Zhou, Y. Liu, C. Zhou, S. Li, W. Wu, M. Song, B. Liu, X. Liang, P.K. Liaw, Microstructures and mechanical properties of C-containing FeCoCrNi high-entropy alloy fabricated by selective laser melting, Intermetallics 94 (2018) 165-171. http://doi.org/10.1016/j.intermet.2018.01.002.

[18] W.Q. Wu, R. Zhou, B.Q. Wei, S. Ni, Y. Liu, M. Song, Nanosized precipitates and dislocation networks reinforced C-containing CoCrFeNi high-entropy alloy fabricated by selective laser melting, Materials Characterization 144 (2018) 605-610. http://doi.org/10.1016/j.matchar.2018.08.019.

[19] J. Joseph, T. Jarvis, X. Wu, N. Stanford, P. Hodgson, D.M. Fabijanic, Comparative study of the microstructures and mechanical properties of direct laser fabricated and arc-melted AlxCoCrFeNi high entropy alloys, Materials Science and Engineering: A 633 (2015) 184-193. http://doi.org/10.1016/j.msea.2015.02.072.

[20] Z.H. Zhang, Y.H. Zhou, S.Y. Zhou, L. Zhang, M. Yan, Mechanically blended Al: Simple but effective approach to improving mechanical property and thermal stability of selective laser-melted Inconel 718, Metallurgical and Materials Transactions A 50a(8) (2019) 3922-3936. http://doi.org/10.1007/s11661-019-05299-6.

[21] A. Grigoriev, I. Polozov, V. Sufiiarov, A. Popovich, In-situ synthesis of Ti2AlNb-based intermetallic alloy by selective laser melting, Journal of Alloys and Compounds 704 (2017) 434-442. http://doi.org/10.1016/j.jallcom.2017.02.086.

[22] I. Polozov, V. Sufiiarov, A. Popovich, D. Masaylo, A. Grigoriev, Synthesis of Ti-5Al, Ti-6Al-7Nb, and Ti-22Al-25Nb alloys from elemental powders using powder-bed fusion additive manufacturing, Journal of Alloys and Compounds 763 (2018) 436-445. http://doi.org/10.1016/j.jallcom.2018.05.325.

[23] P. Chen, S. Li, Y. Zhou, M. Yan, M.M. Attallah, Fabricating CoCrFeMnNi high entropy alloy via selective laser melting in-situ alloying, Journal of Materials Science & Technology 43 (2020) 40-43. http://doi.org/10.1016/j.jmst.2020.01.002.

[24] H. Prasad, S. Singh, B.B. Panigrahi, Mechanical activated synthesis of alumina dispersed FeNiCoCrAlMn high entropy alloy, Journal of Alloys and Compounds 692 (2017) 720-726. http://doi.org/10.1016/j.jallcom.2016.09.080.

[25] B. Gwalani, R.M. Pohan, O.A. Waseem, T. Alam, S.H. Hong, H.J. Ryu, R. Banerjee, Strengthening of Al0.3CoCrFeMnNi-based ODS high entropy alloys with incremental changes in the concentration of Y2O3, Scripta Materialia 162 (2019) 477-481. http://doi.org/10.1016/j.scriptamat.2018.12.021.

[26] H. Springer, C. Baron, A. Szczepaniak, E.A. Jägle, M.B. Wilms, A. Weisheit, D. Raabe, Efficient additive manufacturing production of oxide- and nitride-dispersion-strengthened materials through atmospheric reactions in liquid metal deposition, Materials & Design 111 (2016) 60-69. http://doi.org/10.1016/j.matdes.2016.08.084.

[27] C. Qiu, A new approach to synthesise high strength nano-oxide dispersion strengthened alloys, Journal of Alloys and Compounds 790 (2019) 1023-1033. http://doi.org/10.1016/j.jallcom.2019.03.221.

[28] Z. Li, S. Zhao, R.O. Ritchie, M.A. Meyers, Mechanical properties of high-entropy alloys with emphasis on face-centered cubic alloys, Progress in Materials Science 102 (2019) 296-345. http://doi.org/10.1016/j.pmatsci.2018.12.003.
[29] S. Guan, D. Wan, K. Solberg, F. Berto, T. Welo, T.M. Yue, K.C. Chan, Additive manufacturing of fine-grained and dislocation-populated CrMnFeCoNi high entropy alloy by laser engineered net shaping, Materials Science and Engineering: A 761 (2019) 138056. http://doi.org/10.1016/j.msea.2019.138056.
[30] G. Laplanche, A. Kostka, O.M. Horst, G. Eggeler, E.P. George, Microstructure evolution and critical stress for twinning in the CrMnFeCoNi high-entropy alloy, Acta Materialia 118 (2016) 152-163. http://doi.org/10.1016/j.actamat.2016.07.038.
[31] B. Gludovatz, E.P. George, R.O. Ritchie, Processing, microstructure and mechanical properties of the CrMnFeCoNi high-entropy alloy, JOM 67(10) (2015) 2262-2270. http://doi.org/10.1007/s11837-015-1589-z.
[32] Z.G. Zhu, Q.B. Nguyen, F.L. Ng, X.H. An, X.Z. Liao, P.K. Liaw, S.M.L. Nai, J. Wei, Hierarchical microstructure and strengthening mechanisms of a CoCrFeNiMn high entropy alloy additively manufactured by selective laser melting, Scripta Materialia 154 (2018) 20-24. http://doi.org/10.1016/j.scriptamat.2018.05.015.
[33] Y.K. Kim, J. Choe, K.A. Lee, Selective laser melted equiatomic CoCrFeMnNi high-entropy alloy: Microstructure, anisotropic mechanical response, and multiple strengthening mechanism, Journal of Alloys and Compounds 805 (2019) 680-691. http://doi.org/10.1016/j.jallcom.2019.07.106.
[34] A. Piglione, B. Dovgyy, C. Liu, C.M. Gourlay, P.A. Hooper, M.S. Pham, Printability and microstructure of the CoCrFeMnNi high-entropy alloy fabricated by laser powder bed fusion, Materials Letters 224 (2018) 22-25. http://doi.org/10.1016/j.matlet.2018.04.052.
[35] Y. Zhong, L. Liu, J. Zou, X. Li, D. Cui, Z. Shen, Oxide dispersion strengthened stainless steel 316L with superior strength and ductility by selective laser melting, Journal of Materials Science & Technology 42 (2020) 97-105. http://doi.org/10.1016/j.jmst.2019.11.004.
[36] B. Li, B. Qian, Y. Xu, Z. Liu, F. Xuan, Fine-structured CoCrFeNiMn high-entropy alloy matrix composite with 12 wt% TiN particle reinforcements via selective laser melting assisted additive manufacturing, Materials Letters 252 (2019) 88-91. http://doi.org/10.1016/j.matlet.2019.05.108.
[37] F. Siska, L. Stratil, H. Hadraba, S. Fintova, I. Kubena, V. Hornik, R. Husak, D. Bartkova, T. Zalezak, Strengthening mechanisms of different oxide particles in 9Cr ODS steel at high temperatures, Materials Science and Engineering: A 732 (2018) 112-119. http://doi.org/10.1016/j.msea.2018.06.109.
[38] S.J. Sun, Y.Z. Tian, H.R. Lin, X.G. Dong, Y.H. Wang, Z.J. Zhang, Z.F. Zhang, Enhanced strength and ductility of bulk CoCrFeMnNi high entropy alloy having fully recrystallized ultrafine-grained structure, Materials & Design 133 (2017) 122-127. http://doi.org/10.1016/j.matdes.2017.07.054.
[39] Q. Lin, X. An, H. Liu, Q. Tang, P. Dai, X. Liao, In-situ high-resolution transmission electron microscopy investigation of grain boundary dislocation activities in a nanocrystalline CrMnFeCoNi high-entropy alloy, Journal of Alloys and Compounds 709 (2017) 802-807. https://doi.org/10.1016/j.jallcom.2017.03.194.
[40] U.F. Kocks, H. Mecking, Physics and phenomenology of strain hardening: The fcc case, Progress in Materials Science 48(3) (2003) 171-273. https://doi.org/10.1016/S0079-6425(02)00003-8.

[41] H. Hadraba, Z. Chlup, A. Dlouhy, F. Dobes, P. Roupcova, M. Vilemova, J. Matejicek, Oxide dispersion strengthened CoCrFeNiMn high-entropy alloy, Materials Science and Engineering: A 689 (2017) 252-256. http://doi.org/10.1016/j.msea.2017.02.068.

[42] Y.H. Zhou, Z.H. Zhang, Y.P. Wang, G. Liu, S.Y. Zhou, Y.L. Li, J. Shen, M. Yan, Selective laser melting of typical metallic materials: An effective process prediction model developed by energy absorption and consumption analysis, Additive Manufacturing 25 (2019) 204-217. http://doi.org/10.1016/j.addma.2018.10.046.

[43] C. Tan, K. Zhou, W. Ma, L. Min, Interfacial characteristic and mechanical performance of maraging steel-copper functional bimetal produced by selective laser melting based hybrid manufacture, Materials & Design 155 (2018) 77-85. http://doi.org/10.1016/j.matdes.2018.05.064.

[44] M.I. Zaki, M.A. Hasan, L. Pasupulety, K. Kumari, Thermochemistry of manganese oxides in reactive gas atmospheres: Probing redox compositions in the decomposition course MnO_2 → MnO, Thermochimica Acta 303(2) (1997) 171-181. https://doi.org/10.1016/S0040-6031(97)00258-X.

[45] K.T. Jacob, A. Kumar, Y. Waseda, Gibbs energy of formation of MnO: Measurement and assessment, Journal of Phase Equilibria and Diffusion 29(3) (2008) 222-230. http://doi.org/10.1007/s11669-008-9280-5.

[46] S. Seetharaman, Treatise on Process Metallurgy 1st edn, Elsevier, Oxford, 2014.

[47] H.S. Grewal, R.M. Sanjiv, H.S. Arora, R. Kumar, A. Ayyagari, S. Mukherjee, H. Singh, Activation energy and high temperature oxidation behavior of multi-principal element alloy, Advanced Engineering Materials 19(11) (2017) 1700182. http://doi.org/10.1002/adem.201700182.

[48] F. Ye, Z. Jiao, Y. Yang, Effect of medium temperature precipitation phase and Mn element diffusion mechanism on high temperature oxidation process of repair and remanufacture CoCrFeMnNi high-entropy alloy cladding, Materials Research Express 6(5) (2019) 056521. http://doi.org/10.1088/2053-1591/ab01be.

Chapter 7: In-Situ Alloyed CoCrFeMnNi High Entropy Alloy: Microstructural Development in Laser Powder Bed Fusion

As the printability and mechanical properties of in-situ alloyed HEAs were evaluated in previous chapters, this chapter focuses on the microstructural development during the in-situ alloying processes. By investigating the microstructural development on the single-track scale, the elemental homogenisation and microstructures observed in the as-built HEA samples can be understood more thoroughly.

Published article

Peng Chen[a,b], Xiyu Yao[a], Moataz M. Attallah[b], Ming Yan[a]

Journal of Materials Science & Technology, 123 (2022) 123-135.

[a] Department of Materials Science and Engineering, Southern University of Science and Technology, Shenzhen 518055, China

[b] Advanced Materials Processing Laboratory, University of Birmingham, Birmingham B15 2TT, UK

Abstract

In-situ alloying has the potential to combine the compositional flexibility of high entropy alloys (HEAs) and the advanced forming capability of laser powder bed fusion (LPBF). This study fundamentally investigated the elemental homogenisation and grain development in the in-situ alloying process of CoCrFeMnNi HEA, by analysing the basic units, i.e., tracks and layers, and introducing Mn as an alloying element to the base CoCrFeNi HEA. Different modelling methods were employed to predict meltpool dimensions, and the results indicated the dependence of the modelling on practical meltpool modes. Delimitation of elemental distribution was found in keyhole meltpools since an intensive flow was generated due to recoil pressure. The homogeneity of in-situ alloyed Mn in single tracks was insufficient whether operated in conduction mode or keyhole mode, which required remelting from adjacent tracks and following layers to promote homogenisation significantly. The preferred orientation in single tracks along scanning directions changed from <001> to <101> as the scanning speed increased, although the cross-sections were similar in size with identical linear energy density. Such preference can be inherited during the printing process and lead to different textures in three-layer samples. It was also observed that applying hatch spacing smaller than a half meltpool width could coarsen the grains in a layer. The results from this study provide structure-parameter correlations for future microstructural tailoring and manipulation.

Keywords: Laser powder bed fusion; High entropy alloy; In-situ alloying; Single track; Elemental homogenisation

7.1 Introduction

In the past few years, CoCrFeNi-based high entropy alloys (HEAs), in particular CoCrFeMnNi, have drawn great attention due to their excellent mechanical performance. Their processing via additive manufacturing (AM) & 3D printing has been widely studied as well [1-6]. So far, the CoCrFeMnNi HEA has shown outstanding printability via laser powder bed fusion (LPBF) [7-9]. Its excellent printability also allows researchers to further explore the possibility in terms of compositional flexibility for promoting performance and applications. Approaches such as introducing a minor amount of carbides or TiN nanoparticles to HEAs have led to improved mechanical properties [10-12]. However, LPBF may not be an ideal technique from HEA developing perspective if only pre-alloyed powder is going to be used, since for HEAs the chemical adjustment can be on a scale of 5–35 at. %, while the preparation of pre-alloyed powders for LPBF is often expensive and time-consuming [13, 14]. For rapid prototyping and validation of HEAs, in-situ alloying using blended powder has the potential to combine both the compositional flexibility of HEAs and the advanced forming capability of LPBF that originates from high-power laser [15-17].

The feasibility of in-situ alloying via LPBF has been assessed for conventional alloy systems, including Fe-Ni alloys, Ni superalloys, and Ti-based alloys [15, 16, 18-21]. It has been pointed out that elemental homogenisation could be a primary challenge for LPBF in-situ alloying apart from densification. For HEAs with equiatomic compositions, the homogenisation of alloying elements can be even more challenging [22]. Over the past two years, emerging LPBF in-situ alloying approaches have been carried out to assess the feasibility with different HEA systems, e.g., $Al_{0.26}CoFeMnNi$, CoCrFeMnNi, $AlCrCuFeNi_x$, and etc. [23-31]. The results of these studies indicate that densification and mechanical properties can be comparable to or even better than those of pre-alloyed approaches, while the elemental homogenisation favours processing parameters with relatively high energy density. In an early study on the in-situ alloyed CoCrFeMnNi HEA, a blend of pre-alloyed CoCrFeNi powder and elemental Mn powder has shown good printability [24]. Like other studies, however, only bulk samples were analysed, and the homogenisation of in-situ alloyed was simply correlated to volumetric energy density. On the other hand, although single-track morphology has been correlated with printing quality to predict the possible processing window of LPBF [32, 33], details involved in the track-to-track and layer-to-layer in-situ alloying processes have not been investigated yet, which can be important in order to fully understand the in-situ alloying process, including associated microstructural development and elemental homogenisation.

This study aims to trace the LPBF in-situ alloying process back to its most fundamental unit, the single track. The microstructural heterogeneity of the CoCrFeMnNi HEA fabricated by directed energy deposition (DED) was revealed by using the single-track approach [34]. Most LPBF single-track experiments were carried out on regular substrates with one powder layer coated above, which can only reproduce the conditions of initial exposure in the LPBF process [33, 35]. In this study, single-track experiments will be carried out on as-built surfaces and with continuous recoating to stay consistent in actual building. Figure 7.1 illustrates the logic and focus of this study. Meltpool dimensions, widths, and depths of cross-sections will be measured from the single tracks scanned with and without elemental Mn powder to evaluate the influences of introducing secondary powder. Along with the measured results, modelling methods will be employed to predict the dimensions of the meltpools and verify operating modes [36-38]. Elemental homogenisation and grain development will be compared in single tracks fabricated with different parameters. Since the LPBF process is not a simple pile of individual tracks, the inter-track and inter-layer remelting will be investigated as well through single-layer and three-layer experiments, respectively. In terms of printing parameters, laser power (P) and scanning speed (v) are directly responsible for the energy input; hatch spacing (h) is another focal factor as it determines the remelting efficiency in each layer.

The results of this work demonstrated the applicability of representative modelling methods for conduction or keyhole modes. Mn homogenisation in different stages of the in-situ alloying process was revealed; its correlations with volumetric energy density were further analysed in terms of meltpool modes and scanning routes. For meltpool fabricated using different parameters but with similar cross-sections, their preferred crystalline orientations and grain growth were detailed. Based on the results, a fundamental understanding of the microstructural development in LPBF in-situ alloying is presented. Comprehending the mechanism of in-situ homogenisation and meltpool evolution can also help to advance LPBF processes using different feedstock.

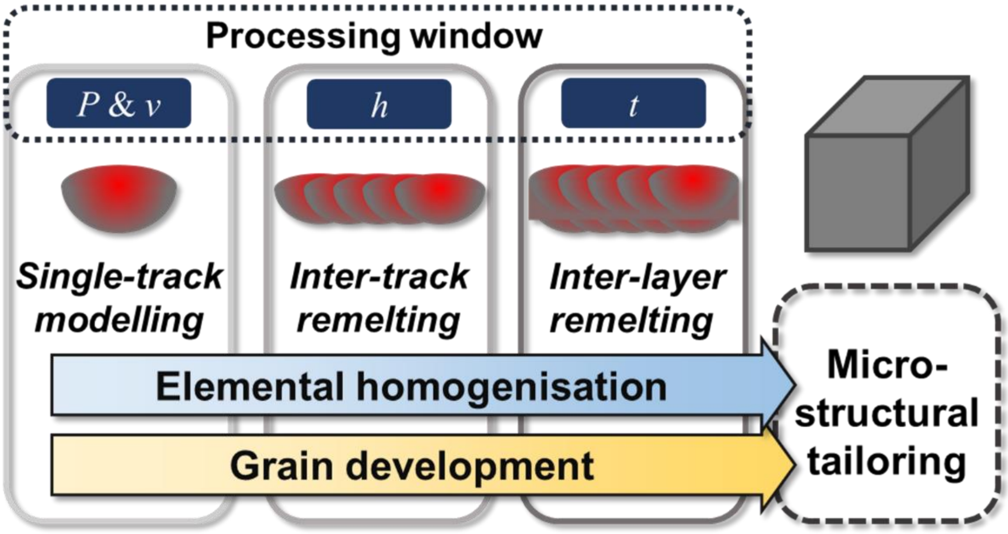

Figure 7.1 A schematic of the study route.

7.2 Materials and Methods

7.2.1 Sample preparation

Pre-alloyed CoCrFeNi powder was produced by Zhongyuan Advanced Materials via gas atomisation. The pre-alloyed powder was overall spherical (Figure 7.2(a)) and with the Dv 50 of 21.5 μm. Elemental Mn powder (99.9% purity) was produced by Aladdin and in irregular shape (Figure 7.2(b)). The powders were firstly sieved by a 73-μm sieve. Then 79 wt. % of pre-alloyed CoCrFeNi powder and 21 wt. % of elemental Mn powder were weighed, and mixed by a WAB Turbula T2F mixer for 4 h for homogenisation. The blended powder is shown in Figure 7.2(c), and its composition is listed in Table 7.1.

LPBF experiments were carried out on an SLM125HL (SLM Solutions) with argon protection. The laser beam radius (r) of the machine was ~33.5 μm. The layer thickness (t) and substrate temperature (T_0) were set as 30 μm and 100 °C (373 K) in all experiments. Before fabricating in-situ alloyed samples, at least 7 layers of pre-alloyed CoCrFeNi powder were scanned on a 316L substrate to ensure recoating quality and avoid contamination from the substrate material. The processing parameters of the pre-alloyed beds are given in Table 7.2. The blended powder was then spread on the top of pre-alloyed beds for in-situ alloying experiments. A simple scanning strategy was employed with 90 ° rotation between adjacent layers, as shown in Figure 7.2(d). The building, transverse, and scanning directions were noted as BD, TD, and SD, respectively in this study. Since the processing window for in-situ alloying of CoCrFeMnNi HEA has been explored by a previous study [24], the laser power and scanning speed for single-track experiments were selected closely to those parameters, and listed in Table 7.2. Identical single-track experiments using the pre-alloyed CoCrFeNi powder were conducted to demonstrate the influences of additional Mn powder. The processing parameters including laser power and scanning speed were noted as ‘*P* & *v*’ to mark samples.

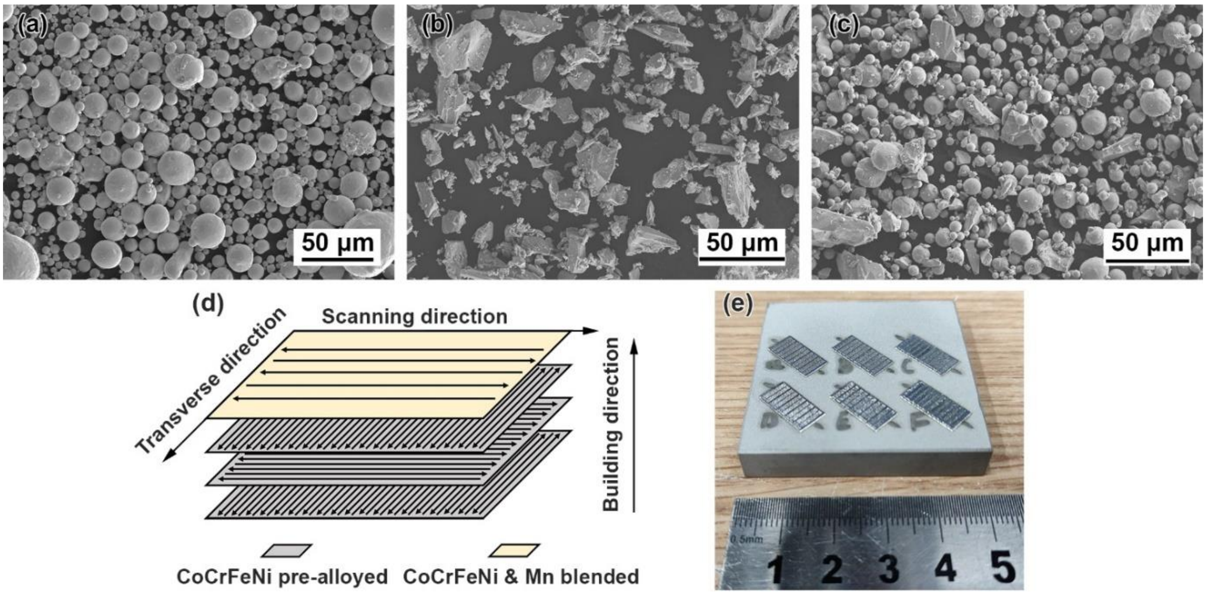

Figure 7.2 SEM images of (a) pre-alloyed CoCrFeNi powder, (b) elemental Mn powder, and (c) the blended powder. (d) An illustration of the scanning strategy for pre-alloyed beds and in-situ alloyed samples, and (e) a 316L substrate holding six pre-alloyed beds with as-built samples.

Table 7.1 Composition of the blended powder used in this study.

	Co	Cr	Fe	Ni	Mn
Blended powder (at. %)	18.8	20.1	20.4	19.3	21.4

Table 7.2 Processing parameters used in the track-based experiments.

	Power, *P* (W)	Scanning speed, *v* (mm/s)	Hatch spacing, *h* (μm)
Pre-alloyed beds	220	600	60
Single-track	150, 200, 250, 300	600, 700, 800, 900, 1000	N/A
Single-layer	150, 300	600, 1000	60, 70, 80, 90, 100
Three-layer	150, 200, 250, 300	600, 700, 800, 900, 1000	60, 100

7.2.2 Microstructural characterisation

Figure 7.2(e) shows as-built single tracks and single layers on a substrate. As-built samples were cut transversely to the scanning direction by electrical discharge machining (EDM). The cross-sections of samples were then grounded, and finished by a Buehler VibroMet 2 Vibratory Polisher. To reveal meltpool structures, the polished samples were electrochemically etched in a 10% oxalic acid solution for 100 s at 2.5 V. A Leica DM2700 optical microscope (OM) was employed for the observation and measurement of meltpools. The depth (*D*) and width (*W*) of meltpools were measured from 5 cross-sections, and the average was used. A ZEISS Merlin field emission scanning electron microscope (SEM) equipped with an energy dispersive spectrometer (EDS) and an electron back-scattered diffraction (EBSD) system was employed for microstructural characterisation, including elemental distribution and grain structures.

7.2.3 Single-track modelling

Predicting the dimensions of LPBFed meltpools through modelling is essential for processing optimisation. Based on the laser parameters in single-track experiments, representative modelling approaches [36-38] were employed to calculate the width and depth of pre-alloyed

CoCrFeNi meltpools. Modelling approaches can also help assess the potential influences of adding elemental Mn powder to the meltpools.

Tang et al. [38, 39] introduced a method that presented an ideal meltpool shape based on the Rosenthal equation. The cross-section of meltpools is hypothesised to be semi-circle. The depth, therefore, equals half of the meltpool width, as follows:

$$D = \frac{W}{2} = \sqrt{\frac{2AP}{e\pi\rho C(T_m - T_0)v}} \tag{7.1}$$

where

A is the laser absorptivity,

ρ is the density (kg/m^3),

C is the thermal capacity (J/(kg*K)),

T_m is the melting temperature (K), and

T_0 is the substrate temperature (K).

Rubenchik et al. [37, 40] provided scaling laws based on the Eagar-Tsai thermal model, which further modified the point heat source in the Rosenthal equation into the Gaussian heat distribution. The universal functions of B and p are used to describe normalised meltpool dimensions independent of materials and machines. The parameters are based on the normalised enthalpy introduced by Hann et al. [41], and defined by:

$$B = \frac{AP}{\pi^{1.5}\sqrt{avr^3}} \tag{7.2}$$

$$p = \frac{a}{vr} \tag{7.3}$$

where *a* stands for the heat diffusivity ($\mathrm{m^2/s}$). The algebraic expressions of depth *D* (*B*, *p*) and width *W* (*B*, *p*) are further given as follows:

$$D\,(B,\,p) = \frac{r}{\sqrt{p}}\begin{bmatrix} 0.008 - 0.0048B - 0.047p - 0.099Bp \\ +(0.32 + 0.015B)p\ln p \\ +\ln B\,(0.0056 - 0.89p + 0.29p\ln p) \end{bmatrix} \tag{7.4}$$

$$W\,(B,p) = \frac{r}{Bp^3}\begin{bmatrix} 0.0021 - 0.047p + 0.34p^2 - 1.9p^3 - 0.33p^4 \\ +B(0.00066 - 0.007p - 0.00059p^2 + 2.8p^3 - 0.12p^4) \\ +B^2(-0.0007 + 0.15p - 0.12p^2 + 0.59p^3 - 0.023p^4) \\ +B^3(0.00001 - 0.00022p + 0.002p^2 - 0.0085p^3 + 0.0014p^4) \end{bmatrix} \tag{7.5}$$

Both methods from Tang et al. and Rubenchik et al. [37, 38] describe a meltpool fulfilled by molten materials. Meanwhile, the temperature at the meltpool surface centre can be much higher than the boiling temperature of materials. Therefore, the meltpool expansion is consistently driven by heat conduction despite the possible vaporisation of materials. Their methods are hence noted as conduction-based ones in this study.

Fabbro [42] introduced a method specifically for keyhole meltpools, namely keyhole-based method in this study. The structure of keyhole meltpools includes an open cavity depressed by recoil pressure since the material vaporises at excessive temperatures. Hence its development is distinct from the conduction meltpool mentioned above [36, 42]. This approach provides an expression of the aspect ratio *R* = *D*/*W*, as written below:

$$R = \frac{R_0}{1 + \frac{v}{V_0}} \tag{7.6}$$

with

$$R_0 = \frac{AP}{n2rK(T_b - T_0)} \tag{7.7}$$

$$V_0 = \frac{n}{m}\frac{a}{r} \tag{7.8}$$

where

K is the thermal conductivity (W/(m*K)),

T_b is the boiling temperature (K).

The parameters, m and n, are correlated to the Pélect number ($Pé = vr/a$) for given printing parameters. In this study, the $Pé$ range is $3.6 < Pé < 6.1$; m and n are set as 5 and 4, respectively [36].

To calculate meltpool dimensions, the involved physical properties of the CoCrFeNi HEA are provided in Table 7.3. Neglecting the temperature dependence of physical properties is one of the simplifications to maintain solvability. Moreover, the absorptivity of 0.3 and 0.6 was adopted for conduction and keyhole meltpools, respectively. Because the absorptivity during LPBF processes had a close dependence on meltpool modes instead of powders, the absorptivity of different liquid metals, such as Ni superalloy, Ti alloy and stainless steel, could get dropped to a close range after melting [43]. There have been other simplifications in the methods mentioned above, e.g., the influences of the powder layer, melt flow, and phase change have not been considered. Nevertheless, the applicability of the simplified models has been demonstrated in research on Al alloy, 316L steel, and Inconel 718 superalloy [44-46]. Their applicability will be further investigated by the comparison with the measured data obtained from single-track experiments in this study.

Table 7.3 Physical properties of CoCrFeNi HEA.

ρ (g/cm^3)	C (J/(kg*K))	K (W/(m*K))	T_m (K)	T_b (K)	A
8.16	444 [1]	21 [47]	1687 [1]	3070*	0.3, 0.6 [43, 48]

* The boiling point is calculated according to the rule of mixtures [49].

7.3 Results

7.3.1 Meltpool morphology

Figure 7.3 provides the cross-section images of in-situ alloyed meltpools that formed using different processing parameters. For each laser setting, two adjacent tracks are included in the picture. As the linear energy density (*LED*, defined by P/v [50]) increases, meltpools enlarge significantly. To further illustrate the dimensions of meltpools, the measured depths of pre-alloyed and in-situ alloyed meltpools are plotted in Figures 7.4(a, b), respectively. The minimum depth of pre-alloyed and in-situ alloyed meltpools are both 60 μm at the lowest *LED* of 0.15 J/mm. Despite the difference between their maximum depths, the measured depths coincide closely within the experimental *LED* range, as shown in Figure 7.4(c). Compared with the increased depth, the measured width increases more moderately as pre-alloyed widths range from 99 μm to 151 μm (Figure 7.4(d)), and in-situ alloyed ones with a range from 91 μm to 140 μm (Figure 7.4(e)). In the whole *LED* range, pre-alloyed meltpools are overall 9% wider than in-situ alloyed meltpools, as shown in Figure 7.4(f). The width-to-depth ratios (W/D) of single-track meltpools are plotted in Figure 7.4(c) as well. Most of them are smaller than 1.5, indicating the meltpools are no longer operated in the conduction mode within the current processing window [33]. The detailed results of meltpool dimensions are provided in Supplementary Figure 7.S1 and Tables 7.S1 & S2.

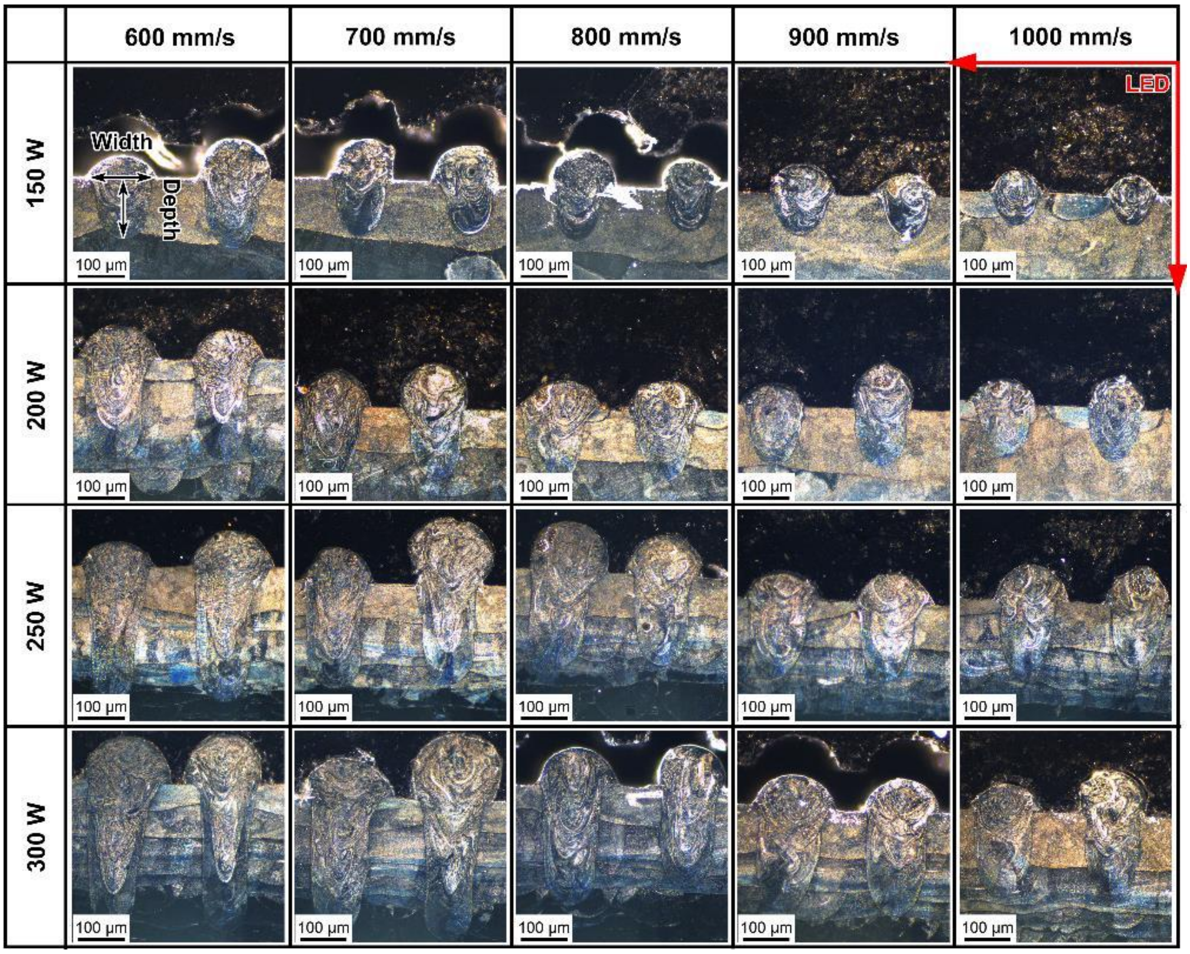

Figure 7.3 OM images of in-situ alloyed single-track meltpools, with an illustration of measuring meltpool dimensions.

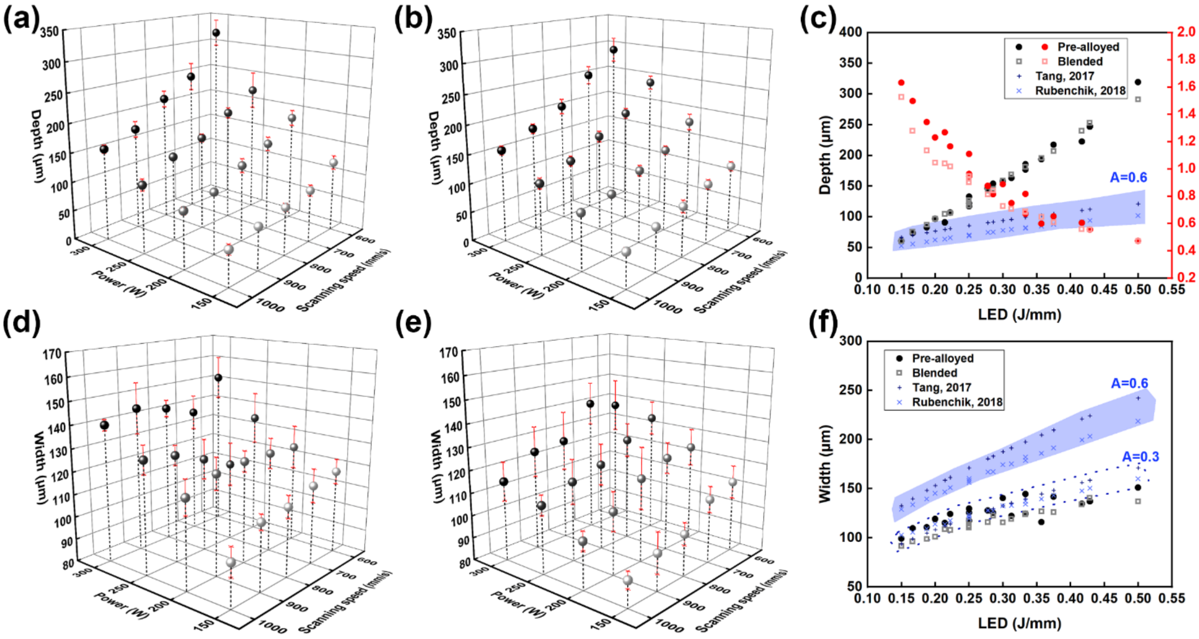

Figure 7.4 Measured depths of (a) pre-alloyed CoCrFeNi meltpools and (b) in-situ alloyed CoCrFeMnNi meltpools. (c) Dependence of measured and predicted depths, as well as width-to-depth ratio on linear energy density. Measured widths of (d) pre-alloyed meltpools and (e) in-situ alloyed meltpools. (f) Dependence of measured and predicted widths on linear energy density.

The predicted depths and widths of pre-alloyed meltpools using conduction-based methods are given in Figures 7.4(c, f), respectively. In Figure 7.4(c), the predicted depths are close to the measured depths at the low *LED* of 0.15 J/mm, which is about the threshold of conduction mode (W/D = 1.5). Then the predicted results deviate from the measured ones as the *LED* increases. Both conduction-based methods predict the results in a similar range but tend to underestimate the depth as meltpools exceed the conduction-mode threshold. The deviation indicates that the development of meltpool depth is no longer dominated by the conduction model. Hence, the methods based on conduction are not applicable in such a high *LED* range. On the other hand, the widths are overestimated by the conduction-based methods, as shown in Figure 7.4(f). It should be noted that the predicted results match the measured ones when the absorptivity is lowered to 0.3, which is normally a value for conduction meltpools and much lower than the actual absorptivity (0.6-0.8) for keyhole meltpools.

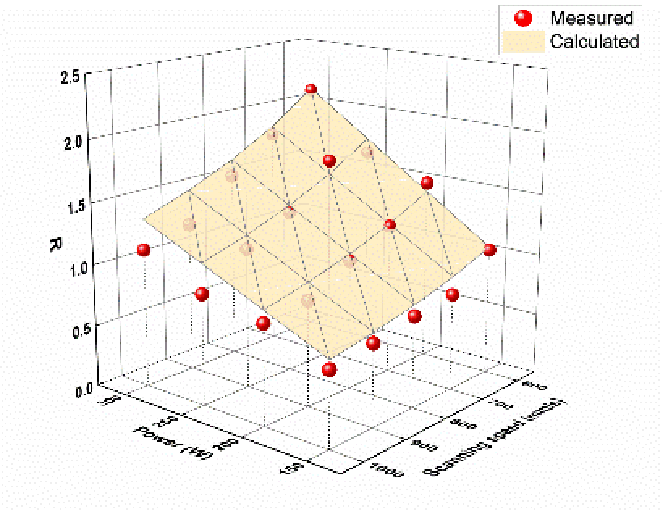

Figure 7.5 The comparison of aspect ratio (*R*) between measured results of pre-alloyed meltpools and predicted results calculated by the keyhole-based method (Fabbro [36]).

On the other hand, the aspect ratios calculated via the keyhole-based method are presented in Figure 7.5. For the printing parameters involved in this study, it shows good agreement with the experimental results, especially at high *LED*. The shape of the keyhole is more coincident with the ideally cylindrical keyhole hypothesised in this method at high *LED*, while the concave depressed by the recoil pressure is relatively shallow when the meltpool is close to the conduction mode. The approaches to the prediction of meltpool dimensions in this study have shown the importance of distinguishing meltpool modes for a given processing window. However, it is hard to determine the keyhole threshold for a particular material without practical observation on meltpools. Further analyses of keyhole formation and the applicability of modelling methods are given in the discussion.

7.3.2 In-situ homogenisation of Mn

Figure 7.6 shows the distribution of Mn and pre-alloyed elements in single tracks fabricated with *LED* of 0.25, 0.5, and 0.3 J/mm, respectively. In the previous in-situ alloying study on the bulk CoCrFeMnNi HEA [24], Mn tends to be better homogenised in samples fabricated with high volumetric energy density (*VED*, defined by *P*/*vht* [7]). Good homogeneity has been achieved using the *VED* of 259.3 J/mm^3, and the corresponding *LED* is 0.35 J/mm. In the present study, however, Mn shows poor homogeneity in all single tracks, although the *LED* of 0.5 J/mm adopted has exceeded that used in the homogeneous bulk sample. The distribution of Mn is also different in individual cross-sections fabricated using identical parameters, indicating heterogeneity along the scanning direction. One thing in common is that the tops of meltpools are mostly rich in Mn. In the single-track experiments, the blended powder was spread on the top of pre-alloyed beds, and thus the diffusion of Mn began from the upper part of meltpools. Meanwhile, the distribution of Mn was also affected by its relatively low liquidus density (~5.5 g/cm^3 at 1800 K) and low boiling temperature (2334 K). Moreover, the liquid metals with distinct surface tensions could behave differently due to the well-known Marangoni effect [51-53]. In general, the single-track mapping results indicate that the in-situ alloyed Mn cannot be effectively homogenised by a single-track meltpool, even with the excessive energy input.

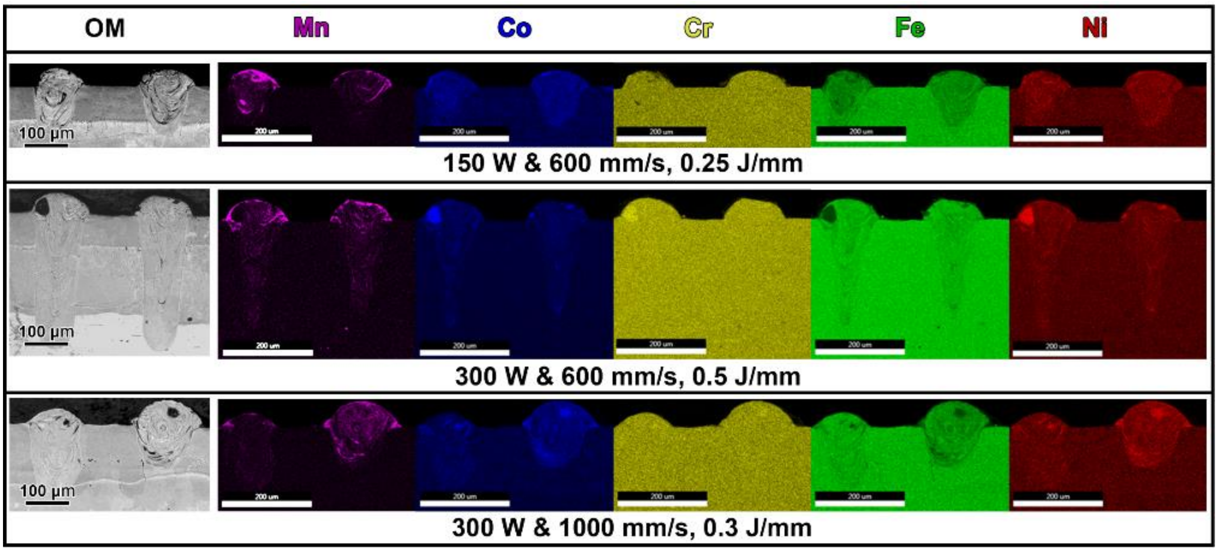

Figure 7.6 EDS mapping results of single tracks labelled by '*P* & *v*, *LED*'.

In single layers, hatching is conducted, and therefore every track is partially remelted by its next track. The Mn mapping results of representative single layers are provided in Figure 7.7. Besides the Mn enrichment near the tops, which is consistent with the single-track meltpools, Mn is also slightly richer in the beginning track of each layer, because the first track of a layer absorbs abundant powder whereas it can only be remelted on one side. As the scanning proceeds, the Mn in the samples with hatch spacing of 60 μm shows better homogeneity. Meanwhile, Mn is also better homogenised in the samples fabricated with the laser power of 300 W. The previous results on meltpool dimensions have shown that the meltpool width is enlarged with a high *LED*. Since the combination of a small hatch spacing and a large meltpool width can lead to more overlapping, the single-layer mapping results indicate that sufficient remelting is critical for the homogenisation of the in-situ alloying. To further reveal the effects of inter-layer remelting, the mapping results of the three-layer samples are provided in Figure 7.7 as well. Two times of inter-layer remelting are introduced by three-layer printing aside from inter-track remelting in single layers. The inner parts of three-layer samples possess significantly improved homogeneity compared with the single-layer samples. Mn oxides have been found in the in-situ alloyed samples; and relative results are provided in Supplementary Figure 7.S2. The formation of the Mn oxides was discussed in detail in a previous study [54].

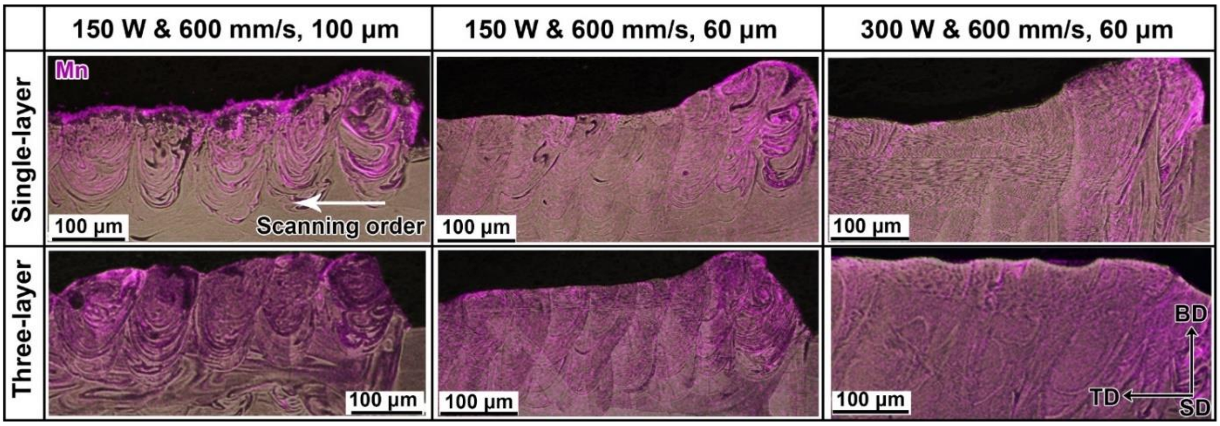

Figure 7.7 EDS mapping results of Mn in the single-layer and three-layer samples labelled by '*P* & *v*, *h*'.

7.3.3 Grain development

The grain development in the LPBF process was revealed via EBSD. Figure 7.8 gives inverse pole figure (IPF) mapping results of single tracks built with an identical *LED* of 0.25 J/mm, and two cross-sections with opposite scanning directions are included for each parameter. Meltpool boundaries in the mapping results and measured dimensions illustrate that these meltpools are similar in size. The results show that most grains can grow continuously across meltpool boundaries rather than nucleation at the boundaries [55]. The epitaxial growth starts from the peripheries and finally converges at the midlines of meltpools after solidification. Although chemical heterogeneity is induced by in-situ alloying, grain development possesses good consistency from pre-alloyed beds to in-situ alloyed tracks. Apart from the similarity in size, preferred orientations along the scanning direction change with different laser parameters. <001> is the dominant orientation with a scanning speed of 600 mm/s, while <101> tends to take advantage as the scanning speed increases to 1000 mm/s.

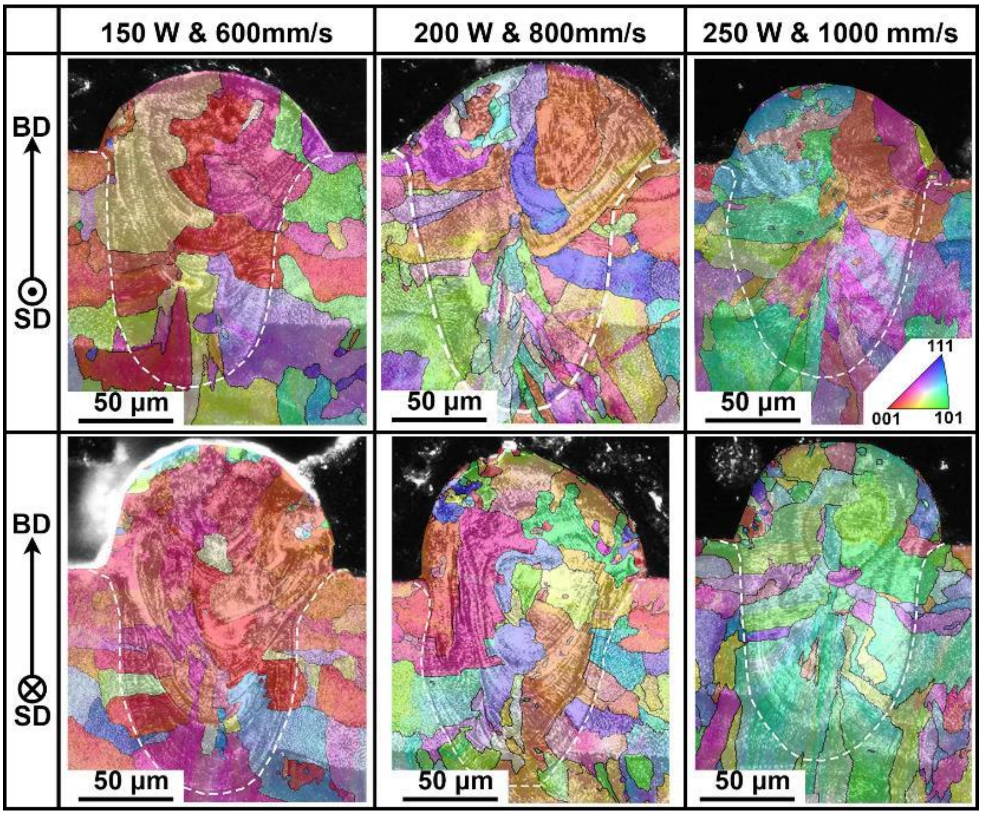

Figure 7.8 IPF mapping results of in-situ alloyed meltpools built with an identical *LED* of 0.25 J/mm.

Further EBSD results of three-layer samples show that preferred orientations in single tracks can be inherited. The intensity of <101> is significantly more substantial in the sample fabricated using a scanning speed of 1000 mm/s, as shown by the IPFs in Figure 7.9. Grain morphology also changes dramatically with laser parameters. In the samples fabricated using 150 W & 600 mm/s, grains are separated by regular vertical boundaries parallel to the BD. Meanwhile, the grains in the samples fabricated using 250 W & 1000 mm/s tend to be randomly distributed but grow more continuously along the BD. In those samples fabricated with the hatch spacing of 60 μm, some grains can grow over 100 μm along the TD. Grain sizes (d_{avg}) have been measured from the six representative samples and correlated to laser parameters and hatch spacing. The samples fabricated of 150 W & 600 mm/s possess the finest grain size, about

55 µm. By applying the parameter of 300 W & 600 mm/s that can enlarge meltpools, or 250 W & 1000 mm/s with a <101> preference, grains are coarsened significantly. Other than laser parameters, the grain size is also affected by hatch spacing as the grains in samples fabricated using the hatch spacing of 60 µm are overall larger than those in samples with the hatch spacing of 100 µm.

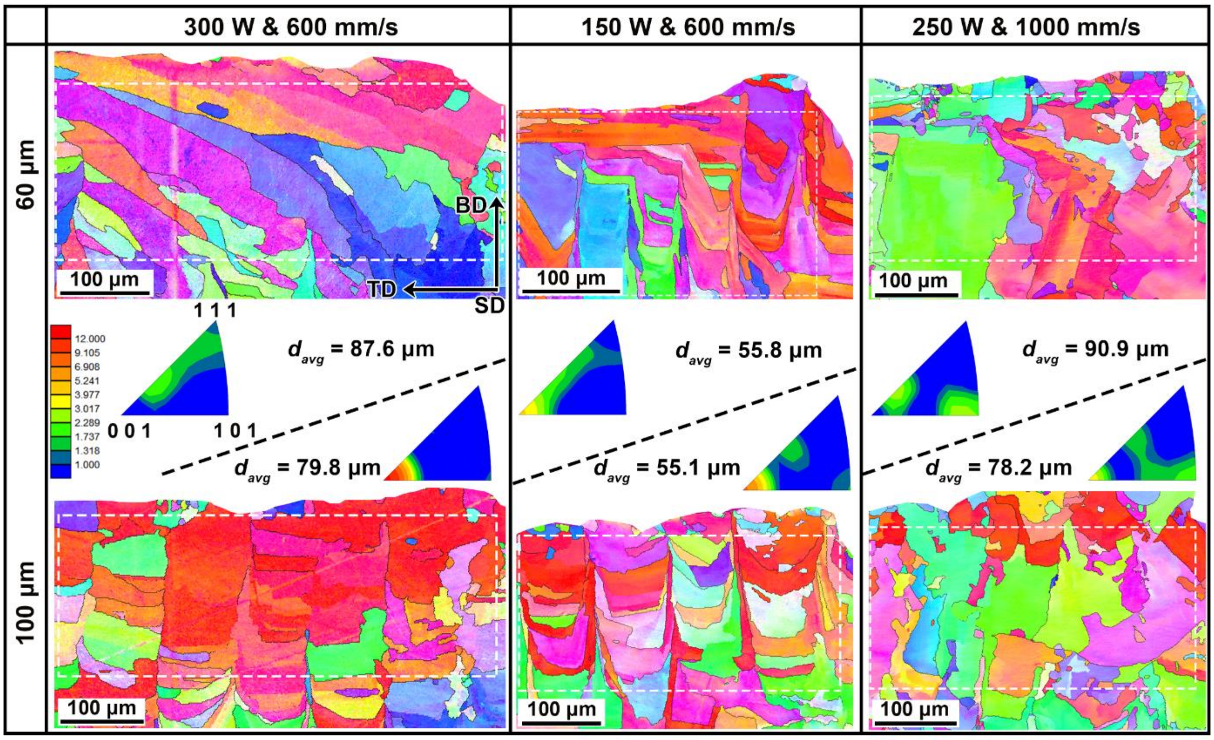

Figure 7.9 IPF mapping results of three-layer samples, with embedded IPFs and average grain size calculated from areas marked by dashed rectangles.

By comparing the grain structures from single-track samples to three-layer samples, the inheritance of preferred orientations and grain growth in the LPBF process are revealed. The correlations between grain development and parameters will be further discussed in this article.

7.4 Discussion

7.4.1 The development of keyhole meltpools

7.4.1.1 Meltpool dimensions

Figure 7.10(a) illustrates the cross-section of an ideal conduction meltpool, which has not been depressed by the recoil pressure on its surface and maintains a semi-circle envelope. The meltpool surface is relatively stable, and its laser absorptivity is about 0.3 for liquid metals. Various conduction methods have shown good applicability for this type of meltpools, and the precision can be improved via modifications such as introducing temperature dependence, convection consumption, gaussian-profiled laser beam, etc. [37]. However, the structure of meltpools will change dramatically and become more complex due to keyhole formation [36]. Figure 7.10(b) presents a schematic of a meltpool with a deep keyhole to illustrate the features of keyhole meltpools. In the keyhole mode, the surface of the meltpool is depressed by the recoil pressure and results in a cavity inside the meltpool. Therefore, the expansion of meltpool is no longer semi-circle like the conduction mode. Because the incident laser penetrates into the keyhole and reflects several times on its inner surface, the absorptivity in the keyhole mode can increase sharply from 0.3 to a range of 0.6–0.8 [43]. As indicated in Figure 7.4(f), the conduction methods, however, can provide an approximate trend of keyhole meltpool widths by using an absorptivity of conduction meltpools (e.g., 0.3). This phenomenon could be addressed by the following consideration. The meltpool boundary predicted by such conduction methods is based on a thermal field heated at the centre of the surface. Meanwhile, in a keyhole meltpool, the development of width can be considered as a heat source with a size similar to the laser beam size working at the boiling point of materials. Hence, the development of width is still an approximation to the models of conduction meltpool. The modification of absorptivity suggests that a large portion of heat input is consumed in the vertical direction due to the formation of keyhole, leading to meltpool depth deeper than the prediction by conduction methods, as illustrated in Figure 7.10(b).

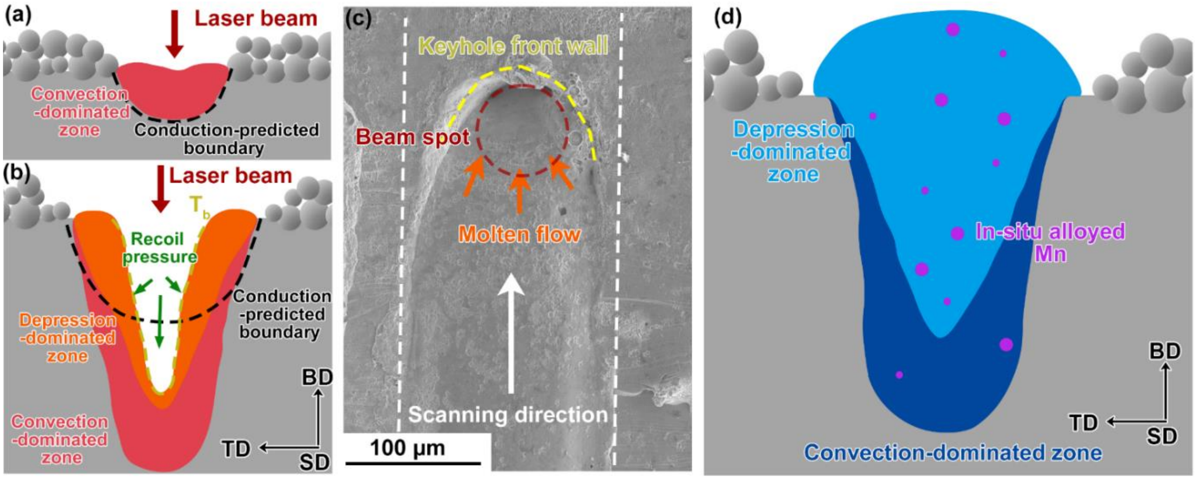

Figure 7.10 Schematics of (a) conduction meltpools and (b) keyhole meltpools. (c) SEM top view at the end of a single-track sample scanned by 300 W & 600 mm/s. (d) Schematic of a solidified in-situ alloyed meltpool.

The in-situ alloyed meltpools are overall narrower than the pre-alloyed meltpools, which might be attributed to the burning loss of Mn. As most single tracks are operated in the keyhole mode, the vaporisation of Mn is inevitable, especially at high energy density due to its lowest heat of vaporisation and lowest boiling point of the five elements. Although the quantification of Mn burning loss is hard to evaluate in single tracks, it has been noticed that the concentration of Mn could drop from 21.53 to 16.67 at. % during the in-situ alloying of CoCrFeMnNi bulk samples [24]. The heat consumed by solid-liquid phase change is less than 10% of the total heat input used to generate the entire thermal field in the scanning process [36], whereas the heat consumed by burning loss could be more significant since the heat of vaporisation is many times of the heat of fusion. On the other hand, the reduction only occurs in width while the depth is overall coincident. According to EDS results, the Mn in meltpools is brought into meltpools from the blended powder covering on pre-alloyed layers and mainly distributes in the upper part of meltpools, which has also been observed in the in-situ alloyed CoCrFeNi HEA using elemental powders [26]. It suggests the heat taken away by Mn vaporisation is mainly from the upper bead of meltpools, where the width was measured. However, the rest part of meltpools, especially the lower part, is still dominated by pre-alloyed layers, and therefore the development of depth is mostly identical with pre-alloyed meltpools.

7.4.1.2 Elemental distribution

Apart from the dimensions, the fluid dynamics in meltpools are also changed dramatically due to the occurrence of keyhole. Figure 7.10(c) shows a top view at the end of a single-track meltpool, which reflects the structure of a moving keyhole meltpool. The keyhole front wall is a smooth curve, and its arc fits well with the beam spot with a diameter of 67 µm. During the scanning process, the molten metal is pushed by the recoil pressure to the bottom and two flanks of the meltpool and then surges back into the cavity as the beam moves forward. The recoil pressure (10^5–10^6 Pa) is orders of magnitude larger than both capillary force (10^4 Pa) and thermocapillary force (10^3–10^4 Pa) which are the two main driven forces of flows in conduction meltpools [56]. As illustrated in Figure 7.10(b), in the zone (marked as depression-dominated zone) close to the keyhole, the flow driven by the recoil pressure overrides the primary flows, i.e., Marangoni flow, driven by convection; meanwhile, the rest (marked as convection-dominated zone) is still mainly affected by convection [57]. Hence, delimitation of elemental distribution occurs in the keyhole meltpool due to the discrepancy of flow zones. As mentioned before, the blended powder is brought into an in-situ alloying meltpool downward, indicating the Mn would primarily distribute in the depression-dominated zone but rarely spread to the convection-dominated zone, as shown in Figure 7.10(d).

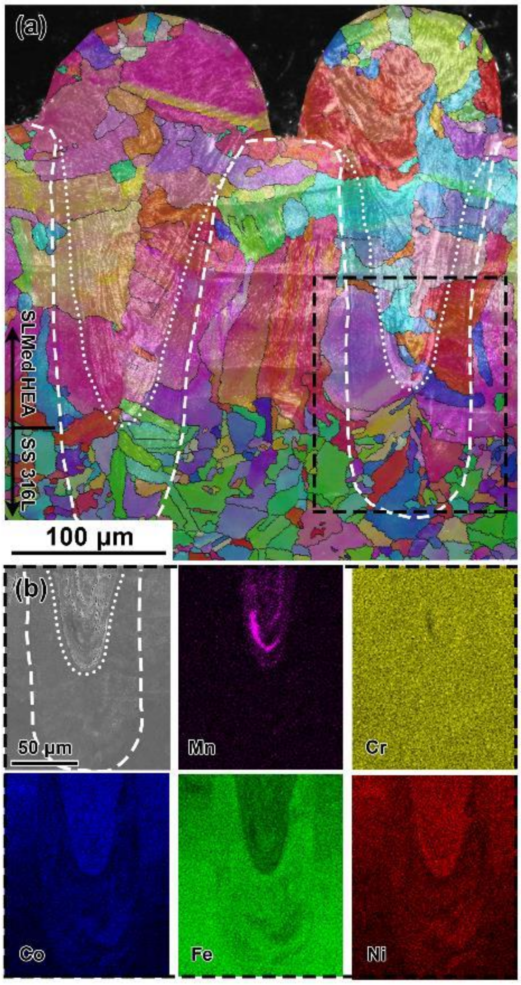

Figure 7.11 (a) IPF mapping & OM results of in-situ alloyed meltpools scanned by 300 W & 600 mm/s, and (b) EDS mapping results of the area marked by the black dashed line. White dashed lines and dotted lines mark the meltpool boundary and internal delimitation, respectively.

Figure 7.11(a) provides two cross-sections of keyhole meltpools. The delimitation of flows can be inherited after solidification and revealed by etching. Despite meltpool boundaries and the flow delimitation, the HEA grains can grow continuously through them during rapid solidification. On the other hand, the homogenisation of Mn is separated by the delimitation, as shown in Figure 7.11(b). The Mn from the blended powder is mainly distributed in the depression-dominated zone, but the heterogeneity of Mn does not break the epitaxial growth of grains. The in-situ alloyed Mn reflects that the flows with disparate intensity co-exist in the keyhole meltpool. Different flow patterns inside LPBF meltpools are hard to be revealed by in-situ monitoring techniques, and are mostly animated by simulation methods. The alloying elements provide clues to the flow distribution during the rapid solidification [56-58]. Once the depression-dominated zone occurs, it overrides the convection-dominated zone in terms of in-situ homogenisation. This phenomenon indicates that applying keyhole meltpools in LPBF in-situ alloying is helpful to the homogenisation of added elements or particles.

7.4.2 In-situ alloying homogenisation in the LPBF process

It has been widely reported in in-situ alloying studies of HEAs that the elemental homogeneity is positively correlated to the *VED* applied [23, 24, 28]. The improvement was attributed to changes in individual meltpools in terms of meltpool size and internal flows. However, as mentioned before, even by operating in the keyhole mode that introduces intensive flows, single tracks cannot achieve ideal homogeneity, whereas the similar laser parameters could produce good homogeneity in the bulk sample [24]. Zhang et al. [18] have reported that the atomic diffusion in meltpools is restricted by the short existing duration of meltpools, and hence its contribution to homogenisation is also not significant. In the LPBF process, single tracks will interact with each other. It suggests that remelting is the critical factor in in-situ homogenisation in the LPBF process. Lin et al. [26] have found that elemental homogeneity can be effectively improved by applying double scanning to remelt each layer.

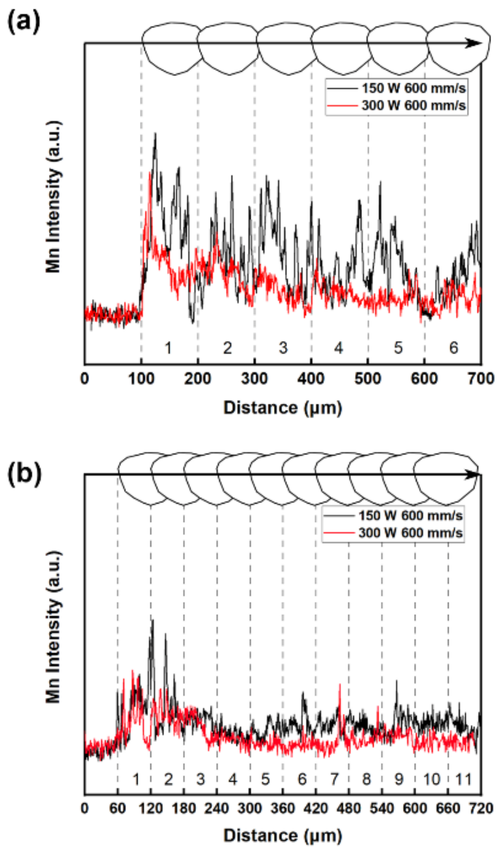

Figure 7.12 EDS line scanning results of Mn in single layers fabricated with hatch spacing of (a) 100 μm, and (b) 60 μm. The scanning lines are drawn 30 μm beneath the surfaces of layers. The arrows in figures mark the scanning consequences of tracks in layers.

Figure 7.12 provides EDS line scanning results of single layers to assess the effect of inter-track remelting. Figure 12(a) shows that the Mn is barely homogenised in the sample 150 W & 600 mm/s since the hatch spacing is close to its meltpool width (111.8 μm), indicating most of the meltpool has not been effectively remelted during the single-layer printing. The homogenisation is significantly improved with the same laser parameters when hatch spacing is set as 60 μm, as shown in Figure 7.12(b). For a given combination of meltpool width and hatch spacing, the horizontal melting cycle M_h can be estimated by $M_h = W/h$. Thus the M_h is improved from 1.12 to1.86 as the hatch spacing decreases from 100 μm to 60 μm. On the other hand, the meltpool width increases to 136.9 μm with a higher laser power of 300 W; hence the M_h with the same hatch spacing can be improved as well.

Inter-layer remelting can be estimated according to given layer thickness and meltpool depth. The in-situ alloying meltpool depth of the sample 300 W & 600 mm/s is 290.7 μm, which is much deeper than the layer thickness of 30 μm. Therefore, the vertical melting cycle (M_v) experienced by each layer is about 9.67 (given by D/t [20]). For a bulk sample built by LPBF, the total melting cycle is therefore estimated by $M_h M_v = WD/ht$. More melting cycles indicate the material solidified previously could be remelted more times in the LPBF process, leading to the improvement of the overall homogenisation. The in-situ homogenisation of Mn in bulk samples has been revealed to be positively correlated to the volumetric energy density [24]. Moreover, the *VED* can also be expressed by *LED*/*ht*; meanwhile, both the width and depth are positively correlated to the *LED*, as shown in Figures 7.4(c, f). Thus the expression of *VED* reflects the melting cycle in bulk samples alternatively, where *P* and *v* stand for meltpool size, while *h* and *t* stand for the density of scanning routes. The melting cycle experienced by the bulk samples with good homogeneity is estimated to be 16.8 according to its parameters which produce the *VED* of 259.3 J/mm^3. It explains the trend that alloying elements are better homogenised in the bulk samples fabricated with a high *VED*.

7.4.3 Grain development in the LPBF process

7.4.3.1 Horizontal grain coarsening

The grain development is correlated to remelting as well. Figure 7.13(a) shows a single layer with coarsened grains growing through multiple meltpools in the TD. Such horizontal growth is abundant in three-layer samples with a small hatch spacing of 60 μm, as shown in Figure 7.9, indicating those bulk samples fabricated using the small hatch spacing could inherit the coarse microstructures. Figure 7.13(b) illustrates the mechanism of horizontal growth affected by remelting. Firstly, in a single-track meltpool, grains grow from the boundary to the midline direction during solidification. Then two different scenarios could occur in layer scanning: (a) For the hatch spacing (100 μm) larger than the half width of the meltpool, only the grains on the remelted side grow continuously into the next track, while the grains on the other side keep their boundaries along the vertical midline. As the scanning continues, such vertical midlines are repeated and separate the layer into grains whose widths approximate the hatch spacing [55, 59]. (b) For the hatch spacing (60 μm) close to or smaller than the half width, the midlines are remelted by the following track. The growth in this situation is not interrupted by the midlines and continues in the TD, resulting in abnormally large grains, e.g., the three-layer sample printed using 300 W & 600 mm/s in Figure 7.9. Because meltpools are wide at the top, grain coarsening is more often observed near the top of a layer, as shown in Figure 7.13(a). This phenomenon can help tailor the grain size in horizontal directions for materials with a wide processing window. Nevertheless, assuming the epitaxial growth in single tracks is dominated by nucleation, the microstructures could be refined by applying a small hatch spacing since the density of meltpool boundaries is increased in this way.

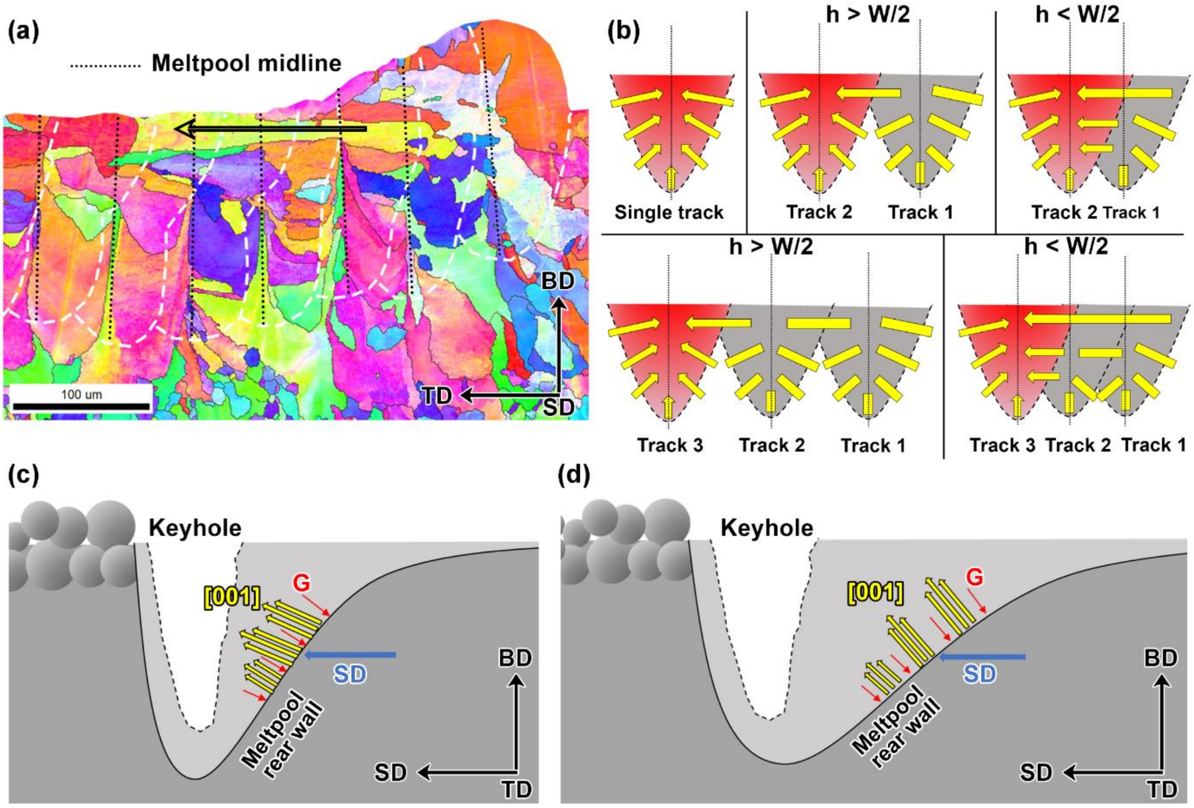

Figure 7.13 (a) IPF mapping of the single-layer sample fabricated with 150 W & 600 mm/s and hatch spacing of 60 µm. (b) Schematic illustrating horizontal grain growth (yellow arrows) with different hatch spacings. Schematic illustrating the grain growth of <001> orientation (notes as [001]) in meltpools with (c) high *P* & *v* and (d) low *P* & *v*, plotted according to in-situ and ex-situ studies of LPBFed meltpools [37, 50, 55, 60].

7.4.3.2 Texture inheritance

The texture is an important factor in the performance of LPBFed parts. Several reports have shown that the texture in LPBFed parts can be tailored via processing optimisation without changing powder or printer [61, 62]. This study shows that the preferred grain orientations in single tracks and can be progressively inherited during the layer-by-layer process. So, to tailor the texture in bulk samples, the texture development in single tracks can be an important starting point.

The cross-sections provided in Figure 7.8 are similar in their dimensions as solidified single tracks. Meanwhile, during the laser scanning process, the meltpool length is mainly correlated to the scanning speed [37, 50]. The meltpools formed with the scanning speed of 1000 mm/s are longer than those printed with the scanning speed of 600 mm/s. The combinations of similar depths but different lengths could lead to different slopes at the rear wall of meltpools [63]. And since the solidification takes place at the meltpools rear wall in the LPBF process, the grain development is also affected. Considering a short meltpool that is nearly movement-free, its rear wall is nearly perpendicular to the scanning direction, and therefore the direction of the local thermal gradient (***G***) at its rear wall is almost antiparallel to the scanning direction [55, 60]. As the scanning speed increases, the meltpool is stretched in the scanning direction, and the direction of ***G*** starts to change from the horizontal direction to the vertical direction. For the face-centred-cubic (FCC) CoCrFeMnNi HEA, <001> is the preferred growth direction aligned with the direction of ***G***. Therefore, the growth of <001> changes from the scanning direction to vertical direction as well, leading to the change of corresponding crystallography orientations in the scanning direction, as illustrated in Figures 7.13 (c, d).

The texture in single tracks also influences the grain morphology in three-layer samples. As the preferred orientation in single tracks changes from <001> to <101>, the regular vertical boundaries disappear, and more importantly, grains are coarsened in the building direction, resulting in increased grain size, as shown in Figure 7.9. Pham et al. [55] studied the side-branching in the LPBF process of FCC alloys, and their results showed that grains could grow continuously through multiple layers to form columnar grains when <101> orientations dominated the SD/TD in bulk samples. Therefore, even similar densification can be obtained using the identical *LED* and scanning strategy, the resultant grain structures in bulk samples can still be distinct. Furthermore, the local hardness distribution in meltpools is also affected by texture, and the relative nano-indentation mapping results are provided in Supplementary Figure 7.S3. By manipulating single-track crystallography and the associated scanning strategy in the whole LPBF process, it is possible to customise grain structures locally in one component.

7.4.4 Defects accumulated in the LPBF process

In this study, the LPBF building process is conducted up to three layers; some defects that may occur in bulk samples can be foreseen by analysing the three-layer samples.

Figure 7.14(a) shows a three-layer sample in which the tracks barely overlap with each other. In this situation, the meltpool width is close to or even smaller than the hatch spacing. Although there is no apparent gap between these tracks in the cross-section, such insufficient hatching can lead to lack-of-fusion pores as multiple layers pile up. Tang et al. [38] introduce a criterion for sufficient overlapping based on meltpool dimensions and processing parameters, as given below:

$$\left(\frac{h}{W}\right)^2 + \left(\frac{t}{L}\right)^2 \leq 1 \tag{7.9}$$

where L is the total length including depth and upper-bead height of meltpools. The measured W and L of single-track meltpool in Figure 7.14(a) are 91.6 μm and 103.7 μm, respectively. With 100 μm for h and 30 μm for t, the calculated result is 1.27, which suggests that lack-of-fusion porosity would occur in as-built parts. The actual bulk samples produced using the corresponding *VED* (50 J/mm^3) were poorly densified due to the abundant lack-of-fusion pores [7, 24].

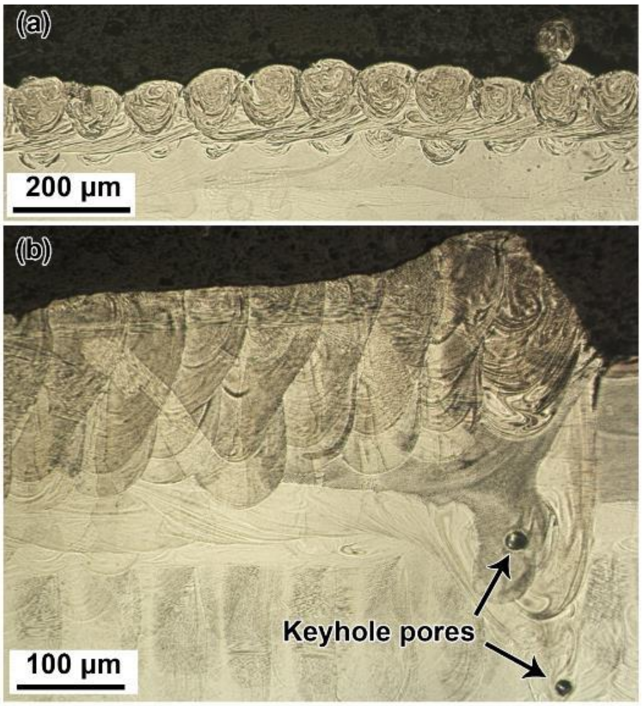

Figure 7.14 OM images of (a) a three-layer sample without good hatching and (b) a three-layer sample with keyhole pores at its edge.

As mentioned in previous sections, the meltpools in this study are mostly operated in the keyhole mode. However, keyhole pores are rarely observed inside those meltpools. It is discussed as follows: One primary pore-forming mechanism under the keyhole mode is that the molten flow from the keyhole rear wall reaches the front wall, resulting in the collapse at the keyhole bottom during laser movement. However, once the scanning speed is fast enough to keep a stable distance between the rear and front walls, the collapse can be avoided in keyhole meltpools. Keyhole meltpools with a stable and open depression zone were in-situ observed in meltpools scanned using scanning speed above 600 mm/s, and laser power below 500 W [50, 56, 64]. Hence the keyhole mode is not identical to a pore trigger. On the other hand, keyhole pores are frequently observed at the edge of three-layer samples, as shown in Figure 7.14(b). The location of these pores is much deeper than the meltpool depth measured from the corresponding single tracks, implying that they are hard to be eliminated by remelting. The formation of such pores is due to the acceleration and deceleration of the laser at the ends of tracks. Especially for high laser power, the beam spot can be held for too long before its move to the next point, leaving a meltpool that much deeper than the stable depth in the rest of the track. Even with a moderate *LED* that theoretically generates a conduction meltpool, keyhole pores may still occur at the boundary of a layer, where tracks start and end. Shift and rotation can be set between layers to avoid such defects from concentrating locally in LPBFed parts. Moreover, to further improve the densification, it is worth dynamically optimising the acceleration and deceleration process as well [20].

7.5 Conclusions

By tracing the LPBF in-situ alloying process back to single tracks, the microstructural evolution and its correlation to printing parameters are revealed in terms of meltpool dimensions, elemental homogenisation, and grain development. The key findings are summarised as below:

- In the *LED* range between 0.15 and 0.5 J/mm, meltpools of the CoCrFeNi HEAs are no longer in the conduction mode, and they start to work in the keyhole mode. The comparison between modelling methods suggests that their applicability further depends on the meltpool modes. The addition of elemental Mn powder led to 9% decrease in meltpool widths, whereas meltpool depths were maintained similarly in the *LED* range.
- The intense flow generated in the keyhole meltpool dominates the homogenisation of Mn due to its superior intensity. Remelting is the most critical factor in achieving homogeneity in the LPBF process, and the total melting cycle can be higher than 10 in a well-homogenised part.

- The correlations between grain structures and printing parameters are evaluated from the scope of single tracks. Using a hatch spacing smaller than the half width of meltpool promotes horizontal grain growth. The texture in LPBF parts reflects the inheritance of preferred orientations from single tracks. Moreover, the preferred orientations in single tracks can be tailored by adjusting laser power and scanning speed, leading to different grain structures in multi-layer building.

7.6 Supplementary Materials

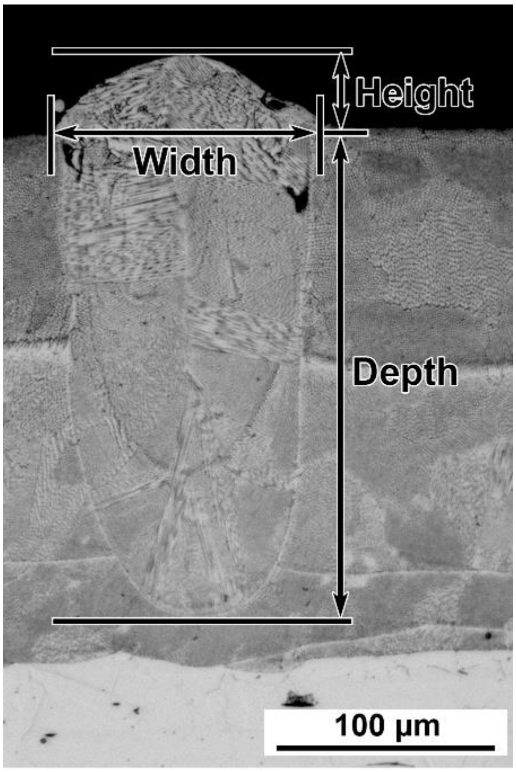

Figure 7.S1 Schematic illustrating the measurement of the width (*W*), depth (*D*), and height (*H*) of a meltpool.

Table 7.S1 Measured dimensions of pre-alloyed CoCrFeNi meltpools.

P (W)	*v* (mm/s)	*LED* (J/mm)	*W* (μm)	*D* (μm)	*H* (μm)
150	600	0.250	117.2	121.7	71.0
150	700	0.214	115.1	90.7	66.3
150	800	0.188	110.7	82.5	54.5
150	900	0.167	109.6	73.2	45.3
150	1000	0.150	99.2	60.8	50.4
200	600	0.333	124.3	185.2	80.2
200	700	0.286	125.1	153.5	53.2
200	800	0.250	125.4	132.6	31.1
200	900	0.222	124.2	106.5	40.3
200	1000	0.200	119.0	96.7	29.4
250	600	0.417	134.5	222.4	103.2
250	700	0.357	115.9	193.3	75.0
250	800	0.313	122.2	162.9	69.3
250	900	0.278	127.7	145.9	45.9
250	1000	0.250	129.7	116.8	40.7
300	600	0.500	151.2	319.2	60.3
300	700	0.429	136.9	246.7	43.7
300	800	0.375	141.6	217.3	36.0
300	900	0.333	144.4	176.7	35.0
300	1000	0.300	140.4	158.0	25.2

Table 7.S2 Measured dimensions of in-situ alloyed CoCrFeMnNi meltpools.

P (W)	*v* (mm/s)	*LED* (J/mm)	*W* (μm)	*D* (μm)	*H* (μm)
150	600	0.250	111.8	118.1	59.8
150	700	0.214	108.5	104.4	56.9
150	800	0.188	98.5	86.9	60.7
150	900	0.167	96.3	75.3	49.1
150	1000	0.150	91.6	60.0	43.6
200	600	0.333	123.6	180.9	69.5
200	700	0.286	122.4	145.4	63.7
200	800	0.250	117.4	126.7	61.5
200	900	0.222	107.8	105.9	62.4
200	1000	0.200	100.9	96.5	56.4
250	600	0.417	133.8	239.8	65.5
250	700	0.357	126.6	195.5	78.0
250	800	0.313	119.1	168.4	69.3
250	900	0.278	115.6	142.0	68.3
250	1000	0.250	110.2	122.1	72.4
300	600	0.500	136.9	290.7	80.9
300	700	0.429	140.4	252.4	73.8
300	800	0.375	125.9	206.9	66.4
300	900	0.333	124.6	180.9	61.3
300	1000	0.300	115.5	158.8	52.9

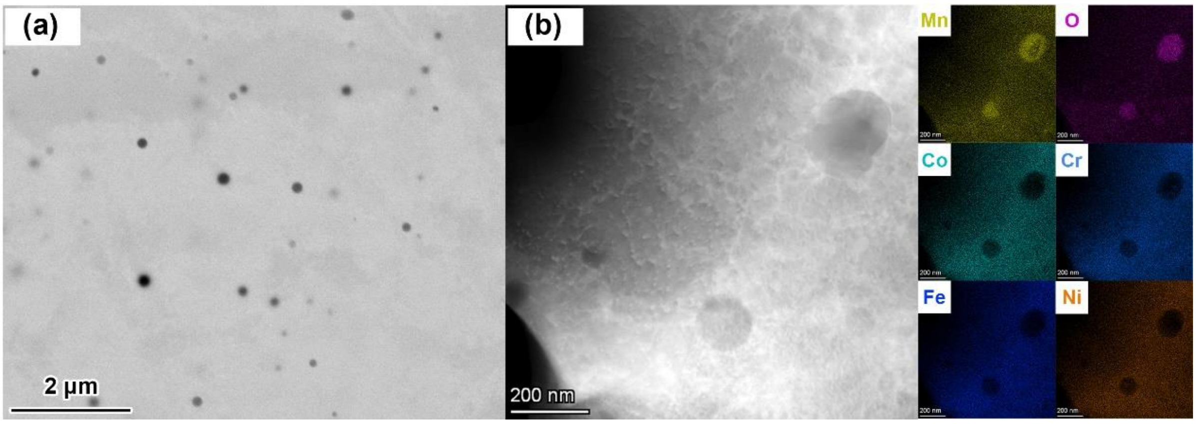

Figure 7.S2 (a) SEM image and (b) scanning transmission electron microscopy (STEM) dark-field image with EDS mapping results showing the Mn oxides in three-layer samples. STEM image was acquired using a Tecnai G2 F20.

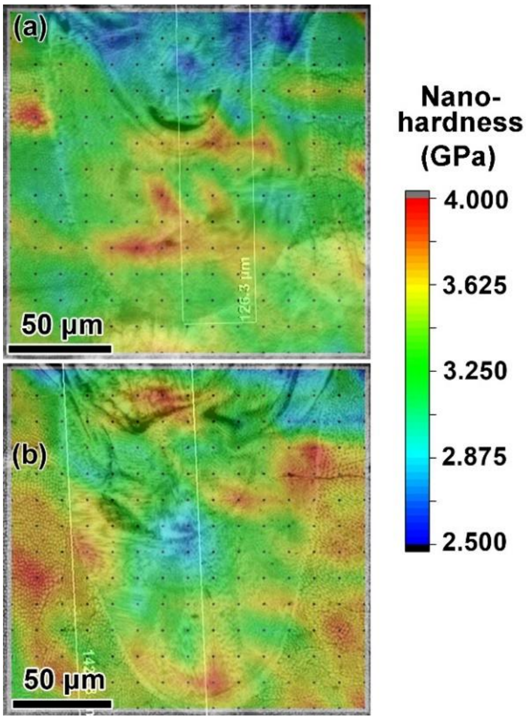

Figure 7.S3 Nano-indentation hardness mapping results of the single-track meltpools produced by (a) 150 W & 600 mm/s and (b) 250 W & 1000 mm/s.*

***Note**:

Nano-indentation was carried out to assess the local hardness distribution of single-track meltpools. A Hysitron TI-950 equipped with a Berkovich indenter was used for the nano-indentation mapping. The height and width of the array were set according to the meltpool dimensions, and the indentations in the array were separated by 10 μm in both row and column. The maximum load was set as 8000 μN; meanwhile the load time, dwell time and unload time were set as 5, 2, and 5 s, respectively for each point.

Figure 7.S3 presents the nano-indentation mapping results of single-track meltpools fabricated using an identical *LED* of 0.25 J/mm. The average hardness results measured from the 150 W & 600 mm/s (<001>-dominated) and 250 W & 1000 mm/s (<101>-dominated) samples are 3.28 GPa and 3.42 GPa, respectively, implying a slight orientation dependency similar to the austenitic alloy [65]. Moreover, the hardness results of the in-situ alloyed meltpools are both higher than the hardness (2.84 GPa) measured from the CoCrFeMnNi HEA prepared using pre-alloyed powder [66]. Regarding the hardness distribution, there is an apparent drop in the area close to the upper bead, showing local discrepancies rather than the uniform local properties reported in AlSi10Mg meltpool [35].

7.7 Acknowledgements

This research was supported by Research and Development Program Project in Key Areas of Guangdong Province [grant number 2019B090907001], Shenzhen Science and Technology Innovation Commission [grant number JCYJ20180504165824643 and JCYJ20170817111811303], and the National Natural Science Foundation of China [grant numbers 51971108, U19A2085].

7.8 References

[1] Y. Brif, M. Thomas, I. Todd, The use of high-entropy alloys in additive manufacturing, Scripta Materialia 99 (2015) 93-96. http://doi.org/10.1016/j.scriptamat.2014.11.037.

[2] X. Li, Additive manufacturing of advanced multi-component alloys: Bulk metallic glasses and high entropy alloys, Advanced Engineering Materials 20(5) (2017) 1700874. http://doi.org/10.1002/adem.201700874.

[3] J. Kim, A. Wakai, A. Moridi, Materials and manufacturing renaissance: Additive manufacturing of high-entropy alloys, Journal of Materials Research 35(15) (2020) 1963-1983. http://doi.org/10.1557/jmr.2020.140.

[4] P.F. Zhou, D.H. Xiao, Z. Wu, X.Q. Ou, Al0.5FeCoCrNi high entropy alloy prepared by selective laser melting with gas-atomized pre-alloy powders, Materials Science and Engineering: A 739 (2019) 86-89. http://doi.org/10.1016/j.msea.2018.10.035.

[5] C. Han, Q. Fang, Y. Shi, S.B. Tor, C.K. Chua, K. Zhou, Recent advances on high-entropy alloys for 3D printing, Advanced Matererials 32(26) (2020) 1903855. http://doi.org/10.1002/adma.201903855.

[6] D. Lin, L. Xu, H. Jing, Y. Han, L. Zhao, F. Minami, Effects of annealing on the structure and mechanical properties of FeCoCrNi high-entropy alloy fabricated via selective laser melting, Additive Manufacturing 32 (2020) 101058. http://doi.org/10.1016/j.addma.2020.101058.

[7] R. Li, P. Niu, T. Yuan, P. Cao, C. Chen, K. Zhou, Selective laser melting of an equiatomic CoCrFeMnNi high-entropy alloy: Processability, non-equilibrium microstructure and mechanical property, Journal of Alloys and Compounds 746 (2018) 125-134. http://doi.org/10.1016/j.jallcom.2018.02.298.

[8] A. Piglione, B. Dovgyy, C. Liu, C.M. Gourlay, P.A. Hooper, M.S. Pham, Printability and microstructure of the CoCrFeMnNi high-entropy alloy fabricated by laser powder bed fusion, Materials Letters 224 (2018) 22-25. http://doi.org/10.1016/j.matlet.2018.04.052.

[9] J. Ren, C. Mahajan, L. Liu, D. Follette, W. Chen, S. Mukherjee, Corrosion behavior of selectively laser melted CoCrFeMnNi high entropy alloy, Metals 9(10) (2019) 1029. http://doi.org/10.3390/met9101029.

[10] J.M. Park, J. Choe, J.G. Kim, J.W. Bae, J. Moon, S. Yang, K.T. Kim, J.-H. Yu, H.S. Kim, Superior tensile properties of 1%C-CoCrFeMnNi high-entropy alloy additively manufactured by selective laser melting, Materials Research Letters 8(1) (2019) 1-7. http://doi.org/10.1080/21663831.2019.1638844.

[11] B. Li, B. Qian, Y. Xu, Z. Liu, F. Xuan, Fine-structured CoCrFeNiMn high-entropy alloy matrix composite with 12 wt% TiN particle reinforcements via selective laser melting assisted additive manufacturing, Materials Letters 252 (2019) 88-91. http://doi.org/10.1016/j.matlet.2019.05.108.

[12] D.E. Jodi, J. Park, N. Park, Strengthening of ultrafine-grained equiatomic CoCrFeMnNi high-entropy alloy by nitrogen addition, Materials Letters 258 (2020) 126772. http://doi.org/10.1016/j.matlet.2019.126772.

[13] T. DebRoy, H.L. Wei, J.S. Zuback, T. Mukherjee, J.W. Elmer, J.O. Milewski, A.M. Beese, A. Wilson-Heid, A. De, W. Zhang, Additive manufacturing of metallic components – Process, structure and properties, Progress in Materials Science 92 (2018) 112-224. http://doi.org/10.1016/j.pmatsci.2017.10.001.

[14] Y. Dong, Y. Li, T. Ebel, M. Yan, Cost-affordable, high-performance Ti–TiB composite for selective laser melting additive manufacturing, Journal of Materials Research 35 (2020) 1922-1935. http://doi.org/10.1557/jmr.2019.389.

[15] M.H. Mosallanejad, B. Niroumand, A. Aversa, A. Saboori, In-situ alloying in laser-based additive manufacturing processes: A critical review, Journal of Alloys and Compounds 872 (2021) 159567. http://doi.org/10.1016/j.jallcom.2021.159567.

[16] S.L. Sing, S. Huang, G.D. Goh, G.L. Goh, C.F. Tey, J.H.K. Tan, W.Y. Yeong, Emerging metallic systems for additive manufacturing: In-situ alloying and multi-metal processing in laser powder bed fusion, Progress in Materials Science 119 (2021) 100795. http://doi.org/10.1016/j.pmatsci.2021.100795.

[17] M. Cagirici, P. Wang, F.L. Ng, M.L.S. Nai, J. Ding, J. Wei, Additive manufacturing of high-entropy alloys by thermophysical calculations and in situ alloying, Journal of Materials Science & Technology 94 (2021) 53-66. http://doi.org/10.1016/j.jmst.2021.03.038.

[18] Z.H. Zhang, Y.H. Zhou, S.Y. Zhou, L. Zhang, M. Yan, Mechanically blended Al: Simple but effective approach to improving mechanical property and thermal stability of selective laser-melted Inconel 718, Metallurgical and Materials Transactions A 50a(8) (2019) 3922-3936. http://doi.org/10.1007/s11661-019-05299-6..

[19] B. Zhang, N.-E. Fenineche, H. Liao, C. Coddet, Microstructure and magnetic properties of Fe–Ni alloy fabricated by selective laser melting Fe/Ni mixed powders, Journal of Materials Science & Technology 29(8) (2013) 757-760. http://doi.org/10.1016/j.jmst.2013.05.001.

[20] R. Duan, S. Li, B. Cai, Z. Tao, W. Zhu, F. Ren, M.M. Attallah, In situ alloying based laser powder bed fusion processing of β Ti–Mo alloy to fabricate functionally graded composites, Composites Part B: Engineering 222 (2021) 109059. http://doi.org/10.1016/j.compositesb.2021.109059.

[21] I. Polozov, V. Sufiiarov, A. Popovich, D. Masaylo, A. Grigoriev, Synthesis of Ti-5Al, Ti-6Al-7Nb, and Ti-22Al-25Nb alloys from elemental powders using powder-bed fusion additive manufacturing, Journal of Alloys and Compounds 763 (2018) 436-445. http://doi.org/10.1016/j.jallcom.2018.05.325.

[22] V.V. Popov, A. Katz-Demyanetz, A. Koptyug, M. Bamberger, Selective electron beam melting of Al0.5CrMoNbTa0.5 high entropy alloys using elemental powder blend, Heliyon 5(2) (2019) e01188. http://doi.org/10.1016/j.heliyon.2019.e01188.

[23] S. Ewald, F. Kies, S. Hermsen, M. Voshage, C. Haase, J.H. Schleifenbaum, Rapid alloy development of extremely high-alloyed metals using powder blends in laser powder bed fusion, Materials (Basel) 12(10) (2019) 1706. http://doi.org/10.3390/ma12101706.

[24] P. Chen, S. Li, Y. Zhou, M. Yan, M.M. Attallah, Fabricating CoCrFeMnNi high entropy alloy via selective laser melting in-situ alloying, Journal of Materials Science & Technology 43 (2020) 40-43. http://doi.org/10.1016/j.jmst.2020.01.002.

[25] S. Luo, C. Zhao, H. Yang, Q. Liu, Z. Wang, X. Zeng, Selective laser melting of dual phase AlCrCuFeNix high entropy alloys: formability, heterogeneous microstructures and deformation mechanisms, Additive Manufacturing 31 (2019) 100925. http://doi.org/10.1016/j.addma.2019.100925.

[26] D. Lin, L. Xu, X. Li, H. Jing, G. Qin, H. Pang, F. Minami, A Si-containing FeCoCrNi high-entropy alloy with high strength and ductility synthesized in situ via selective laser melting, Additive Manufacturing 35 (2020) 101340. http://doi.org/10.1016/j.addma.2020.101340.

[27] K. Sun, W. Peng, L. Yang, L. Fang, Effect of SLM processing parameters on microstructures and mechanical properties of Al0.5CoCrFeNi high entropy alloys, Metals 10(2) (2020) 292. http://doi.org/10.3390/met10020292.

[28] Y. Hou, H. Su, H. Zhang, X. Wang, C. Wang, Fabricating homogeneous FeCoCrNi High-entropy alloys via SLM in situ alloying, Metals 11(6) (2021) 942. http://doi.org/10.3390/met11060942.

[29] F. Huber, D. Bartels, M. Schmidt, In-situ alloy formation of a WMoTaNbV refractory metal high entropy alloy by laser powder bed fusion (PBF-LB/M), Materials (Basel) 14(11) (2021) 3095. http://doi.org/10.3390/ma14113095.

[30] Y. Kuzminova, A. Shibalova, S. Evlashin, I. Shishkovsky, P. Krakhmalev, Structural effect of low Al content in the in-situ additive manufactured CrFeCoNiAlx high-entropy alloy, Materials Letters 303 (2021) 130487. http://doi.org/10.1016/j.matlet.2021.130487.

[31] J. Gao, Y. Jin, Y. Fan, D. Xu, L. Meng, C. Wang, Y. Yu, D. Zhang, F. Wang, Fabricating antibacterial CoCrCuFeNi high-entropy alloy via selective laser melting and in-situ alloying, Journal of Materials Science & Technology 102 (2022) 159-165. http://doi.org/10.1016/j.jmst.2021.07.002.

[32] C. Guo, Z. Xu, Y. Zhou, S. Shi, G. Li, H. Lu, Q. Zhu, R.M. Ward, Single-track investigation of IN738LC superalloy fabricated by laser powder bed fusion: Track morphology, bead characteristics and part quality, Journal of Materials Processing Technology 290 (2021) 117000. http://doi.org/10.1016/j.jmatprotec.2020.117000.

[33] L. Johnson, M. Mahmoudi, B. Zhang, R. Seede, X. Huang, J.T. Maier, H.J. Maier, I. Karaman, A. Elwany, R. Arróyave, Assessing printability maps in additive manufacturing of metal alloys, Acta Materialia 176 (2019) 199-210. http://doi.org/10.1016/j.actamat.2019.07.005.

[34] H. Li, Y. Huang, J. Sun, Y. Lu, The relationship between thermo-mechanical history, microstructure and mechanical properties in additively manufactured CoCrFeMnNi high entropy alloy, Journal of Materials Science & Technology 77 (2021) 187-195. http://doi.org/10.1016/j.jmst.2020.10.052.

[35] N.M. Everitt, Nanoindentation shows uniform local mechanical properties across melt pools and layers produced by selective laser melting of AlSi 10Mg alloy, Advanced Materials Letters 7(1) (2016) 13-16. http://doi.org/10.5185/amlett.2016.6171.

[36] R. Fabbro, M. Dal, P. Peyre, F. Coste, M. Schneider, V. Gunenthiram, Analysis and possible estimation of keyhole depths evolution, using laser operating parameters and material properties, Journal of Laser Applications 30(3) (2018) 032410. http://doi.org/10.2351/1.5040624.

[37] A.M. Rubenchik, W.E. King, S.S. Wu, Scaling laws for the additive manufacturing, Journal of Materials Processing Technology 257 (2018) 234-243. http://doi.org/10.1016/j.jmatprotec.2018.02.034.

[38] M. Tang, P.C. Pistorius, J.L. Beuth, Prediction of lack-of-fusion porosity for powder bed fusion, Additive Manufacturing 14 (2017) 39-48. http://doi.org/10.1016/j.addma.2016.12.001.

[39] D. Rosenthal, Mathematical theory of heat distribution during welding and cutting, Welding Journal 20(5) (1941) 220-234.

[40] T.W. Eagar, N.S. Tsai, Temperature-fields produced by traveling distributed heat-sources, Welding Journal 62(12) (1983) 346-355.

[41] D.B. Hann, J. Iammi, J. Folkes, Keyholing or Conduction – Prediction of Laser Penetration Depth, in: S. Hinduja, L. Li (Eds.) Proceedings of the 36th International MATADOR Conference, Springer London, London, 2010, pp. 275-278.

[42] R. Fabbro, Melt pool and keyhole behaviour analysis for deep penetration laser welding, Journal of Physics D: Applied Physics 43(44) (2010) 445501. http://doi.org/10.1088/0022-3727/43/44/445501.

[43] J. Ye, S.A. Khairallah, A.M. Rubenchik, M.F. Crumb, G. Guss, J. Belak, M.J. Matthews, Energy coupling mechanisms and scaling behavior associated with laser powder bed fusion additive manufacturing, Advanced Engineering Materials 21(7) (2019) 1900185. http://doi.org/10.1002/adem.201900185.

[44] P. Promoppatum, S.-C. Yao, P.C. Pistorius, A.D. Rollett, A comprehensive comparison of the analytical and numerical prediction of the thermal history and solidification microstructure of Inconel 718 products made by laser powder-bed fusion, Engineering 3(5) (2017) 685-694. http://doi.org/10.1016/j.Eng.2017.05.023.

[45] L.R. Goossens, B. Van Hooreweder, A virtual sensing approach for monitoring melt-pool dimensions using high speed coaxial imaging during laser powder bed fusion of metals, Additive Manufacturing 40 (2021) 101923. http://doi.org/10.1016/j.addma.2021.101923.

[46] M. Döring, G. Boussinot, J.F. Hagen, M. Apel, S. Kohl, M. Schmidt, Scaling melt pool geometry over a wide range of laser scanning speeds during laser-based Powder Bed Fusion, Procedia CIRP 94 (2020) 58-63. https://doi.org/10.1016/j.procir.2020.09.012.

[47] H.P. Chou, Y.S. Chang, S.K. Chen, J.-W. Yeh, Microstructure, thermophysical and electrical properties in AlxCoCrFeNi (0≤x≤2) high-entropy alloys, Materials Science and Engineering: B 163(3) (2009) 184-189. http://doi.org/10.1016/j.mseb.2009.05.024.

[48] J. Trapp, A.M. Rubenchik, G. Guss, M.J. Matthews, In situ absorptivity measurements of metallic powders during laser powder-bed fusion additive manufacturing, Applied Materials Today 9 (2017) 341-349. http://doi.org/10.1016/j.apmt.2017.08.006.

[49] H. Yao, J.W. Qiao, M. Gao, J. Hawk, S.G. Ma, H. Zhou, MoNbTaV medium-entropy alloy, Entropy 18(5) (2016) 189. http://doi.org/10.3390/e18050189.

[50] Q. Guo, C. Zhao, M. Qu, L. Xiong, L.I. Escano, S.M.H. Hojjatzadeh, N.D. Parab, K. Fezzaa, W. Everhart, T. Sun, L. Chen, In-situ characterization and quantification of melt pool variation under constant input energy density in laser powder bed fusion additive manufacturing process, Additive Manufacturing 28 (2019) 600-609. http://doi.org/10.1016/j.addma.2019.04.021.

[51] M.J. Assael, K. Kakosimos, R.M. Banish, J. Brillo, I. Egry, R. Brooks, P.N. Quested, K.C. Mills, A. Nagashima, Y. Sato, W.A. Wakeham, Reference data for the density and viscosity of liquid aluminum and liquid iron, Journal of Physical and Chemical Reference Data 35(1) (2006) 285-300. http://doi.org/10.1063/1.2149380.

[52] I. Korobeinikov, R. Endo, S. Seetharaman, O. Volkova, Density of liquid manganese measured using the maximum bubble pressure method, Metallurgical and Materials Transactions B 52(2) (2021) 571-575. http://doi.org/10.1007/s11663-020-02044-y.

[53] C. Tan, Y. Chew, G. Bi, D. Wang, W. Ma, Y. Yang, K. Zhou, Additive manufacturing of steel–copper functionally graded material with ultrahigh bonding strength, Journal of Materials Science & Technology 72 (2021) 217-222. http://doi.org/10.1016/j.jmst.2020.07.044.

[54] P. Chen, C. Yang, S. Li, M.M. Attallah, M. Yan, In-situ alloyed, oxide-dispersion-strengthened CoCrFeMnNi high entropy alloy fabricated via laser powder bed fusion, Materials & Design 194 (2020) 108966. http://doi.org/10.1016/j.matdes.2020.108966.

[55] M.S. Pham, B. Dovgyy, P.A. Hooper, C.M. Gourlay, A. Piglione, The role of side-branching in microstructure development in laser powder-bed fusion, Nature Communications 11(1) (2020) 749. http://doi.org/10.1038/s41467-020-14453-3.

[56] N. Kouraytem, X. Li, R. Cunningham, C. Zhao, N. Parab, T. Sun, A.D. Rollett, A.D. Spear, W. Tan, Effect of laser-matter interaction on molten pool flow and keyhole dynamics, Physical Review Applied 11(6) (2019) 064054. http://doi.org/10.1103/PhysRevApplied.11.064054.

[57] S.A. Khairallah, A.T. Anderson, A. Rubenchik, W.E. King, Laser powder-bed fusion additive manufacturing: Physics of complex melt flow and formation mechanisms of pores, spatter, and denudation zones, Acta Materialia 108 (2016) 36-45. http://doi.org/10.1016/j.actamat.2016.02.014.

[58] Y. Feng, X. Gao, Y. Zhang, C. Peng, X. Gui, Y. Sun, X. Xiao, Simulation and experiment for dynamics of laser welding keyhole and molten pool at different penetration status, The

International Journal of Advanced Manufacturing Technology 112(7-8) (2021) 2301-2312. http://doi.org/10.1007/s00170-020-06489-y.

[59] N. Nadammal, S. Cabeza, T. Mishurova, T. Thiede, A. Kromm, C. Seyfert, L. Farahbod, C. Haberland, J.A. Schneider, P.D. Portella, G. Bruno, Effect of hatch length on the development of microstructure, texture and residual stresses in selective laser melted superalloy Inconel 718, Materials & Design 134 (2017) 139-150. http://doi.org/10.1016/j.matdes.2017.08.049.

[60] C. Zhang, K. Feng, H. Kokawa, B. Han, Z. Li, Cracking mechanism and mechanical properties of selective laser melted CoCrFeMnNi high entropy alloy using different scanning strategies, Materials Science and Engineering: A 789 (2020) 139672. http://doi.org/10.1016/j.msea.2020.139672.

[61] B. Attard, S. Cruchley, C. Beetz, M. Megahed, Y.L. Chiu, M.M. Attallah, Microstructural control during laser powder fusion to create graded microstructure Ni-superalloy components, Additive Manufacturing 36 (2020) 101432. http://doi.org/10.1016/j.addma.2020.101432.

[62] J. Zou, Y. Gaber, G. Voulazeris, S. Li, L. Vazquez, L.-F. Liu, M.Y. Yao, Y.J. Wang, M. Holynski, K. Bongs, M.M. Attallah, Controlling the grain orientation during laser powder bed fusion to tailor the magnetic characteristics in a Ni-Fe based soft magnet, Acta Materialia 158 (2018) 230-238. http://doi.org/10.1016/j.actamat.2018.07.064.

[63] C. Tan, F. Weng, S. Sui, Y. Chew, G. Bi, Progress and perspectives in laser additive manufacturing of key aeroengine materials, International Journal of Machine Tools and Manufacture 170 (2021) 103804. http://doi.org/10.1016/j.ijmachtools.2021.103804.

[64] Z. Gan, O.L. Kafka, N. Parab, C. Zhao, L. Fang, O. Heinonen, T. Sun, W.K. Liu, Universal scaling laws of keyhole stability and porosity in 3D printing of metals, Nature Communications 12(1) (2021) 2379. http://doi.org/10.1038/s41467-021-22704-0.

[65] T. Chen, L. Tan, Z. Lu, H. Xu, The effect of grain orientation on nanoindentation behavior of model austenitic alloy Fe-20Cr-25Ni, Acta Materialia 138 (2017) 83-91. http://doi.org/10.1016/j.actamat.2017.07.028.

[66] Z. Xu, H. Zhang, W. Li, A. Mao, L. Wang, G. Song, Y. He, Microstructure and nanoindentation creep behavior of CoCrFeMnNi high-entropy alloy fabricated by selective laser melting, Additive Manufacturing 28 (2019) 766-771. http://doi.org/10.1016/j.addma.2019.06.012.

Chapter 8: Conclusions, General Discussion and Future Work

This thesis aimed to develop an AM processing route for HEAs via LPBF in-situ alloying. The distinct printability of FCC CoCrFeMnNi and BCC AlCoCrFeNi HEAs were revealed: The in-situ alloyed CoCrFeMnNi HEA could be densified with high *VED* and free of carking. However, the in-situ alloyed AlCoCrFeNi HEA had an inevitable cracking tendency. The mechanical properties of the in-situ alloyed CoCrFeMnNi HEA were assessed, and the ODS effect originating from oxide particles was realised. Finally, the microstructural development in the in-situ alloying process was investigated by single-track experiments. This chapter summarises the key conclusions in Chapters 4 to 7 and evaluates the contributions of this research to the current knowledge; A general discussion integrates the results from different chapters; Recommendations for future study are also raised.

8.1 Overall Conclusions

8.1.1 In-situ alloying of CoCrFeMnNi HEA

In Chapter 4, parametric studies were conducted to explore the feasible processing window of CoCrFeNi & Mn blended powder. Regarding LPBF formability, the densification of as-built CoCrFeMnNi samples was realised. Phase formation and elemental distribution were characterised and analysed. Conclusions are summarised as follows:

- The blend of pre-alloyed CoCrFeNi and elemental Mn powders had a printable *VED* range which was comparable to the pre-alloyed CoCrFeNi powder. Lack-of-fusion porosity was effectively controlled with the *VED* around 120 J/mm^3, and the densification was maintained as the *VED* increased to 259.3 J/mm^3, without significant keyhole porosity or cracking.

- The in-situ alloyed CoCrFeMnNi HEA showed an FCC single phase in XRD spectra, and the Mn peaks were not detected, indicating the Mn mainly was dissolved into the FCC matrix. EDS mapping revealed that the homogenisation of Mn was meliorated with the increasing energy input. In the sample built with the *VED* of 259.3 J/mm^3, the distribution of Mn was overall uniform with minor homogeneity. However, the burning loss of Mn was evident due to the high energy input, as the Mn content dropped from the nominal ~21 at. % to the 16.7 at. % in the in-situ alloyed sample.
- Columnar grains developed along the building direction, resulting in coarse grain structures and the strong <001> preference in the horizontal plane of in-situ alloyed CoCrFeMnNi HEA.
- Preliminary mechanical testing showed that the in-situ alloyed CoCrFeMnNi HEA possessed a microhardness of 261 HV and tensile strength of 681 MPa, which were higher than those fabricated using pre-alloyed powder. However, the fracture elongation of 12.5% suggested that the ductility of the in-situ alloyed HEA was relatively limited.

8.1.2 In-situ alloying of AlCoCrFeNi HEA

In Chapter 5, the LPBF processability of CoCrFeNi & Al blended powder was assessed. Besides the processing and characterisation techniques used in Chapter 4, a high-temperature substrate was employed to restrain cracking, and Micro-CT was used to analyse the defect in as-built samples. Conclusions are listed as follows:

- Unlike the CoCrFeNi pre-alloyed powder or CoCrFeNi & Mn blended powder, the CoCrFeNi & Al blended powder lacks LPBF printability. Porosity and cracking cannot be eliminated despite a wide processing map being explored.

- The cracking tendency in as-built AlCoCrFeNi samples was inevitable even with pre-heating at 600 ℃, which could restrain the effect of thermal stress. The cracking initiated at the Al segregations was considered the critical factor.
- The burning loss of Al was more evident than Mn, although with moderate energy input. The in-situ alloyed AlCoCrFeNi samples possessed BCC + FCC dual phases rather than a BCC single phase of the nominal equiatomic composition.
- The microhardness of in-situ alloyed AlCoCrFeNi HEA was in a wide range from 270 to 568 HV, which was located between the hardness of the soft FCC phase and hard BCC phase in the $Al_xCoCrFeNi$ HEA system.

8.1.3 In-situ alloyed ODS HEA

In Chapter 6, the mechanical properties, including microhardness, tensile and compression properties of the in-situ alloyed CoCrFeMnNi HEA, were examined and compared with the pre-alloyed ones. The forming mechanisms of oxide particles and their influences on mechanical properties were analysed. Conclusions have been raised as follows:

- The in-situ alloyed CoCrFeMnNi HEA possessed reinforced microhardness and yield strength compared with the typical values of pre-alloyed CoCrFeMnNi HEAs.
- There was significant tensile-compression asymmetry of ductility in the in-situ alloyed CoCrFeMnNi HEA. Abundant oxide particles were observed on the fracture surface of tensile samples. Micro-voids were induced by the oxide particles during the tensile deformation, thus, leading to the early failure.
- The oxide particles also hindered the glide of the HEA matrix and resulted in dislocation accumulation during deformation. The in-situ alloyed CoCrFeMnNi HEA was hence strengthened by the ODS effect.

- In general, the contributions of the Hall-Petch relationship, dislocation strengthening, and the Orowan strengthening were evaluated. The Orowan strengthening originated from the oxide particles and constituted ~44% of the theoretical yield strength.
- The oxide particles were identified as MnO and Mn_2O_3. The MnO particles formed due to in-situ oxidation during the process, while the Mn_2O_3 particles were originally the oxide layer on the Mn powder.

8.1.4 Microstructural development during the in-situ alloying process

Chapter 7 provided the results of single-track experiments to understand the microstructural development during the in-situ alloying process of CoCrFeMnNi HEA. The dimensions of single-track meltpools were studied via modelling and experimental methods. Grain growth and elemental homogenisation were systematically characterised and correlated to the processing parameters. The following conclusions have been summarised:

- The modelling methods based on the Rosenthal equation tended to underestimate the meltpool depth when the meltpool evolved into the keyhole mode, indicating the reliability of modelling methods was correlated to actual meltpool modes.
- Compared with the pre-alloyed meltpools, the addition of Mn slightly decreased the meltpool width in the *LED* range from 0.15 to 0.5 J/mm, whilst the meltpool depth stayed close.
- In-situ alloyed Mn was mainly distributed in the upper regions of keyhole meltpools, where the internal flow was dominated by the intense flow initiated by the recoil pressure rather than the Marangoni effect.

- The local homogenisation of Mn improved with the melting cycle. Therefore, remelting was recognised as the critical factor in elemental homogeneity during the in-situ alloying process.
- <001> orientations aligned with the heat flux during solidification, and resulted in the change of the dominant orientation along the scanning direction, e.g., in the single tracks scanned with 0.25-J/mm *LED*, the preferred orientation along the scanning direction changed from <001> to <101> as the scanning speed increased from 600 mm/s to 1000 mm/s.
- The reduction of hatch spacing could prolong the epitaxial growth between adjacent scanning tracks. Hence the grains were coarsened in the transverse directio.

8.2 General Discussion

As the results and conclusions in Chapters 4 to 7 are presented as individual journal papers, some outcomes from different chapters are integrated into a consolidated discussion presented below.

8.2.1 Printability of in-situ alloying

In Chapters 4 & 5, LPBF in-situ alloying approaches were carried out to fabricate equiatomic CoCrFeMnNi and AlCoCrFeNi HEAs using the blended powders of pre-alloyed CoCrFeNi and elemental Mn/Al powders. These two HEAs showed distinct printability, although their raw powders both contained ~80 wt. % of the pre-alloyed CoCrFeNi powder. The CoCrFeMnNi HEA, which has an FCC structure as the pre-alloyed CoCrFeNi powder, possesses a wide processing window comparable to that of the CoCrFeNi HEA. In contrast, the AlCoCrFeNi HEA, which transforms from FCC to BCC with Al addition, cannot avoid cracking and porosity in the as-built samples. Moreover, the cracking tendency cannot be controlled by high-temperature pre-heating at 600 °C.

As summarised in the literature review (Table 2.4), the results of this study also indicate that FCC & FCC-dominated HEAs possess better in-situ alloying printability than BCC & BCC-dominated HEAs. In addition to the differences between their mechanical properties, as discussed in the literature review, this section specifically discusses the volume change induced by the alloying element (blended powders) and phase transformation during in-situ alloying processes.

Although the actual volume change from the powder to as-built sample is difficult to measure experimentally, the molar volume (V_m) of the HEAs before and after the processes can be given by [1]:

$$V_m = \alpha^3 \frac{N_A}{N_{atoms}} \tag{8.1}$$

where α is the lattice parameter, N_A is Avogadro's constant (6.022×10^{23} mol^{-1}), and N_{atoms} is the number of atoms per lattice (2 for BCC and 4 for FCC). The lattice parameters from the XRD results at room temperature are ~3.57, ~3.60 and ~2.87 Å, respectively, for the pre-alloyed FCC CoCrFeNi, in-situ alloyed FCC CoCrFeMnNi and BCC AlCoCrFeNi HEAs. Therefore, the molar volume of the HEAs was estimated using Eq. 8.1 and is listed in Table 8.1. The molar volume of the primary HEA matrix increases by 2.5 and 3.9% with the addition of Mn and Al, respectively. Hence, the volume change caused by Al addition is more significant considering the HEA matrix. This also indicates that the lattice distortion caused by the heterogeneous element distribution can be more severe in the in-situ alloyed AlCoCrFeNi HEA samples.

Table 8.1 Room-temperature molar volume of HEAs and elements in the in-situ alloying study.

Material	Phase	V_m (cm^3/mol)
CoCrFeNi	FCC	6.85
Mn	BCC	7.35
Al	FCC	10.00
CoCrFeNi & Mn	Blended power	6.95
CoCrFeMnNi	FCC	7.02
CoCrFeNi & Al	Blended powder	7.47
AlCoCrFeNi	BCC	7.12

Moreover, using the molar volume, the molar volume change (ΔV_m) from the blended powder to the in-situ alloyed HEA can be determined by:

$$\Delta V_m = \frac{V_{m,HEA}}{\sum n_i V_{m,i}} - 1 \qquad (8.2)$$

where $V_{m,HEA}$ is the molar volume of the in-situ alloyed HEA, n_i is the molar ratio of the component powder, and $V_{m,i}$ is the corresponding molar volume of the powder. A few restrictions must be mentioned before discussing the molar volume change: (a) Both blended powders are assumed to be ideally equiatomic, so the molar ratios of CoCrFeNi powder and elemental Mn/Al powder are 80 and 20 at. %; (b) The elemental burning loss in in-situ alloyed HEAs is neglected because it varies with processing parameters, and for the as-built samples, such burning loss could lead to a reduction in the resulting volume; (c) For the BCC + FCC dual-phase structure in the in-situ alloyed AlCoCrFeNi samples, only the primary BCC phase is considered as the resulting phase; (d) All materials are compared in the solid state at room temperature, without considering thermal expansion and solid-liquid phase changes during processes. In general, the results of Eq. 8.2 show that the molar volume changes from the blended powders to their resulting HEAs are 1.0 and –4.7%, respectively, for the in-situ alloyed CoCrFeMnNi and AlCoCrFeNi HEAs.

The above results suggest that the in-situ alloying of Al leads to more significant volume changes in the powder-to-bulk and HEA matrix transitions. Particularly the –4.7% volume change from the powder to bulk indicates that considerable shrinkage of materials occurs during the solidification of meltpools. The shrinkage of materials can lead to an extra accumulation of stress compared with the pre-alloyed and Mn-addition approaches. Such shrinkage is also hard to mitigate by pre-heating. At the same time, the HEA transition with Mn addition leads to the expansion of materials (1.0%), which could neutralise the overall shrinkage of the meltpools during solidification and reduce the accumulation of thermal stress in the as-built samples. This may explain why the CoCrFeNi & Mn blended powder could be processed using higher energy density than the pre-alloyed CoCrFeNi powder.

The above discussion is based on an ideal situation without elemental vaporisation and only considers the volume change of the solid phases. A suggestion for the elemental screening of in-situ alloying can still be provided: In addition to the mechanical properties of the resulting materials, the volume change from the blended powders to as-built materials should also be modified to avoid intense shrinkage. The vaporisation of additional elements could mitigate the volume change of the resulting materials, but the trend of shrinkage/expansion is determined by the composition of the blended powder.

8.2.2 Acceleration of in-situ alloying using the single-track experiment

As summarised in the introduction chapter, one purpose of developing the in-situ alloying route is to reduce the production cycle of the customised powder, thereby improving the overall efficiency of alloy development, as well as the compositional flexibility of HEAs. However, the results in Chapters 4 & 5 show that even when using the pre-alloyed CoCrFeNi powder with a wide processing window, the printability of the blended powders can still vary drastically. Although this study was carried out as one of the early approaches in the field of LPBF in-situ alloying of HEAs, it still shows that the processing development of blended powders could be prolonged, especially considering that a much wider processing map was involved when the CoCrFeNi & Al blended powder was adopted. In Chapter 5, ~150 AlCoCrFeNi bulk samples were prepared in 7 building experiments (~25 samples on a regular 100 mm × 100 mm substrate, and ~12 samples on a 60 mm × 60 mm high-temperature substrate) to explore the processing map. In addition to the preparation of the samples, the characterisation of bulk samples is also time-consuming as they need to be handled sequentially for most characterisation methods. Such processing development is also necessary for other new pre-alloyed powders; however, elemental homogenisation is an additional challenge when blended powders are adopted. The results in Chapter 4 show that some in-situ alloyed samples with good densification still lack chemical homogeneity.

Chapter 7 reports the design of single-track experiments to reveal the microstructural development of the in-situ alloyed CoCrFeMnNi HEA, which has already shown good printability via the processing route of bulk building. However, to further accelerate the processing development of in-situ alloying, such experiments based on single tracks could be useful to narrow parameter ranges or aid in screening some compositions with poor printability.

The number of layers required for single-track samples is much less than that required for bulk samples, i.e., a single-track sample comprises no more than 15 layers while a 12-mm height bulk sample comprises 400 layers with a layer thickness of 30 μm. Furthermore, at least 300 tracks can be prepared on a 50 mm × 50 mm substrate, and set up with different laser parameters. Therefore, the required time and powder can be significantly reduced by employing single-track approaches. Moreover, as shown in Figure 8.1, 40 groups (5 tracks per group) of single-track samples can be mounted and polished together for SEM characterisation; hence, the analysis of single-track samples can be carried out more efficiently than that of bulk samples.

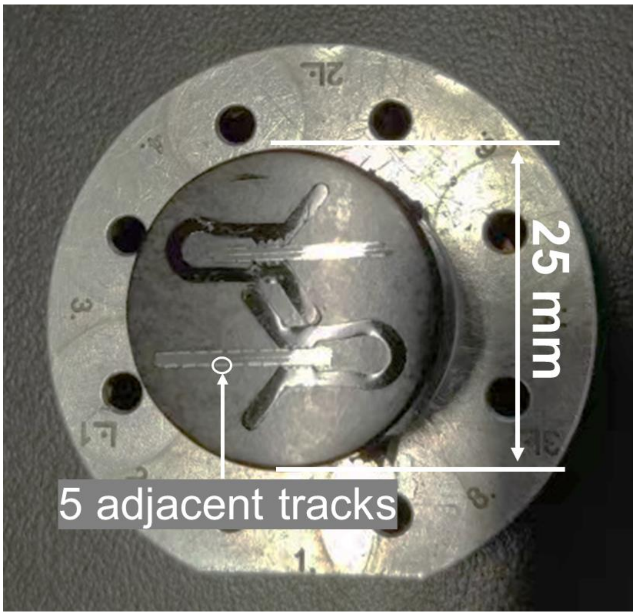

Figure 8.1 Single-track samples mounted together for SEM characterisation.

In this study, the processing development focused on blended powders based on the pre-alloyed powder of a principal HEA. Ideally, to ensure good printability of blended powders, the selected principal HEA should possess a wide processing window, similar to that of the CoCrFeNi HEA. But in actual alloy development, preliminary studies on new HEA powders may not be available. At the beginning of processing development, single-track experiments can be performed to acquire meltpool dimensions to exclude some processing parameters leading to defects like lack-of-fusion or keyhole pores. Chapter 5 shows that the bulk samples of AlCoCrFeNi HEA can only be prepared with linear energy density below ~0.12 J/mm. Such low energy density is insufficient to eliminate lack-of-fusion pores according to the single-track results in Chapter 7. It should be noted that some elements may considerably influence the resulting meltpool dimensions, although the dimensions of the CoCrFeNi and CoCrFeMnNi meltpools are very similar in this study. Although simulation methods have been developed to optimise AM processes, it is still worthwhile to verify or calibrate simulation methods through practical single-track experiments, especially considering that the use of blended powders and meltpools operated in the keyhole mode is still challenging for simulation. Single-track experiments also have a significant limitation: The stress accumulation that could lead to failure can hardly be revealed by analysing single tracks or samples with only a few layers. In the bulk building carried out in Chapters 4 & 5, severe cracking of samples was mostly observed after scanning at least tens of layers. Therefore, single-track approaches can help narrow down parameter ranges efficiently while further bulk building is still necessary to assess the printability of a new powder.

At the same time, elemental homogenisation in the in-situ alloyed samples can hardly be distinguished by observing single-track cross-sections. However, some parameters with good homogenisation can be determined after building a few more layers, i.e., some three-layer samples already show good homogenisation as discussed in Chapter 7. As the simulation of the elemental homogenisation in LPBF meltpools could be highly complicated [2], building in-situ alloyed samples with a few layers can help efficiently reveal the resulting elemental distribution in the bulk samples. Ideally, with a known meltpool depth (D) and a given layer thickness (t), the final distribution of alloying elements in the first layer can be determined after building ~D/t

layers because the beginning layer is not remelted further. For the processing map of the CoCrFeNi-based HEA, scanning of 10 layers should be sufficient to provide a preview of the elemental homogenisation in bulk samples because the deepest meltpool depth is ~300 μm and the layer thickness is 30 μm. Hence, the minimum volumetric energy density for elemental homogenisation can be established before massive bulk building experiments. Moreover, with a given processing window allowing both good printability and homogenisation, the distribution of in-situ formed oxide particles can also be investigated in this manner to tailor the mechanical properties of bulk materials.

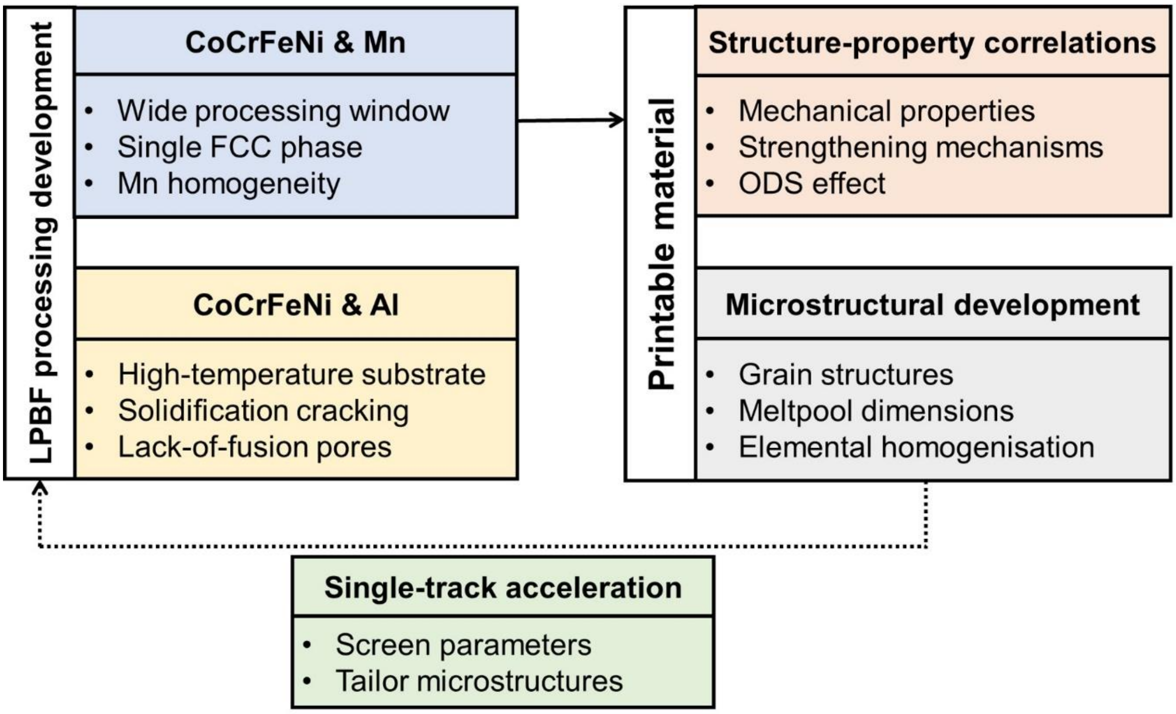

Figure 8.2 Plot illustrating the processing route in this study and the potential acceleration enabled by the understanding of microstructural development.

Figure 8.2 illustrates the processing route in this study, which starts with conventional bulk building. In general, experiments based on single tracks cannot replace bulk building in processing development. However, they can be performed in a high-throughput manner to accelerate the screening of parameter ranges and tailoring of microstructures.

8.3 Future Work

This thesis validated LPBF in-situ alloying of two representative HEAs and demonstrated that the ODS effect could be introduced via in-situ oxidation of Mn. After the reports of current work, similar approaches have been conducted by other researchers, and more CoCrFeNi-based HEA variations have been in-situ alloyed successfully. However, such in-situ alloying approaches are still at an initial stage that focuses on the printability of specific powder blends. A quantitative understanding of the in-situ alloying process could accelerate the development of HEAs with tailored microstructures and engineered performance, i.e., HEAs designed for LPBF in-situ alloying. Further research topics are proposed to improve the reliability of LPBF in-situ alloying:

- It is necessary to systemically study the burning loss of alloying elements in terms of nominal contents, powder morphology, thermal-physical properties, and processing parameters. The quantitative analysis of burning loss is critical to the compositional control of final products.
- To achieve elemental homogenisation in as-built parts requires large meltpools and dense scanning routes, which are not efficient from the consideration of productivity, especially for mass production. The homogenisation treatment of moderately homogenised parts is thus recommended as an alternative processing route.
- The modelling of fluid dynamics and thermal dynamics of in-situ alloyed meltpools is a challenging but critical field. It can help to transfer the processing windows of comprehended compositions to their variations.

- An in-situ alloying database should be founded as more and more approaches are carried out, and more composition-parameter reports are available.
- Based on the outstanding printability of FCC HEAs, more HEAs with functional additions can be validated rapidly through in-situ alloying.
- The distribution of in-situ formed oxide particles requires comprehensive study. Multiple factors, including the content and morphology of reactive elements, oxygen level in the building chamber and raw powders, as well as the processing parameters, should be considered when tailoring the distribution of oxide particles for better mechanical performance.
- For materials with wide processing windows like the CoCrFeMnNi HEA, spatial-microstructure tailoring is possible by modifying the scanning strategies and laser parameters locally according to the geometry of components.

8.4 References

[1] Z. Sun, X. Tan, C. Wang, M. Descoins, D. Mangelinck, S.B. Tor, E.A. Jägle, S. Zaefferer, D. Raabe, Reducing hot tearing by grain boundary segregation engineering in additive manufacturing: example of an AlxCoCrFeNi high-entropy alloy, Acta Materialia 204 (2021) 116505. http://doi.org/10.1016/j.actamat.2020.116505.

[2] S.L. Sing, S. Huang, G.D. Goh, G.L. Goh, C.F. Tey, J.H.K. Tan, W.Y. Yeong, Emerging metallic systems for additive manufacturing: In-situ alloying and multi-metal processing in laser powder bed fusion, Progress in Materials Science 119 (2021) 100795. http://doi.org/10.1016/j.pmatsci.2021.100795.